ISSN 1980-9743

Soils and Rocks

An International Journal of Geotechnical and Geoenvironmental Engineering

Volume 39, N. 2
May-August 2016

Soils and Rocks
Volume 39, N. 2
2016

Soils and Rocks is an International Journal of Geotechnical and Geoenvironmental Engineering published by

ABMS - Brazilian Association for Soil Mechanics and Geotechnical Engineering
Av. Queiroz Filho, 1700 – Torre A Sky, Sala 106 – Vila Hamburguesa
05319-000, São Paulo, SP
Brazil

SPG – Portuguese Geotechnical Society
LNEC, Avenida do Brasil, 101
1700-066 Lisboa
Portugal

Issue Date: *August 2016*

Issue: *400 copies and 800 online-distributed copies*

Manuscript Submission: *For review criteria and manuscript submission information, see Instructions for Authors at the end.*

SOILS and ROCKS

An International Journal of Geotechnical and Geoenvironmental Engineering

Editor Waldemar Coelho Hachich - University of São Paulo, Brazil

Co-editor Manuel Matos Fernandes - University of Porto, Portugal

Soils and Rocks publishes papers in English in the broad fields of Geotechnical Engineering, Engineering Geology and Geo-environmental Engineering. The Journal is published in April, August and December. Subscription price is US$ 90.00 per year. The journal, with the name "Solos e Rochas", was first published in 1978 by the Graduate School of Engineering, Federal University of Rio de Janeiro (COPPE-UFRJ). In 1980 it became the official magazine of the Brazilian Association for Soil Mechanics and Geotechnical Engineering (ABMS), acquiring the national character that had been the intention of its founders. In 1986 it also became the official Journal of the Brazilian Association for Engineering Geology and the Environment (ABGE) and in 1999 became the Latin American Geotechnical Journal, following the support of Latin-American representatives gathered for the Pan-American Conference of Guadalajara (1996). In 2007 the journal acquired the status of an international journal under the name of Soils and Rocks, published by the Brazilian Association for Soil Mechanics and Geotechnical Engineering (ABMS), Brazilian Association for Engineering Geology and the Environment (ABGE) and Portuguese Geotechnical Society (SPG). In 2010, ABGE decided to publish its own journal and left the partnership.

Soils and Rocks

1978,	1 (1, 2)
1979,	1 (3), 2 (1,2)
1980-1983,	3-6 (1, 2, 3)
1984,	7 (single number)
1985-1987,	8-10 (1, 2, 3)
1988-1990,	11-13 (single number)
1991-1992,	14-15 (1, 2)
1993,	16 (1, 2, 3, 4)
1994-2010,	17-33 (1, 2, 3)
2011,	34 (1, 2, 3, 4)
2012-2015,	35-38 (1, 2, 3)
2016,	**39 (1, 2,**

ISSN 1980-9743 CDU 624.131.1

ISSN 1980-9743

SOILS and ROCKS

An International Journal of Geotechnical and Geoenvironmental Engineering

Publication of

ABMS - Brazilian Association for Soil Mechanics and Geotechnical Engineering

SPG - Portuguese Geotechnical Society

Volume 39, N. 2, May-August 2016

Table of Contents

Manuel Rocha Lecture

Manuel Rocha (1913-1981) was honoured by the Portuguese Geotechnical Society with the establishment of the Lecture Series bearing his name in 1984.

Having completed the Civil Engineering Degree at the Technical University of Lisbon (1938) he did post-graduate training at MIT. He was the driving force behind the creation of the research team in Civil Engineering that would lead to the foundation of the National Laboratory for Civil Engineering (LNEC), in Lisbon. He was Head of LNEC from 1954 to 1974 and led it to the cutting edge of research in Civil Engineering.

His research work had great impact in the area of concrete dams and rock mechanics. He was the 1st President of the International Society for Rock Mechanics and organized its 1st Congress in Lisbon (1966). He did consultancy work in numerous countries. He was Honorary President of the Portuguese Geotechnical Society, having promoted with great commitment the cooperation between Portugal and Brazil in the area of Civil Engineering, and member of the National Academy of Sciences of the USA. Recognized as a brilliant researcher, scientist and professor, with a sharp, discerning intellect allied to a prodigious capacity for work and management, he was truly a man of many talents.

The 2015 Manuel Rocha Lecturer was Prof. **Ennio Marques Palmeira**, born in Rio de Janeiro, Brazil, in 1953. He is Professor of Civil Engineering at the University of Brasília, Brazil. He obtained his BSc. and MSc. in Civil Engineering from the Federal University of Rio de Janeiro (Brazil) and PhD. from the University of Oxford (UK). He is a Member of the Brazilian Academy of Sciences, Honorary Member of the International Geosynthetics Society (IGS) and received the Scientific Merit Award from the Brazilian Presidency. He was Mercer Lecturer 2006-2008 (IGS/ISSMGE) and received 50 national and international awards, including the IGS Award in two occasions. He was the Editor of Soils and Rocks, is Associate Editor of the Canadian Geotechnical Journal and Editorial Board Member of 5 other international journals. He has over 350 publications in peer-reviewed international journals, conference proceedings and book chapters. Eight of his articles received awards from international journals on geosynthetics. Several theses of his past students received national or international awards. Prof. Palmeira has been involved with research on geosynthetics for 38 years.

Soils and Rocks
v. 39, n. 2

Sustainability and Innovation in Geotechnics: Contributions from Geosynthetics

E.M. Palmeira

Abstract. Geosynthetic are construction materials with several applications in geotechnical and geoenvironmental engineering. They are usually capable of providing more practical and economical solutions than traditional construction materials. The extensive use of the latter for centuries has reduced the availability or increased the cost of such materials for constructions and developments in many regions. In addition, restrictive environmental regulations have limited or prohibited the exploitation and use of some traditional construction materials. In such situations geosynthetics can provide cost-effective and environmentally friendly solutions for geotechnical problems. Their use can be even more beneficial to the environment when associated with or to enable the use of alternative or waste materials in engineering works. Among such possibilities there are the uses of wasted tires, plastics and recycled construction and demolition residues with geosynthetics. This paper presents and discusses the use of geosynthetics associated with non-conventional construction materials in different geotechnical and geoenvironmental applications. Advantages and limitations of such combinations are discussed. The development and application of alternative low-cost geosynthetic products are also addressed.
Keywords: geosynthetics, geotechnics, alternative construction materials, residues, wastes.

1. Introduction

Geosynthetics have been increasingly used in the last decades in several geotechnical and geoenvironmental works as reinforcement, drains, filters, barriers and protective layers. As a construction material, geosynthetics are easy to transport and to install in the field and commonly provide less expensive engineering solutions which are quicker to be executed. In addition, geosynthetics may enable the use of downgrade materials or provide solutions causing less impact to the environment (less emissions of harmful gases to the atmosphere, for instance). These aspects of the use of geosynthetics have been increasingly important. The exploitation of natural resources for traditional construction materials is being rigorously controlled and restricted by environment protection regulations in many parts of the world. Solutions with geosynthetics can accommodate the use of residues or wastes (construction and demolition wastes, for instance) in situations where the use of natural materials would be more expensive, less practical or restricted. Besides, traditional construction solutions and procedures that emit excessive amounts of harmful gases and with significant energy and water consumption are becoming less and less attractive or even prohibited.

Stucki *et al.* (2011), Frischknecht *et al.* (2012) and Heerten (2012) presented examples of situations where the use of geosynthetics can be significantly beneficial to the environment in comparison with their traditional counterparts. Figures 1(a) to (c) show different geotechnical or geoenvironmental solutions for a filter in a pavement (Fig. 1a), a drainage system in a landfill cover system (Fig. 1b) and a retaining structure (Fig. 1c). The environmental benefits of using geosynthetic solutions in such cases were evaluated by Stucki *et al.* (2011) and Frischknecht *et al.* (2012). The following environmental impacts produced by each solution were assessed: acidification, eutrophication (effects of phosphate and nitrate accumulation on aquatic systems), emission of gases that increase global warming, cumulative renewable and non-renewable energy demands (CED in Figs. 1d) and water use. Comparisons for other geotechnical problems and environmental impacts are presented in Stucki *et al.* (2011) and Frischknecht *et al.* (2012). Figure 1(d) shows that the use of a geotextile filter in a pavement would produce 85% less impacts than a traditional granular filter (Fig. 1a). Reductions of the values of the environmental impacts considered between 55% and 98% were obtained when the use of a geocomposite and of a granular drain in the cover layer of a landfill were compared (Figs. 1b and d). In this case, the use of the geocomposite would consume approximately 98% less water than the gravel drainage layer. Figure 1(d) also shows comparisons between retaining wall solutions where for a geosynthetic reinforced wall the environmental impacts would be between 68% and 83% less than in the case of a conventional concrete retaining wall (Fig. 1c).

The combined use of geosynthetics and unconventional, low grade or waste materials can bring additional benefits to the environment. These are the cases where geosynthetics are used with recycled construction and demolition wastes in pavements, reinforced structures and drainage systems (Santos *et al.*, 2010), for instance. Some

Ennio Marques Palmeira, PhD, Full Professor, Departamento de Engenharia Civil e Ambiental, Universidade de Brasília, Brasilia, DF, Brazil. e-mail: palmeira@unb.br.
Invited Lecture, no discussion.

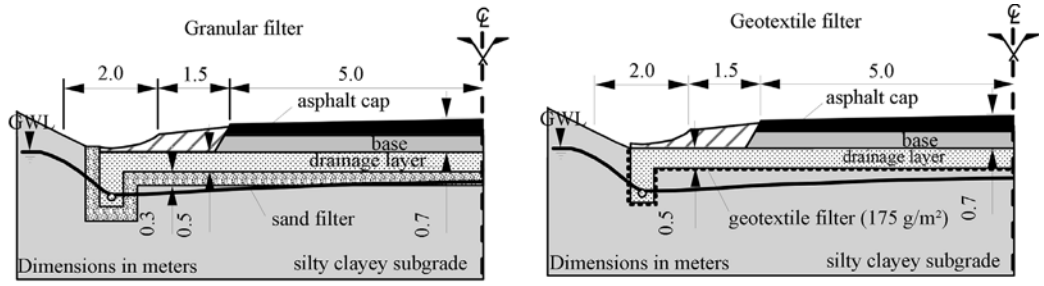

(a) Geotextile filter versus granular filter in a pavement.

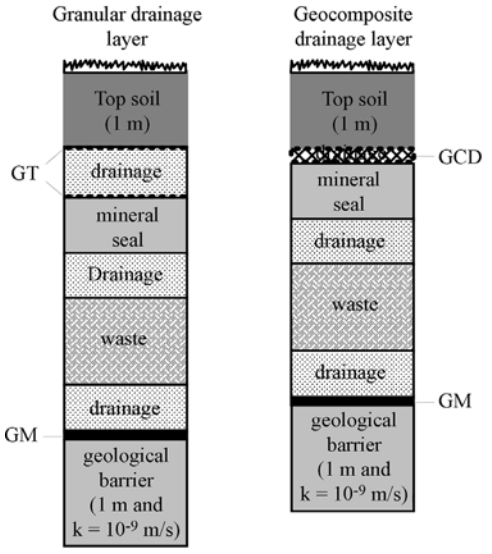

(b) Geocomposite vs. granular drain.

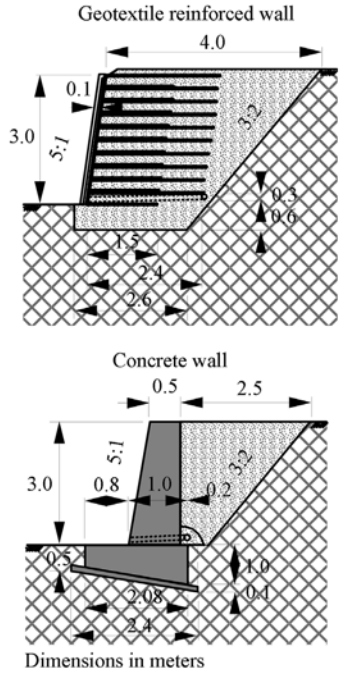

(c) Geotextile reinforced vs. concrete wall.

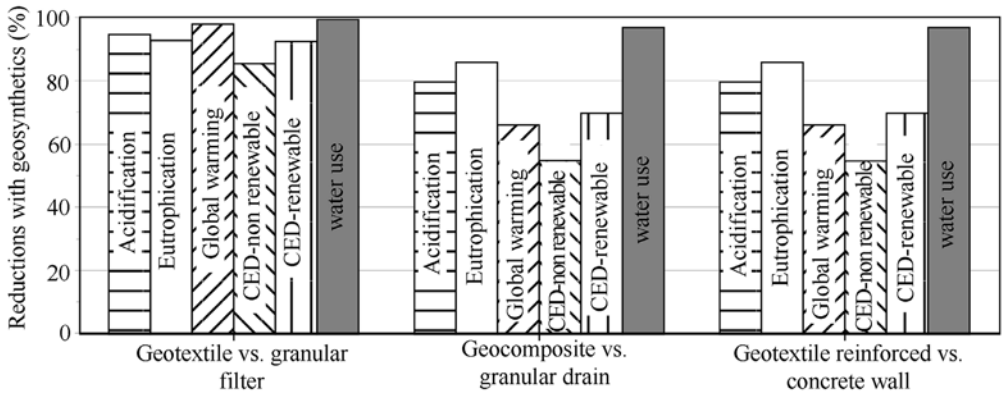

(d) Geocomposite for drainage vs. granular drainage layer in a landfill cover layer.

Figure 1 - Comparisons among environmental impacts of different geotechnical solutions (data from Stucki *et al.*, 2011; Frischknecht *et al.*, 2012).

materials commonly disposed in landfills, such as PET bottles and wasted tires, can find a better destination when employed in the manufacture of low cost or alternative geosynthetic products (Silva, 2007) or associated with traditional geosynthetic products in engineering solutions.

This paper presents and discusses the use of geosynthetics in geotechnical and geoenvironmental works with emphasis on sustainable and low cost engineering solutions. The performance of low cost geosynthetic products is also approached.

2. Geosynthetics in combination with low grade construction materials

2.1. Soil-reinforcement applications

This section presents some applications where geosynthetics were used as reinforcement in combination with low grade or alternative construction materials. The case-histories analysed address applications in unpaved roads, railways and retaining structures.

2.1.1. Geotextile reinforcement of an unpaved road on soft soil

Palmeira (1981) reported a case-history where a low grade fill material was used in combination with geotextile reinforcement in an instrumented unpaved road built on a soft clay deposit in Baixada Fluminense, Rio de Janeiro, Brazil. The typical thickness of the soft soil deposit was 10 m and its undrained strength varied between 6 kPa and 14 kPa with depth. The fill material used had 66% in mass passing the #200 sieve. Gravel fills are recommended in this type of application because of their mechanical properties and greater level of interaction with reinforcement. Thus, the material used was way outside the recommended standard fill material (usually with less than 10% in mass of particles smaller than 0.074 mm). A nonwoven geotextile was used as reinforcement. This type of geosynthetic is certainly not the best choice for this type of application, but was the only one available for the work at that time (~ 35 years ago) in Brazil. Although very extensible when tensioned under in-air conditions, nonwoven geotextile can have their tensile stiffness significantly increased when confined in soil (McGown *et al.*, 1982; Mendes, 2006; Mendes *et al.*, 2007). Figure 2 presents a view of the site during construction of the unpaved road. The road was instrumented to allow the measurements of settlements (full-profile settlement gauge), strains along the surface of the soft soil (magnetic extensometers) and strains in the reinforcement (magnetic extensometers). The road was subjected to the traffic of heavy trucks that transported fill material for the construction of a larger experimental embankment, as part of the research programme on embankments on soft soils of the Road Research Institute (IPR) of the National Department of Transportation Infrastructure (DNIT).

Figure 2 - Unpaved road construction.

Different types of reinforcement installation were investigated. Figure 3 shows schematically the 6 instrumented test sections, where it can be seen that the way in which the extremities of the reinforcement layer were anchored was varied from a reasonably short length reinforcement (low anchorage, Section S1) to a case where the extremities of the reinforcement were fixed to wood piles (Section S6) to maximize reinforcement anchorage. Sections S2 and S3 (the latter abandoned because of instrumentation damage during the first passages of trucks) served as reference unreinforced sections.

Figure 4 presents the settlement profiles of the base of the road after 200 passage of heavy trucks. It can be noted that in general less settlement was obtained in reinforced sections in comparison with the unreinforced one and that the better the anchorage of the geotextile extremities the better the road performance. A large value of settlement (local failure) was observed beneath the truck wheel in the unreinforced section S2, which explains the damage caused to the instrumentation of the other reference section (S3). This type of mechanism can be identified also in section S2 (less reinforcement anchorage), but with less intensity. However, local failures did not occur in the other reinforced test sections.

The fill thickness in each section required to sustain the traffic of trucks was also obtained at the end of the experiment (after 400 passages of trucks). This allowed assessing the reduction of fill thickness promoted by the reinforcement in comparison with the unreinforced section.

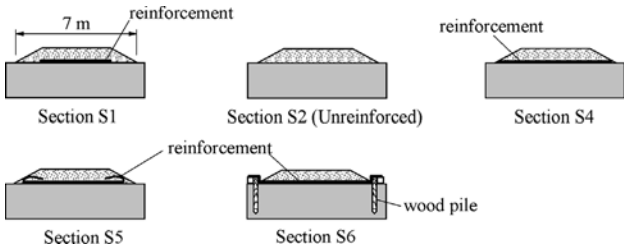

Figure 3 - Schematic arrangements of the test sections investigated (Palmeira, 1981).

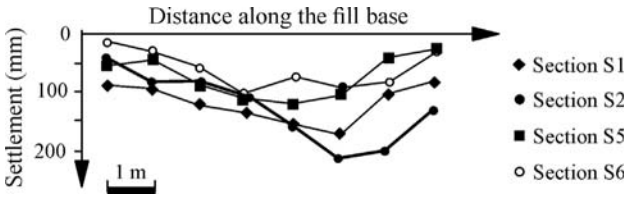

Figure 4 - Settlement profiles of the base of the road (Ramalho-Ortigao & Palmeira, 1982).

Figure 5 shows the reduction of fill thickness in some reinforced road sections. The thickness reduction varied between 9% and 23% depending on the section considered and the better the reinforcement anchorage the greater the thickness reduction. Therefore, despite the poor quality of the fill material employed besides not the best type of geosynthetic reinforcement having been used, the reinforcement presence caused significant reductions in fill thickness and savings in fill material volumes. The use of poor fill materials in reinforced soil walls is also presented and discussed Zornberg & Mitchell (1994) and in Mitchell & Zornberg (1995).

2.1.2. Recycled construction and demolition waste associated with geosynthetic reinforcement in unpaved roads

Góngora (2011) studied the use of recycled construction and demolition waste (RCDW) as fill material in reinforced and unreinforced roads using a large scale test equipment. Figure 6 shows the equipment used in the tests, which was composed of a 1000 mm diameter rigid steel tank, a reaction frame and a hydraulic system to provide the load on the fill surface. A 200 mm diameter steel platen applied the load on the road surface, which was measured by a load cell. Displacement transducers allowed the measurement of loading plate settlements. The vertical stress applied by the plate on the road surface was equal to 560 kPa, which is a typical value for truck tire calibration in Brazil. This pressure was applied under a frequency of 1 Hz. Conventional gravel and RCDW were used as fill materials for the unpaved roads and a geogrid as reinforcement was installed at the fill-subgrade interface in the reinforced case. The subgrade material consisted of a fine grained soil (62% in mass passing the #200 sieve) with California Bearing Ratio (*CBR*) of 4%. The properties of the soils and geogrid used in the tests are presented in Tables 1 and 2, respectively. The tests were interrupted when a rut depth at the fill surface of 25 mm was reached.

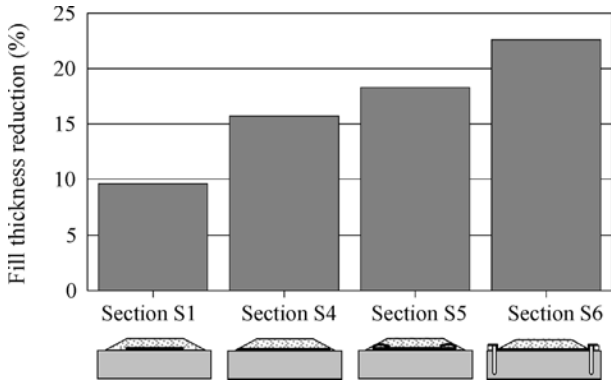

Figure 5 - Fill thickness reduction in some reinforced road sections.

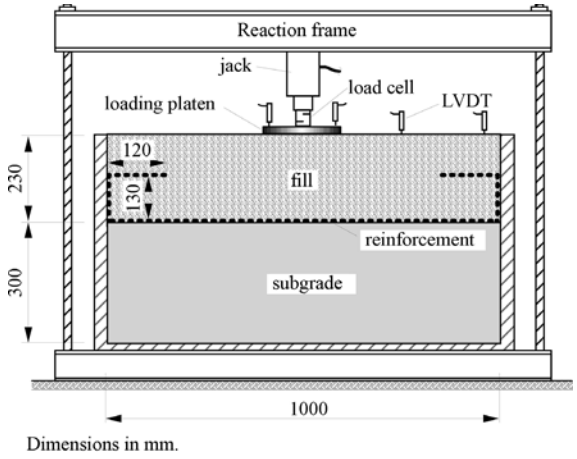

Figure 6 - Large scale tests on reinforced and unreinforced unpaved roads (Góngora & Palmeira, 2012).

Table 1 - Properties of the soils tested.

Property	Subgrade	Gravel	RCDW
D_{10} (mm)[1,2]	-	1.6	5.9
D_{50} (mm)	0.025	10.5	35.9
D_{85} (mm)	0.19	16.7	47.4
CU	-	7.1	6.8
G	2.68	2.65	2.74
w (%)	27.1	-	-
γ_d (kN/m^3)	14.0	17.6	16.9
w_L (%)	39	-	-
w_P (%)	29	-	-
CBR (%)	4.2	-	-
LAAT (%)	-	36.0	56

Notes: (1) D_n = diameter for which n percent in mass of the remaining particle diameters are smaller than that diameter, CU = Soil coefficient of uniformity = D_{60}/D_{10}, G = soil particles density, w = moisture content, γ_d = dry unit weight, w_L = liquid limit, w_P = plastic limit, CBR = California Bearing Ratio, LAAT = Los Angeles Abrasion Test, (2) Grain size analysis tests using dispersing agent for the subgrade material.

Table 2 - Properties of the geogrid.

Aperture dimensions (mm)	30 x 30
Tensile strength (kN/m)	200
Tensile stiffness at 5% strain	1500
Percentage of grid open area (%)	33
ASM (N-m/deg.)[2]	1.54

Notes: (1) Geogrid manufactured with polyester fibres protected by a PVC cover; (2) ASM = Aperture Stability Modulus, also known as in-plane torsional rigidity modulus (Kinney & Xiaolin, 1995; Kinney, 2000), obtained at 2 N-m torque, minimum value.

The results of loading plate vertical settlement *vs.* number of load repetitions for unreinforced and reinforced roads are presented in Figs. 7(a) and (b). Regarding tests on unreinforced roads (Fig. 7a), the RCDW fill performed slightly better with a 25 mm rut depth being reached for the gravel fill at a number of load repetitions (*N*) of 1630, whereas for the RCDW fill that rut depth was reached for *N* equal to 1710. The presence of the geogrid reinforcement greatly improved the performance of the roads for both types of fill, as shown in Fig. 7(b). However, the performance of the road built with RCDW was significantly better than that of the road built with the natural gravel material. In terms of Traffic Benefit Ratio (TBR, defined as the number of load repetitions of the reinforced road for a given rut depth divided by the number of load repetitions of the unreinforced road for the same rut depth), the value of TBR for the reinforced RCDW fill was equal to 33.5, whereas a TBR of 15 was obtained for the reinforced conventional gravel fill.

It should be pointed out that the ratios between geogrid aperture dimension and fill particle dimension are different for fill materials tested (Tables 1 and 2). This may have influenced the performance of the reinforced road to some extent. However, the results show that good performance may be achieved with a proper combination of geogrid reinforcement and RCDW fill in unpaved roads on weak subgrades.

Greater fill particles breakage was noted in the tests with RCDW, which is consistent with the results of Los Angeles abrasion tests (Table 1). Therefore, the possible influence of fill particle breakage should be properly considered when using RCDW as fill material in unpaved roads (Góngora & Palmeira, 2012).

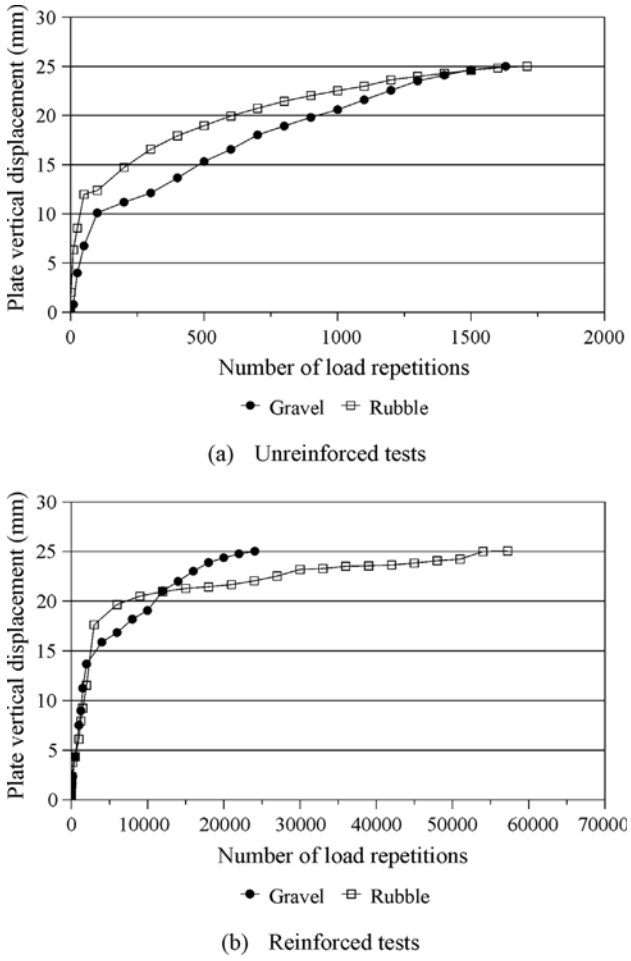

Figure 7 - Results of tests on unpaved roads built with different types of fill materials (Gongora, 2011).

2.1.3. Geosynthetic reinforcement of an alternative sub-ballast material in a railway

Geosynthetics can be used for different functions in railways, such as drainage, filtration, separation and reinforcement. Instrumented experimental sections in the Victoria-Minas railway, in Brazil, allowed a study on the use of reinforced alternative sub-ballast material (Fernandes, 2005). The railway is over 100 years old and is owned by Vale Mining Company, being 989 km long. It is responsible for 40% of the total loads carried by railways in the country with a daily traffic of 16 compositions (2 locomotives of 160 tons plus 100 wagons with approximately 100 ton each - 300 kN axle load). Different types of geosynthetics and reinforcement arrangements were investigated in six instrumented test section (S1 to S6), which were subjected to the normal traffic of the railway. The typical cross-section of the experimental sections is presented in Fig. 8.

Figure 9 shows the grain size distribution curves of the materials used in the test sections. The alternative sub-ballast material consisted of a mixture between a local soil (silty sand, 50% in mass, average particle diameter of 0.13 mm), a fine mining waste (sandy silt, 25% in mass, average particle diameter of 0.032 mm) and the traditional sub-ballast (sandy gravel, 25% in mass, average particle diameter of 5.1 mm) commonly used in railways in the region.

The experimental test section S1 was a reference section, constructed with the standard sub-ballast material. Alternative sub-ballast material was used in the construction of sections S2 to S5 with geosynthetic layers (geogrid or

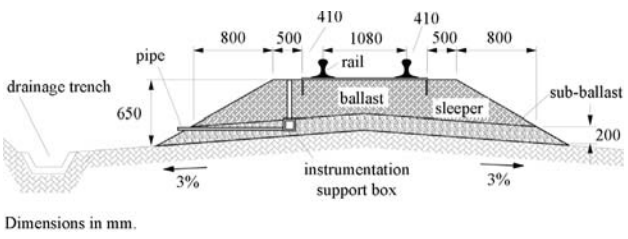

Figure 8 - Typical cross-section of the instrumented railway test sections (Fernandes *et al.*, 2008).

nonwoven geotextile) installed at different positions. The alternative sub-ballast material was also used in section S6, but without the presence of reinforcement. The same ballast material was used in all test sections. Due to space limitations, in this paper only the results obtained for test sections S1, S2, S3 and S6 are presented and discussed. Additional information can be found in Fernandes (2005) and Fernandes *et al.* (2008). Figure 10 shows schematically a longitudinal cross-section of the railway with the relevant dimensions and positions of the geogrid reinforcement in test sections S2 and S3. A view of the railway track in one of the test sections is presented in Fig. 11.

The geogrid reinforcement was manufactured from polyester with 30 mm x 30 mm square apertures, tensile strength of 65 kN/m, ultimate tensile strain of 10% and a secant tensile stiffness at 5% strain equal to 520 kN/m.

Strain-gauges in the sub-ballast, temperature transducers and moisture content transducers were employed. Benkelman beam tests were carried out as part of the research programme (Fig. 11).

Figure 12 shows results of Benkelman beam tests performed on the railway superstructure, with a two trucks locomotive with 8 axles each and total weight of 1600 kN being used to provide the necessary load on the structure. From the results it can be noted that the reinforced alternative sub-ballast material (sections S2 and S3) behaved similarly to the traditional material (section S1) in terms of vertical displacements of the track. However, large vertical displacements were obtained in section S6, where unreinforced alternative sub-ballast material was used. These results show the significant influence of the geogrid in reinforcing the alternative sub-ballast material.

The results of horizontal strains from strain gauges installed in the sub-ballast layer against the number of axles that passed on the sections are shown in Fig. 13 for the sections where the strain-gauges in that particular position survived the repetitive heavy loading from the traffic of trains. The strains in Section 3 (alternative sub-ballast reinforced with geogrid) were smaller than in the reference section S1. Section S6 showed considerably larger horizontal strains, which is consistent with its results of vertical displacements from Benkelman beam tests (Fig. 12).

Ballast particles breakage is a common occurrence in railways due to the heavy and repetitive load from the traf-

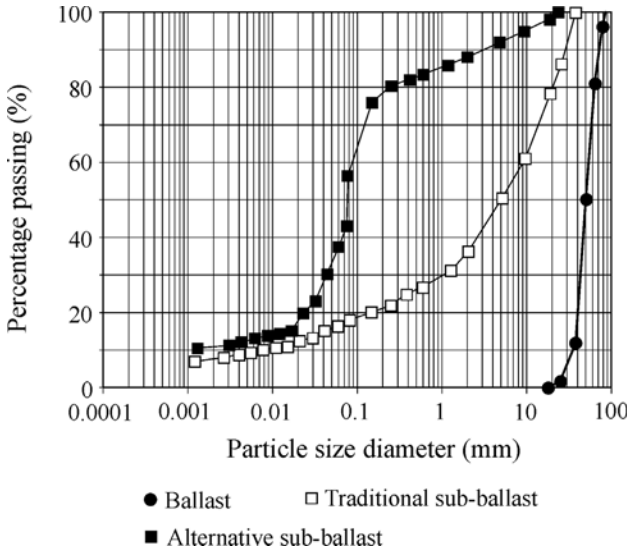

Figure 9 - Grain size distribution curves of the materials used in the experimental sections.

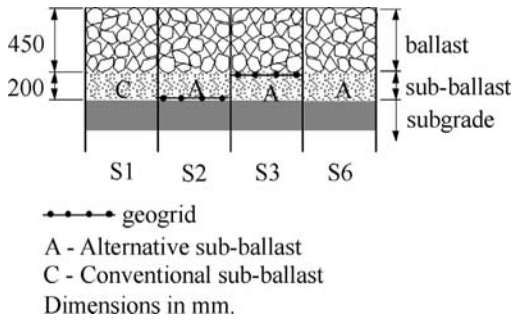

Figure 10 - Longitudinal cross-section of the track.

Figure 11 - View of one of the test sections.

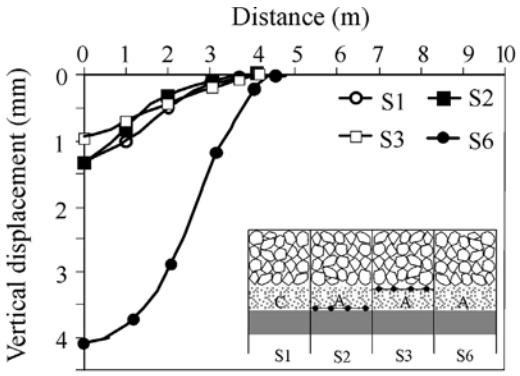

Figure 12 - Vertical displacement profiles from Benkelman beam tests (Fernandes *et al.*, 2008).

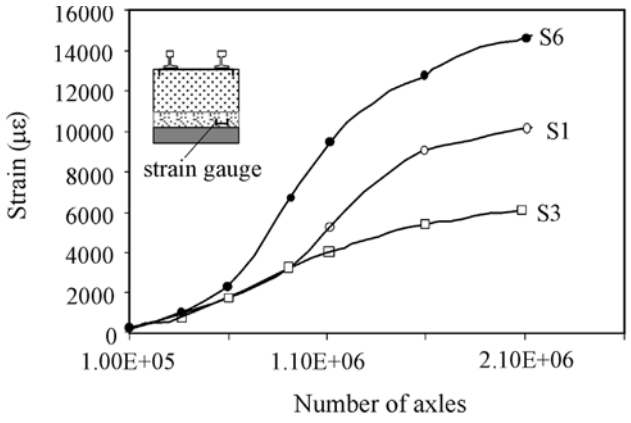

Figure 13 - Horizontal strains in the sub-ballast *vs.* number of axles for some experimental sections.

fic of trains. The percentage (B_g, in mass) of broken ballast particles were determined as per Marsal (1973) and the results obtained are depicted in Fig. 14. The results show less particle breakage in the reinforced sections S2 and S3 in comparison with unreinforced sections S1 and S6.

It should be pointed out that the monitoring period of the test sections was 2 years. So, despite the good performance of the sections reinforced with geogrid, a longer testing time would be necessary to evaluate the influence of reinforcement on the long term performance of the track. Another aspect to be considered in the long term is possible mechanical damage of the reinforcement. Significant damages were noticed in exhumed specimens of the geotextiles used in sections S4 and S5 of the same research programme (Fernandes *et al.*, 2008). However, the influence of mechanical damages can be minimized if proper design methodologies are employed. The results obtained are quite promising in showing that geosynthetic reinforcement may allow the use of low grade and low cost sub-ballast material in railway construction.

2.1.4. Recycled construction and demolition waste in geosynthetic reinforced walls

Another combined use of geosynthetics and recycled construction and demolition waste (RCDW) is described by Santos (2011). In this case, two instrumented 3.6 m high geosynthetic reinforced walls were built with RCDW backfill on collapsible porous foundation soil in the Foundations Experimental Site of the Graduate Programme of Geotechnics of the University of Brasília, Brasília, Brazil. Figure 15 shows a typical cross-section of the walls as well as the instrumentation used. One of the walls (Wall 1) was reinforced with geogrid, whereas the other was reinforced with nonwoven geotextile (Wall 2). The walls were constructed in a container bounded by lubricated reinforced masonry walls. The moving frame technique was employed to build the walls (wrapped around faces). The instrumentation allowed the measurement of settlements along the top of the backfill, face horizontal displacements, vertical and horizontal total stresses, reinforcement strains (strain-gauges and tell-tales for geogrid and geotextile strain measurements, respectively) and horizontal displacement of the foundation soil (inclinometer close to the wall toe, Fig. 15). Figure 16 shows a bird eye view of the testing facilities and Figs. 17(a) and (b) show the faces of Walls 1 and 2 after the end of construction, respectively.

The RCDR used to build the walls had particle sizes with up to 100 mm in diameter, but with approximately 95% in mass smaller than 50 mm and 12% in mass smaller than 0.074 mm (D_{50} = 2.1 mm, CU = D_{60}/D_{10} = 106). A rather light compaction was applied to the fill during construction. Geogrid reinforcement manufactured with polyester fibres,

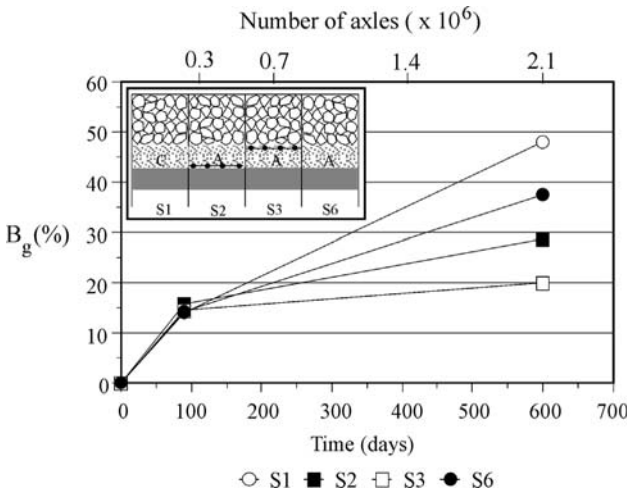

Figure 14 - Percentage of broken ballast particles *vs.* number of axles (Fernandes *et al.*, 2008).

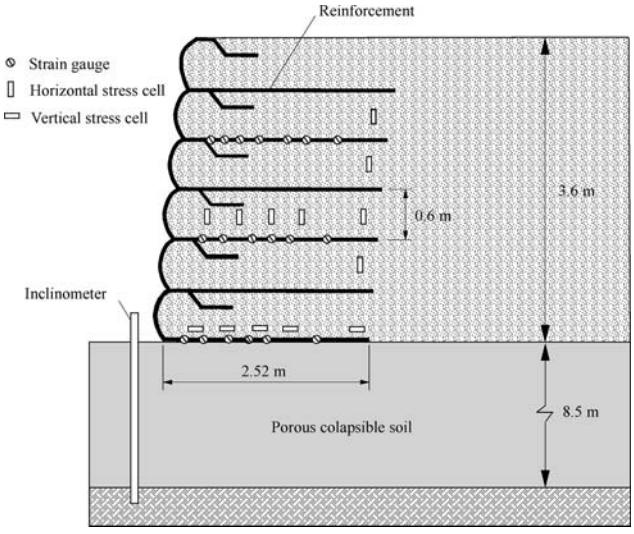

Figure 15 - Typical cross-section of the reinforced walls built with RCDW (modified from Santos, 2011).

Figure 16 - View of the reinforced walls testing facility.

Figure 17 - Faces of Walls 1 and 2 at the end of construction.

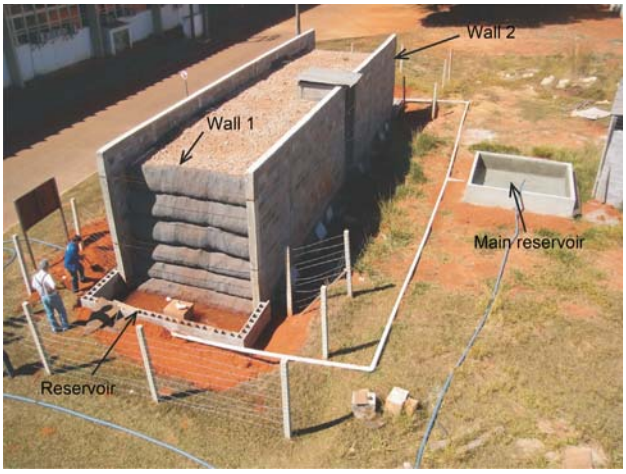

Figure 18 - General view of the test arrangement to induce foundation soil collapse by inundation (Santos *et al.*, 2014).

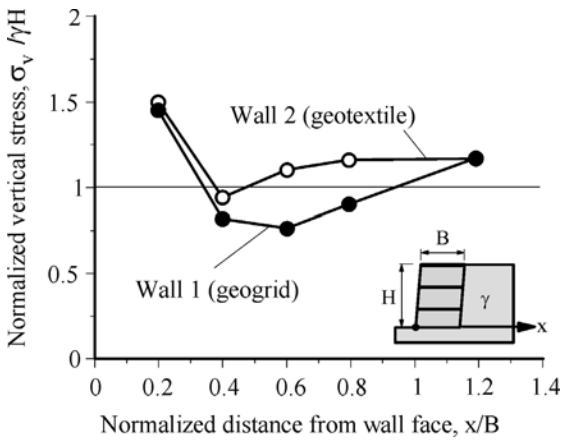

Figure 19 - Normalized vertical stress along wall base (modified from Santos *et al.*, 2014).

with tensile strength of 20 kN/m, secant tensile stiffness of 300 kN/m at 5% tensile strain and ultimate tensile strain of 12% was used as reinforcement in Wall 1. The reinforcement used in Wall 2 was a needle-punched nonwoven geotextile, made of polypropylene, with mass per unit area equal to 300 g/m^2, tensile strength of 19 kN/m and ultimate tensile strain of 70%. Although being quite extensible materials under in-air conditions, the tensile stiffness of nonwoven geotextiles can increase significantly when these materials are confined by soil (McGown *et al.*, 1982; Tupa, 1994; Mendes, 2006; Mendes *et al.*, 2007; Palmeira, 2009).The vertical spacing between reinforcement layers was equal to 0.6 m in both walls.

Because the walls were constructed on a porous collapsible foundation known as Brasília porous clay, it would be interesting also to induce the foundation soil structure collapse by increasing its moisture content by inundation. To accomplish that pools were constructed at the face of the walls, as shown in Fig. 18.

Some results obtained by Santos (2011) are presented in Figs. 19 to 22 (Santos *et al.*, 2014). Figure 19 shows the variation of vertical stresses normalised by the soil overburden pressure along the bases of the walls 107 days after construction. Some differences between results were due to less soil homogeneity along the ground surface in the region of Wall 1 (Santos *et al.*, 2014).

Figure 20 presents results of normalised settlements along the backfill surface one year after construction and after foundation soil collapse caused by inundation. Significant increases on wall settlements can be noted, particularly for Wall 1 whose foundation soil surface was more collapsible and less homogeneous than that below Wall 2.

The variations of horizontal displacements along the foundation soil depth close to the wall toe are presented in Figs. 21(a) and (b) one year after construction and after foundation soil collapse, respectively. The horizontal displacements below Wall 1 were slightly greater than those below Wall 2 in the region close to the ground surface. For greater depths the horizontal displacements of the foundation soil were similar for both walls. The additional displacements caused by foundation soil collapse were also more significant close to the ground surface.

Figures 22(a) and (b) show the tensile strains along the reinforcement length for the 3rd reinforcement layer lo-

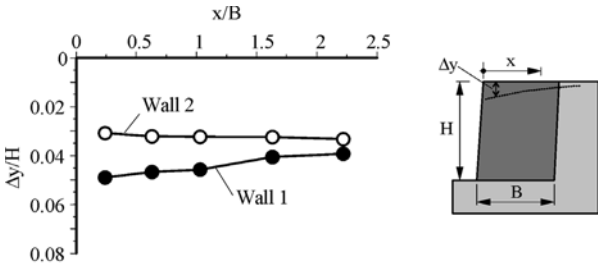

(a) 1 year after construction.

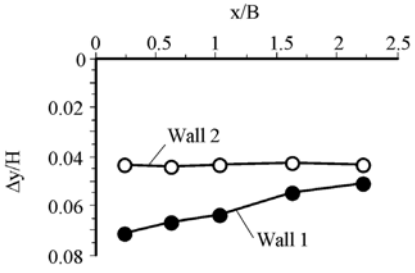

(b) After foundation soil collapse.

Figure 20 - Normalised settlements along the RCDW backfill surface (modified from Santos *et al.*, 2014).

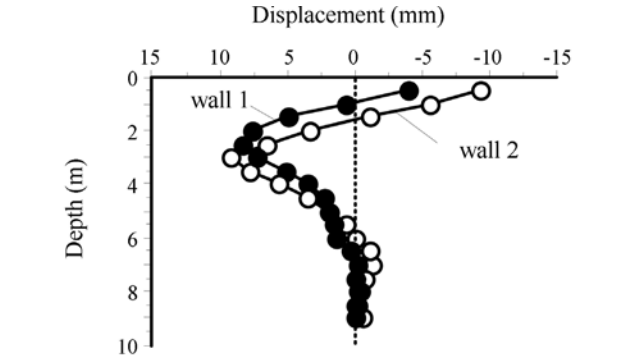

(a) 1 year after construction.

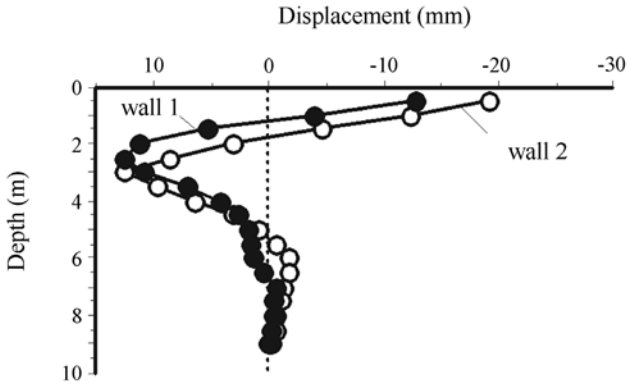

(b) After foundation soil collapse.

Figure 21 - Horizontal displacements of the foundation soil (modified from Santos *et al.*, 2014).

cated at an elevation of 1.2 m from the wall base. Considerably large strains in the geotextile reinforcement close to the wall face can be noted as a consequence of the wrapped around wall face type and the lower tensile stiffness of the geotextile under unconfined conditions. For greater distances from the wall face the strains in both types of reinforcement were similar. Foundation soil collapse influenced little the strains in the reinforcement, except for the reinforcement layer at the base of the wall, where some influence was noted (Santos *et al.*, 2014).

The results obtained show that RCDW may be successfully used as backfill material in geosynthetic reinforced walls. The ratios between maximum wall face horizontal displacement and wall height were in the range 2% to 3%, which is considered acceptable by some design codes (Santos *et al.*, 2014). It should be noted that the walls were constructed on a foundation soil prone to structural collapse when wetted and the backfill material was rather loose. Thus, under these circumstances the overall behaviour of the walls can be considered quite satisfactory in comparison with those where traditional granular fill materials are used.

3. Geosynthetics and alternative materials in geoenvironmental works

3.1. Some alternative construction materials for drainage systems

Some materials, usually considered as waste by the general public, can be combined with geosynthetics in environmental protection works. These are the cases of wasted tires, PET bottles, plastic wastes and construction

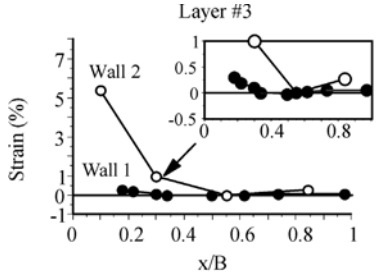

(a) 1 year after construction.

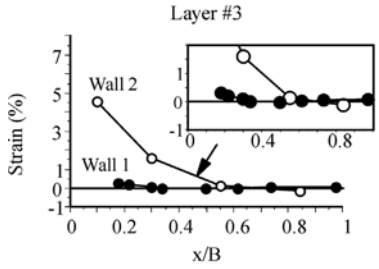

(b) After foundation soil collapse.

Figure 22 - Tensile strains along the reinforcement length - reinforcement at 1.2 m elevation (modified from Santos *et al.*, 2014).

and demolition residues. Some of these materials are presented in Fig. 23 and can occupy a significant volume in landfills. They may also be disposed in dumps, with considerable damages to the environment and hazards to human health. Because these materials are accumulated in landfill in great volumes, they can be used in the landfill itself to provide a better destination to these wastes with low cost and environmentally friendly solutions. The use of such materials may be particularly interesting in drainage systems of landfills and, in some cases, of some geotechnical works. Some examples of the combination of unconventional construction materials and geotextile filters are shown in Fig. 24.

As any construction material, unconventional ones must be studied and have their relevant engineering properties determined in order to be used in engineering projects. Depending on the material considered, this may require large scale tests to be performed. Figure 25 shows images of large scale tests carried out on tire chips and compressed PET bottles to assess compressibility and hydraulic properties of these materials.

Tables 3 to 5 present typical results of some physical, mechanical and hydraulic properties of tire chips, compressed PET bottles and construction and demolition waste (loose state) obtained in large scale tests as part of a research programme on a better utilization of waste materials in geotechnical and geoenvironmental works (Paranhos *et al.*, 2003; Palmeira *et al.*, 2006; Paranhos & Palmeira, 2002). The results show flat and round particle shapes for the tire chips and compressed PET bottles, respectively, in contrast to the irregular shape of the RCDW particles (Table 3). The mass of compressed PET bottles was considerably more permeable than those of the other materials

a) Construction and demolition waste.

b) Tires (whole, chips, shreds, etc).

c) Compressed PET bottles.

Figure 23 - Some alternative construction materials.

a) Geotextile filter combined with compressed PET bottles.

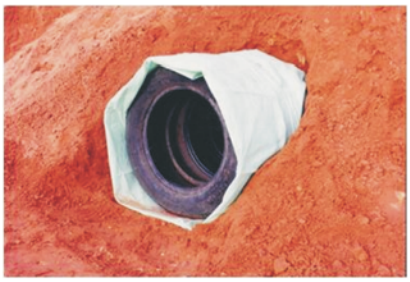

b) Geotextile filter combined with tires (whole) in Brasilia's landfill.

c) Geotextile filter combined with tire chips.

Figure 24 - Examples of alternative construction materials combined with geotextile filter in drainage systems.

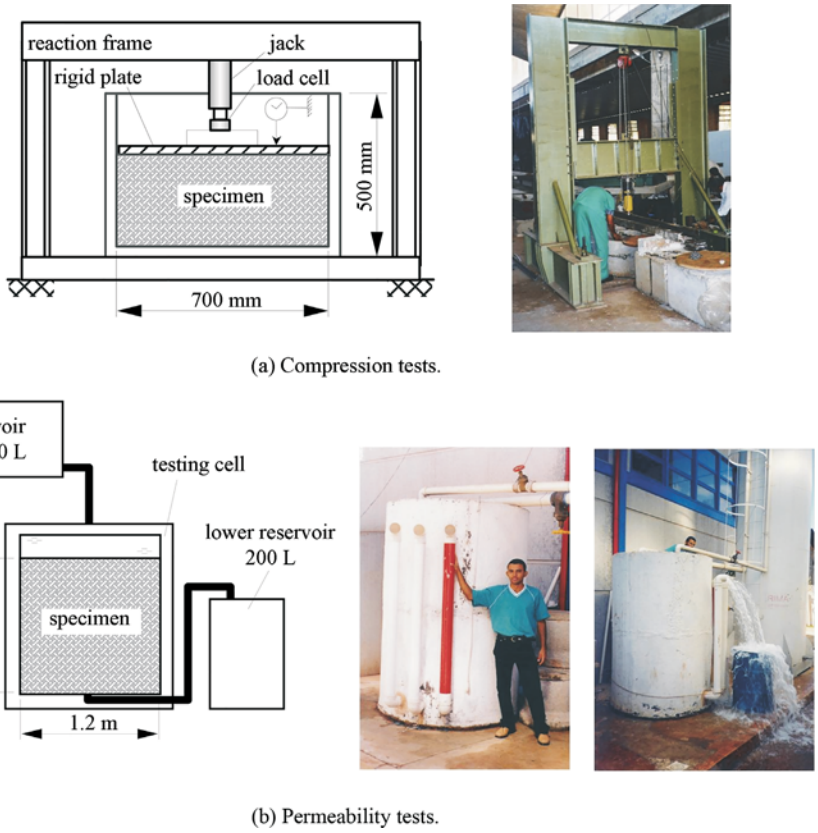

Figure 25 - Large scale tests on tire chips and compressed PET bottles.

tested (Table 4). Even under a loose state, RCDW was of the order of 10 times less compressible that the tire chips and compressed PET bottles (Table 5).

Despite presenting poorer mechanical properties than conventional construction materials, the unconventional construction materials tested can effectively substitute sand and gravel in drainage systems with significant cost savings and environmental benefits, depending on site conditions and project requirements. This is particularly beneficial in regions were conventional granular materials are expensive or cannot be used because of constraints imposed by environmental regulations.

Figures 26(a) and (b) present cross-sections of experimental domestic waste cells which conventional granular (gravel, Fig. 26a) and unconventional (whole tires and tire chips, Fig. 26b) drainage systems. The experimental cells were constructed in the Brasilia's landfill (Joquei Clube landfill), approximately 14 km from the city of Brasília, Brazil. The cells were 15 m x 15 m x 2.4 m and were capa-

Table 3 - Some physical properties (Paranhos *et al.*, 2003).

Properties	PET bottles	Tire chips	RCDR
Shape of grains	round	lamellar	irregular
D_{90} (mm)	95	45	35
CU	1.0	1.5	2.0
Density (kg/m^3)	92.0	367.0	1113.0
Void ratio	2.11	2.19	0.95

Notes: D_{90} = diameter for which 90% in mass is of the remaining diameters are smaller; CU = coefficient of uniformity (D_{60}/D_{10}).

Table 4 - Results of permeability tests (Palmeira *et al.*, 2006).

Material	Permeability coefficient (cm/s)
RCDR	10
Tire chips	15
Compressed PET bottles	50

Table 5 - Results of compressibility tests (Paranhos & Palmeira, 2002).

Material[(1)]	E_{oed} (MPa)[(2)]
RCDR	6.5[(3)]
Tire chips	0.46[(4)]
Compressed PET bottles	0.5[(4)]

Notes: (1) Specimens in a loose state; (2) E_{oed} = oedometric compression modulus; (3) In the range of linear behaviour; (4) At 50% of the maximum stress applied in the test.

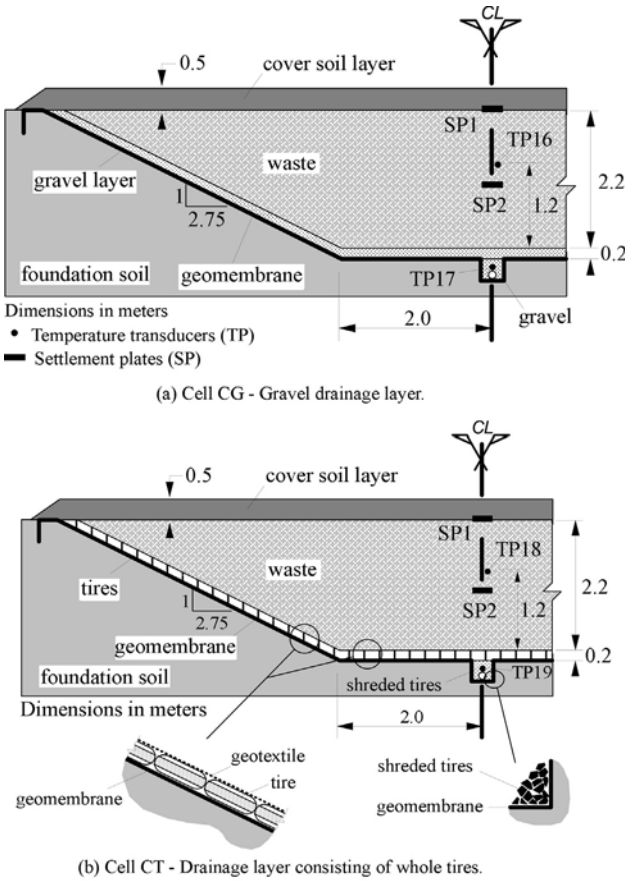

Figure 26 - Experimental domestic waste cells with different drainage systems (Junqueira *et al.*, 2006).

ble of accumulating approximately 50 tons of domestic waste each. The lining system of the cells consisted of HDPE geomembranes. The waste thickness (2.4 m) in the cells was representative of the thickness of the waste in the landfill, which at the time occupied a large area in plan, but with similar waste thickness. In the cell with the conventional drainage system (cell CG, Fig. 26a) the latter consisted of a 0.2 m thick gravel layer. No filter provision was made for this cell. Table 6 shows the properties of the gravel used in cell CG. This table also shows the relevant properties of the cover soil (0.3 m thick) used in both cells. The alternative drainage system (cell CT, Fig. 26b) consisted of whole tires arranged in plan in a regular pattern (Fig. 27) underneath a nonwoven, needle punched, geotextile filter. Table 7 presents the relevant properties of the geotextile filter used in Cell GT. At the centre of each cell there was a drainage trench (0.3 m x 0.3 m) with a perforated pipe 100 mm in diameter. In cell CG the drainage trench was filled with gravel whereas in cell CT it was filled with tire chips.

It should be noted that in a drainage system such as the one in cell CT the geotextile on the whole tires will be subjected to sagging in the central void of each tire and in

Table 6 - Properties of the soils in Cell CG.

	Gravel	Cover soil[3]
D_{10} (mm)[1]	53	—-
D_{50} (mm)	60	—-
D_{85} (mm)	65	0.20
CU[2]	1.2	—-
γ (kN/m^3)	19.7	13.4
k (cm/s)	24	0.003 to 0.009[4]

Notes: (1) D_n (for n = 10, 50 and 85) = Diameter for which n % (in mass) of the remaining particles have diameters smaller than D; (2) CU = Soil coefficient of uniformity = D_{60}/D_{10}, (3) 79% in mass passing in the # 200 sieve in tests with the use of dispersing agent; (4) Obtained in field permeability tests (Junqueira, 2000; Silva, 2004).

Table 7 - Geotextile properties.

Property	
Mass per unit area (g/m^2)	150
Thickness (mm)	1.5
Normal permeability (cm/s)	0.4
Permittivity (s^{-1})	2.5
Fitration opening size (mm)[1]	0.15

Note: (1) Obtained in hydrodynamic tests.

Figure 27 - Cell CT during construction (Junqueira *et al.*, 2006).

the space between tires. This will cause tensile forces in the geotextile layer that must be taken into account in design. A measure to minimize this mechanism would be to fill those voids with tire chips, for instance. Another important aspect that must be considered is the possibility of geotextile filter and/or geomembrane damages caused by metallic reinforcements or meshes (when present) used in the manufacture of tires.

The composition of the domestic waste in both cells was the following: 49% of organic matter, 18% of plastics,

22% of paper/cardboard, 2% of metals and 9% of other materials. Chemical tests were periodically performed on the effluents (leachate) of the cells to determine relevant parameters such as pH, chemical oxygen demand (COD), ammoniac nitrogen, nitrate content, chloride content, electrical conductivity and solids in suspension. When applicable, the chemical tests performed followed the recommendations presented in APHA (1996). Tanks stored the leachate that drained from the cells allowing leachate flow rate measurements and sample collections for physical and chemical analyses.

The instrumentation employed in the cell during the monitoring period consisted of temperature transducers and settlement plates installed at different locations in the waste mass (Fig. 26). The measurement of precipitation in the region was accomplished with a pluviometer close to the experimental cells.

Because of geometrical conditions and properties of the cover soil used the climate conditions in the region influenced markedly the generation and composition of the leachate, waste degradation and microbiological processes. The climate in the region is characterised by well-defined dry and rainy season. The rainy season takes place from October to April each year, whereas the dry season takes place from May to September. The temperature in the region varies between 18 °C and 25 °C during most of the year and the average precipitation is approximately 1350 mm/year.

Further information on materials and methodology of this research programme are reported by Junqueira (2000), Junqueira & Palmeira (2000), Silva (2004), Junqueira *et al.* (2006) and Palmeira & Silva (2007).

Some results obtained in a 2 years monitoring period are shown in Figs. 28 to 32. Figures 28 and 29 show very little, if any, differences in the ratio between effluent volume and precipitated volume on the cells (Fig. 28) and between cumulative effluent volumes (Fig. 29) from the cells, showing that the different types of drainage systems did not affected these results (Junqueira *et al.*, 2006).

Figures 30 to 32 depict the variations of some leachate parameters with time (Junqueira *et al.*, 2006). In general, the values of pH and COD of the leachate were not influenced by the type of drainage system (Figs. 30 and 31). The pH values obtained are consistent with data in the literature (Tchobanoglus *et al.*, 1993). The small differences in COD values obtained (Fig. 31) can be attributed to the variability of the waste characteristics.

Figure 32 presents the variation of suspended solids in the leachate with time for both cells, where it can be noted that the presence of the geotextile filter in cell CT, in contrast with no filter in cell CG, reduced the amount of suspended solids. Despite the greater drainage capability and pore spaces of the gravel layer, the sedimentation of solids in the drainage system with time can cause its clogging because of the lack of a filter layer. The geotextile filter in cell CT was capable of retaining part of the solids in suspension without compromising the drainage capability of the system.

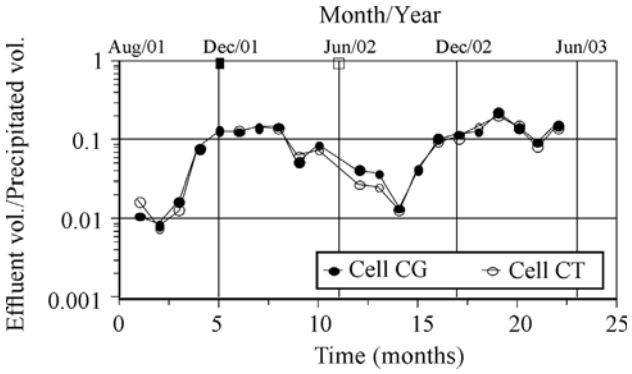

Figure 28 - Normalised effluent volume *vs.* time (Junqueira *et al.*, 2006).

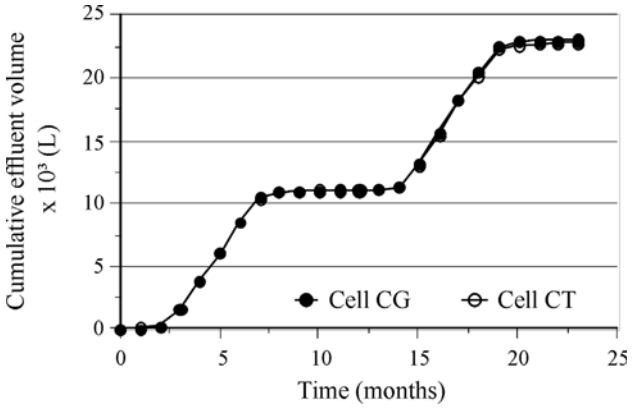

Figure 29 - Cumulative effluent volume *vs.* time (Junqueira *et al.*, 2006).

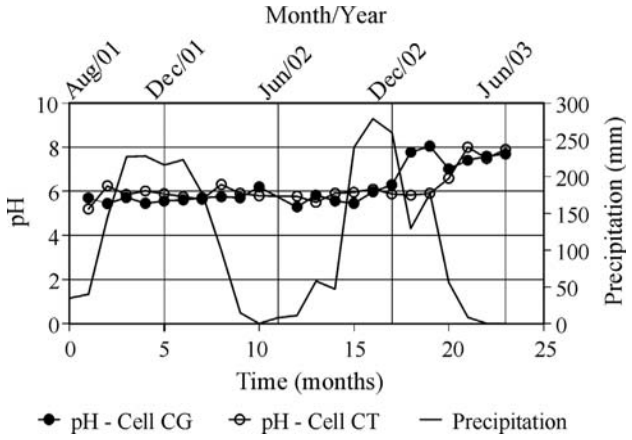

Figure 30 - Variation of effluent pH with time (Junqueira *et al.*, 2006).

3.2. Alternative materials in geosynthetic manufacture

Alternative materials, such as some of the ones described in the previous section, can be used to manufacture low cost geosynthetics. This section presents and discusses

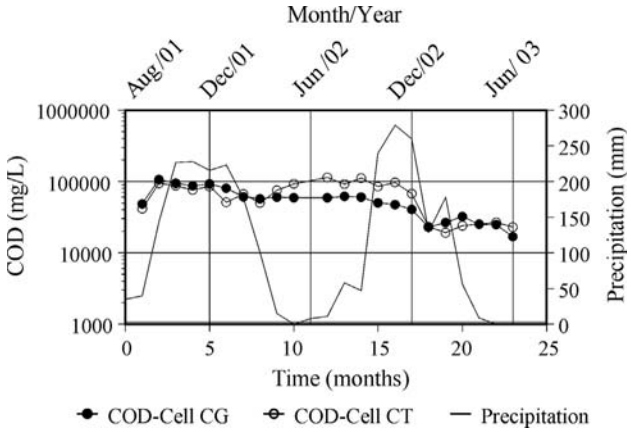

Figure 31 - Variation of effluent COD with time (Junqueira *et al.*, 2006).

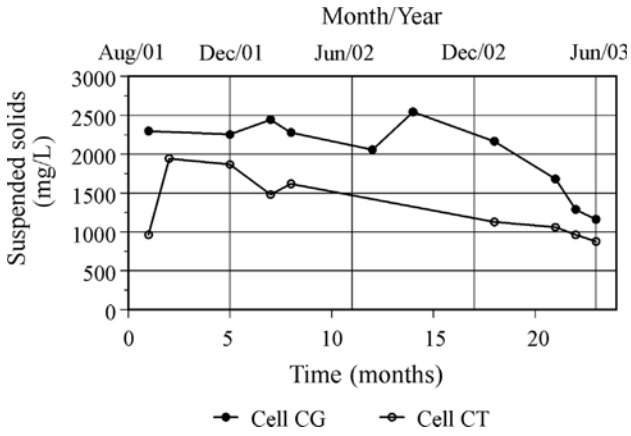

Figure 32 - Variation of suspended solids with time (Junqueira *et al.*, 2006).

some of these combinations where waste like materials can find a better use in the manufacture of alternative geosynthetic products.

Alternative low cost materials can be used to substitute geospacers in geocomposites for drainage. This provides a better use for some materials that are usually disposed in landfills besides reducing the costs of geocomposite products, which is particularly relevant in non-industrialized and less developed countries (Silva, 2007; Silva & Palmeira, 2007). Figure 33 (Silva & Palmeira, 2007) shows some alternative geocomposites whose drainage capacities were investigated by means of compression and transmissivity tests as per ASTM D4716 (ASTM, 1995). These products consisted of combinations of nonwoven geotextile filters with PET bottle caps or wasted tire strips (20 mm wide).

The results of transmissivity tests on some typical conventional and on alternative geocomposite products are shown in Figs. 34(a) to (c) in terms of discharge capacity along the geocomposite plane *vs.* vertical stress. As expected, the discharge capacity decreases with the product

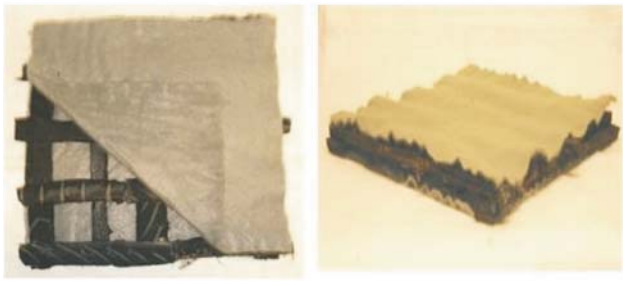

Figure 33 - Alternative geocomposites for drainage (Silva, 2007).

compression caused by increasing normal stresses and this reduction was more intense in the tests with the geocomposites with cores made of PET bottle caps and tire strips, depending on the normal stress considered and the spacing between caps or strips. Nevertheless, the results obtained for the less compressible alternative geocomposite was similar to those obtained for the conventional products (Fig. 34a). The latter can also be made cheaper if recycled materials are used in their fabrication. Despite the satisfactory results obtained in the tests with the alternative geocomposite products, it should be pointed out that besides drainage capacity factors such as durability must also be taken into account, particularly in applications in landfills, for instance.

Barrier systems can also incorporate the use of alternative materials to reduce costs. This may be the case of mixing some products with bentonite in geocomposite clay linners (GCL). Despite cost reduction, the mixing of such products can alter some relevant properties of a GCL, such as bentonite low permeability coefficient (typically less than 10^{-11} m/s) and expansibility. Nevertheless, in less critical and severe applications the use of alternative barriers may provide cost-effective and sustainable engineering solutions for environmental protection.

Figures 35(a) to (c) show the influences of the presence of alternative materials in the bentonite on some relevant properties (Viana & Palmeira, 2010; Viana *et al.*, 2011). The alternative materials mixed to the sodic bentonite were sand, lateritic clay and rubber grains (from wasted tires, Fig. 35a). Figure 35(a) shows that the internal friction angle of the hydrated mixture increases with the alternative

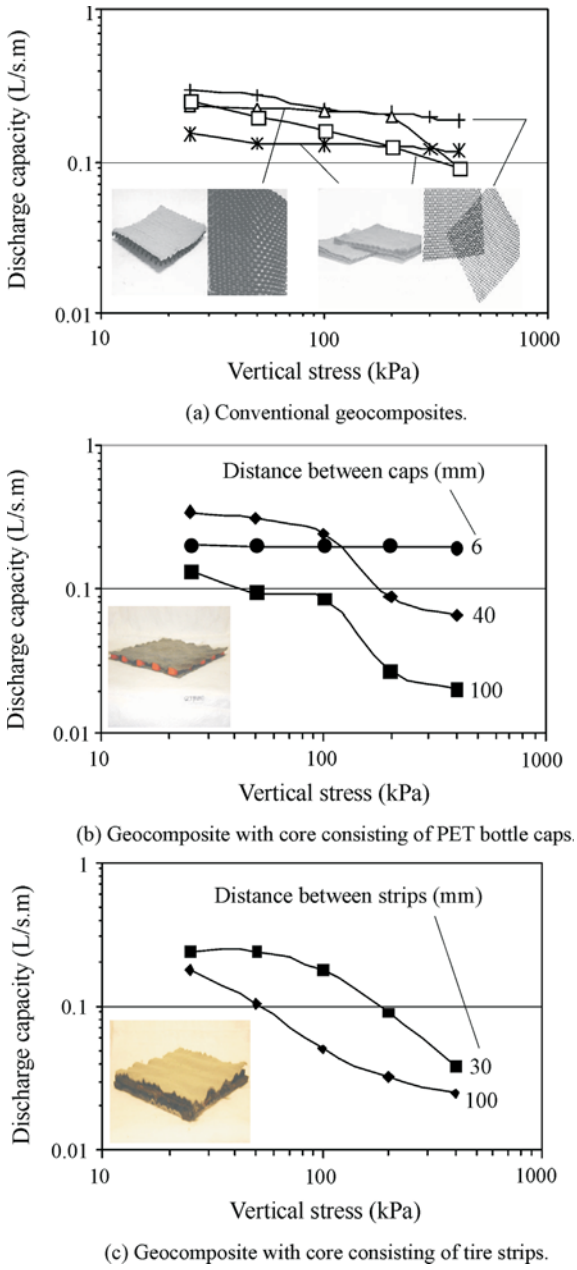

Figure 34 - Transmissivity test results (Silva & Palmeira, 2007).

material content. In this figure R_ϕ is the ratio between the tangent of the friction angle of the mixture and the tangent of the friction angle of the bentonite alone. The friction angle of the core material in a GCL is of utmost relevance in the analysis of possible internal failure when this type of product is used in slopes of waste disposal areas. Figure 35(b) shows that the mixture expansibility was reduced with the increase of the content of rubber grains and normal stress, whereas Fig. 35(c) shows that the mixture permittivity increased significantly with the content of rubber grains. The results in Figs. 35(b) and (c) are certainly potential limitations for the performance of a barrier incorporating the mixtures tested. However, the results obtained may still be satisfactory for less severe and less critical applications or when the GCL incorporating such mixtures is used as a secondary barrier or for protection (and barrier) under a geomembrane.

Vianna *et al.* (2011) also performed tests on a GCLs manufactured with mixtures between alternative materials and sodic bentonite (Fig. 36a). The GCLs were manufactured with mixtures of 50% in mass of alternative material (sand, clay or rubber grains) and 50% of bentonite. Needle-punched nonwoven geotextiles made of polyester were employed as GCL cover and carrier layers. The geotextile layers were stitched to each other to increase GCL internal strength. Two conventional GCL products (codes GCL A and GCL B) were also tested for comparisons. The tests carried out were ramp (inclined plane - 600 mm x 600 mm specimens, Fig. 36b) and expansibility tests.

Figure 36(a) presents the results of expansibility tests in terms of GCL expansion *vs.* time for the products tested. The results show that the expansibility of the alternative GCLs was of the order of half of that observed for the conventional GCLs A and B. This is consistent with the results obtained in the tests on the bentonite-alternative material mixtures reported earlier in this paper. It should be noted that the expansibility of the GCL is smaller than the free expansibility of its core due to the restrictive action of the stitches.

Figure 36(b) shows results of ramp tests on GCL A and on the alternative GCL-Rubber with a core consisting of a mixture of bentonite and rubber grains (50% in mass of rubber grains) in terms of mobilized shear stress *vs.* normal stress. It should be pointed out that results from ramp tests can be significantly more reliable than those from conventional direct shear tests under low stress levels. This may be the case of a slope in a waste disposal area where a thin cover soil layer (or granular drainage layer) is the only surcharge on the liner (Palmeira, 2009). In the ramp tests only the extremity of the carrier geotextile (at the bottom of the GCL) was fixed to the ramp in order to favour GCL internal failure. However, no internal failure was observed in tests on GCL A and on GCL-Rubber. Therefore, the results in Fig. 36(b) do not represent failure envelopes, but the representation of relationships between mobilized shear stress and normal stress on the GCL for the ramp inclinations indicated. It can be noted that similar results were obtained for alternative and conventional GCLs either in tests under dry conditions or after GCL hydration. These similar results were a consequence of the influence of the strength of the stitches crossing the GCL.

4. Some Low Cost and Simple Solutions with Geosynthetics

One of the most interesting advantages of geosynthetics is the possibility of providing simple and cost effective solutions in situations where the application of traditional engineering approaches would be significantly more

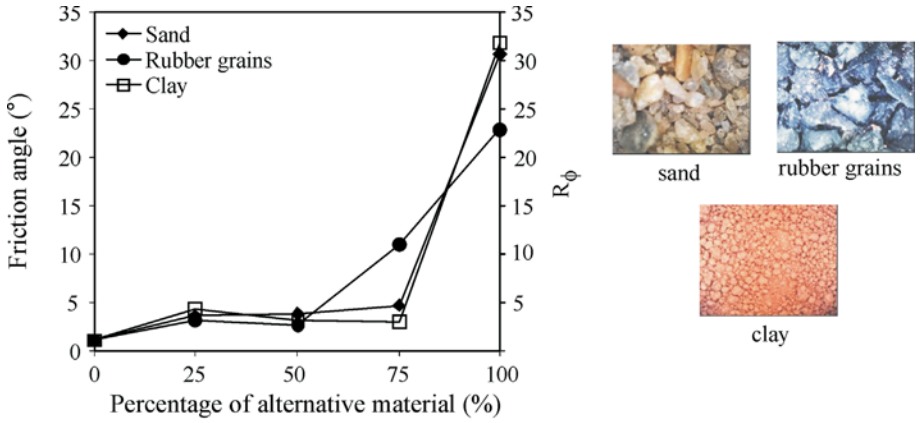

(a) Friction angle versus percentage (in mass) of alternative material.

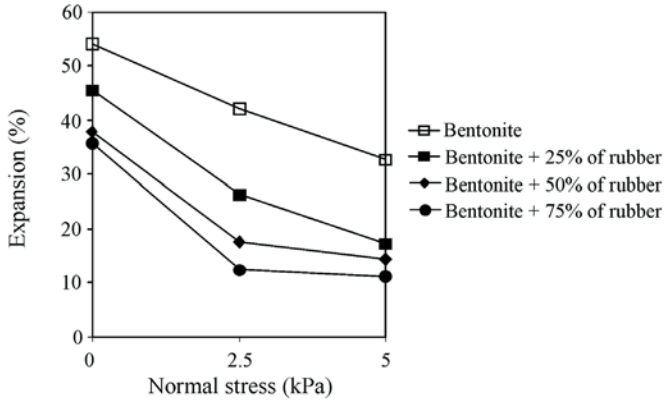

(b) Expansibility of the mixture versus normal stress.

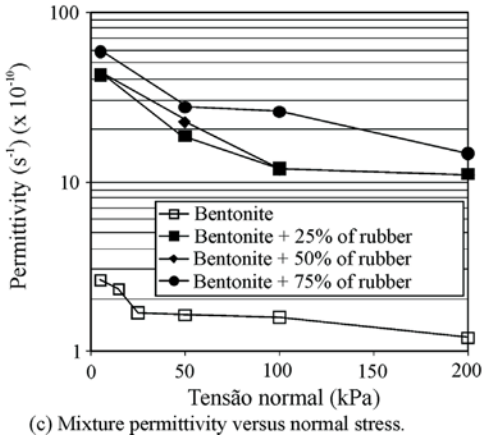

(c) Mixture permittivity versus normal stress.

Figure 35 - Influence of alternative material content on some properties of bentonite mixtures - hydrated specimens (Viana & Palmeira, 2010; Viana *et al.*, 2011).

difficult or expensive. One example of this situation is a case where scarcity of natural construction materials or lack of proper workmanship is present. Figure 37 shows silt fence solutions to treat gullies in low income or in remote areas. In this type of work a nonwoven geotextile is used to serve as barrier to sediments (Farias, 2005). If the fences are properly designed, with time the accumulation of sediments behind each barrier will tend to stop the erosive process and favour natural vegetation growth. Large scale flume tests on silt fences reported by Farias *et al.* (2006) have shown that in many situations low cost nonwoven geotextiles may be employed in this type of problem and the easy construction process allows the use of local labour.

A simple solution to improve the quality of water for remote communities is reported by Bernardes (2015). In this case the difficulty in finding or transporting proper nat-

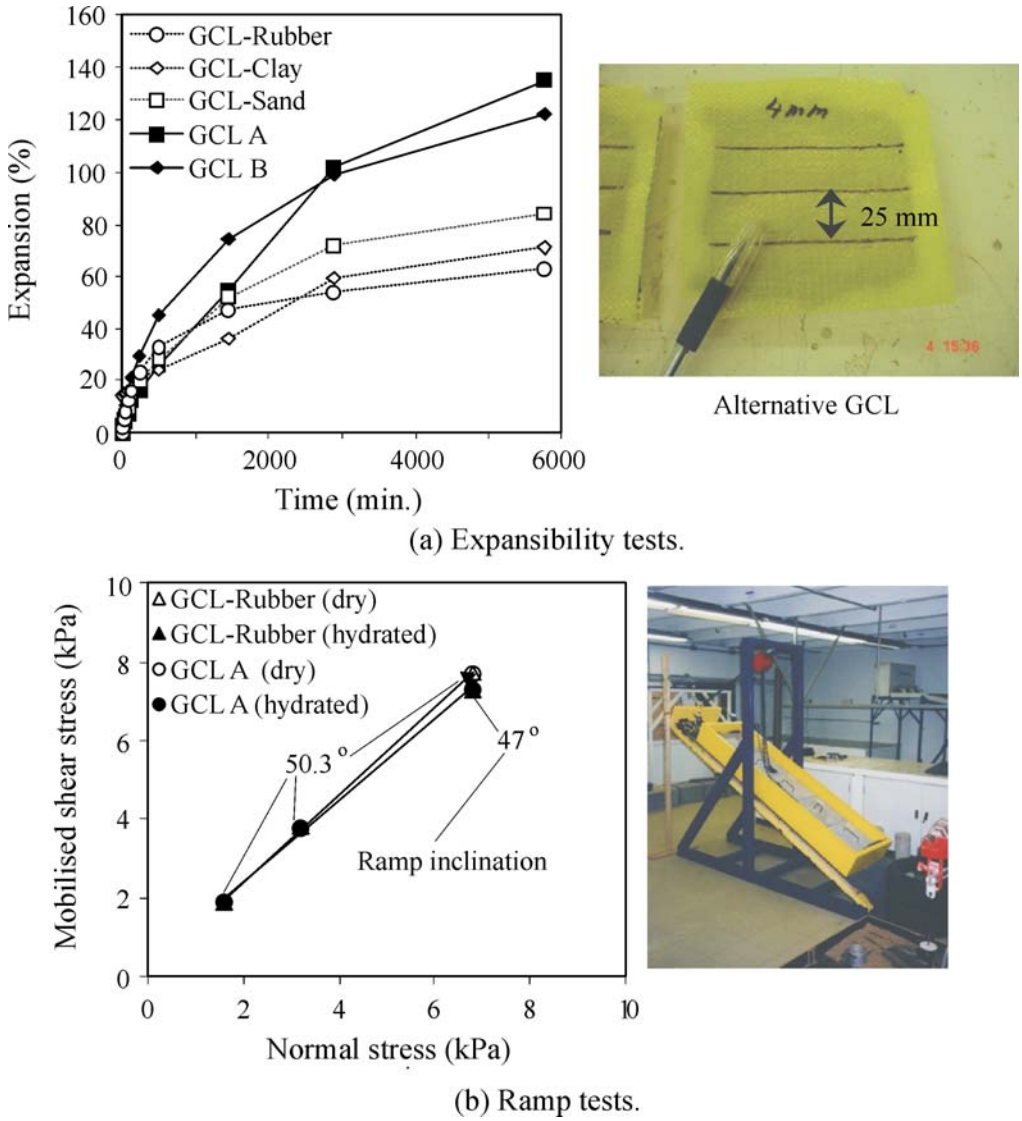

Figure 36 - Tests on an alternative GCL (Viana *et al.*, 2011).

Figure 37 - Examples of a low cost erosion control solution involving the use of geotextiles (Courtesy of Dr. Rideci J. Farias and Furnas Centrais Elétricas).

ural materials for water treatment for the community of São Raimundo, in the Brazilian Amanzon, led to the combined use of sand and geotextile filters. This community is approximately 1200 km distant (by river) from the city of Manaus, capital of the state of Amazonas, and can only be reached by boat. Therefore, the transportation of traditional construction materials is very difficult. However, light weight geotextiles can be easily transported by boat to the site. To filter the water for consumption for the community a simple filter arrangement installed at the bottom of storage tanks was tested, as schematically shown in Fig. 38(a). The filter consisted of a layer of sand enveloped by a nonwoven geotextile. Besides improving water filtration, the use of the geotextile made the construction of the system easier for members of the community. The presence of intestinal parasites in children, common due to ingestion or handling of untreated water, was monitored before and af-

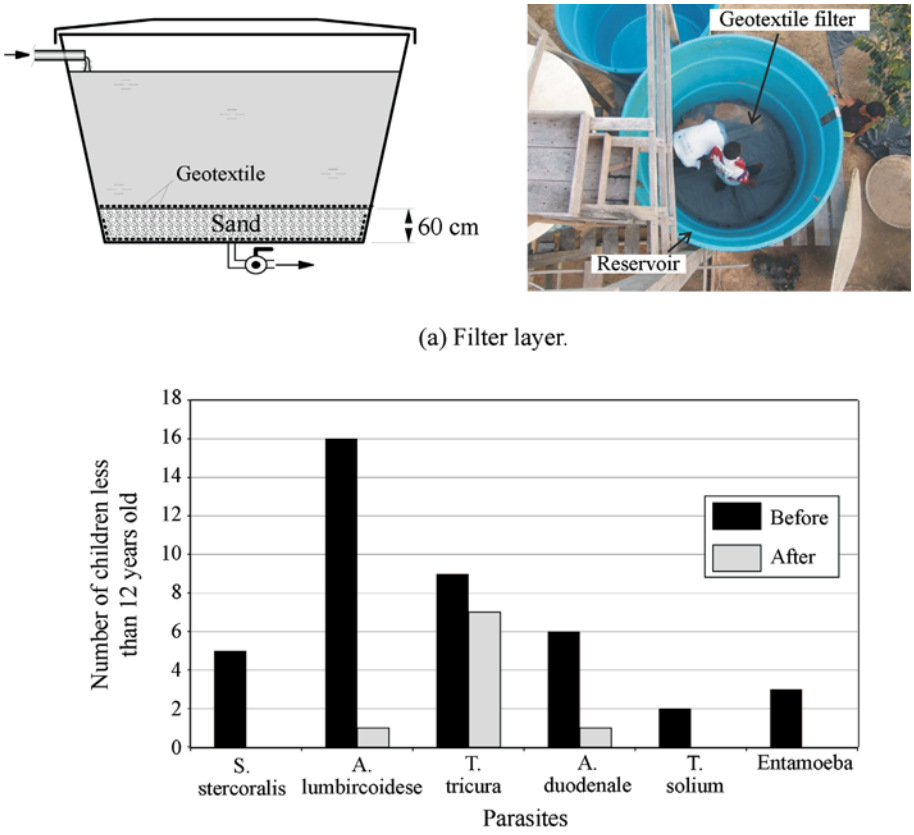

Figure 38 - Combined sand-geotextile filter for water treatment in the remote community of São Raimundo, Amazon, Brazil (Bernardes, 2015).

ter the use of the alternative filter. Figure 38(b) shows significant reductions in the contamination of children less than 12 years old by parasites in the water after the implementation of a very simple water filtering process. Infections caused by some types of parasites were simply eradicated after water filtration.

Another simple application of geotextile filters is to reduce the contaminant potential of leachates. Figure 39 shows an arrangement of vertical nonwoven geotextile layers (similar to silt fences) investigated by Silva (2014) aiming at filtering leachate from a dump in the city of Cuiabá, state of Mato Grosso, Brazil, as a preliminary treatment for the leachate before its disposal in the nature. Different types of nonwoven geotextiles (largest filtration opening size, FOS, of 0.15 mm for the lightest geotextile tested) and number of vertical panels were tested and some relevant effluent parameters of the leachate were measured after it had crossed the filter layers. A vertical sand (D_{10} = 0.18 mm, D_{50} = 0.29 mm, D_{85} = 0.5 mm, Coefficient of uniformity = 1.7) filter in a similar arrangement was also tested for comparison. According to Terzaghi's classical filter criteria the equivalent filtration opening size of the sand filter ($\cong D_{15}/4$) would be of the order of 0.048 mm, therefore smaller than that of the geotextile with mass per unit area of 600 g/m^2 (FOS = 0.060 mm).

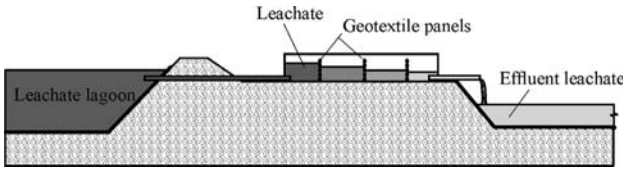

Figure 39 - Test arrangement for preliminary leachate treatment.

Figures 40(a) and (b) show the variations of chemical oxygen demand, biological oxygen demand and contents of some heavy metals (Fe, Cr and Zn) of the effluent with the mass per unit area of the geotextile filter in each panel (arrangement with three panels). Reductions of up to 40% and 18% in COD and BOD of the effluent, respectively, due to the filtering action of the geotextile can be noted (Figs. 40a and b). Under the same conditions the reduction in COD and BOD by a sand filter was approximately 9%, therefore considerably less than those of the geotextile filter. Reductions between 22% and 51% in some heavy metal contents can be noted in Fig. 40(b) and in most cases the performance of the geotextile filter was similar or better than that of the sand filter. No significant gains were noted in the re-

duction of most parameters for geotextiles with mass per unit area greater than 600 g/m^2. The toxic potential of the effluent was also reduced between 6% and 32% with the use of the geotextile filter panels, as shown in Fig. 40 (c). Also in this case the geotextile filter performed better or similarly to the sand filter in most cases. The results obtained show that the use of geotextile filter panels may provide an efficient preliminary treatment for leachate, which is more practical (the geotextile layer can be even reused after washing) and less detrimental to the environment than the use of a sand filter. This type of solution would be particularly indicated and viable for the preliminary treatment of leachate from landfills of small to medium size communities.

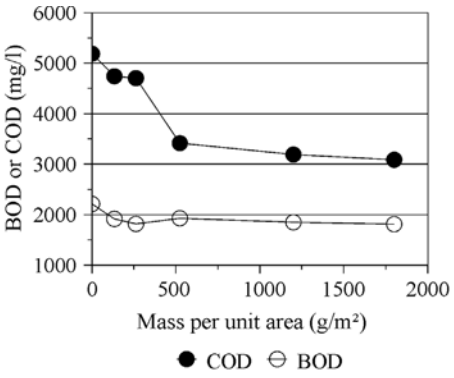

(a) Reduction in BOD and COD.

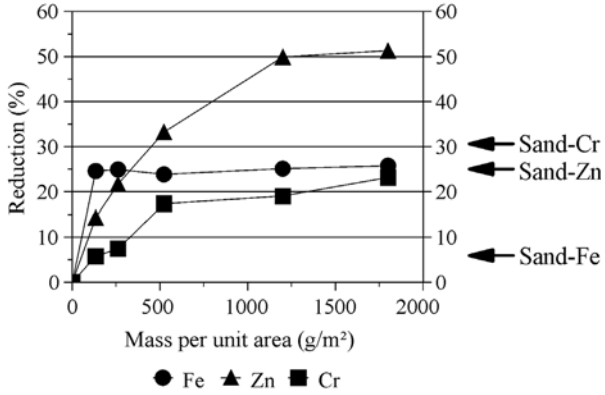

(b) Reductions in some heavy metal – Geotextile and sand filters.

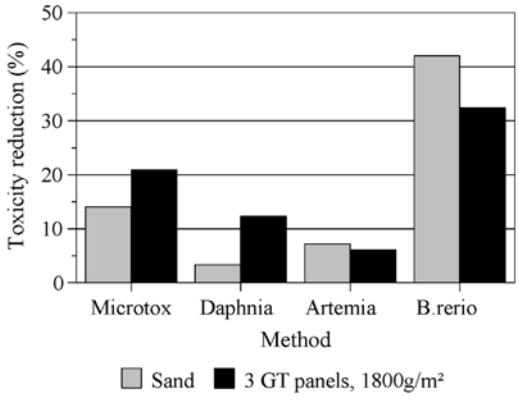

(c) Reductions in leachate toxicity.

Figure 40 - Leachate filtration with nonwoven geotextiles (Silva, 2015).

Another simple and low-cost geosynthetic application was presented by Greenwood (2012) regarding barrier systems against floods. Figure 41 shows the system where a geomembrane layer attached to a cover is elevated by the action of a float when the level of the river rises. Thus, the barrier is raised simultaneously with the water level avoiding or minimizing the consequences of the flood. The system can be hidden in pathways close to the river for aesthetic reasons. The system can also be used in urban areas.

5. Future Developments

The future certainly will require increasingly creative solutions for geotechnical and geoenvironmental works that produce less damage to the environment. Thus, engineering solutions that cause significant environmental impacts during its construction or life time will certainly be less and less acceptable by environmental protection standards. Geosynthetics may provide solutions with less impact to the environment than their counterparts and by being manufactured, future geosynthetic products will be able to incorporate innovations and developments from engineering materials science. Some more sophisticated materials used today in other fields in engineering are likely to become cheap enough to be also used in geotechnical engineering applications. This may be the case of membranes with sensors that are capable of locating highly stressed regions or perforations, as schematically presented in Fig. 42 (Borns, 1997). These sensors were developed by Sandia National Laboratories, USA, and were first incorporated in materials for defense and space applications (Borns, 1997).

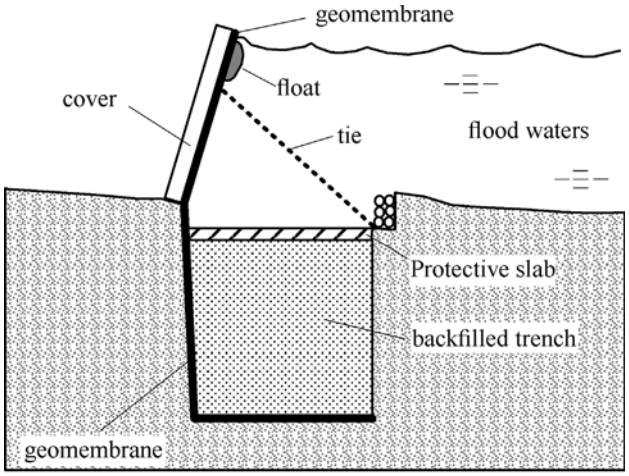

Greenwood (2012)

Figure 41 - System against floods with geomembrane.

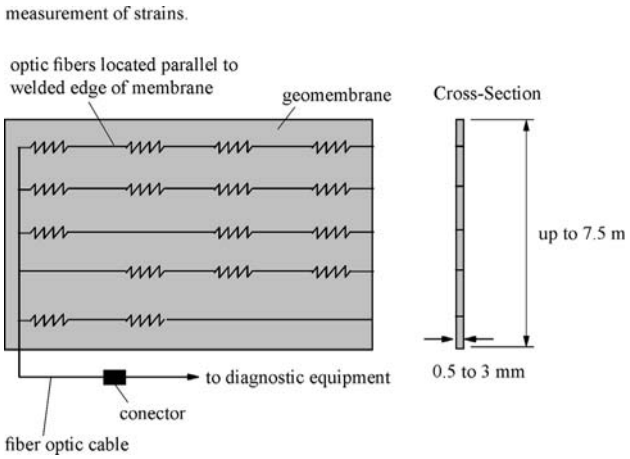

Figure 42 - Geomembrane with damage detection system (Borns, 1997).

Geosynthetic reinforcements can be manufactured today with systems that allow the measurement of strains.

Electrically conductive geosynthetics (*EKG*, Fig. 43) are already a reality and are made of a polymer material capable of conducting electricity (Jones *et al.*, 2006). The development of such material revived the use of the electro-osmosis for the acceleration of the consolidation of soft saturated fine grained soils, drainage of fine wastes, soil improvement and removal or reduction of pollutants in soils. Before *EKG* the use of electro-osmosis was very expensive or unpractical due to corrosion of metallic components of the system.

Recent research in biotechnology at Pennsylvania State University, USA, has led to the development of multiphase polymer (Fig. 44) derived from the genetic code of squid ring teeth that is capable of self-healing in contact with water (Messer 2015; Correio Braziliense, 2015). If the manufacture of a geomembrane with such polymer is feasible, such geomembrane will be able to self-seal a cut or perforation when in contact with water. So, the extension of the innovations produced in materials science to geosynthetics seems limitless. The use of nanotechnologies will also produce more sophisticated and even intelligent engi-

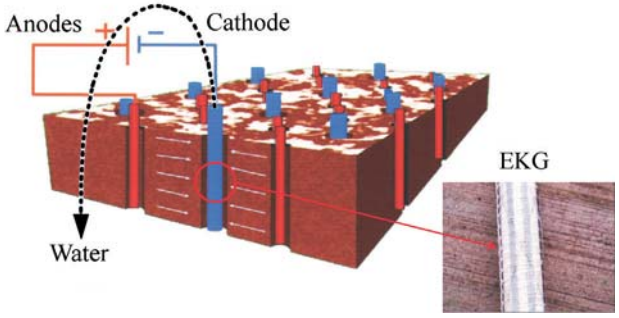

Figure 43 - Electro-osmotic consolidation with EKG (modified from Jones *et al.*, 2006).

Figure 44 - Self-healing polymer (Messer, 2015).

neering plastics that will certainly find applications in geotechnical and geoenvironmental works in the future. Regardless of the complexity or the sophistication of the product used, one of the main characteristics of geosynthetics will continue to be their capability of producing quick and easy alternative solutions for geotechnical and geoenvironmental engineering problems.

6. Conclusions

This paper presented and discussed the results of studies on sustainable solutions involving the use of geosynthetics as well as combinations of geosynthetic products with alternative construction materials or wastes in geotechnical and geoenvironmental works to enhance the beneficial effects to the environment. Geotechnical and geoenvironmental engineering solutions incorporating geosynthetics can significantly reduce the impacts to the environment in comparison with their traditional counterparts. Geosynthetics can also provide simple and sustainable solutions for a variety of problems. Combinations of geosynthetics with alternative construction materials, residues or wastes may reduce construction costs and the volumes occupied by wastes in landfills. Simple solutions incorporating geosynthetics can also have important repercussions in solving problems in remote areas and for erosion and flood controls, where traditional natural materials or specialized labour are not available. The main conclusions of the studies and case-histories reported in this paper are summarised as follows.

Several residues commonly viewed as waste can be employed in a more environmentally friendly way in civil engineering with favourable repercussions on cost reductions and in the reduction of environmental hazards. Materials such as wasted tires, construction and demolition waste and PET bottles can be recycled or properly processed in order to be used as fill or drainage materials in constructions.

Compressed PET bottles or tire chips and geotextile filters can be combined in drainage systems. The former materials can substitute good quality granular drainage materials, which may be scarce, very expensive or have their use restricted by environmental regulations. Whole tires

can also be used to form drainage blankets underneath a geotextile filter in drainage systems of landfills.

Research results have shown that geosynthetic reinforced walls with recycled construction and demolition waste (RCD-RR) backfills have performed very well. Similar good performance of RCD-R was observed in tests on geogrid reinforced unpaved roads constructed on weak subgrade. Field tests on geosynthetic reinforced alternative ballast consisting of a mixture of nonstandard material and mine waste also yielded to very good performance of a railway track. The use of such materials can reduce construction costs particularly in regions were good quality fill materials are scarce or expensive.

Low cost geosynthetics can also be produced with the incorporation or combination with alternative materials. Results of tests on geocomposites for drainage incorporating PET bottle caps and tire strips as drainage were comparable to those obtained for conventional geocomposite products. Regarding barrier layers in environmental or hydraulic applications, rubber grains from wasted tires can be mixed to bentonite to reduce the cost of GCLs. Despite the increase in permittivity and reduction in expansibility of a GCL incorporating rubber grains in comparison with standard products, the test results obtained suggest that such alternative GCLs can be employed in less critical situations or as protective or secondary barrier layers underneath geomembranes.

A better use of residues and wastes in engineering works is certainly important for the reduction of natural material exploitation and for the preservation of the environment. For such uses it is necessary the existence of an efficient and economical system for the collection, recycling, processing and supplying of these residues for geotechnical and geoenvironmental works. The combination of geosynthetics with such residues may provide less expensive and more environmentally friendly solutions.

Despite the benefits of using residues in engineering projects as discussed above, one has to bear in mind that the excessive demand for a particular type of residue will increase its cost, which may compromise its use in some applications. Thus, a given residue utilization that is feasible in a geotechnical engineering application today may not be so in the future, depending on the competition for that residue from other industries. Besides, some residues or their degradation may be hazardous to the soil or ground water. Therefore, thorough evaluation of the benefits, limitations and impacts caused by the use of the residue must be made before hand. However, the demand for a better use of residues in civil engineering will certainly increase in the future, requiring ingenuity and innovative solutions for the application of such materials in civil engineering works.

Materials and polymer sciences will keep on producing new and more powerful geosynthetic products for engineering applications. With the continuous development of polymers aided by new nanotechnologies, more and more sophisticated geosynthetic products can be foreseen in the future. Despite increasing complexity of the product itself the geosynthetics will certainly maintain their character as effective and simple materials to be used in geotechnical and geoenvironmental works.

Acknowledgments

First, the author would like to thank the Portuguese Geotechnical Society (SPG) for the invitation to deliver the 32nd Manuel Rocha Lecture. He would also like to thank the support from the following institutions that funded or contributed in different ways to the research activities described in this paper: University of Brasilia, CNPq-National Council for Scientific and Technological Development, CAPES-Ministry of Education, FAP/DF-Foundation for Research Support of the Federal District and Finatec/UnB. The author is also indebted to the following geosynthetics manufacturers for their support: BBA, Huesker, Maccaferri, Nortene, Ober and Sansuy. He also thanks the contribution and information provided by Prof. Ricardo S. Bernardes and Carolina Bernardes, from the University of Brasília, on the São Raimundo Community project. The contributions from several past and present research students are also appreciated.

References

APHA (1996). Standard Methods for the Examination of Water and Wastewater. 20th edition. American Public Health Association, Washington, DC.

ASTM (1995). Test method for constant head hydraulic transmissivity (in-plane flow) of geotextiles and geotextile related products - ASTM D4716. American Society for Testing and Materials, West Conshohocken, PA, USA.

Bernardes, R.S. (2015). Personal communication.

Borns, D.J. (1997). Geomembrane with incorporated optical fiber sensors for geotechnical and environmental applications. Proc. International Containment Technology Conference, St. Petersburg, Florida, p. 1067-1073.

Correio Braziliense (2015). A fiber that regenerates. Correio Braziliense, Brasília, DF, Brazil (in Portuguese).

Farias, R.J.C. (2005). The Use of Geosynthetics in Erosion Control Works. PhD. Thesis, Graduate Programme of Geotechnics, University of Brasilia, DF, 186 p. (in Portuguese).

Farias, R.J.C.; Palmeira, E.M. & Carvalho, J.C. (2006). Performance of geotextile silt fences in large flume tests. Geosynthetics International, Thomas Telford Publ., UK, 13(3):133-144.

Fernandes, G. (2005). Behaviour of Geosynthetic Reinforced Railway Tracks Constructed with Fine Grained Soils and Mining Wastes. PhD. Thesis, Graduate Programme of Geotechnics, University of Brasilia, Brasilia, 253 p. (in Portuguese).

Fernandes, G.; Palmeira, E.M. & Gomes, R.C. (2008). Performance of geosynthetic reinforced alternative subballast material in a railway track. Geosynthetics International, 15(5):311-321.

Frischknecht, R.; Stucki, M.; Büsser, S. & Itten, R. (2012). Comparative life cycle assessment of geosynthetics *vs.* conventional construction materials. Ground Engineering, 45(10):24-28.

Gongora, I.A.G. (2011). Utilization of Geosynthetics as Reinforcement in Unpaved Roads: Influence of the Type of Reinforcement and Fill Material. MSc. Dissertation, University of Brasilia, 86 p. (in Portuguese).

Gongora, I.A.G. & Palmeira, E.M. (2012). Influence of fill and geogrid characteristics on the performance of unpaved roads on weak subgrades. Accepted for publication in Geosynthetics International, Thomas Telford, UK.

Greenwood, J. (2012). Have geosynthetics changed geotechnical engineering? BGA-IGS Lecture 2012, London, UK.

Jones, C.J.F.P.; Glendinning, S.; Huntley, D.T. & Lamont-Black, J. (2006). Soil consolidation and strengthening using electrokinetic geosynthetics - Concepts and analysis.. J. Kuwano & J. Koseki (eds) Geosynthetics. Millpress, Rotterdam, v. 1, p. 411-414.

Junqueira, F.F. (2000). Analyses of Domestic Waste Behaviour and Draining Systems with Reference to the Joquei Club Dump. PhD. Thesis, Graduate Programme on Geotechnical Engineering, University of Brasilia, 288 p. (in Portuguese).

Junqueira, F.F. & Palmeira, E.M. (2000). A study on the behaviour of domestic waste under controlled conditions. Proc. 5th International Symposium on Environmental Geotechnology and Global Sustainable Development. Belo Horizonte, MG, 8 p.

Junqueira, F.F.; Palmeira, E.M. & Silva, A.R.L. (2006). Performance of drainage systems incorporating geosynthetics and their effect on leachate properties. Geotextiles and Geomembranes, 24(5):311-324.

Kinney, T.C. (2000). Standard Test Method for Determining the "Aperture Stability Modulus" of a Geogrid. Shannon & Wilson, Inc., Seattle, 5 p.

Kinney, T.C. & Xiaolin, Y. (1995). Geogrid aperture rigidity by in-plane rotation. Proc. Geosynthetics'95, Nashville, Tennessee, v. 2, pp. 525-537.

Marsal, R.J. (1973). Mechanical properties of rockfill. R.C. Hirschfeld & S.J. Poulos (eds) Embankment Dam Engineering - Casagrande Volume. John Wiley & Sons, New York, pp. 109-200.

McGown, A.; Andrawes, K.Z. & Kabir, M.H. (1982). Load-extension testing of geotextiles confined in soil. Proc. 2nd International Conference on Geotextiles, Las Vegas, v. 3, pp. 793-798.

Mendes, M.J.A. (2006). Load-Deformation Behaviour of Geotextiles Under Confinement. MSc. Dissertation, University of Brasília, Brasília, 151 p. (in Portuguese).

Mendes, M.J.A.; Palmeira, E.M. & Matheus, E. (2007). Some factors affecting the in-soil load-strain behaviour of virgin and damaged nonwoven geotextiles. Geosynthetics International, 14(1):39-50.

Messer, A.E. (2015). Water heals a bioplastic. Penn State News, University of Pennsylvania, USC, at http://news.psu.edu/story/367826/2015/09/01/research/water-heals-bioplastic, September 1st 2015.

Mitchell, J.K. & Zornberg, J.G. (1995). Reinforced soil structures with poorly draining backfills. Part II: Case histories and applications. Geosynthetics International, 2(1):265-307.

Palmeira, E.M. (1981). The Use of Geotextiles for the Reinforcement of Embankments on Soft Soils. MSc. Thesis, Coppe/Federal University of Rio de Janeiro, 282 p. (in Portuguese).

Palmeira, E.M. (2009). Soil-geosynthetic interaction: Modelling and analysis. Geotextiles and Geomembranes, 27(5):368-390.

Palmeira, E.M.; Silva, A.R.L. & Paranhos, H. (2006). Recycled and alternative materials in drainage systems of waste disposal areas. Proc. 5th International Conference on Environmental Geotechnics, Cardiff, v. 2, pp. 1511-1518.

Palmeira, E.M. & Silva, A.R.L. (2007). A study on the behaviour of alternative drainage systems in landfills. Proc. XI International Waste Management and Landfill Symposium - Sardinia 2007, Sardinia, 10 p.

Paranhos, H.S. & Palmeira, E.M. (2002). Utilization of Wasted PET Bottles, Rubble and Tires as Drainage Materials in Geotechnical and Geoenvironmental Works. Research Report, RHAE/CNPq Programme, Graduate Programme of Geotechnics, University of Brasilia, Brasilia, 89 p. (in Portuguese).

Paranhos, H.S.; Palmeira, E.M. & Silva, A.R.L. (2003). Utilization of alternative materials in drainage and filtration in waste disposal areas. Brazilian Conference on Geenvironmental Engineering/REGEO 2003, Porto Alegre, RS, 7 p. (in Portuguese).

Ramalho-Ortigao, J.A. & Palmeira, E.M. (1982). Geotextile performance at an access road on soft ground near Rio de Janeiro. Proc. 2nd International Conference on Geotextiles, Las Vegas, v. 1, pp. 353-358.

Santos, E.C.G. (2011). Experimental Evaluation of Reinforced Walls Built with Recycled Construction and Demolition Residues (RCDR) and Fine Soil. PhD. Thesis, Graduate Programme of Geotechnics, University of Brasilia, Brasilia, 50 p. (in Portuguese).

Santos, E.C.G.; Palmeira, E.M. & Bathurst, R.J. (2014). Performance of two geosynthetic reinforced walls with recycled construction waste backfill and constructed on

collapsible ground. Geosynthetics International, 21(4):256-269.

Santos, E.C.G.; Vilar, O.M. & Palmeira, E.M. (2010). The use of recycled construction and demolition waste in geosynthetic reinforced structures: Influence of the recycling process. Proc. 6th International Conference on Environmental Geotechnics - 6ICEG, New Delhi, v. 1. pp. 1105-1108.

Silva, A.R.L. (2004). A Study on the Behaviour of Drainage Systems of Waste Disposal Areas under Different Scales. PhD. Thesis, Graduate Programme of Geotechnics, University of Brasilia, Brasilia, 329 p. (in Portuguese).

Silva, C.A. (2007). Transmissivity Tests on Geocomposites for Drainage. MSc. Dissertation, University of Brasília, Brasília, 106 p. (in Portuguese).

Silva, C.A. & Palmeira, E.M. (2007). Transmissivity tests on geocomposites for drainage under large normal stresses. Proc. 5th Brazilian Symposium on Geosynthetics/REGEO, Recife, PE, v. 1, pp. 1-7 (in Portuguese).

Silva, S.A. (2014). Geotextiles in the Reduction of Polluting Capacity of Leachate. PhD. Thesis, University of Brasília, 117 p.

Stucki, M.; Büsser, S.; Itten, R.; Frischknecht, R. & Wallbaum, H. (2011). Comparative Life Cycle Assessment of Geosynthetics *vs.* Conventional Construction Materials. Research Report, Swiss Federal Institute of Technology, Zurich, 81 p.

Tchobanoglous, G.; Theisern, H. & Vigil, S. (1993). Integrated Solid Waste Management - Engineering Principles and Management Issues. McGraw-Hill Series in Water Resources and Environmental Engineering, New York, 975 p.

Tupa, N. (1994). A Study on the Adherence and Interaction between Soils and Geosynthetics. MSc. Dissertation, Graduate Programme of Geotechnics, University of Brasilia, Brasilia, DF, 188 p (in Portuguese).

Viana, P.M.F. & Palmeira, E.M. (2010). Alternative GCLs: Permittivity evaluation. Proc. 3rd International Symposium on Geosynthetic Clay Liners, Würzburg, v. 1, 9 p.

Viana, P.M.F.; Palmeira, E.M. & Viana, H.N.L. (2011). Evaluation of the use of alternative materials in geocomposite clay liners. Soils and Rocks, 34(1):65-77.

Zornberg, J.G. & Mitchell, J.K. (1994). Reinforced soil structures with poorly draining backfills. Part I: Reinforcement interactions and functions. Geosynthetics International, 1(2):103-148.

Articles

Soils and Rocks
v. 39, n. 2

A Case of Study About the Influence of Organic Matter in Municipal Solid Waste Settlement

M.C. Melo, R.M.S. Farias, R.M. Caribé, R.B.A. Sousa, V.E.D. Monteiro

Abstract. Municipal solid waste (MSW) settlement can be understood as volume reduction of the waste mass disposed in a landfill. Such phenomenon is mainly the result of organic matter degradation. Settlement can also be generated by MSW distortions, particle rearrengements, and other factors. These factors can be accurately analyzed if studied in an MSW experimental cell once it simulates the landfill behavior in a known and controlled way. This study aims to analyze the behavior of an experimental cell filled with MSW and how the biodegradation can influence the settlement over time and depth. The methodology was composed of waste sampling, experimental cell construction and filling, volatile solids analysis, and settlement measurements. The MSW gravimetric and volumetric analyses were performed in order to quantify the amount of organic matter contained inside the experimental cell. The tests indicated that the amount of organic matter drastically decreased in all MSW layers, and settlement varied according to the depth of the experimental cell due to mechanical factors and organic matter consumption.

Keywords: organic matter, settlement, municipal solid waste, experimental cells.

1. Introduction

Landfill settlement is mainly a result of organic matter loss from the Municipal Solid Waste (MSW) disposed. It can also be generated by MSW rearrangement, mass deformation and other factors. The settlement is mainly generated by the degradable organic matter (OM) present in the waste mass composition. The complex biological degradation processes with numerous metabolic pathways can create MSW settlement. However, the waste biodegradation depends on environmental factors inside the landfill, which directly influence the settlement velocity and magnitude. According to Wall & Zeiss (1995), MSW settlement may range from 25% to 50% of the initial waste height. However, the literature does not cover many topics involving the influence of organic matter in waste settlement.

Most of the MSW constituents disposed in landfills is organic matter (especially in developing countries), so it is important to determine how much the organic matter influences the occurrence of settlement. The speed of organic matter degradation and hence the speed of settlement are issues that have to be analyzed so that the mechanical behavior of landfills can be understood.

These issues can be better analyzed if studied in a controlled environment by using a MSW experimental cell which can simulate the behavior of a full-scale landfill. In Brazil and all around the world, there are studies being developed with experimental cells filled with MSW taking into account the peculiarities of different regions.

This paper aims to study the behavior of organic matter inside an MSW experimental cell regarding to its biodegradation and how it influences the settlement over time and depth.

2. Studied Literature

The organic matter in the waste mass inside the landfill is degraded through two processes: aerobic and anaerobic digestion (Alcantara, 2007; Araujo *et. al.*, 2009). The anaerobic process is the most significant in terms of biodegradation because the oxygen inside the landfill runs out quickly after the landfill impermeabilization (Moreda, 2000).

Leite (1997) states that the process of anaerobic biodegradation of MSW organic matter is quite complex. The physical and chemical composition of MSW and the presence of significant cellulolytic material demand some time to complete the bio stabilization of organic matter. According to Modesto (2002), the decomposition rate of anaerobic processes is slow and it requires a much longer time for the organic matter stabilization than in aerobic digestion. In the anaerobic digestion, most of the biodegradable organic matter is converted into biogas, and only a small portion of organic matter is converted into microbial mass. Melo (2003) and Monteiro *et. al.* (2006) suggest that anaerobic

Márcio Camargo de Melo, PhD., Associate Professor, Departamento de Saúde, Universidade Federal de Campina Grande, Campina Grande, PB, Brazil. email: melomc90@gmail.com.
Raliny Mota de Souza Farias, MSc. Student, Departamento de Engenharia Civil, Universidade Federal de Pernambuco, Recife, PE, Brazil. email: raliny.mota@gmail.com.
Rômulo de Medeiros Caribé, PhD. Student, Departamento de Engenharia Química, Universidade Federal de Campina Grande, Campina Grande, PB, Brazil. email: romulomedeiros@gmail.com.
Raul Batista Araujo de Sousa, Undergraduate Student, Departamento de Engenharia Civil, Universidade Federal de Campina Grande, Campina Grande, PB, Brazil. email: raulbatista01@gmail.com.
Veruschka Escarião Dessoles Monteiro, PhD., Associate Professor, Departamento de Engenharia Civil, Universidade Federal de Campina Grande, Campina Grande, PB, Brazil. email: veruschkamonteiro@hotmail.com.
Submitted on December 19, 2014; Final Acceptance on May 3, 2016; Discussion open until December 30, 2016.

digestion of MSW occurs because of the succession of different types of microorganisms, including the fungi, that can accelerate the conversion process of some compounds, such as cellulose, lignocellulose and less complex materials.

2.1. Settlement in municipal solid waste landfills

The deformability of the waste disposed in landfills is a very important aspect related to the landfill behavior. According to Nascimento (2007), settlement studies are important for the evaluation of landfill components, such as cover soil layer, leachate and biogas drainage systems (Kudrna, 2009; Sharma, 2007).

MSW landfills settlement is defined as a vertical displacement of the landfill surface caused by waste or cover layer weight, external loads and, mainly, the waste complex biological degradation processes that results in leachate and biogas production. Melo (2003) states that primary and secondary settlement can happen simultaneously and the waste mass rearrangement happens because of the successive gaps collapse.

Melo (2003) and McDougall *et al.* (2004) brought some new Acknowledgments in the study of waste settlement. They affirm that initial settlement in landfills is very intense because of the initial amount of organic matter. The rate of settlement decreases with time as the number of gaps decreases too. Organic matter degradation turns solid particles into liquids and gases, so the gaps once filled with the solid phase are now occupied by the liquid and gas phases. Initially, there are successive gaps enlargements due to the waste degradation, followed by collapses of these gaps. After a period of intense settlement, there is a period of zero settlement, when there is no settlement occurrence. However, once the weight of the waste mass is large enough to create gaps collapse, a new phase of settlement occurs.

It is difficult to define if the settlement is primary (first 30 days) or secondary. Melo (2003) says that both (primary and secondary) settlement occur simultaneously because as soon as the waste is disposed in the landfill, the microorganisms colonization takes place, causing the mass loss.

2.2. Gravimetric and volumetric composition of municipal solid waste

The gravimetric and volumetric characterization of MSW is an important tool in waste management and it indicates the amount of weight and volume that each type of waste occupies in the landfill cells (Pereira *et al.*, 2010). According to Pereira *et al.* (2010), knowing some aspects (weight and volume) of each MSW constituent individually is important because it shows the amount of existing biodegradable compounds within the waste mass, which contributes to the correct sizing of drainage systems and leachate treatment systems and to the evaluation of biogas generation potential.

The gravimetric composition of MSW is important to understand the waste mass behavior, and it expresses the presence of each component related to the total weight of the waste sample (Jucá & Melo, 2000). Both gravimetric and volumetric compositions are linked to the mechanic behavior of waste, and both are affected by the specific weight and compression of that waste. El-Fadel & Khoury (2000) states that high initial specific weight values associated with a high magnitude of waste compression reduces both primary and secondary settlement rates.

3. Materials and Methods

3.1. Development of the research

An experimental cell was built on Universidade Federal de Campina Grande (Federal University of Campina Grande by English translation) campus, in the city of Campina Grande, state of Paraíba, Brazil. The experimental cell or lysismeter filled with MSW was projected as an attempt to simulate and analyze a landfill behavior and how it loses mass due to waste decomposition. The experimental cell allows controlling the acceleration of the waste decomposition.

3.1.1. The experimental cell construction

The experimental cell was built with handmade bricks, and it had a diameter of 2 m, height of 3 m and volume capacity of 9 m^3. The instrumentation was made with surface settlement gauges (plates A and B), thermocouples, piezometers (to measure the liquid level) and biogas drains (Fig. 1). For cover and bottom soil layers, a low permeability soil was chosen (velocity: 10^{-8} m/s).

3.1.2. Waste collection, sampling and lysimeter filling

The procedure used in order to perform the waste collection and sampling was recommended by the ABNT: NBR 10007 (2004). The waste was collected and its homogenization was performed based on LIPOR's (2000) methodology - adapted by Leite (2008) and Pereira *et.al.* (2010). The determination of the MSW gravimetric and volumetric composition was based on the same method previously listed.

The MSW was collected from three different neighborhoods in Campina Grande. The criteria used to choose neighborhoods were the social class. This way, neighborhoods representing the high, middle and low classes were chosen (one neighborhood for each class). After the collection, the MSW was homogenized and quartered (according to ABNT NBR 10007, 2004) so that a final sample was obtained to fill the experimental cell.

3.1.3. Field parameters monitoring and laboratory trials

After filling, MSW samples from the lysimeter were collected in order to determine their mechanical, physical, chemical and microbiological parameters. Table 1 shows

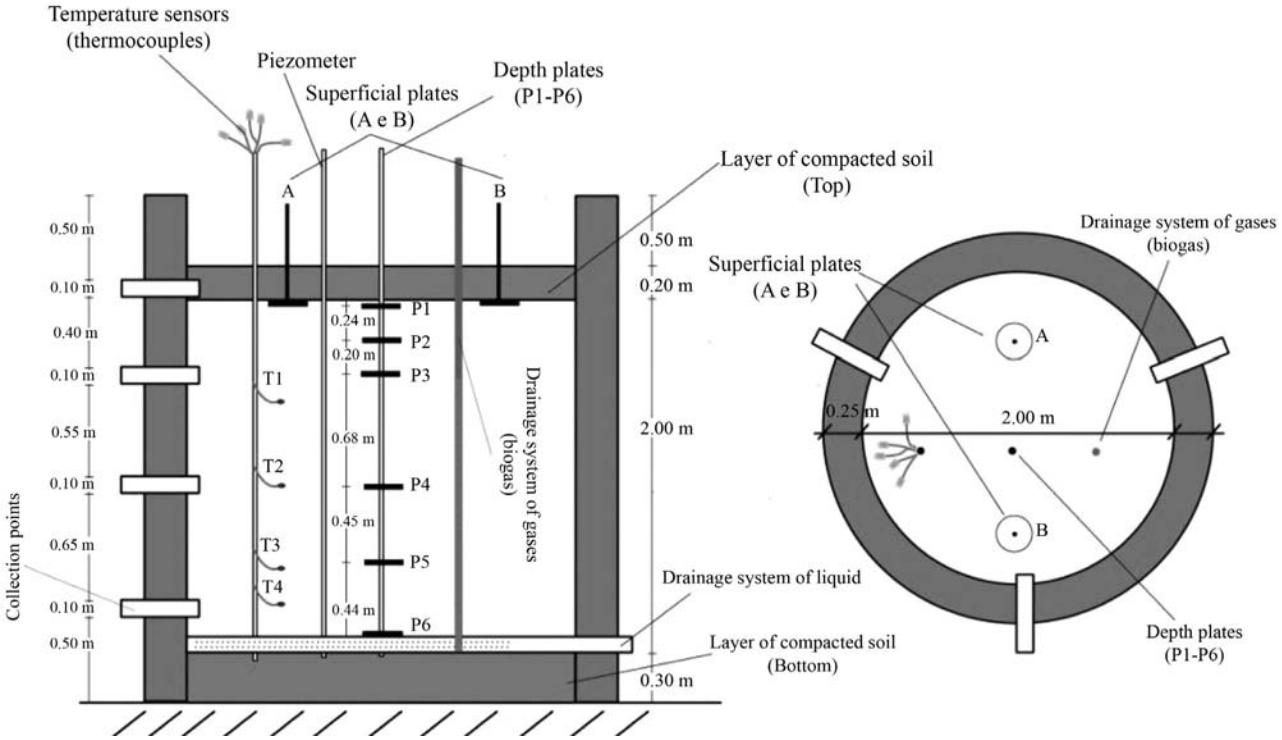

Figure 1 - Top view and vertical cut of MSW experimental cell.

Table 1 - Physicochemical parameters monitored over time.

Parameters	Method
Volatile solids	WHO (1979)
Water content	NBR 6457 (ABNT, 1986); Manassero *et al.* (1996)
Alkalinity	Standard Methods (AWWA/APHA/WEF, 1998)
PH	
Total alkalinity	
Volatile fatty acids	
Chlorides	
COD	
BOD	

the physicochemical parameters of the MSW in the lisymeter monitored over time.

4. Results and Discussions

4.1. Physical characterization of the MSW deposited in the experimental cell

The physical characterization of the MSW was composed of gravimetric and volumetric composition tests and MSW density determination. For the gravimetric composition, Table 2 shows that the MSW has about 66% of organic matter, indicating a high percentage of waste mass deformation that results in large settlement values since the biodegradation increases with the amount of putrescible material in the MSW composition (Dixon & Jones, 2005).

Table 2 also shows that the amount of plastics reached a value of 11% of total waste weight. Such percentage of plastics reflects their low density that usually contributes to a lower value on the total weight compared to organic matter. The volumetric composition for loose and compressed MSW shows a higher percentage of plastics than the one found in gravimetric composition. Grisolia *et al.* (1995) states that compressed materials such as metals and plastics can release retained liquids or gases, causing an apparent decrease in their volume. The organic matter releases its liquid, so the volume variation is even higher. Such observation is directly related to settlement creation and water content within the waste mass.

The volumetric composition of organic matter for compacted and loose waste was 37% and 38%, respectively (Table 2) . This data could initially lead to the conclusion that settlement due to the degradation of organic matter would also be around that value. However, McDougal *et al.* (2004) and Firmo *et al.* (2010) suggest that not all the organic matter is biodegradable and Melo (2003) affirms that inhibitors products intrinsic to the degradation of organic matter can exist in the waste mass disposed in landfills. Those elements can decrease the metabolic activity of microorganisms and, consequently, the waste decomposition.

In regards to plastics, Fucale (2002) reports that these materials can work as a reinforcement matrix of the landfill structure. Plastic retards the degradation of organic matter

Table 2 - Values obtained by the physical characterization of MSW.

Waste	Gravimetric composition (%)	Volumetric composition - loose waste (%)	Volumetric composition - compressed waste (%)	Density - loose waste (kg/m^3)	Density - compressed waste (kg/m^3)
Plastic	11	29	27	58	87
Metals	3	5	7	97	103
Sanitary and textiles	4	4	4	146	209
Others	6	8	9	107	138
Glasses	4	4	5	157	164
Composite	1	5	4	44	80
Paper and cardboard	5	7	7	122	169
Organic matter	66	38	37	268	400

because it creates waterproof pockets, but they can provide better stability to landfills.

The volumetric composition of loose and compacted waste for paper and cardboard, composite, sanitary, textiles, glass, metals and others was less than 40% of the total waste volume. Nevertheless, these materials use to have very high values, according to studies conducted by Catapreta & Simoes (2008).

Table 2 also shows that loose and compacted waste densities for the organic matter was 270 kg/m^3 and 400 kg/m^3, respectively. The density values of the compressed waste is greater that the non-compressed waste ones because after compression, the volume is reduced, so the density increases.

Loose and compacted waste density results were, respectively, 400 kg/m^3 and 700 kg/m^3, which is in accordance with the technical literature (Leite, 2008; Landva & Clark 1990; Kaimoto & Cepollina, 1996). These authors report that a compressed density of 700 kg/m^3 is excellent for mechanical operation in landfills.

4.2. MSW settlement

4.2.1. MSW settlement over depth

The plates to measure the MSW settlement were arranged according to the specified depths showed in Table 3. The largest MSW deformations occurred with the plate 1 (Fig. 2). Plate 1 is located in the center of the experimental cell, in the top layer, right before plate 2 (from top to the bottom). The settlement values measured by plates 1 and 2 were 0.37 m and 0.40 m, respectively, by the end of the monitoring time.

Surface plates 'A' (on the left side of plate 1) and 'B' (on the right side of plate 1) showed settlement values of 0.35 m and 0.33 m, respectively. Such results were predictable since these plates were 2.00 m far from the bottom layer.

Plates 1 and 2 had higher rates of settlement than surface plates because the central region of the cell has less influence of the friction caused by the lysimeter walls. The walls interact with the stuck waste by impeding its consolidation. Melo (2003) and Alcantara (2007) found the same results when studying small-size experimental cells and full-scale cells as reported in their studies.

Table 3 - Position of settlement plate inside the experimental cell.

Plate	Settlement plate position (m)
Plate-a superficial	0
Plate-b superficial	0
Plate 1	0
Plate 2	-0.23
Plate 3	-0.43
Plate 4	-1.11
Plate 5	-1.56
Plate 6	-2.00

The settlement values observed in the experimental cell represented a typical behavior of a full-scale cell once the settlement magnitude decreased over time as it is usually observed in landfills (Fig. 2). Mariano (1999), Melo (2003) and Monteiro (2003) found out that the settlement decreases as the depth increases in full scale MSW cells. Such behavior occurs since the waste in the deepest layers are more influenced by the compression due to the weight of the top layers, so as the plates on the surface have more available space to move downwards. The same behavior was observed in this study, as it is seen in Table 4. The plate 6 did not move because it is located in the bottom layer already, so the high waste compaction retarded the settlement in that layer.

The largest settlement values occurred in the early months after waste disposal. The highest settlement speed rates also occurred in these days (first 90 days after closing the experimental cell). During the first 30 days, the settlement occurred because of the loads imposed by the waste mass and compacted cover soil weights (Fig. 2). According to Valozer (1989), in the early days, the microbiota of the waste mass is still adapting itself to the environment in the experimental cell, so the settlement created is mostly due to

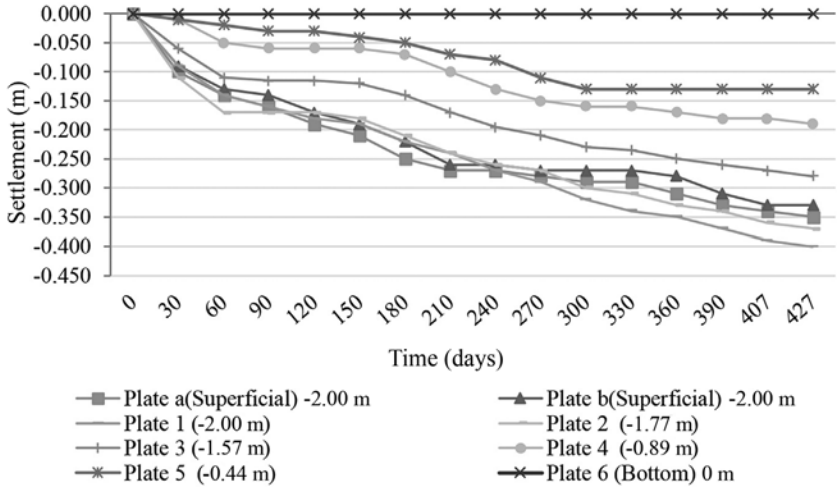

Figure 2 - MSW settlement values in different lysimeter depths over time.

Table 4 - Final MSW settlement values for each plate located in the experimental cell.

Plate	Final settlement (m)
Plate-a (superficial)	0.35
Plate-b (superficial)	0.33
Plate 1	0.40
Plate 2	0.37
Plate 3	0.28
Plate 4	0.19
Plate 5	0.13
Plate 6	0

mechanical factors. After this phase, settlement was generated by the degradation of organic matter from the MSW.

4.2.1.1. Settlement due to MSW biodegradation

In regards to the settlement fraction related to MSW biodegradation (Table 5), the surface plates 'A' and 'B' showed a waste mass deformation of 71% and 73%, respectively. For plate 1, 77% of settlement was originated by degradation of organic matter, and for plate 2, 70% of settlement was created due to biodegradation. The waste layers in which plates 3, 4 and 5 are located had the largest amount of vertical deformation caused by biodegradation.

As the depth increased, a higher biodegradation settlement percentage was found. Immediate settlement occurred during the experimental cell filling process when the lower waste layers were constantly compacted by the upper layers. The settlement during the filling process was not recorded. Only when the experimental cell was closed, the settlement measurements started, so the results taken from the first day of measurement does not represent the magnitude of the immediate settlement in the lower waste layers. This way, the biodegradation settlement (non-immediate settlement) will always be proportionally greater in deeper waste layers because immediate settlement practically ended by the time that settlement measurements started.

The studied literature only makes observations about the general behavior of MSW settlement. However, the settlement of the organic fraction of the waste is not thoroughly analyzed. In Brazilian cities, the organic fraction corresponds to the highest percentage of MSW composition (by terms of weight and volume). In order to predict the lifespan of a landfill, it is necessary to take into account the waste degradation time for each layer considering also the immediate settlement.

4.2.2. MSW settlement velocity

The settlement velocity (Fig. 3) shows how considerable were the MSW settlement occurrence on the first 30 days after the experimental cell closing. The settlement rate was up to 10 times higher in some of the plates during the first 30 days if compared to the other days. However, the settlement speed decreased after 90 days. Plates 4 and 5 had

Table 5 - Settlement percentage due to MSW weight and organic matter degradation.

Settlement/plate	Plate-a (superficial)	Plate-b (superficial)	Plate 1	Plate 2	Plate 3	Plate 4	Plate 5	Plate 6
Instant settlement (%)	29	27	23	30	21	5	8	0
Settlement due to degradation (%)	71	73	77	70	79	95	92	0

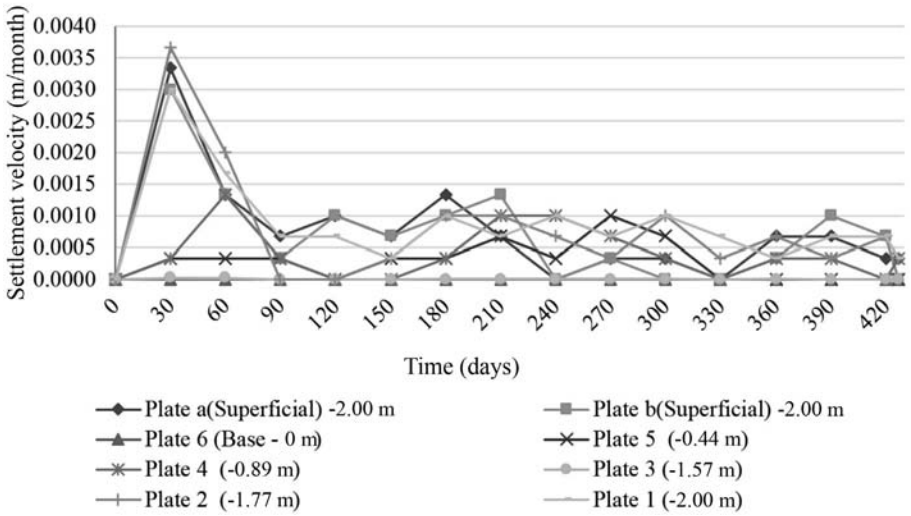

Figure 3 - Settlement velocity of the waste layers.

the lowest settlement rate over time if compared to the other plates.

Plate 5 (Fig. 3) showed zero settlement speed after 330 days of monitoring which indicates that either the organic matter is unavailable to the microorganisms by excessive compression, or there is an accumulation of liquids at that region, retarding the settlement. Leite *et al.* (2007) affirm that excessive compression may inhibit the degradation of organic compounds. For the other plates, the settlement is decreasing, but it will still take place for a while because there is still organic matter to be degraded inside the experimental cell.

4.2.3. Settlement vs. organic matter

The value of 66% of the initial organic matter in the MSW composition indicates that the experimental cell is filled with approximately 2,900 kg of organic compounds. However, not all the organic material is biodegradable. The degradation of organic material results in settlement, so it must be measured since it will determine the landfill lifespan (Melo, 2003; Monteiro, *et al.*, 2006).

The rate putrescible organic matter within the waste mass per volume of the experimental cell is 400 kg/m^3, which indicates a total of 1,700 kg of highly degradable organic compounds. The results obtained by many researchers around the world show that even the putrescible waste fraction might take a considerable amount of time to be completely degraded. Within the waste mass, there are materials that are aggressive to the microorganisms due to the release of toxic substances, the waste heterogeneity and the different temperatures and pH ranges (Mcdougall *et al.*, 2004; Melo, 2003). Such fact explains why many landfills produce biogas for decades after their closure.

Firmo *et al.* (2010) states that, despite the volatile solids (VS) amount of 87% for plastics, 64% for rubber and leather, 98% for textiles and 81% for paper/cardboard, these materials are considered moderately or slowly biodegradable once they also contain a high fraction of non-biodegradable substances.

Regarding to the total content of organic matter in the studied experimental cell, the settlement account would be around 1.33 m, which corresponds to 66% of total reduction of waste height. That did not occur because not all the organic matter is biodegradable, and the waste disposal time (427 days) is still too short if compared to full-scale landfill cells (20-30 years). According to the results found in the monitored experimental cell, the settlement was much smaller than the one suggested by theoretical methods when considering the easily degradable compounds.

Most studies about settlement do not take into account that waste deformation is divided into: i) immediate settlement (30 days after MSW disposal); ii) settlement created by degradation of putrescible organic matter; iii) settlement due to hardly degradable organic matter; iv) settlement originated from the rearrangements of inert waste particles. All these types of settlement occur in different periods and they generate a high volume reduction.

The Table 6 shows the quantity of initial organic matter for each waste layer of the experimental cell.

According to Table 6, most of the settlement should happen in the bottom layer, but this is contradictory with the results showed before. The settlement in the bottom layer was the lowest one even when there was more organic matter available in that layer.

Table 6 - Quantity of organic matter (OM) by MSW extract.

MSW layer	Total quantity of OM (kg)
Top layer	640
Intermediate layer	1,000
Bottom layer	1,300

Figures 4 to 6 show the existent relation between settlement and volatile solids decreasing by the action of microorganisms over time. In the top layer (0 to -1.57 m), vertical deformations distributed and verified by the settlement plates have a very similar displacement pattern (Fig. 4). As it was already expected, large vertical displacements occurred when the amount of organic matter was high. However, settlement still happened when almost all the organic matter was already degraded (after 210 days), and this is probably because of the settlement produced by the inferior layers.

Concerning the intermediate layer (Fig. 5) of the experimental cell (-1.57 m to -0.89 m), settlement data had a better correlation with the organic matter (VS) decreasement over time. There was a high occurrence of settlement on the first 60 days of measurements while the volatile solids content was between 50-70%. After this period (between 60 to 120 days), there was organic matter degradation due to the increasing of gaps, but such fact does not create considerable vertical displacements. The collapse of these gaps will only happen when they cannot support the upper loads.

There is still occurrence of settlement after 120 days, but it is less intense because of the continued consummation of organic matter and the association with settlement of the bottom layer. After 120 days, there was a gradual decreasing of organic matter from 50% to 40%. On the first 60 days, there was a vertical displacement of 0.115 m, which is much accentuated if compared with the later settlement occurred in the following 307 days (day 120 to 427) of monitoring.

Figure 6 shows the settlement that happened in the bottom layer (-0.89 m to 0 m). The bottom layer has the plates 4, 5 and 6, but only plates 4 and 5 indicated settlement occurrence and, as the organic matter was degraded, the settlement occurred. The initial settlement (like in the superior layers) were also greater during the first days of

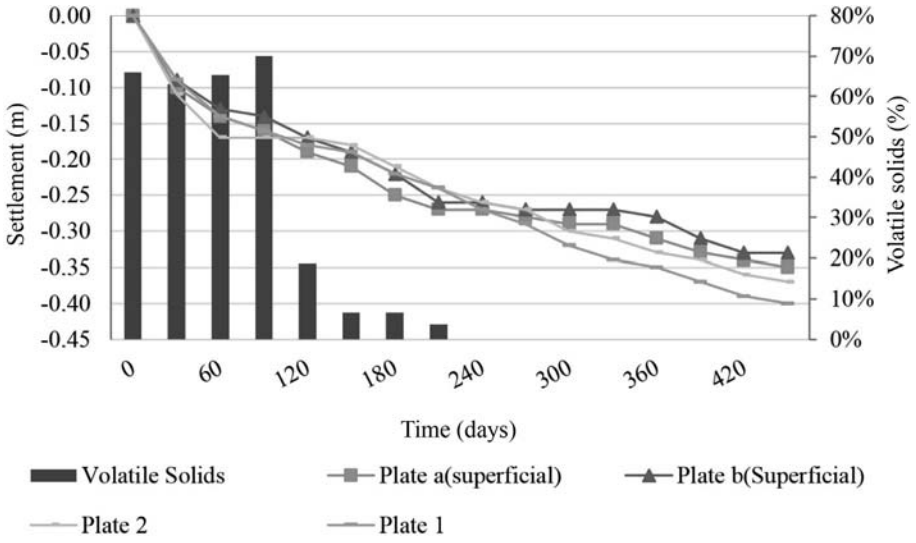

Figure 4 - Settlement *vs.* volatile solids (Top layer).

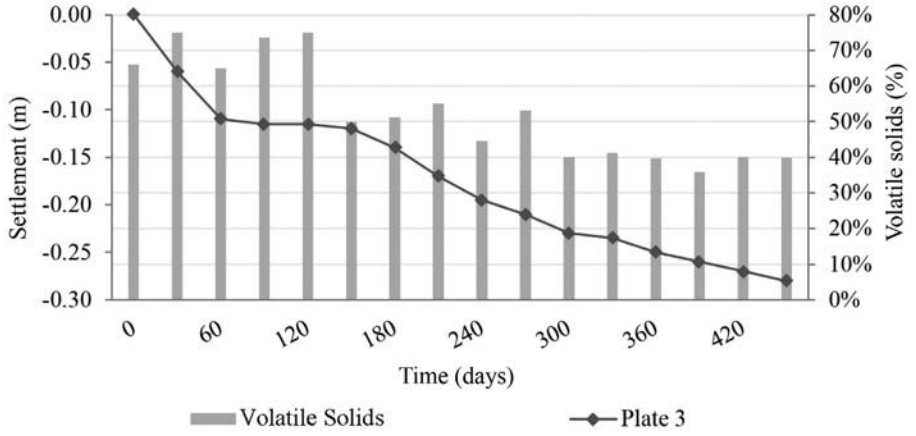

Figure 5 - Settlement *vs.* volatile solids (Intermediate layer).

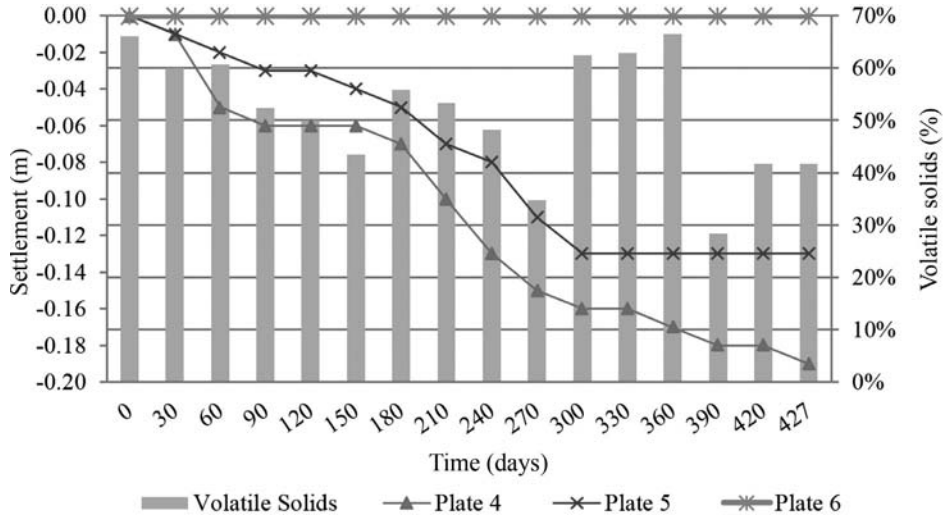

Figure 6 - Settlement *vs.* volatile solids (Bottom layer).

monitoring when there was a higher concentration of volatile solids.

For all the bottom plates, there was a period of zero settlement between 90 and 120 days. After this period, there was another settlement phase between 120 and 300 days, followed by another zero displacement phase. After 300 days, there was no settlement occurrence on plate 5, which is probably due to the excessive compression since there was still organic matter left in this plate.

During the volatile solids monitoring process, it was observed that, in the bottom layer, the VS values randomly increased instead of decreasing. Such result is due to the influence of the accumulated leachate, which is composed of organic matter and other constituents. On the first 150 days, the volatile solids were related to the settlement once the deformation patterns were inversely proportional to the volatile solids decreasing.

As it is seen in Table 7, the MSW top layer had 600 kg of organic matter transformed into liquids, biogas and energy, which corresponds to 93% of organic matter volume reduction. The intermediate layer presented a reduction of 40%, which is around of 400 kg of transformed organic matter. For the bottom layer, an organic matter volume reduction of 38% occurred. Table 7 also shows that the initial amount of organic matter inside the experimental cell was 2,900 kg and the final amount was 1,440 kg, which means a total organic matter reduction of approximately 49%. Therefore, there is a height reduction of about 0.66 m, which is 33% of the initial height.

Overall, the results of the organic matter decomposition in this study were greater than the ones for full-scale cells taken into account the same monitoring time (Melo, 2003; Monteiro *et al.*, 2006). It indicates that cells with smaller dimensions might accelerate the organic matter decomposition process once they have a bigger surface area that facilitates the exchange of energy and matter with the environment.

Table 8 shows that most of the settlement happens in the intermediate layer, although this is not the thickest layer. The intermediate layer had greater vertical deformation due to the loads imposed by the top layer and the loss of liquids to the bottom layer. Even with the intense settlement in the intermediate layer, most of the settlement created by organic waste degradation happened in the top layer due to the influence of the external environment.

5. Conclusions and Suggestions

The results obtained through physical characterization showed that organic matter represents most of the MSW (66%) from the city of Campina Grande. This large amount of organic matter is probably the reason for the high MSW settlement values found in the experimental cell studied in this research.

The amount of organic matter decreased in all MSW layers of the experimental cell. The MSW settlement oc-

Table 7 - Organic matter (OM) initial quantity and transformation into other constituents.

MSW layer	Organic matter initial quantity (kg)	Organic matter final quantity (kg)	Transformed OM quantity (kg)
Top layer	640	40	600
Intermediate layer	1,000	600	400
Bottom layer	1,300	800	500

Table 8 - Height and MSW amount variation over time and depth.

MSW layer	MSW initial height (m)	MSW final height (m)	MSW initial amount (kg)	MSW final amount (kg)	Reduction (%)
Top layer	0.43	0.40	950	880	7
Intermediate layer	0.68	0.59	1,500	1,290	14
Bottom layer	0.89	0.83	1,960	1,820	7

curred due to organic matter degradation and mechanical factors. The top layer had the best results regarding the settlement and degradation of organic matter, as it is more influenced by the local environmental conditions.

Acknowledgments

The National Council of Scientific and Technological Development ("CNPq" by Portuguese abbreviation) and the Federal University of Campina Grande supported this research.

References

ABNT (1986). Soil samples - Preparation for Compactation and Characterization Tests - NBR 6457. Associação Brasileira de Normas Técnicas, Rio de Janeiro, Brazil, 9 p.

ABNT (2004). Sampling of Solid Waste - NBR 10007. Associação Brasileira de Normas Técnicas, Rio de Janeiro, Brazil, 21 p.

Alcantara, P.B. (2007). Evaluation of the Influence of Municipal Solid Waste Composition in Simulated Landfills Behavior. PhD Dissertation, Department of Civil Engineering, Universidade Federal de Pernambuco, Recife, Brazil.

APHA/AWWA/WEF (1998). Standard Methods for the Examination of Water and Wastewater. American Public Health Association, Washington, USA.

Araujo, M.V.; Melo, M.C.M.; Leite, H.E.A.S.; Araújo, E.P. & Monteiro, V.E.D. (2009). Fungi quantification in a biorreactor of municipal solid waste from the city of Campina Grande-PB. Proc. 25 °Congresso Brasileiro de Engenharia Sanitária e Ambiental, CBESA, Recife, Brazil, v. 1.

Catapreta, C.A.A. & Simões, G.F. (2008). Volumetric characterization of urban solid waste disposed in an experimental sanitary landfill. Proc. XXXI Congreso Interamericano de Ingenieria Sanitaria y Ambiental, AIDIS, Santiago, Chile.

Dixon, N. & Jones, V. (2005). Engineering properties of municipal solid waste. Geotextiles and Geomembranes Journal 23(3):205-233.

El-Fadel, M. & Khoury, R. (2000). Modeling settlement in MSW landfills: a critical review. Critical Reviews in Environmental Science and Technology 30(3):327-361.

Firmo, A.L.B.; Melo, E.S.R.L.; Guimarães, L.J.N. & Valle, G.A. (2010). Evaluation of biogas potential generation of the municipal solid waste components from the Muribeca Landfill. Proc. 3º Simposio Iberoamericano de Ingeniería de Residuos, João Pessoa, Brazil.

Fucale, S.P. (2002). Strength of municipal solid waste landfills. Proc. I Seminário de Tese de Doutorado, Recife, Brazil.

Grisolia, M.; Napoleoni, Q. & Tancredi, G. (1995). Contribution to a technical classification of MSW. Proc. International Landfill Symposium, Cagliari, Italy, v. 5, pp. 761-768.

Kaimoto, L.S.A. & Cepollina, M. (1996). Considerations about some conditions and geotechnical criteria for executive design of sanitary landfills. Proc. Simpósio Internacional de Qualidade Ambiental, Porto Alegre, Brazil.

Kudrna, Z. (2009). Long-term deformations of municipal landfill bodies and their effects on functional safety of superficial sealing. Acta Geodyn. Geomater. 6(4):465-473.

Landva, A.O. & Clark, J.I. (1990). Geotechnics of Waste Fills - Theory and Practice. ASTM, Philadelphia, pp. 86-103.

Leite, H.E.A.S. (2008). Study of the Behavior of MSW Landfills in an Experimental Scale Biorreactor in the City of Campina Grande - Paraíba. MSc. Dissertation, Department of Civil Engineering, Universidade Federal de Campina Grande, Campina Grande, Brazil.

Leite, H.E.A.S.; Monteiro, V.E.D. & Silva, S.A. (2007). A study proposal about settlement in municipal solid waste landfills in an experimental scale associated to biodegradation. Proc. VI Congreso Chileno de Geotecnia, Valparaíso, Chile.

Leite, V.D. (1997). Anaerobic Treatment Process of Municipal Solid Waste Inoculated with Industrial Sewage Sludge. PhD Dissertation, Escola de Engenharia de São Carlos, Universidade de São Paulo, São Carlos, Brazil, 197 p.

LIPOR (2000). Technical Textbooks Lipor n.º 1 - Solid Waste Characterization. Porto, Portugal.

Manassero, M.; Van Impe, W.F. & Bouazza, A. (1996). Waste disposal and containment. Proc. 2nd International Congress on Environmental Geotechnics, Osaka, Japão, v. 3, pp. 1425-1474.

Mariano, M.O.H. (1999). Study of Settlements in the Muribeca Landfill. MSc Dissertation, Department of Civil Engineering, Universidade Federal de Pernambuco, Recife, Brazil.

Mcdougall, J.R.; Pyrah, I.C.; Yuen, S.T.S.; Monteiro, V.E.D.; Melo, M.C. & Juca, J.F.T. (2004). Decomposition and settlement in landfilled waste & other soil-like materials. Géotechnique 54(9):605-610.

Melo, M.C. (2003). An Analysis of Settlement Associated with Biodegradation in the Municipal Solid Waste Landfill of Muribeca. MSc. Dissertation, Department of Civil Engineering, Universidade Federal de Pernambuco, Recife, Brazil.

Melo, V.L.A. & Jucá, J.F.T. (2000). Studies of reference for environmental diagnosis in solid waste landfills. Proc. XXVII Congresso Interamericano de Engenharia Sanitária e Ambiental, Porto Alegre, Brazil.

Modesto, H.S. (2002). Study of Scale Anaerobic Batch Reactors for Treating Organic Waste. MSc. Dissertation, Department of Civil Engineering, Universidade Federal de Campina Grande, Campina Grande, Brazil.

Monteiro, V.E.D. (2003). Physical, Chemical and Biological Analysis in the Study of the Behavior of Solid Waste from the Muribeca Landfill. PhD. Dissertation, Department of Civil Engineering, Universidade Federal de Pernambuco, Recife, Brazil.

Monteiro, V.E.D.; Melo, M.C.; Alcântara, P.B.; Araújo, J. M.; Alves, I.R.F.S. & Jucá, J.F.T. (2006). Study of MSW behavior in an experimental cell and its correlation with microbiological, physical and chemical aspects. Engenharia Sanitária e Ambiental, 11(3):223-230.

Moreda, I.L. (2000). El Asentamiento en un Rellleno Sanitario y su Relación com la Biodegradación. Proc. XXVII Congreso Interamericano de Ingeniería sanitaria y Ambiental, Porto Alegre, Brazil.

Nascimento, J.C.F. (2007). Mechanical Behavior of Municipal Solid Waste. MSc Dissertation, Escola de Engenharia de São Carlos, Universidade de São Paulo, São Carlos, Brazil.

Pereira, F.T.G.; Leite, H.E.A.; Garcez, L.R.; Araujo, E.P.; Melo, M.C. & Monteiro, V.E.D. (2010). Gravimetric composition of the municipal solid waste from the city of Campina Grande-PB. Proc. 2º Simpósio Nordestino de Resíduos Sólidos, SINRES, Teresina, Brazil.

Sharma, H.D.A. (2007). Municipal solid waste landfills settlement: postclosure perspectives. J. Geotech. and Geoenviron. Eng. 133(6):619-629.

Vazoller, R.F. (1989). Studies about Isolation, Characterization and Growth of Pure Cultures of Methanogenic Bacteria from Sewage Sludge Digesters. MSc Dissertation, Instituto de Ciências Biomédicas, Universidade de São Paulo, São Paulo, Brazil.

Wall, D.K. & Zeiss, C. (1995). Municipal landfill biodegradation and settlement. J. of Env. Eng. 121(3):214-223.

WHO (1979). Methods of Analysis of Sewage Sludge Solid Wastes and Compost. International Reference Center for Wastes Disposal, Switzerland.

Supporting Mechanism and Effect of Artificial Pillars in a Deep Metal Mine

Z. Kang, Z. Hongyu, Z. Junping, W. Xiaojun, Z. Kui

Abstract. The supporting mechanism for overburden strata supported by artificial pillars is a complex issue. A calculation method for the size optimization of an artificial pillar in a deep area based on Protodyakonov's ground pressure theory was proposed. In this study, the sizes of artificial pillars in different mining sections in a specific mine were calculated. In addition, the stability of these artificial pillars and the supporting effect for the overburden strata in the gob areas were studied. First, the size parameters of the artificial pillars in different mining sections were determined. Second, the supporting mechanism and stability of the artificial pillars were studied by means of numerical calculation. A regular pattern in which a larger gob area span corresponds to greater settlement of the overburden strata were found. The overburden strata are stable based on the distribution condition of the plastic zone. Finally, field measurements were performed, revealing continuous increases in both the pressure borne by the artificial pillars in two middle sections at the primary stage and the settlement displacement of the overburden strata. After reaching a certain level, the increasing trend slowed and finally plateaued. The maximum stress of the artificial pillar at a depth of -430 m was 0.78 MPa, and its maximum relative settlement of the overburden strata was 4.4 mm. Similarly, the maximum stress of the artificial pillar at a depth of -460 m was 0.43 MPa, and its maximum relative settlement of the overburden strata was 2.7 mm. The study results showed that the designed artificial pillars are capable of supporting the overburden strata with good stability in the mining process and can effectively prevent the destruction of surrounding rocks and overburden strata in the gob area for the purpose of supporting the mine.

Keywords: great depth, overburden strata, artificial pillar, supporting mechanism, mechanical characteristics.

1. Introduction

With the gradual reduction of mineral resources, adopting artificial pillars instead of natural pillars to support overburden rocks has become increasingly important. The overburden strata around the goaf are supported by artificial pillars instead of ore pillars in rare and precious metal mines. However, these pillars have different supporting mechanisms, resulting in an unclear movement mechanism for overburden strata supported by artificial pillars and threatening the mine safety. Few studies have been conducted on the instability mechanism of overburden strata around the goaf (Liu *et al.*, 2013; Chen & Zhou, 2010). Because the supporting abilities of artificial pillars are influenced by complex factors, including filling technologies, filling material properties and design strength, their supporting performance often falls short of expectations (Gu & Li, 2006; Luo *et al.*, 2010; Ghasemi *et al.*, 2012). Many scholars have studied the design of artificial pillars; among their findings are indications that changing the ratio and adding new materials can improve the strength of the filling pillar (Tu *et al.*, 2014; Lind, 2005; Palei & Das, 2009). However, studies on improving the strength of artificial pillars have progressed slowly due to the restrictions of the field conditions and filling processes as well as high filling costs. Based on the relevant literature domestically and abroad, the strength of artificial filling pillars is generally less than 5 MPa. Conventionally, the size of an artificial pillar is determined according to area bearing capacity theory (Brady & Brown, 2006), which calls for larger artificial pillars for deeper mining depths. However, this theory does not fully take into account relevant factors that may affect the reasonable size of the artificial pillar, resulting in excessively wide backstoping pillars in deep areas, a waste of filling materials and increased filling cost. Therefore, in this study, the supporting mechanism is investigated, and a new design method is developed to determine the size of the artificial pillar.

2. Mechanical Model of the Artificial Pillar

When the room and pillar method is used in the mining process, the length of the artificial pillar is generally the

Zhao Kang, PhD., Associate Professor and Deputy Director of Civil and Mechanics Laboratory Center, School of Architectural and Surveying Engineering, Jiangxi University of Science and Technology, Ganzhou 341000, China. e-mail: zhaok_666666@163.com.
Zhao Hongyu, MSc., Student, School of Architectural and Surveying Engineering, Jiangxi University of Science and Technology, Ganzhou 341000, China. e-mail: zhaohongyu@163.com.
Zhang Junping, MSc., Student, School of Architectural and Surveying Engineering, Jiangxi University of Science and Technology, Ganzhou 341000, China. e-mail: 1192991685@qq.com.
Wang Xiaojun, PhD., Associate Professor and Director of Mining Engineering Department, School of Architectural and Surveying Engineering, Jiangxi University of Science and Technology, Ganzhou 341000, China. e-mail: wangxiaojun@163.com.
Zhao Kui, PhD., Full Professor and President, School of Architectural and Surveying Engineering, Jiangxi University of Science and Technology, Ganzhou 341000, China. e-mail: Yglmf-zk@163.com.
Submitted on March 15, 2015; Final Acceptance on August 7, 2015; Discussion open until December 31, 2015.

inclined length in the middle section, and the height is the thickness of the ore body. Both are determined by the occurrence conditions of the ore body. Therefore, the width of the artificial pillar is the design key for the structural parameters in this mining method. Based on the bearing theory of artificial pillars (Fig. 1), the weight of the overburden rock within the plastic zone without a pressure arch must first be determined. Each middle section is divided into rooms and pillars in the orebody trend in the mining process. The backstoping is completed in two steps: Step 1 is backstoping the pillar and then refilling concrete into the pillar as a whole, and Step 2 is backstoping the room between the concrete pillars. According to the Protodyakonov's ground pressure theory, the radius of the plastic zone can be expressed as (Wang *et al.*, 2012; Cai, 2002; Diederichs *et al.*, 2002)

$$R_p = R_0\left[\frac{(P_0 + c\cos\varphi)(1-\sin\varphi)}{c\cot\varphi}\right]^{\frac{1-\sin\varphi}{2\sin\varphi}} \quad (1)$$

In this formula, R_0 is the excavation radius, m; P_0 is the vertical gravity stress of the mining depth, MPa; c is the cohesive force of the rock, MPa; and φ is the internal friction angle of the rock, °.

Experimental results show that the plastic zone radius (R_p) is affected slightly by the excavated sectional form. In calculations, R_p can be approximated by the equivalent excavated radius, *i.e.*, the circumradius of the different sectional forms. As for the ore block, the equivalent excavated radius (R_0) can be obtained as follows.

R_0 and P_0 are calculated with the following formulas:

$$R_0 = \sqrt{\left(\frac{L}{2}\right)^2 + \left(\frac{h}{2}\right)^2} \quad (2)$$

$$P_0 = \gamma H \quad (3)$$

The load intensity of the top pressure within the unit length without the pressure arch is:

$$q_d = \gamma\left(R_p - \frac{h}{2}\right) \quad (4)$$

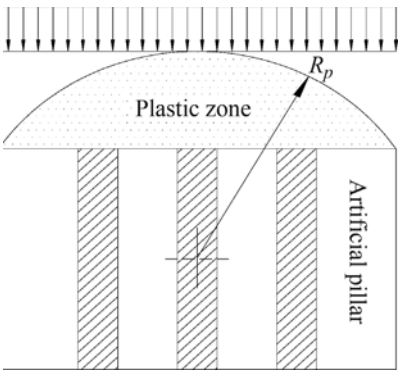

Figure 1 - Schematic diagram of the pillar bearing mechanism.

In this formula, q_d is the load intensity of the top pressure within the unit length without the pressure arch, kN/m; γ is the unit weight of the surrounding rock, kN/m^3; and h is the height of the mining space, m.

In the calculation of the total load, the mining span must be maximal. Therefore, the whole mining span must be considered to obtain the total load within the mining span above the artificial pillar.

$$Q_d = q_d \times L \quad (5)$$

In this formula, Q_d is the total load, kN; L is the span of the mining space, m, namely, the total length along the strike of the ore body; H is the depth of the mining space, m.

Equations 2 and 3 are substituted into Eq. 1 to give R_p.

According to strength theory, the width of the artificial pillar is determined by its own strength, the pressure borne by the artificial pillar and the dead-weight. Due to the impact of the filling process and the site conditions, the strength values of the artificial pillar can be obtained by reducing the pilot testing values.

$$\sigma \le \frac{S_p}{n} = [\sigma] \quad (6)$$

In this formula, S_p is the intensity value of the sample of the artificial pillar tested in the laboratory, MPa; σ is the average stress of the artificial pillar, MPa; $[\sigma]$ is the permissible stress of the artificial pillar, MPa; and n is the strength reduction factor, which is determined by the actual site conditions and construction technology. n varies between 1.5 and 2.

The unit length of the artificial pillar is used to calculate:

$$\frac{Q_d + NQ_m}{NB} \le \sigma \quad (7)$$

In this formula, N is the number of the artificial pillars; B is the width of the artificial pillar, m; Q_m is the dead-weight of the unit length of every artificial pillar, kN.

$$Q_m = Bh\gamma_1 \quad (8)$$

where γ_1 is the init weight of the artificial pillar.

The calculation formula of the width of the artificial pillar can be determined by solving Eqs. 1-8 simultaneously:

$$B = \frac{n\gamma L\left[(L^2 + h^2)^{\frac{1}{2}}\left[\left(\frac{(\gamma H + c\cot\varphi)(1-\sin\varphi)}{c\cot\varphi}\right)\right]^{\frac{1-\sin\varphi}{2\sin\varphi}} - h\right]}{2N(S_p - nh\gamma_1)} \quad (9)$$

Considering the effects of the ratio of the geometric shapes, such as the effect of the aspect ratio on the bearing capacity of the artificial pillar, the width of the artificial pillar must be corrected (Ji, 1991):

$$B_C = B\sqrt{\frac{h}{B}} = \sqrt{BH} \quad (10)$$

Based on Eqs. 9 and 10, the calculation formula for the width of the artificial pillar can be obtained. In the design of the width of the artificial pillar, the width must be provisionally estimated based on different numbers of artificial pillars. The calculation result is then compared with the actual locations of the mine rooms and artificial pillars to determine the most reasonable width for the artificial pillar.

3. Example of the Jiaochong Mine, China

The gold mine in Jiaochong, China, is 500 m beneath the ground with a surface elevation of +160 m. The length of the ore body is 90 m with an average thickness of 5 m. It is mined by the room and pillar method, and artificial pillars are used to replace natural pillars to ensure the stability of the surrounding rocks of the gob area. The mine is divided into seven mining sections: -390 m, -410 m, -430 m, -460 m, -500 m, -540 m and -580 m. Currently, the sections above -410 m are finished. Backstoping has been performed in the section at -430 m. The section at -460 m is developed. Due to the impact of the surface environment, the main well is arranged in the region of the theoretical moving zone. Therefore, studying the effect of the mining processes of the sections at -430 m and -460 m on the overburden surrounding rocks and the surface movement is important, making the study of the size design and the stability of the artificial pillar crucial. The strike length of the mine section at -430 m is -85 m. The strike length of the mine section at -460 m is -65 m. The average inclination angle of the ore body is 30°. To ensure the stability of the surrounding rocks in the gob area and the reasonable design of the structural parameters of the ore blocks, a reasonable size for the artificial pillar must be determined. The physical and mechanical parameters of the overburden rock and mine backfill and the mining depth and spans are substituted into Eq. 9, developed by the author, and the corrected Eq. 10 with different selected N values for the trial calculation gives the following results:

Reasonable size of the artificial pillar in the section at -430 m:

$$B_{-430} = 6.6015 \text{ m} \quad N=4$$

Reasonable size of the artificial pillar in the section at -460 m:

$$B_{-460} = 5.7713 \text{ m} \quad N=3$$

4. Analysis of the Supporting Mechanism and Stability Effect of the Artificial Pillar

4.1 Supporting mechanism and mechanical characteristics

To verify the stability of the designed artificial pillar and the supporting effect for the overburden rocks in the gob area, the stability of the artificial pillar and the moving conditions of the overburden rocks in the sections at -430 m and -460 m were studied. The dimensional parameters of the mine rooms and the artificial pillars (with concrete used as the filling material) can be seen in Table 1, and the layout can be seen in Fig. 2.

Numerical modeling of the case study was performed using the finite difference modeling software FLAC^{3D} by Itasca. The mine has a bottom buried depth of 790 m, 124614 nodes and 117096 units. The physical and mechanical parameters of the model are shown in Table 2. The dimensions of the model are 600 m 600 m 400 m (Fig. 3). A gradient mode is adopted for meshing, with more dense and even grids used in the areas emphasized in this research. The model uses displacement boundary conditions: using the roll around support ($u_x = 0$, $u_y = 0$) and fixing the bottom ($u_x = 0$, $u_y = 0$, $u_z = 0$), the upper boundary is the gravity stress of the overburden rock (σ_{zz} = -10.92 MPa), the horizontal stress in the direction of the ore body tendency is 1.25 times the vertical stress ($\sigma_x = 12.5\ \sigma_z$), and the horizontal stress along the ore body is 0.75 times the vertical stress along the run of ore body ($\sigma_x = 0.75\ \sigma_z$). The Mohr-Coulomb strain softening standards are used in the calculations.

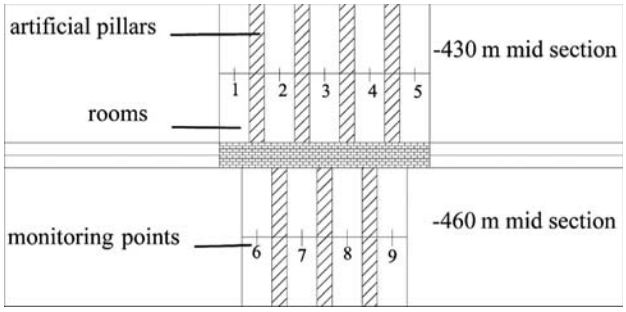

Figure 2 - Schematic diagram of the stope structure positions and the monitoring points in different sections.

Table 1 - Parameter design for the ore block structure.

Mid-section	Ore block structure parameter			
	Number of pillars per section	Pillar width (m)	Number of rooms per section	Room width (m)
-430 m	4	6.6	5	11.7
-460 m	3	5.8	4	11.9

Table 2 - Mechanical parameters of the rock mass.

Constituent	Unit weight (kN/m^3)	Elastic modulus (MPa)	Cohesion (MPa)	Friction angle (°)	Poisson's ratio	Tensile strength (MPa)
Surrounding rock	28	60000	15	45	0.2	7.5
Ore body	27.1	65000	15	42	0.19	7.5
Artificial pillar	21	230	0.171	35	0.25	0.01

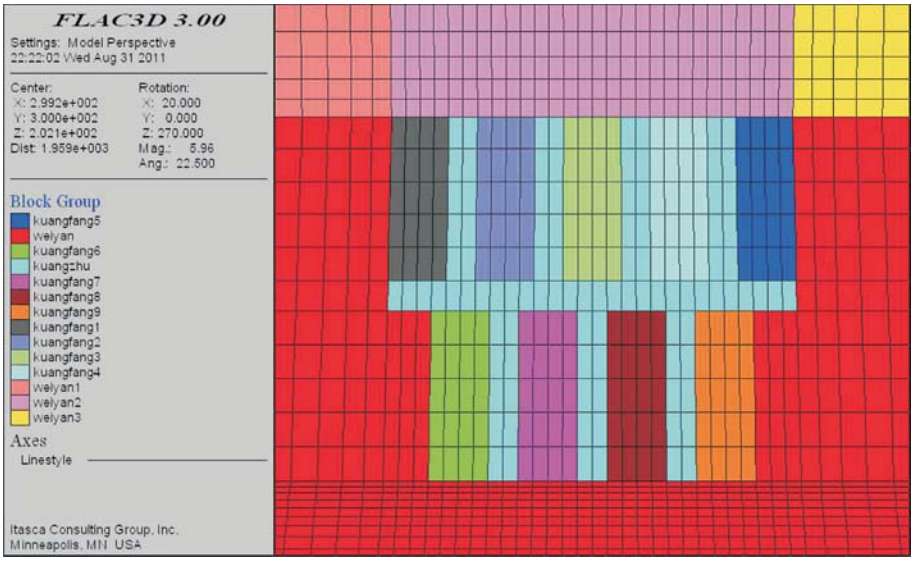

Figure 3 - Model of the mine rooms and artificial pillars.

In the mining process, the stress was significantly changed, especially in the area of the surrounding rocks outside the mine rooms at both ends. The stress in the bottom of the area of the surrounding rocks outside the mine rooms reached 61.03 MPa (Fig. 4), which was less than the maximum compressive strength of the surrounding rock, 75 MPa. However, in these areas, the safety monitoring should be enhanced and reinforcement measures should be implemented to ensure safety. According to the diagram of the maximum principal stress, the strain of the artificial pillar is relatively stable, without stress concentration (Zhao, 2012). The pressure on the pillar is also less than its compressive strength. The damage of any material starts with the appearance of a plastic zone. After the completion of mining, the artificial pillar had no plastic zones. Only two of the sections had plastic zones in the mining process. After the two sections were finished, the stress on the artificial pillar was stable, which indicates that the structural parameters of the designed artificial pillar can better prevent the formation and destruction of plastic zones in the overburden rocks in the gob area. The stress diagram and the plastic zone distribution show that the compressive stress or tensile stress is less than the breaking strength of instability, which will prevent the instability of the overburden rocks and the failure of the artificial pillar itself. The plastic zone distribution diagram of the mine rooms and overburden rocks also shows the superior supporting effect of the artificial pillar and the relatively stable stoping structures.

The stability and supporting effect of the artificial pillar are reflected by the displacement of the mine roof panels. To study the stability and supporting effect of the artificial pillar, displacement monitoring points #1-#5 were set up in the middle of the roof panel inside the mine room in the section at -430 m, and displacement monitoring points #6-#9 were set up in the middle of the roof panel inside the mine room in the section at -460 m. According to the calculation results, after the mining in the two sections was completed, monitoring point #3 in the roof panel inside the mine room in the section at -430 m had a maximum displacement settlement of 8.02 mm. Points #6 and #9 in the roof panels inside the two mine rooms on both ends of the gob area had a relatively small displacement settlement of 4.86 mm. Although the settlement of the roof panels in the gob area was relatively large, the stability of the roof panels was minimally affected based on the plastic zone distribution of the roof panels. After the section at -460 m was mined completely, monitoring points #7 and #8 of the roof panel in the gob area had a maximum settlement of 7.76 mm and a minimum settlement of 5.30 mm. Comparing the maximum values of the settlement in these two

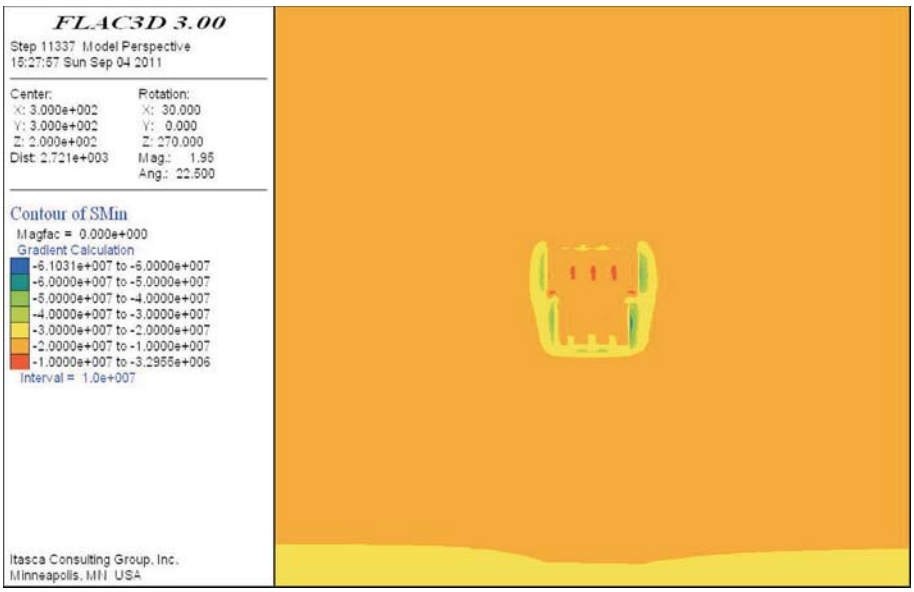

Figure 4 - Contour map of maximum principal stress.

sections, it can be observed that the settlement of a roof panel in a mine room is closely related to the section span such that larger spans correspond to greater settlement (the span of the section at -430 m is 85 m, and the span of the section at -460 m is 65 m).

4.2 Discussion of the field measurement supporting effect

The parameters in Table 1 show that although the backstoping depth of the section at -460 m is larger than that of the section at -430 m, its backstoping span is smaller. Therefore, the width is much more influential than the backstoping depth. According to Eqs. 9 and 10 established by the author, the reasonable width of the artificial pillar in the section at -460 m is less than that in the section at -430 m. To verify the practicality and rationality of the design, the monitoring data from the actual site are used to determine whether the design can meet the safety requirements. Therefore, monitoring equipment was set up in the mining sections. To study the supporting effect of the designed artificial pillar, the stress of the overburden rock, the displacement and the acoustic emission were monitored.

The stress variation status of the artificial pillar was monitored by vibrating wire strain gauges. After finishing the backstoping of the first-stage artificial pillar in the sections at -430 m and -460 m, a concrete pressure gauge was set up in the bottom of the striped uphill before filling the artificial pillar. The monitoring values of the concrete pressure gauge were recorded during and after the second-stage backstoping process. The stress variations and stress variation rates were obtained from the monitoring results to determine the areas with potential stress concentration and destruction. The monitoring results provide a reference basis to analyze the destruction type or the destruction scope of the artificial pillar or overburden rock. A sudden rise of the stress variation rate or a stress approaching the ultimate strength of the overburden rock can be regarded as an instability criterion for the artificial pillar or overburden rock.

Stress monitoring was conducted for nine months with concrete pressure gauges in these two sections (monitoring in the section at -430 m started in January 2008, and monitoring in the section at -460 m started in January 2009). The stress monitoring graph (Fig. 5) shows that the pressure of the roof panels on the top of the artificial pillar increased during the backstoping of the mine rooms at both ends. After completing the backstoping, the pressure variation curve plateaus. This result indicates the variation distribution of the vertical pressure of the artificial pillar used to bear the weight of overburden rocks. Based on the monitoring values, the maximum vertical stress of the artificial pillar in the section at -430 m is 0.78 MPa, and the maximum vertical stress of the artificial pillar in the section at -460 m is 0.43 MPa. Compared to the designed width of the artificial pillar according to the above formula, the width of the artificial pillar in the section at -430 m is larger than that in the section at -460 m, which is due to the larger mining span of the section at -430 m. Therefore, the on-site monitoring data indicate that the mining span of the artificial pillar is more influential than the mining depth.

The displacement in the sections at -430 m and -460 m was monitored with a VWM-type vibrating wire multipoint displacement meter. The displacement monitoring was performed for eight months for the roof panels in the gob area of the mine rooms (monitoring in the section at -430 m started in August 2009, and monitoring in the section at -460 m started in April 2010). Monitoring holes were drilled in the roof panels inside the gob area of the mine rooms. The relative amount of subsidence, collapse

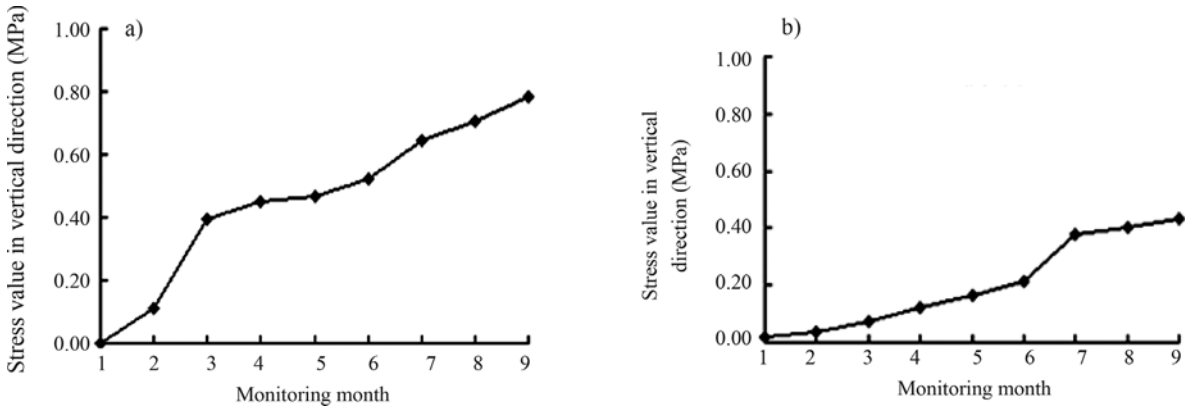

Figure 5 - Monitoring results recorded by the pressure gauge. (a) Stress monitoring of the artificial pillar in the section at -430 m. (b) Stress monitoring of the artificial pillar in the section at -460 m.

degree and destruction extent can be obtained through monitoring. When the monitoring holes are relatively deep, the bottom of the hole with a small displacement amount is regarded as the monitoring reference point. A sudden rise of the variation rate in multiple monitoring points or a sudden rise of the displacement value can be considered as the instability criterion of the overburden rock.

Typical monitoring data for the roof panels in the mine room of the two sections were selected for analysis. In the early months of the backstoping, the settlement amount of the roof fluctuated, and the settlement amount was also large. When the stress of the overburden rock in the mine rooms was transferred to the artificial pillar, the settlement amount of the roof decreased and gradually leveled off (Fig. 6). This result indicates that the movement patterns of the overburden rock controlled by artificial pillars with different widths are the same. They all exhibit a large amount of settlement in the primary stage. The settlement data feature more sudden fluctuations. When the distribution of the stress of the overburden rock becomes more stable, the settlement change of the roof in the gob area is also stable and can meet the safety requirements. Different distances from the hole bottom result in different relative displacements, with greater distances from the hole bottom (that is, shorter distances from the orifice) leading to greater relative displacement. The difference in the roof settlement in these two sections is reflected in the following aspects. First, larger gob area backstoping spans correspond to larger amounts of roof settlement. For example, the maximum relative settlement in the section at -430 m is 4.4 mm, and the maximum relative settlement in the section at -460 m is 2.7 mm. The settlement monitoring curve indicates that a larger span causes larger jumps in the settlement amount (the maximum absolute difference between the two groups of the monitoring data in the section at -430 m is approximately 0.8 mm, and the maximum absolute difference between the two groups of the monitoring data in the section at -460 m is approximately 0.5 mm), which indicates that the variation is large, with strong instability. Second, a larger backstoping span of the gob area results in a longer fluctuation cycle time of the displacement settlement curve. The main cause of this phenomenon is the large span, which results in a long stress redistribution duration for the roof and transfers to different directions during the stress redis-

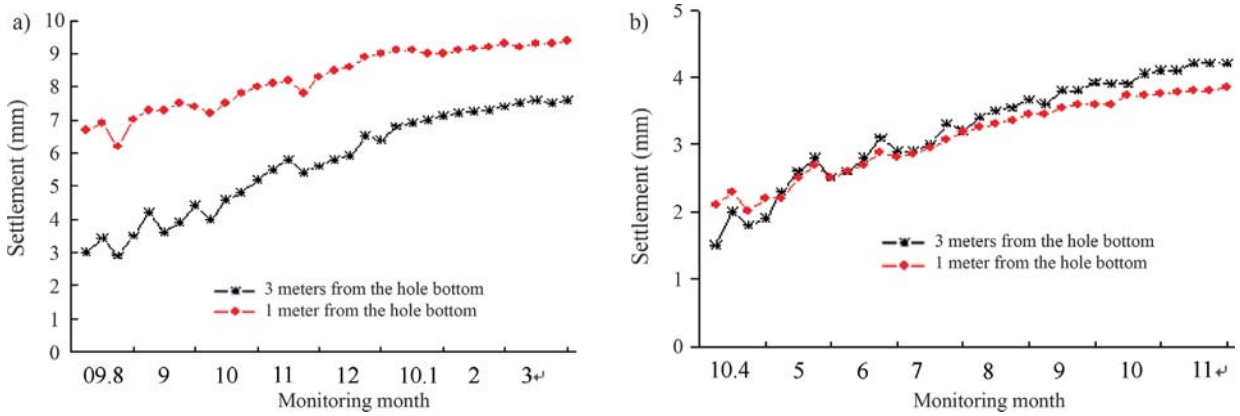

Figure 6 - Monitoring results obtained from the multipoint displacement meter. (a) Displacement monitoring of the mine room roof in the section at -430 m. (b) Displacement monitoring of the mine room roof in the section at -460 m.

tribution. In addition, the stress becomes more concentrated on the artificial pillars on both sides as time passes. A smaller span will lead to shorter stress redistribution time and more regular transfers of the stress distribution. The stress is more easily transferred to the focal points of stress, namely, both sides of the artificial pillar.

Such parameters as acoustic emission frequency and energy of rock mass can reflect the destruction process of the mass to some extent. In geotechnical engineering, the acoustic emission monitoring technique mainly evaluates and predicts the stability of rock mass using three indexes: total events, large events and energy rate. Because the span in the section at -430 m is relatively large and has many instability factors, the acoustic emission monitors were only set up in the key surrounding rocks of the gob area in this section. The monitoring data acquired by the acoustic emission probe at a certain period of time were selected for analysis. Table 3 shows that only a few sporadic acoustic emission signals of the overburden rock are observed in the absence of outside interference. The acoustic emission energy is small, and the acoustic emission phenomenon is infrequent and of short duration, which indicates that the monitored overburden rock in the gob area is stable.

Table 3 - A portion of the acoustic emissions monitoring data.

Monitoring time	Number of large events/Φ	Number of total events/N	Energy rate /E	Notes	Monitoring time	Number of large events/Φ	Number of toatal events/N	Energy rate /E	Notes
2010.01.12/00:10:44	0	0	0		2010.01.12/10:00:00	20	46	157	Period of preparation for rock drilling
2010.01.12/00:11:05	0	0	0		2010.01.12/10:00:21	4	12	35	
2010.01.12/00:11:27	0	0	0		2010.01.12/10:00:43	1	10	41	
2010.01.12/00:11:49	0	0	0		2010.01.12/10:01:04	1	3	16	
2010.01.12/00:11:59	0	0	0		2010.01.12/10:01:15	0	0	0	
2010.01.12/00:12:10	0	0	0		2010.01.12/10:01:25	0	0	0	
2010.01.12/00:12:20	0	0	0		2010.01.12/10:35:41	67	186	692	
2010.01.12/00:12:42	0	0	0		2010.01.12/10:36:03	45	78	725	
2010.01.12/00:12:53	0	0	0		2010.01.12/10:41:00	25	67	176	
2010.01.12/00:13:03	**1**	**3**	**6**		2010.01.12/10:41:10	47	120	0	
2010.01.12/00:20:00	0	0	0		2010.01.12/10:41:20	1	23	675	
2010.01.12/00:20:23	0	0	0		2010.01.12/10:41:42	89	143	832	
2010.01.12/00:20:33	0	0	0		2010.01.12/10:41:52	50	100	256	
2010.01.12/00:20:44	**1**	**1**	**1**		2010.01.12/10:42:03	47	66	0	
2010.01.12/00:20:55	0	0	0		2010.01.12/10:42:14	87	143	164	
2010.01.12/00:21:06	0	0	0		2010.01.12/10:42:25	99	146	240	
2010.01.12/00:21:27	0	0	0		2010.01.12/10:42:46	37	66	386	
2010-01-12/00:21:38	0	0	0		2010-01-12/10:42:56	14	24	365	
2010-01-12/00:21:48	0	0	0		2010-01-12/10:44:10	21	67	503	
2010-01-12/00:22:09	**3**	**5**	**7**		2010-01-12/10:44:32	55	167	647	
2010-01-12/00:22:21	0	0	0		2010-01-12/10:44:42	78	143	868	
2010-01-12/00:22:31	0	0	0		2010-01-12/10:44:53	99	169	1044	
2010-01-12/00:22:53	0	0	0		2010-01-12/10:57:00	43	156	678	
2010-01-12/00:23:03	0	0	0		2010-01-12/10:57:10	67	157	967	
2010-01-12/00:30:12	0	0	0		2010-01-12/10:57:32	43	67	654	
2010-01-12/00:30:33	0	0	0		2010-01-12/10:57:53	23	43	303	
2010-01-12/00:30:44	0	0	0		2010-01-12/10:58:04	34	54	878	

Period without mining disturbance

Period of rock drilling blasting and ore-drawing

5. Conclusion

(1) A new calculation method is proposed for the design of rational artificial pillar dimensions for deep mining. This method can compensate for the shortcomings of setting the dimension parameters of artificial pillars according to area bearing capacity theory. It can also provide a reference basis for the design of artificial pillars, optimize the pillar dimensions, and reduce the artificial pillar filling cost in mines.

(2) According to the numerical results, the compressive stress or tensile stress experienced by the artificial pillar is much lower than the compressive strength or tensile strength, which indicates that the artificial pillar is stable. With the support of the artificial pillar, the settlement of the overburden rock roof in the gob area is controlled. The maximum displacement settlement amount is 8.02 mm in the roof panel inside the mine room in the section at -430 m, and the maximum displacement settlement amount is 7.76 mm in the roof panel inside the mine room in the section at -460 m, which does not affect the stability of the artificial pillar and the roof overburden rock.

(3) The on-site monitoring data reveal that the vertical stress of the artificial pillar in the section at -430 m is larger than that in the section of -460 m, which indicates that the impact of the mining span of the artificial pillar exceeds the mining depth.

(4) When the backstoping span in the gob area is large, there is a larger settlement of the overburden rock roof, the settlement fluctuation is greater, and the overburden rock is more unstable. Additionally, the larger the backstoping span, the longer the period of the re-distribution process of the roof and the settlement cycle.

(5) In the absence of outside interference, only a few sporadic acoustic emission signals of the overburden rock appear. The acoustic emission is characterized by low energies and a short duration, which indicates that the monitored overburden rock in the gob area is stable.

(6) The various study methods used show that the structural parameters of the designed artificial pillar are reasonable and can effectively prevent movement of the overburden rock in the gob area to meet safety requirements.

Acknowledgments

The authors gratefully acknowledge the National Natural Science Foundation of China (Grant 51304083), the Science and Technology Program of Jiangxi Province (20132BBG70106), the Jiangxi Province Science Foundation for Youths (20142BAB216020), and the Natural Science Foundation of Jiangxi University of Science and Technology (NSFJ2014-K02).

References

Brady, B.H. G. & Brown, E. T. (2006). Rock Mechanics for Underground Mining. Third edition. Kluwer Academic Publishers, New York, 377 p.

Cai, M.F. (2002). Rock Mechanics and Angineering. Science Press, Beijing: 126 p (in Chinese).

Chen, Q.F. & Zhou, K.P. (2010). Action mechanism of low-grade backfill on stability of mining environment structure. Rock and Soil Mechanics, 31(9):2811-2816.

Diederichs, M.S.; Coulson, A.; Falmagne, V.F.; Rizkala, M. & Simser, B. (2002). Application of rock damage limits to pillar analysis at Brunswick Mine. In: Proceedings of the North American Rock Mechanics Conference, UTPress, Toronto, pp. 1325-1332.

Ghasemi, E.; Ataei, M.; Shahriar, K.; Sereshki, F.; Jalali, S.E. & Ramazanzadeh, A. (2012). Assessment of roof fall risk during retreat mining in room and pillar coal mines. International Journal of Rock Mechanics and Mining Sciences, 54:80-89.

Gu, D.S. & Li, X.B. (2006). Modern Mining Science and Technology for Metal Mineral Resources. Metallurgical Industry Press, Beijing, 235 p.

Ji, W.D. (1991). Mining Rock Mechanics. Metallurgical Industry Press, Beijing, 38 p.

Liu, C.L.; Tan, Z.X.; Deng, K.Z. & Li, P.X. (2013). Synergistic instability of coal pillar and system and filling method based on plate model. International Journal of Mining Science and Technology, 23:145-149.

Lind, G. (2005). An integrated risk management approach for underground coal pillar extraction in South Africa. Journal of the South African Institute of Mining and Metallurgy, 105(2):137-147.

Luo, H.; Yang, S.J. & Tao, G.Q. (2010). Stability analysis of ore pillar and application using concept of dynamic fuzzy reliability based on Finite Element Method Artificial Neural Network-Monte Carlo Simulation. Journal of China Coal Society, 35(4):551-554.

Palei, S.K. & Das, S.K. (2009). Logistic regression model for prediction of roof fall risks in bord and pillar workings in coal mines: An approach. Safety Science, 47(1):88-96.

Tu, H.S.; Tu, S.H.; Zhang, X.G.; Li, Z.X. & Jia, S. (2014). Technology of back stoping from level floors in gateway and pillar mining areas of extra-thick seams. International Journal of Mining Science and Technology, 24:143-149.

Wang, X.J.; Feng, X.; Zhao, K.; Yang, T.B. & Zhao, K. (2012). Reasonable width calculation and analysis of artificial pillar in deep mining. Journal of Mining & Safety Engineering, 29(1):54-59.

Zhao, K. (2012). Study of Overburden Movement Mechanism and Prevention in Jiaochong Gold Mine. Ph.D. Thesis, University of Science and Technology, Beijing,79 p (in Chinese).

Influence of the Test Specimen Diameter on the Measurement of Electrical Resistivity in Sands by Using Laboratory Devices

M.C. Pregnolato, H.L. Giacheti, A.S.P. Peixoto

Abstract. Electrical resistivity tests have long been used in geo-environmental site characterization because they provide qualitative data to identify the presence of contaminants in soil. The measurement of soil electrical resistivity is affected by many intervening factors, which are usually studied separately in the laboratory and are important to ensure the correct interpretation of in situ test data. This paper presents the evaluation of the influence of the diameter of test specimens on electrical resistivity measurements of a particulate medium in the laboratory, using two different techniques, copper plates and a resistivity probe. The data were discussed considering Archie's Law, and it indicates that the geometry of test specimen has a greater effect than the measurement technique. The larger test specimen allows more current pathways for electron propagation because electric current travels along the path of least resistance to the passage of electrons. The findings from this research can be used to guide a laboratory test investigation and its data interpretation.
Keywords: electrical resistivity, copper plates, resistivity probe, Archie Law, site characterization.

1. Introduction

Multidisciplinary geotechnical research involves combining different methods for geo-environmental site characterization like: surface and subsurface exploration; geophysical surveys to supplement drilling; sampling methods; and laboratory tests of soil, gas and liquids samples.

The resistivity piezocone test (RCPTU) stands out among in situ tests as a tool for defining subsurface stratigraphy and simultaneously measuring electrical resistivity which is routinely employed in Geotechnical Engineering and Geophysics to characterize subsoil and in soil analyses (Bryson & Bathe, 2009), as well as in other areas of science such as Agronomy (Corwin & Lesch, 2005; Molin & Rabello, 2011), Archaeology and Geology (Schoor, 2002).

Although the electrical resistivity is an intrinsic property of each material, there are several intervening factors affecting it and several experimental researches offered significant insight on this subject. Those studies include that of Abu-Hassanein & Benson (1994), who analyzed compacted clays and demonstrated the influence of moisture content, compaction energy and the initial saturation of the test specimen on electrical resistivity. Daniel (1997) studied in laboratory two compacted soils (calcine tailing and pure quartz rock flour) and analyzed the impact of the degree of soil saturation, porosity and type of interstitial fluid on electrical resistivity in piezocone penetration tests. Aquino (2010) studied compacted clay and correlated electrical resistivity with soil index properties. Long *et al.* (2012), who studied marine clay, demonstrated that its electrical resistivity was determined by the salt content in the interstitial fluid and the percentage amount of clay in the sample.

Two different techniques are commonly used in the laboratory to measure electrical resistivity: conductive plates installed at the top and bottom of a test specimen (Abu-Hassanein & Benson, 1994; Aquino, 2010), or a resistivity module (RCPTU) embedded in a test specimen (Daniel, 1997; Pacheco, 2004). These techniques provide different descriptions of the variation in electrical resistivity, since their geometric, electrical and physical characteristics differ.

In this context, this paper evaluates the effect of compaction mold geometry on the electrical resistivity of construction sand, using a resistivity probe developed at UNESP Bauru (Fig. 1) and copper plates to determine the distribution of the electric potential in the particulate medium.

The analyzes of electrical resistivity were done in two different test specimens with 155 mm and 450 mm diameter, but equal height in order to verify the influence of distortions along electrical current propagation pathways and the distribution of stresses within the soil during the tests, as well as their effect on the electrical resistivity measurement.

2. Background

Electrical resistivity is, by definition, an intrinsic property of homogeneous materials. However, the subsoil usually consists of a complex distribution of different mate-

Marluci Cristina Pregnolato, MSc., Universidade Estadual Paulista "Júlio de Mesquita Filho", Bauru, SP, Brazil. e-mail: marlucicp@hotmail.com.
Heraldo Luiz Giacheti, PhD., Full Professor, Departamento de Engenharia Civil e Ambiental, Universidade Estadual Paulista "Júlio de Mesquita Filho", Bauru, SP, Brazil. e-mail: giacheti@feb.unesp.br.
Anna Silvia Palcheco Peixoto, PhD., Associate Professor, Departamento de Engenharia Civil e Ambiental, Universidade Estadual Paulista "Júlio de Mesquita Filho", Bauru, SP, Brazil. e-mail: anna@feb.unesp.br.
Submitted on April 10, 2015; Final Acceptance on May 3, 2016; Discussion open until December 30, 2016.

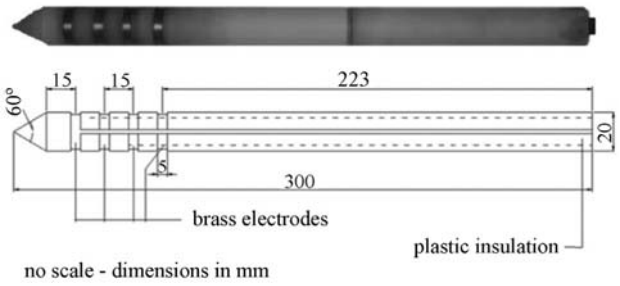

Figure 1 - Electrical resistivity probe developed at UNESP-Bauru.

rials with different resistivity. Natural soils have different electrical properties because of their different genesis, grain size, structures, moisture content and temperature. The characteristics of any material and soils are therefore strongly related to electrical conductivity and can be quantified by means of geoelectrical properties. They are relevant for the indirect investigation of soils (Kong *et al.*, 2012) and can be used in various issues, such as soil physical properties (Archie, 1941), soil and groundwater contamination (Campanella & Weemees, 1990), soil improvement and stabilization (Liu *et al.*, 2006 and 2007), sand liquefaction (Arulmoli *et al.*, 1985), and soil microstructure (Fukue *et al.*, 1999).

Several factors can affect soil electrical resistivity (Kibria & Hossain, 2012). One of the main factor is the moisture content (McCarter, 1984), although the effects of the degree of soil saturation (Abu-Hassanein & Benson, 1996), pore density and structure (Gupta & Hanks 1972), soil organic content (Ekwue & Bartholomew, 2010), composition of soil pore water (Kalinski & Kelly, 1993), and geological formation (Giao *et al.*, 2003) are also important.

The three-phase composition of soil is another important factor in the analysis of electrical resistivity. The distribution of electrical current occurs in the soil's three components, *i.e.*, the liquid, solid and gaseous phases. However, most of the electrical current travels through the interstitial fluid since electrical charges are transported more easily in the liquid environment, generating electrolytic current (Lunne *et al.*, 1997).

2.1. Formation factor

The formation resistivity factor of soil (F) was first studied by Archie (1941), based on the laboratory determination of the electrical resistivity of a large number of sand samples saturated with solutions of water and sodium chloride, 20,000 mg to 100,000 mg of NaCl per liter, and with porosity varying from 10% to 40%.

Archie (1941) determined that the formation resistivity factor is the ratio between the resistivity of sand saturated with water and sodium chloride solution (ρ_0) and the resistivity of a water and sodium chloride solution (ρ_f), Eq. 1:

$$F = \frac{\rho_0}{\rho_f} . \quad (1)$$

By this equation, the formation resistivity factor is related with grain shape and it is considered that the electrical conduction varies solely as a function of the geometry of the pores formed between the grains, and hence, the mineralogy. According to Weemees (1990), the absence of electrical conduction through the particles is considered fundamental.

In the case of soil containing significant amounts of clay minerals, *i.e.*, that can conduct electrical charges along the surface of its particles, resistivity measurements do not distinguish the electrical conduction phenomena, so the measured resistivity takes into account an apparent formation factor (Jackson *et al.*, 1978). Therefore, the formulation to obtain the formation factor depends on the type of soil under analysis, which may involve more complex equations for clayey materials or simpler ones for sandy materials.

Based on empirical observations, Archie (1941) related the formation factor with sand porosity, Eq. 2, and this first mathematical relationship is known as Archie's law:

$$F = n^{-m} \quad (2)$$

where m is a constant determined experimentally and n is the soil porosity.

Archie (1941) characterized the constant m as being dependent on the degree of cementation of individual particles; later, Guyod (1944) described m as being dependent on the type of soil parent rock (Jackson *et al.*, 1978).

Based on his findings of marine sediments, Taylor-Smith (1971) proposed two simple formulations to describe the results of cohesive (sediment-rich clays) and non-cohesive materials, as follows: $F = n^{-1.5}$ with $n < 0.6$ for sands, and $F = n^{-2.0}$ with $n < 0.6$ for clays (Jackson e*t al.*, 1978).

Archie's formulation (1941), Eq. 3, underwent changes through the inclusion of the fitting constant a proposed by Winsauer *et al.* (1952), as reported Jackson *et al.* (1978), and also based on the study of unsaturated conditions, which resulted in Eq. 3:

$$\rho_b = a \cdot \rho_f \cdot n^{-m} \cdot S_r^{-S} \quad (3)$$

where a and s are constants that can be determined experimentally, ρ_b is the apparent soil resistivity, ρ_f is the interstitial fluid resistivity, and S_r is the degree of saturation.

Thus, the relationship presented in Eq. 3 is an important empirical relationship in studies of sand, which can be regarded as an indirect relationship of Archie's Law, which has been widely used by other authors such as Daniel *et al.* (2003), Pacheco (2004) and Oliveira (2004).

Parameter a is a constant that depends on soil porosity, whose value for unconsolidated soil varies around 1.0 (Oliveira, 2004).

Jackson *et al.* (1978) studied the influence of the shapes of natural and synthetic particles on the formation of factor, as well as their particle size distribution curve, and demonstrated that exponent *m* is entirely dependent on particle shape. In their study, the values of *m* for marine sand varied from 1.2 to 1.9, and these values were not affected by the particle size distribution in sand, although the magnitude of *m* tends to increase with the increase in percentage deviation from particle sphericity.

According to Daniel *et al.* (2003), the values of constants *m* and *s* ranged from 1.3 to 2.2 and from 1.0 to 2.5, respectively. In contrast, in his studies of consolidated sandstone and washed unconsolidated sand stored in the laboratory, Archie (1941) found that constant *m* varied from 1.3 to 2.0 and constant *s* showed values close to 2.0 in the saturated condition.

Daniel *et al.* (2003) also showed that factor S_r^{-s} varies much more than factor n^{-m}, although exponents *m* and *s* are of the same magnitude (Fig. 2), because the degree of saturation (S_r) may vary from 0 to 1 in any soil, while soil porosity (*n*) typically varies from 0.25 to 0.50.

Peixoto *et al.* (2014) studied the formation factor of a saturated sedimentary sand by means of permeability tests, using different concentrations of percolation fluids (Table 1). In that study, they applied two formulations to determine the formation factors: that of Archie (1941), represented by factor *F*, and that of Waxman and Smits (1968), which is presented as *F** and was calculated by Eqs.

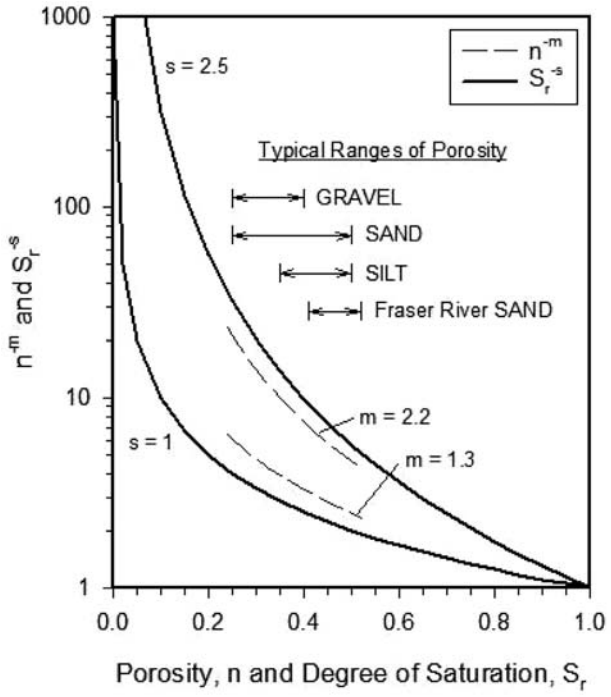

Figure 2 - Sensitivity of Archie's Law to variations in soil porosity and degree of saturation.Source: Daniel *et al.* (2003).

Table 1 - Saturated soil resistivity (ρ_{sat}), electrical conductivity of water (C_w), resistivity of water in the reservoir before percolation (ρ_w), formation factor adjusted by Archie (*F*), and formation factor adjusted by Waxman & Smits (1968) (*F**) as cited by Peixoto *et al.* (2014).

	ρ_{sat} (Ω.m)	C_w (μS/cm)	ρ_w (Ω.m)	*F*	*F**
Distilled water	680.37	1.00	10000.00	0.07	-
Tap water	577.26	133.6	74.87	7.71	
250 PPM	146.39	523.5	19.11	7.67	7.02
500 PPM	71.05	1025.7	9.75	7.29	

4 and 5. The formation factor resulted in *F** equal to 7.0, confirming Archie's Law (*F*) for sandy soils.

$$F^* = \frac{1}{C_0}(C_e + C_w) \quad (4)$$

where: C_0, C_e and C_w are the specific conductance (conductivity) of the core, clay exchange cations and equilibrating salt solution, respectively.

According to Waxman and Smits (1968), $C_e = 0$ for clean sands, and *F** reduces to *F*, the usual formation resistivity factor, Eq. 5:

$$F^* = \frac{C_w}{C_0}. \quad (5)$$

The Eq. 5 can be rewritten as Eq. 6 for a better understanding:

$$F^* = \frac{\rho_0}{\rho_w}. \quad (6)$$

3. Materials and Methods

3.1. Materials

The measurement of electrical resistivity was carried out on samples with the same height (197 mm) and with two different diameters (155 mm and 450 mm) in order to assess possible distortions on the current propagation pathways. The large diameter was designed to minimize distortions and possible edge effects when measuring the resistivity, *i.e.*, the 450 mm diameter of the large test specimen was designed to be approximately three times that of the small test specimen (155 mm) (Table 2 and Fig. 3).

A washed sand was used and the main characteristics are presented in Table 3. The sample was prepared with drying-air and sifting it through four sieves; one with a nominal aperture of 9.52 mm and the other three with nominal apertures of 4.76 mm (Fig. 4) in order to eliminate the bigger particles and for a better homogenization of the test samples.

Table 2 - Dimensions of the containers used in the electrical resistivity evaluation tests performed with copper plates and with the resistivity probe.

Description	Test specimen dimensions	
	Small	Large
Test specimen diameter (mm)	155	450
Effective height of test specimens, h_{cp} (mm)	196	198
Test specimen volume (mm^3)	3688.82	31458.73
Copper plate diameter (mm)	111	111
Copper plate area (mm^2)	9677	9677
Ratio d_{cp}/h_{cp}	0.79	2.27

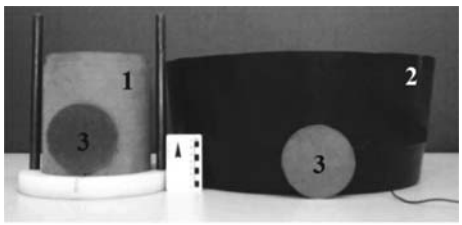

1 - Small cylinder (155 mm)
2- Large cylinder (450 mm)
3 - Copper plate

Figure 3 - Containers used in the electrical resistivity tests performed with copper plates and the resistivity probe.

Table 3 - Washed sand main characteristics.

Test	Description	Value
Specific gravity of the solids	γ_s (kN/m^3)	26.87
Overall particle size	clay, Ø < 0.002 (%)	-
	silt, 0.002 < Ø < 0.060 (%)	-
	fine sand, 0.060 < Ø < 0.20 (%)	20
	medium sand, 0.20 < Ø < 0.60 (%)	64
	coarse sand, 0.60 < Ø < 2.00 (%)	14
	fine gravel, 2.00 < Ø < 6.00(%)	2

3.2. Methods

Four groups of tests were defined: copper plate with 155 mm diameter test specimen (CP 155); copper plate with 450 mm diameter test specimen (CP 450); resistivity device with 155 mm diameter test specimen (RD 155); and resistivity device with 450 mm diameter test specimen (RD 450). Nine tests were carried out varying the moisture content from hygroscopic moisture up to the fully saturated condition for each test group (36 tests total). The void ratio of the sample was controlled, however some values were higher than it was expected. In these cases, the test data were not considered. So, the test data were divided into 5 sets (A, B, C, D and E), each of them containing one test data of each test groups (CP 155, CP 450, RD 155, RD450).

Figure 4 - Pluviation device used for homogenization of the sand before the tests.

Twenty tests with the moisture content varying from hygroscopic up to the fully saturated condition for each test group were considered. A total of 5 sets (A, B, C, D and E), one test data of each test groups (CP 155, CP 450, RD 155, RD450) is presented in Table 4.

This approach allowed analyzing the variation of the electrical resistivity values as a function of the soil physical indices for both test specimens (small and large), using the two aforementioned techniques (Fig. 5).

The test specimens were prepared by using a modified pluviation method (Fig. 6), sifting the sand through only one sieve with nominal aperture of 19 mm. The use of just one sieve instead a set of sieves as proposed by Pacheco (2004) was necessary because it was not possible to pass the saturated sand through a set of sieves. It is important to point out that the size of the sieve (19 mm) was kept constant in all the tests, regardless of the moisture content of the sand.

Measuring electrical resistivity by the copper plate and resistivity device techniques differs in terms of the position of the measuring instruments and the generated electrical field. The values of frequency, root mean square voltage, V_{rms} (which means the corresponding voltage of alternate current) and sine-wave were kept constant in both techniques. The measured voltage and current values were inserted in the operating equations of the measuring devices to determine the electrical resistivity.

Table 4 - List of test sets as a function of temperatures (T_{soil}), soil resistivity (ρ_b), fluid resistivity (ρ_f), formation factor (F), moisture content (w), void ratio (e), porosity (n) and degree of saturation (S_r).

Set	Technique/Diameter (mm)	T_{soil} (°C)	ρ_b (Ω.m)	ρ_f (Ω.m)	F	w (%)	e	n	S_r (%)
A	CP 155	24.8	2990	71	42	2.0	0.85	0.46	6.3
	RD 155	24.8	17508	71	248	2.0	0.83	0.45	6.5
	CP 450	23.5	1157	71	16	2.0	1.02	0.50	5.2
	RD 450	24.2	3221	71	46	2.0	0.92	0.48	5.8
B	CP 155	23.3	697	71	10	5.5	0.91	0.48	16.0
	RD 155	23.6	1493	71	21	5.7	0.90	0.47	16.9
	CP 450	23.3	489	71	7	7.2	0.99	0.50	19.3
	RD 450	23.1	2884	71	41	6.7	0.98	0.49	18.3
C	CP 155	24.6	190	73	3	17.1	0.64	0.39	71.5
	RD 155	24.4	312	73	4	15.2	0.74	0.42	55.0
	CP 450	24.9	391	73	5	20.2	0.86	0.46	63.1
	RD 450	24.6	661	73	9	18.6	0.85	0.46	58.5
D	CP 155	25.3	141	66	2	19.5	0.54	0.35	96.1
	RD 155	25.6	477	66	7	18.4	0.55	0.36	88.8
	CP 450	25.3	152	66	2	21.4	0.61	0.38	93.7
	RD 450	24.9	187	73	3	22.3	0.61	0.38	97.0
E	CP 155	25	138	73	2	18.6	0.48	0.32	100.0
	RD 155	24.8	205	73	3	19.4	0.50	0.33	100.0
	CP 450	24.5	138	73	2	22.3	0.63	0.39	95.1
	RD 450	25.5	153	66	2	20.4	0.54	0.35	100.0

Each test specimen was subjected to the following measurements: soil temperature, sand weight, electrical current, voltage, soil moisture content, and water and soil conductivity. The electrical measurement of each specimen was correlated with its respective soil physical index.

3.3. Formulation to determine the constants of Archie's Law

The results of the evaluation of the edge effect of the compaction mold on the washed sand were analyzed using Archie's Law (Eq. 3). The ratio between soil electrical resistivity and fluid electrical resistivity is called the formation factor (F), so Eq. 3 can be rewritten as Eq. 6:

$$F = a \cdot n^{-m} \cdot S_r^{-S} \ . \quad (6)$$

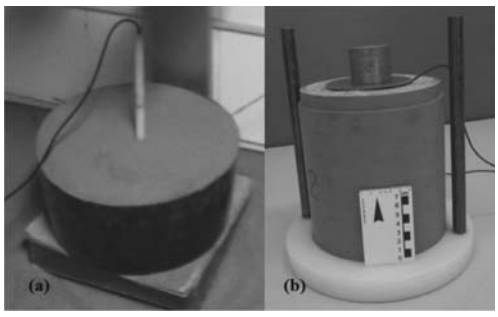

Figure 5 - Test specimens and measuring instruments: (a) 450 mm diameter tested with the resistivity device, (b) 155 mm diameter tested with copper plates, using a standard weight on top of the upper plate.

Figure 6 - Pluviation device used for molding the test specimens.

To apply this formulation, however, it was necessary to first determine the empirical constants *m*, *s* and *a*, which were calculated using the data from the tests performed with the circular copper plates and the resistivity probe. The method used to calculate these constants was the same as that used by Daniel (1997), which is detailed below.

3.3.1. Calculation of the porosity exponent (constant m)

Under conditions in which the degree of saturation is constant, the constant *m* can be determined by isolating n^{-m} of Eq. 6 and applying the logarithmic operation on both sides, which leads to Eq. 7:

$$\log\left(F \frac{S_r^{\,S}}{a} \right) = (-m) \log n \,. \tag{7}$$

In Eq. 8, it is attributed the value of a single constant *C* to factor (S_r^{-s}/a) of Eq. 7:

$$\log(F \cdot C) = (-m) \log n \,. \tag{8}$$

Thus, it is possible to plot the formation factor (*F*) on the di-log scale as a function of porosity (*n*) and obtain exponent *m* by including a power trend line.

3.3.2. Calculation of the exponent of the degree of saturation (constant s)

Given that *m* is a known parameter, S_r^{-s} can be isolated in Eq. 6, similarly to the way constant *m* was calculated, and the logarithmic operation can be applied on both sides of the equality, Eq. 9:

$$\log\left(F \cdot \frac{n^{\,m}}{a} \right) = (-S) \log S_r \,. \tag{9}$$

The parameter *s* can be obtained by plotting the results of $F.n^m$ *vs.* degree of saturation and fitting the points by means of a power trend, since *a* is a constant.

3.3.3. Calculation of coefficient a

After identifying the exponent *m and the* exponent *s*, the constant *a* can be determined by plotting the formation factor (*F*) *vs.* $n^{-m}.S_r^{-s}$ and calculating the angular coefficient of the fitted points on a straight line, given the linear relationship between the axes.

4. Test data and analysis

The test data are separated in five groups, each of them comprising four prepared specimens according to the moisture content. In other words, the measurements were taken from two test specimens for each container diameter (155 mm and 450 mm), using the copper plates and the resistivity device for each diameter (Table 4).

The average temperature in these tests was 24.9 °C, with a variation of 2.5 °C between the maximum and minimum. Because the test specimens were grouped in sets of tests and the maximum variation in temperature for a given set was 1.3 °C (Table 4), the resistivity device curves were used in lieu of each test temperature, precluding the need to adapt a standard temperature to correct the values of electrical resistivity.

The first index to be calculated was the porosity exponent *m*, using Eq. 6 to Eq. 8 and assuming S_r^{-s} equal to 1. So, only the test data from the samples with degree of saturation higher than 94.0% and with no edge effects (set D - CP 155 and CP 450 and set E - CP 155, RD 155, CP 450, RD 450) were considered. The porosity values were related graphically to the formation factor, on a graphic di-log scale as shown in Fig. 7.

Because *m* is an empirical constant, R^2 is assumed to have lower values. Although the calculated value of R^2 was equal to 0.6116, the calculated value of exponent *m*, of -1.894, falls within the range reported in the literature, and is similar to the value of -1.96 reported by Daniel (1997) for pure fine sand. In this calculation, the void ratio was between 0.30 and 0.40, while the results reported by Daniel (1997) were between 0.30 and 0.50, indicating an equivalence between the test data.

The Eq. (9) was used to calculate the exponent of the degree of saturation, *s,* with *m* equal to 1.894. The $F.n^m$ term was calculated using all the five set data and they are presented in Table 4. After that, exponent *s* was graphically obtained. The calculation of the exponent *s* presented an R^2 value of 0.8145 (Fig. 8), which is higher than that calculated for exponent m and adequate for this magnitude. Therefore, the calculated value of -1.258 for constant *s* is a good fitting for this parameter and falls within the range reported in the literature, which varies from 1.0 to 2.5, according to Daniel *et al.* (2003).

As for exponent *m* and exponent *s*, it should be noted that although they are of the same order of magnitude, the variation of factor S_r^{-s} is greater than that of factor n^{-m} because the degree of saturation varies more widely than soil porosity. Thus, the value of exponent *m*, which presented the lowest R^2, is related with the factor that varies the least according to Archie's Law.

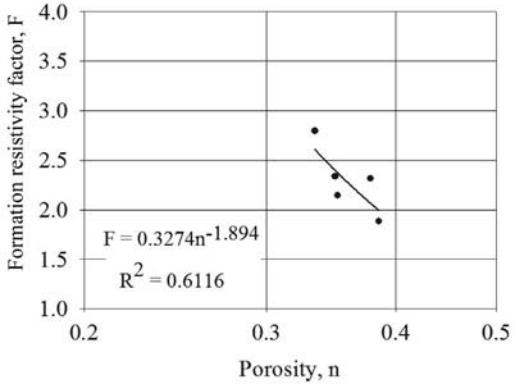

Figure 7 - Definition of the exponent m by using data points with a degree of saturation higher than 94%.

The constant a was calculated from exponent m and exponent s based on the graph presented in Fig. 9, which relates the formation factor (F) with factors $n^{-m}.S_r^{-s}$ by means of a linear relationship. The R^2 value was equal to 0.5949 due to the low soil moisture of two data points, with $n^{-m}S_r^{-s}$ around the value 140. All the 5 set of data were used in this analysis. The value of $a = 1.030$ is consistent with values reported in the literature.

The void ratio of the soil sample was related with the electrical resistivity calculated by Archie's Law to assess the influence of the geometry of the test specimens in determining the electrical resistivity values. Figure 10 depicts the electrical resistivity measured by the copper plates, ignoring only set A, because the propagation of electrical current in an almost dry environment ($w = 2\%$) was very low.

The data measured with the copper plates showed two trend lines with high values of R^2 (Fig. 10), indicating that the distribution of voltages varied with the diameter of the test specimen. A comparison of the values of R^2 of the test specimens revealed that the one with a diameter of 155 mm showed the highest value.

Figure 11 illustrates the results of the tests performed with the resistivity device. In this case, also, the two points

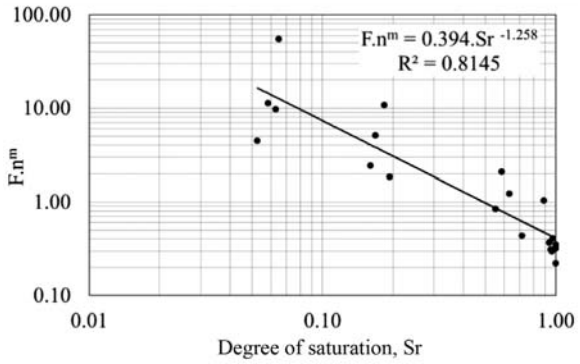

Figure 8 - Definition of the exponent s assuming a m value equal to -1.894.

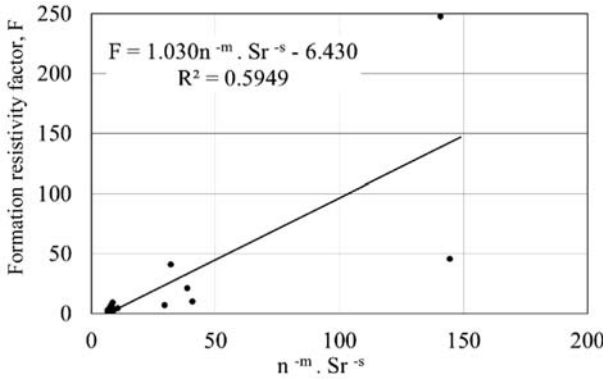

Figure 9 - Definition of the coefficient a for m = -1.894 and s = -1.258.

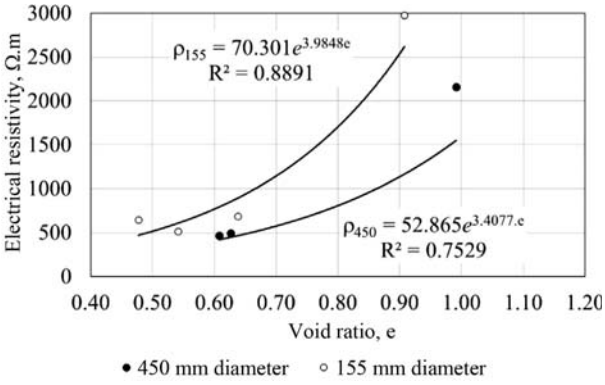

Figure 10 - Electrical resistivity of the test specimens with diameters of 155 mm and 450 mm measured with the copper plates.

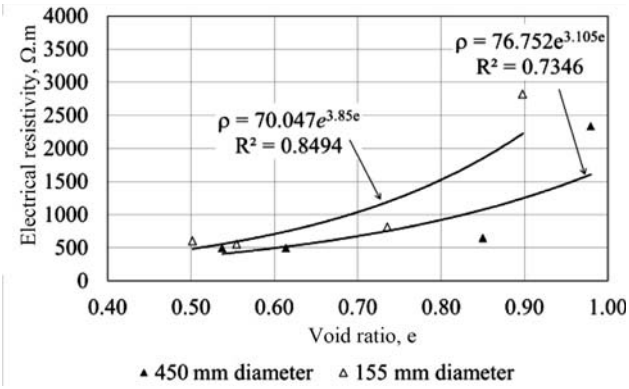

Figure 11 - Electrical resistivity of the test specimens with diameters of 155 mm and 450 mm measured with the resistivity device.

with a degree of saturation of about 5.0%, *i.e.*, set A in Table 4, was ignored.

The average temperature in these tests was 24.9 °C, with a variation of 2.5 °C between the maximum and minimum. Because the test specimens were grouped in sets of tests and the maximum variation in temperature for a given set was 1.3 °C (Table 4), the resistivity device curves were used in lieu of each test temperature, precluding the need to adapt a standard temperature to correct the values of electrical resistivity.

The fitting curves obtained in the tests with the resistivity probe also showed two different trends, depending on the diameter of the test specimen (Fig. 11). Again, good R^2 values were obtained on both curves, the higher one obtained in the test on the 155 mm diameter test specimen.

The similarity of the fitted curves obtained by the two electrical resistivity measurement techniques thus allowed for a comparison of the measurements of the test specimen with the two diameters taken with the copper plates and the resistivity probe (Fig. 12).

The electrical resistivity measured for the same test specimen by using the resistivity probe and the copper plates showed very similar fitting curves, all with high values of R^2, particularly for the small test specimen. The val-

ues of electrical resistivity showed higher variations as a function of the test specimen diameter than of the measurement techniques.

It was therefore possible to consider a single adjustment of the electrical resistivity data for each test specimen on the same curve, considering the two different devices used in this study (Fig. 13).

An analysis of the R^2 values presented in Fig. 13 leads to the conclusion that, for each test specimen diameter, the fitting of the two resistivity measurement techniques to a single curve was perfectly adequate, since the resulting values of R^2 are similar to those presented in Fig. 12, in which the curves were calculated separately.

In Fig. 13, the two extreme data from the two test specimens, with electrical resistivity of about 3.000 Ω.m and degree of saturation of about 17%, were the ones that presented the highest absolute difference in resistivity between the test specimen diameters. Hence, the high absolute difference in resistivity between the test specimens stems from the difficulty of current propagation at high values of electrical resistivity, a condition in which there is greater distortion of current propagating through a particulate medium.

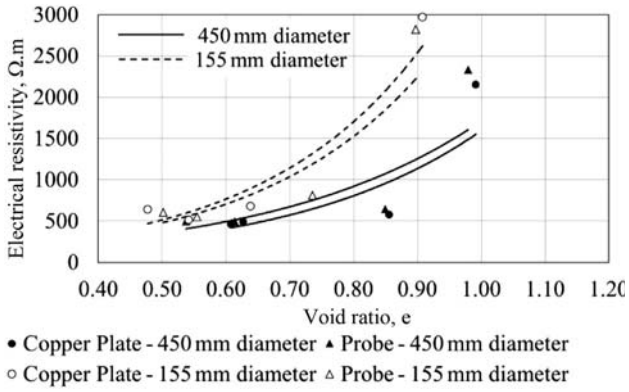

Figure 12 - Electrical resistivity of the test specimens with the two diameters measured with the resistivity probe and with the copper plates.

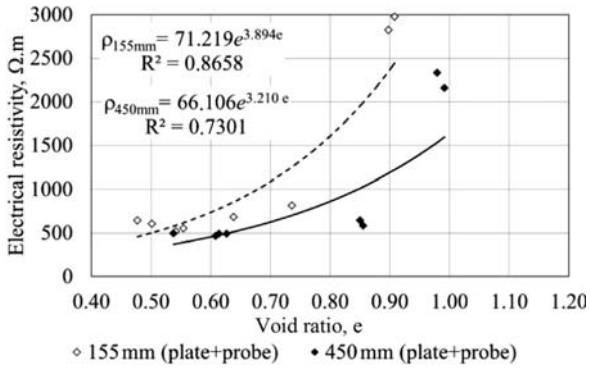

Figure 13 - Adjustment of electrical resistivity as a function of test specimen geometry, using both resistivity measurement techniques.

5. Conclusions

The electrical resistivity data obtained by the two techniques were quite similar and allowed for the fitting of a single curve as a function of the test specimen diameter. Although the geometric and electrical characteristics of the techniques used in this study differ and provide different soil voltage distribution, the two techniques were equally efficient in measuring the electrical resistivity of sand prepared in the laboratory.

It was found that the test specimen geometry, *i.e.*, its diameter, was more relevant in determining the soil electrical resistivity value than the testing technique (copper plate or resistivity probe). The difference in the distribution of voltage in the test specimens with different diameters is the reason for it. The 450 mm test specimen allows more current pathways for electron propagation, because electric current travels along the path of least resistance to the passage of electrons, so the electrical resistivity values are lower than those obtained in the 155 mm diameter test specimen in the same test condition (degree of saturation, porosity and void ratio). It is concluded that the resistivity data obtained for both test specimen diameters and by the two different techniques are valid and can be employed to study soil resistivity in laboratory.

The use of electrical resistivity in geo-environmental site characterization tests is qualitative, *i.e.*, it varies within a range of values. Therefore, when a reference value is exceeded, it is a strong indicative of the presence of contaminants, requiring additional tests and soil, liquid and gas sampling for further site investigation. In these cases, the findings from this research can be used to guide the laboratory test investigation and its data interpretation.

References

Abu-Hassanein, Z.S. & Benson, C.H. (1996). Electrical resistivity of compacted clays. In: J. Geotech. Eng., 122(5):397-406.

Abu-Hassanein, Z.S. & Benson, C.H. (1994). Using Electrical Resistivity for Compaction Control of Compacted Soil Liners. In: Proceedings of the First International Conference on Tailings & Mine Waste'94, pp. 177-188.

Aquino, F.R. (2010). Comparative Study between Electrical Resistivity and Geotechnical Characteristics of Compacted Clayey Soil. MSc. Dissertation, Department of Civil and Environmental Engineering, University of Brasília, Brasília, Brazil, 117 p.

Archie, G.E. (1941). The Electrical Resistivity Log as an Aid in Determining Some Reservoir Characteristics. Trans. Am. Inst. Min. Eng., 146:54-62.

Arulmoli, K.; Arulanandan, K. & Seed, H.B. (1985). New Method for Evaluating Liquefaction Potential. J. Geotech. Engrg. Div., 111(1):95-114.

Bryson, L.S. & Bathe, A. (2009). Determination of Selected Geotechnical Properties of Soil Using Electrical Conductivity. Geotechnical Testing Journal. 32(3):1-10.

Campanella, R.G. & Weemees, I. (1990). Development and Use of na Eletrical Cone for Groundwater Contamination Studies. Soil Mechanics Series nº 140, Department of Civil Engineering, The University of British Columbia, Vancouver, Canadá, 42 p.

Corwin, D.L. & Lesch, S.M. (2005). Apparent soil electrical conductivity measurements in agriculture. In: Computers and Electronics in Agriculture, Amsterdam, v. 46, p. 11-43.

Daniel, C. (1997). An Investigation of the Factors Affecting Bulk Soil Electrical Resistivity. Bachelor Thesis, Department of Civil Engineering The University of British Columbia, Vancouver, BC.

Daniel, C.R.; Campanella, R.G.; Howie, J.A. & Giacheti, H.L. (2003). Specific depth cone resistivity measurements to determine soil engineering properties, Journal of Environmental and Engineering Geophysics, 8(1):15-22.

Ekwue, E. & Bartholomew, J. (2010). Electrical conductivity of some soils in Trinidad as affected by density, water and peat content. Biosystems Eng., 108(2):95-103.

Fukue, M.; Minato, T.; Horibe, H. & Taya, N. (1999). The micro-structures of clay given by resistivity measurements. Eng. Geol. (Amsterdam), v. 54:43-53.

Giao, P.; Chung, S.; Kim, D. & Tanaka, H. (2003). Electric imaging and laboratory resistivity testing for geotechnical investigation of Pusan clay deposits. J. Application Geophys., 52(4):157-175.

Gupta, S.C. & Hanks, R.J. (1972). Influence of Water Content on Electrical Resistivity of the Soil. Soil Sci. Soc. Am. Proc., 36(6):855-857.

Guyod. H. (1944). Fundamental data for the interpretation of electric logs. Oil Weekly, October 30, v. 155. p. 38.

Jackson, P.D.; Smith, D.T. & Stanford, P.N. (1978). Resistivity- Porosity-Particle Shape Relationships for Marine Sands. Geophysics, 43:1250-1268.

Kalinski, R. & Kelly, W. (1993). Estimating water content of soils from electrical resistivity. GTJ. ASTM, 16(3):323-329.

Kibria, G. & Hossain, M.S. (2012). Investigation of geotechnical parameters affecting electrical resistivity of compacted clays. Journal of Geotechnical and Geoenvironmental Engineering, 138(12):1520-1529.

Kong, L.; Bai, W. & Guo, A. (2012). Effects of cracks on the electrical conductivity of a fissured laterite: A combined experimental and statistical study. Geotechnical Testing Journal, 35(6):1-9.

Liu, S.Y.; Han, L.H.; Du, Y.J. & Gu, M.F. (2007). Experimental Study on Electrical Resistivity of Soil-cement. Environ. Geol., 54(6):1227-1233.

Liu, S.Y.; Zha, F.S. & Yu, X J. (2006). Laboratory measurment techniques of the electrical resistivity of soils. J. Eng. Geol., 14(2):216-222.

Long, M.; Donohue, S.; L'Heureux, J.S.; Solberg I.L.; Ronning J.S.; Limacher R.; O'Connor, P.; Sauvin, G.; Romoen M. & Lecomte, I. (2012). Relationship between electrical resistivity and basic geotechnical parameters for marine clays. Canadian Geotechnical Journal, 49(10):1158-1168.

Lunne, T.; Robertson, P.K. & Powell, J. (1997), Cone Penetration Test in Geotechnical Practice. Blackie Academic & Professional, London, 311 p.

McCarter, W. (1984). The electrical resistivity characteristics of compacted clays. Geotechnique, 34(2):263-267.

Molin, J.P. & Rabello, L.M. (2011). Studies on the measurement of soil electrical conductivity. In: Eng. Agríc., 31(1):90-101.

Oliveira, F.S. (2004). Experimental Study of a Polluted area by Lodo biosolids in DF Via by Resistivity Cone. MSc. Dissertation, Department of Civil and Environmental Engineering, University of Brasília, Brasília, 111 p.

Pacheco, A.O. (2004). Resistivity Cone Tests on Soil Saturated. COPPE/UFRJ, Rio de Janeiro, 151 p.

Peixoto, A.S.P.; Yamasaki, M.T.& Lodi, P.C. (2014). Evaluation of electrical resistivity in a tropical sandy soil compacted. The Electronic Journal of Geotechnical Engineering, 19:629-644, 2014.

Schoor, M. (2002). Detection of sinkholes using 2D electrical resistivity imaging. Journal of Applied Geophysics 50:393-399.

Taylor-Smith, D. (1971). Acoustic and electric techniques for sea-floor sediment identification: Proc. Int. Symp. on Engineering Properties of Sea-Floor Soils and their Geophysical Identification, Seattle, Washington, p. 253-267.

Waxman, M.H. & Smits, L.J.M. (1968). Electrical conductivities in oil-bearing shaly sands. Society of Petroleum Engineers Journal, 243:107-122.

Weemees, I.A. (1990). Development of an Electrical Resistivity Cone for Groundwater Contamination Studies. M.A.Sc. Thesis. Department of Civil Engineering, University of British Columbia. Vancouver, 86 p.

Winsauer, W.O.; Shearia H.M.; Masson P.H. & Williams M. (1952). Resistivity of brine saturated sands in relation to pore geometry, Bull. Am. Assoc. et. Geol., 3 6(2):253-277.

Kinematic Assessment of Multi-Face Round Slopes Using Hemispherical Projection Methods (HPM)

L. Jordá-Bordehore, R. Jordá-Bordehore, P.L. Romero-Crespo

Abstract. This paper presents a new approach to stability analysis of multi-face slopes, employing the concept of restricted daylight envelope. The methodology was applied to the back analysis of a real case of a curved, convex slope in metamorphic slates in Madrid, Spain. The Barton & Bandis (1990) criterion was employed for the field estimation of shear strength in rough discontinuities and to determine the friction cone, required for the kinematic analysis. The results suggest that the methodology reflects adequately the real situation and simplifies the studies of planar failure in complex geometries.

Keywords: rock mechanics, slope stability, stereographic projection, back analysis.

1. Introduction and Objectives

The existing methods for stereographic projection are widely extended for slope analysis in jointed rocks and possible failure modes (Wyllie & Mah, 2004; Hoek & Bray 1981; Hudson & Harrison, 1997; Gonzalez-Vallejo *et al.*, 2002; Lisle, 2004; Lisle & Leyshon, 2004; Koca *et al.*) since the first studies by Markland (1972) and John (1968, 1972). Most kinematic analyses of rock slopes consider exclusively single-face slopes (SFS), *i.e.*, consider that the surface of the slope presents constant strike (Yoon *et al.*, 2002). However, slopes can be found in nature with several faces or even curved faces, and it is not realistic to simplify these to "single-face" slopes.

In stereographic projection, the sliding envelope of a multi-face slope (MFS) is the union of single-face envelopes formed on the surface of the slope as proposed by Yoon *et al.* (2002). It is herein proposed to combine the methodology of Yoon *et al.* (2002) for multi-face slopes with conventional methodology for kinematic assessment of single-face slopes (daylight envelope and pole analysis) (Hudson and Harrison, 1997; Willie and Mah, 2004).

The work of Yoon *et al.* (2002) is one of the few existing methodological compilations on the kinematic assessment of MSF. These authors analysed the issue, both for planar and wedge failures, considering the orientation of the plane vector mode. The planar failure by definition applies to single planar discontinuities, in MSF and curved slopes only one planar surface is considered in the kinematic assessment. In the revised methodology proposed the assessment focus in the daylight envelope and pole plot of the discontinuities instead of the plane - vector analysis proposed by Yoon *et al.* (2002). In the case of wedges, the plane vector methodology is habitually employed; however, for planar failure, this approach is not common. In planar failures pole and daylight approach are more intuitive than plan vector or Dip Direction analysis. The work of Richards (2003) analyses wedges through the daylight envelope of poles. However, as indicated for the case of planar failure of slopes and toppling of strata, the most common approach is to analyse the location of discontinuity poles regarding the daylight envelope (Wyllie & Mah, 2004; Hudson & Harrison, 1997; Lisle, 2004).

The objective of this study is to present a methodology that unifies traditional criteria for rock slope analysis based on poles (Hudson & Harrison, 1997; Willie & Mah, 2004; Lisle, 2004) with the conclusions of the work of Yoon *et al.* (2002) for multi-face slopes. A study location was selected, which presented planar failure that could not be entirely justified by conventional single-face slope criteria. Since the slope has not a unique strike angle, we ask ourselves, which of them choose? In MFS, the slope can failed without any vertical release surfaces.

The suggested methodology for back analysis is effective to explain the mechanism of planar failure of real curved slopes, for slate rocks in El Atazar, Madrid.

2. Methodology

2.1. Kinematic assessment of rock slopes

The problems of wedge stability, planar failure, and toppling of strata are clearly three-dimensional-type problems. The visualization of the possible interactions between discontinuity planes and slopes is extremely complex to solve utilizing isometric projection, but it is considerably simplified with stereographic projection, where the planes are reduced to points (through poles). Kinematic assessment is based on the analysis of the relative orientation of

Luis Jordá-Bordehore, PhD., Escuela Superior Politécnica del Litoral, Facultad de Ingeniería en Ciencias de la Tierra, Campus Gustavo Galindo, km 30.5, Vía Perimetral, P.O. Box 09-01-5863, Guayaquil, Ecuador. e-mail: ljorda@espol.edu.ec.
Rafael Jordá-Bordehore, PhD., Rudnik Ciencias de la Tierra S.L. Calle Cañada 5, 28720, Bustarviejo, Madrid, España. e-mail: rafael_jorda@hotmail.com.
Paola Leonor Romero-Crespo, PhD., Escuela Superior Politécnica del Litoral, Facultad de Ingeniería en Ciencias de la Tierra, Campus Gustavo Galindo, km 30.5 Vía Perimetral, P.O. Box 09-01-5863, Guayaquil, Ecuador. e-mail: plromero@espol.edu.ec.
Submitted on July 6, 2015; Final Acceptance on June 9, 2016; Discussion open until December 30, 2016.

the discontinuity planes or poles relative to the slope, establishing four main types of failure - planar, wedge, toppling or circular failure.

2.2. Kinematic assessment of planar failure

Five simple geometric criteria (Willie & Mah, 2004) must be fulfilled to guarantee the kinematic possibility of planar failure:

1. The plane where the block slides must present a maximum strike difference, with respect to the face of the slope, of approximately ± 20°. This means the plane and the face of the slope must be noticeably parallel.
2. Sub-vertical release surfaces commonly exist, which present negligible sliding resistance to define the lateral limits of the plane and of the block. When release joints occur planar failure could be considered as a peculiarity of wedge failures, with one set being the sliding plane and the second the release surface.
3. The sliding plane must "daylight" on the slope face. This means that the plane must present lower dip than the slope.
4. The dip of the sliding plane must be greater than the friction angle.
5. The upper part of the sliding surface intersects the surface of the slope or finishes in a tension crack. Both tension cracks and release surfaces help to define the unstable block.

It is practice to consider, in these simplified analyses, that the shear strength of discontinuities only relate to the friction component and that cohesion is negligible. The aforementioned conditions are depicted three-dimensionally in Fig. 1a, and a simple example is shown in Fig. 1b for stereographic projection utilizing equal angle projection.

The friction cone has been added, which is built by counting φ degrees (friction angle of the plane) from the centre of the stereogram outwards. The poles located within the limit of the circle (cone) and the centre correspond to planes that present lower dips than the shear angle and therefore are kinematically stable. The possible sliding planes are laterally limited, as differences over 20° in direction or dip, for both sides, do not result in sliding (Willie & Mah, 2004) and may prevent sliding. The limits of the sliding plane boundaries in planar sliding failures are often ignored in stability analysis. The "final valid" envelope that encompasses the poles of the potentially unstable planes for planar failure is denominated **restricted daylight envelope** (Fig. 1b).The restricted envelope is the geometric site (focus) of all poles that represent a plane with dip direction located in the same semi space of the slope; also, these poles present lower dip than the plane, but still higher dip than the shear circle.

The coloured zone in Fig. 1b corresponds to the geometric site of potential planar failure, including the dip condition, orientation regarding the slope, lateral limits and shear. All discontinuity poles that are located within this zone, referred to as restricted daylight envelope or restricted envelope with unstable poles, can yield planar failure.

2.3. Planar failure of a two-face slope

The sliding of a discontinuity plane in a two-face slope (Fig. 2a) occurs when the discontinuity daylights on any of the two faces, and meets the conditions given by Willie & Mah (2004). We consider a two face slope as relatively sharp corner or "nose like" where an abrupt change of strike occurs in a short distance. The corner is a "free face" for each of the faces and therefore for this point the release surface condition and the 20° difference in strike do not apply (Fig. 2a). Yoon *et al.* (2002) analysed the phenomenon via stereographic projection, but consider the maximum slope line of the sliding plane and the restricted envelopes of the plane by the friction cone. The criterion described in Hudson & Harrison (1997) - adding 20° to each side of the daylight envelope- was not considered by Yoon *et al.* (2002).

The sliding mode shown in Fig. 2 is denominated by type 2 single plane sliding (Yoon *et al.*, 2002). The sliding block is formed by the discontinuity or sliding plane and the two faces of the slope (RS and LS).

2.4. Multi-face slope - curved, convex slope

The same methodology applied to a two-face slope can be applied to MFS (Yoon *et al.*, 2002). It is habitual to find curved slopes in highways (Fig. 3), both convex and concave (positive and negative MSF, respectively). The former are more habitual when rock structures are bypassed with minimum perturbation, while the latter are produced in highways with open slopes, in routes excavated using blasting techniques and circular shaped quarries. In these types of slopes, planar failure is produced if discontinuity daylights in any of the tangent directions to the slope (Fig. 4), and fulfils the condition that the discontinuity pole is located within the daylight envelope of the slope, i.e.:

1. The sliding plane daylights in any tangent face of the slope, *i.e.*, the plane presents lower dip than the slope.
2. The dip of the sliding plane is higher than the friction angle.
3. The superior part of the sliding plane intersects the upper face of the slope, or finishes in a tension crack.
4. Maximum strike difference is 20° between the sliding plane and the tangent exterior faces of the slope.

It must be highlighted that some conditioning factors for simple slopes were eliminated, such as release surfaces and the 20° lateral limits for strike difference (which are only applied to the exterior faces). For the kinematic representation and analysis of a convex slope (nose-shaped), it is very useful to initially simplify the slope in three faces (Fig. 4). Facing the front of the slope, there is a left-tangent limit plane (LS) and a right-tangent limit plane (RS). Also,

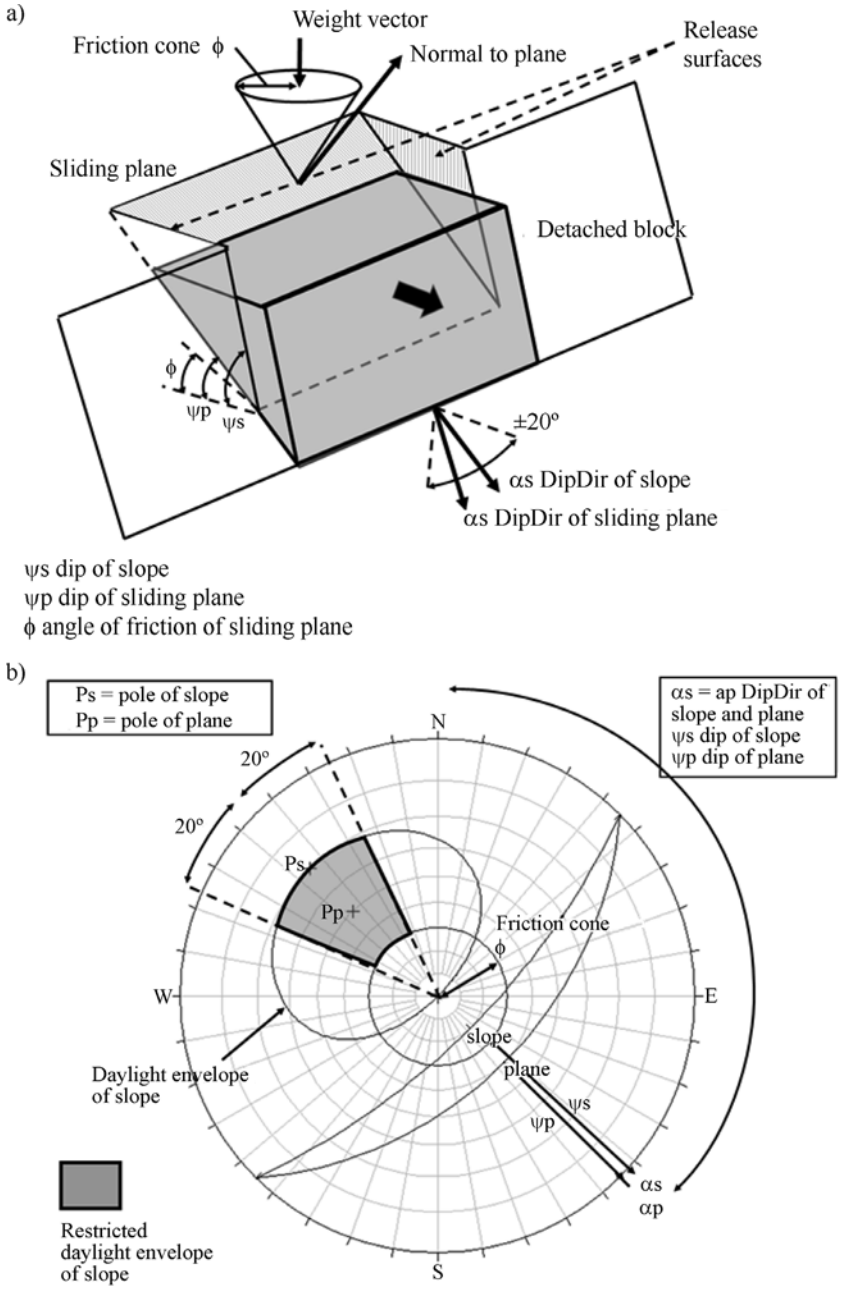

Figure 1 - (a) 3D scheme of a potential planar failure, with the interacting geometries and elements. (b) Scheme of the conditions that yield planar failure in stereographic projection. Data utilized to build the generic-type figure were: dip direction and slope dip 135/70, sliding plane or surface 135/50, friction angle 30°, and lateral limits for dip direction or direction between slope and plane for the production of sliding are established at 20°. Representation of planes, poles and cones through Dipsv5: equal angle low hemisphere.

a third plane situated between LS and RS can be considered, which characterizes the "roundness" or pointed shape of the slope (CS).

Figure 4b shows the analysis of a curved slope through stereographic projection - HPM in equal angle mode. Construction of the figure considered a simplification of the slope in three faces: left (LS), central (CS), and right (RS). The assumed friction angle - and therefore, friction cone - is common to all faces. Given that the interest lies in the analysis of planar failure through the poles, construction of the friction cone involved counting the angle φ from the centre of the stereogram outwards. Three daylight envelopes were built for each of the faces of the slope, between the centre of the stereogram and the pole of each one of the faces (in Fig. 4b: PRS, PCS and PLS). Twenty degrees (20°) are added to the exterior faces RS and LS due to slip limits, according to the single-face methodology. In this way, within the limits (± 20°), the three daylight enve-

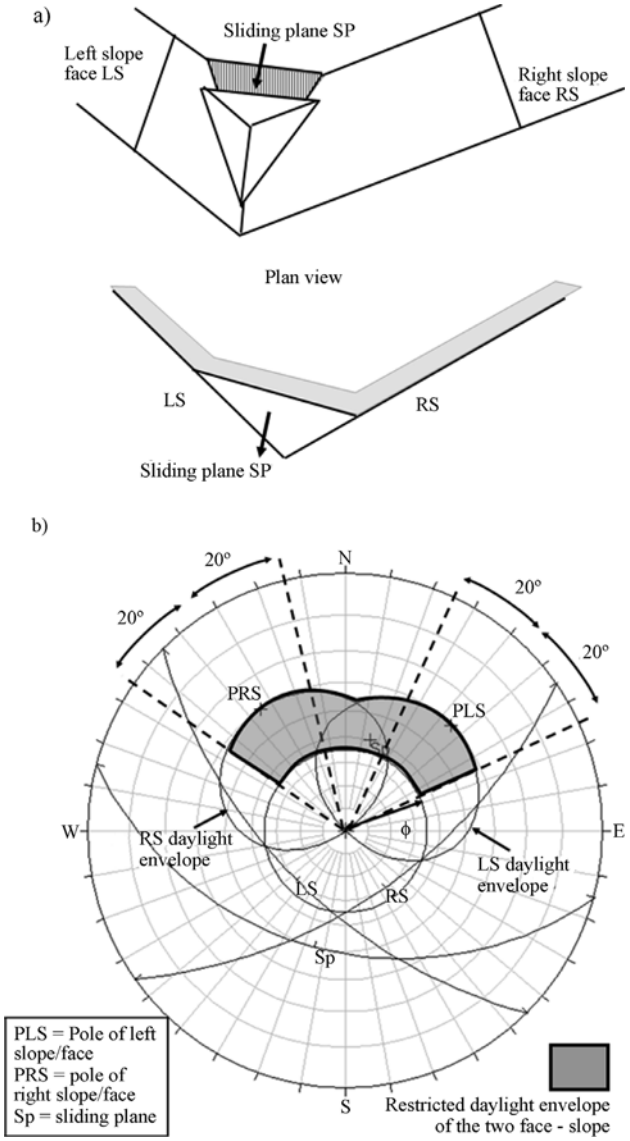

Figure 2 - (a) Sliding modes in isometric and plan views, for a two-face slope. RS indicates the right face or slope, and LS indicates the left face or slope, based on the schemes of Yoon *et al.* (2002). (b) Stereographic projection of the upper scheme. The projection was built considering unspecific planes for dip direction and dip: RS (145/60), LS (225/60), sliding surface (195/40) and assumed friction angle for both planes φ = 35°.

lopes, and the friction cone, the restricted daylight envelope of the multi-slope - round face is built, which will be the envelope for all poles that belong to potentially unstable planes. All the plane poles - strata or discontinuities - that fall within the interior of this differentiated zone in Fig. 3b are potentially unstable.

2.5. Field estimation of shear strength in rough discontinuities

The discontinuity friction angle is necessary to draw the friction circle - required in all kinematic analyses via

Figure 3 - Some examples of curved slopes in highways and routes in Los Andes mountain range: a) convex - concave in La Paz (Bolivia); b) flexural toppling in convex slope, Huancayo - Ayacucho road; c) concave slope in a road nearby, Quito, Ecuador.

stereographic projection (see Figs. 1b, 2b and 4b). Friction is obtained from the Barton & Bandis (1990) failure criterion, with φ_i linearized to obtain the instantaneous friction for the average stress state that acts in the potential sliding discontinuity. This failure criterion (Barton & Bandis, 1990) is a widely used empirical relationship for the modelling of shear strength in rock discontinuities. The criterion is based on two equations that represent the failure envelope. Equation 1 follows Barton & Choubey (1977):

$$\tau = \sigma_n \tan\left[\varphi_r + JRC \log_{10}\left(\frac{JCS}{\sigma_n}\right)\right] \quad (1)$$

Barton & Choubey (1977) suggest that the residual friction of discontinuities φ_r, can be obtained from Eq. 2:

$$\varphi_r = (\varphi_b + 20) + 20\left(\frac{r}{R}\right) \quad (2)$$

where φ_b is the basic friction angle of the failure surface. This value is tabulated and can be found in scientific literature (Barton, 1973; 1976, Barton & Choubey, 1977; Barton and Bandis, 1990), JRC is the joint roughness coefficient and JCS is the joint wall compressive strength (Barton, 1973 and 1976), and *r* is the Schmidt hammer rebound number on wet and weathered fracture surfaces and *R* is the rebound number on dry un-weathered sawn surfaces (Hoek, 2007).

Field estimation of *JRC* - Joint Roughness Coefficient. *JRC* is a number that can be estimated by comparing the appearance of a discontinuity surface with standard profiles published by Barton & Choubey (1977) and is widely reproduced in literature. The appearance of the discontinuity surface is compared visually with the profiles of the

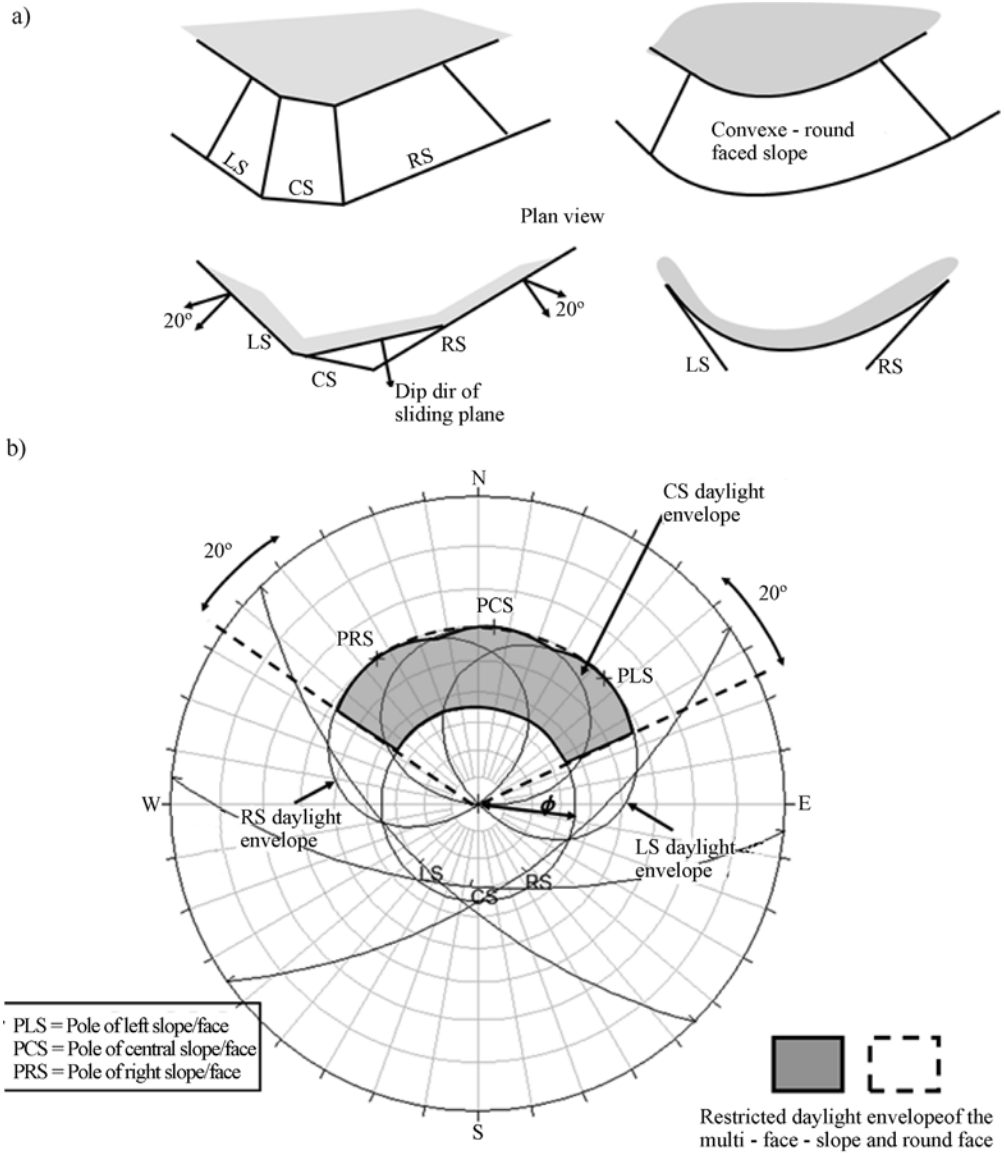

Figure 4 - (a) 3D scheme and plan view of a three-face slope and a round slope. For representation of the latter, it is habitual to utilize modified schemes based on Yoon *et al.* (2002) and build the slope with three faces. (b) Stereographic projection of a three-face slope. For the scheme, the following planes (dip direction/dip) were utilized: Left LS (225/60), Central CS (185/69) and Right RS (145/60), friction angle φ = 35°, using DIPSv5 software.

standard figure for surfaces 10 cm long (Barton & Choubey, 1977) and the *JRC* value that most closely matches that of the discontinuity surface is chosen (Hoek, 2007).

The most utilized field technique for determination of joint wall compressive strength (*JCS*) uses the Schmidt hammer rebound equipment that was initially developed for concrete, but throughout 50 years has been systematically used for rocks, since the first works of Deere & Miller (1966).

Influence of scale on *JRC* and *JCS*: Barton & Bandis (1982) proposed scale corrections for *JRC* according to the following equation:

$$JRC_n = JRC_0 \times \left(\frac{L_n}{L_0}\right)^{-0.02 \times JRC_0} \quad (3)$$

where: JRC_0 and L_0 (length) refer to 10 cm laboratory samples or fragments, with the same longitude of the normalized profiles (Barton & Choubey, 1977), and JRC_n and L_n refer to the real size of the block and discontinuity analysed in situ.

Given that there is a great possibility of finding weaknesses in a large surface, *JCS* decreases when the scale is increased (Hoek, 2007). Barton & Bandis (1982) also propose an equation to correct the scale of *JCS*:

$$JCS_n = JCS_0 \times \left(\frac{L_n}{L_0} \right)^{-0.03 \times JRC_0} \quad (4)$$

where: JCS_0 and L_0 refer to the reference scale 10 cm, and JCS_n and L_n refer to the real size of the block where is the joint is located. Please note that the quotient must be coherent regarding the units, and therefore L_0 is considered in meters L_0 = 10 cm = 0.1 m.

Instantaneous cohesion and friction. Given the historical development of rock mechanics, many analyses use the parameters of Mohr-Coulomb (cohesion *c*, and friction angle φ) to calculate safety factors regarding sliding:

$$\tau = c + \sigma_n \times \tan \varphi. \quad (5)$$

The Barton & Bandis (1990) criterion (Eqs. 1 and 2) is a non-lineal relationship and is not represented in terms of *c* or φ. Therefore it was necessary to develop a specific formulation that encompassed theses aspects (Hoek *et al.*, 1995); for example, kinematic analysis based on structural data of planes and wedges employs the concept of "friction cone" (Markland 1972; Hoek & Bray 1981; Hudson and Harrison, 1997; Willie & Mah, 2004; Lisle 2004) that required the value of the internal friction angle φ of the discontinuity.

The instantaneous friction angle φi for a normal stress σ_n can be calculated from the following relationship (Hoek, 2007):

$$\varphi_i = \arctan\left(\frac{\partial \tau}{\partial \sigma_n} \right) \quad (6)$$

where:

$$\frac{\partial \tau}{\partial \sigma_n} = \tan\left(JRC \log_{10} \frac{JCS}{\sigma_n} + \varphi_r \right) - \frac{\pi JRC}{180 \ln 10} - \left[\tan^2 \left(JRC \log_{10} \frac{JCS}{\sigma_n} + \varphi_r \right) + 1 \right]. \quad (7)$$

Instantaneous cohesion c_i is calculated from

$$c_i = \tau - \sigma_n \tan \varphi_i . \quad (8)$$

As Hoek (2007) remarked, the average normal stress σ_n that acts on the discontinuity planes is utilized to select the adequate values of c_i and φ_i for a specific application.

3. Study Site: Curved Slope with Planar Failure in Slates. El Atazar, Spain

The El Atazar reservoir (Spain) has a double-curvature vault dam, with 134 m height from foundation. It was one of the first of this kind to be built in Spain. It is located 100 km north of Madrid. Its construction started in

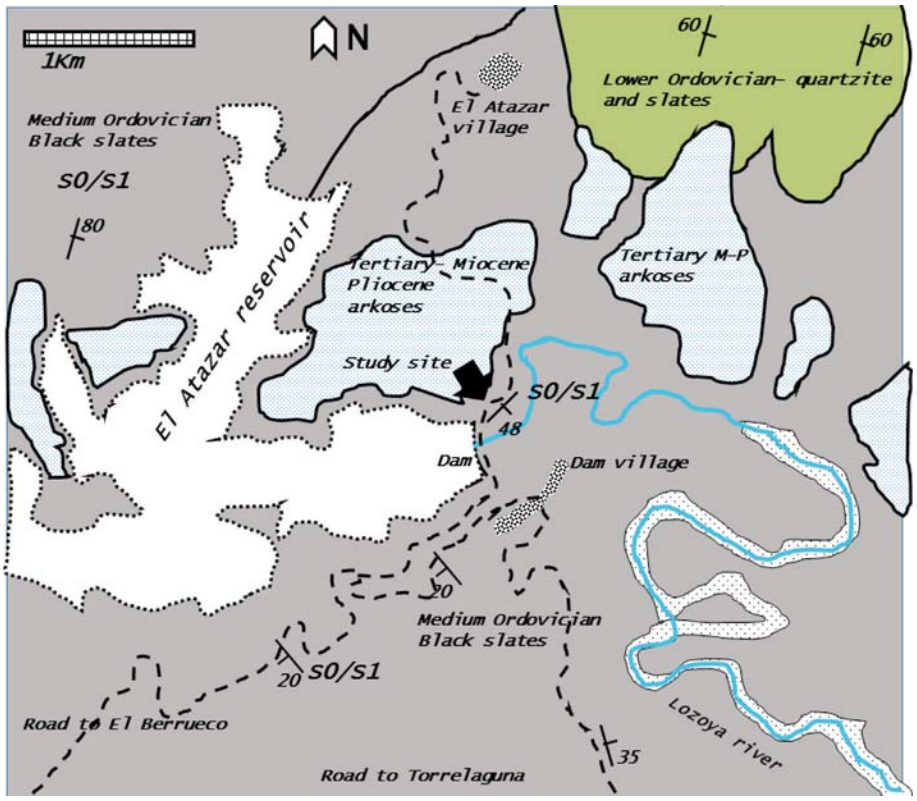

Figure 5 - The study zone is located in metamorphic terrain, schist, and black slates of the Medium Ordovician.

1965, with inauguration in 1972 by the dictator Francisco Franco. The final cost of the work was increased due to geotechnical issues with the Ordovician slates where it is set (Fig. 5). Currently a paved road crosses the dam and reaches the small village of El Atazar, which gives its name (Fig. 6).

The north side of the reservoir presented the most geotechnical problems throughout the construction; among other issues, this slope required important reinforcements of the rock mass, such as cables and walls. The highway bypasses a rocky prominence, due to a fold where planar failure was produced in a curved slope, at the time of construction. This sliding is nowadays completely stabilized (Fig. 6) and has been analyzed by the afore described methodology. In July 2014, a geomechanical station was carried out along the sliding (approximately 30 lineal meters, see Fig. 7) where besides censing the discontinuities (Fig. 8), field data were also collected on the main parameters for discontinuity resistance.

4. Results and Discussion

Three main join sets had been recognized in El Atazar curved slope (Table 1, Fig. 8).

Only in situ observations were utilized for the obtainment of the necessary parameters to establish shear strength in the discontinuities. Through the Schmidt hammer rebounds in altered joints, the value r = 25.4 was obtained, and for unaltered joints R = 31.1. The value of joint wall compressive strength *JCS* was R = 29.2 (N-type hammer) and *JCS* was obtained from the abacus of the employed equipment itself *JCS* = 24 MPa.

JRC was estimated in the field from the normalized profiles and roughness tester or Barton's comb (Fig. 9). Observationally, the roughness profile at macro scale of the main joint would be approximately 8-10. Equations 3 and 4 will be utilized for adequate consideration of the *JRC* and *JCS* scales. The height of the slope is 8 m but in the last 2 m there has not been any landslides, and therefore for the persistence of the joint S_0 the value of L = 6 m will be utilized.

For joint wall compressive strength *JCS*:

$$JCS_6 = 24 \times \left(\frac{6}{0.1}\right)^{-0.03 \times 15} = 3.84. \quad (9)$$

In the case scale effect is considered for JRC_0 determined by Barton's comb, JCR_6 = 4.35 as demonstrated below. However, *JRC* = 8-10 will be employed in calculations, as determined in situ throughout the entire length of S_0 foliation.

$$JRC_6 = 15 \times \left(\frac{6}{0.1}\right)^{-0.02 \times 15} = 4.35. \quad (10)$$

Determination of the residual friction angle through Equation 2 utilizes rebound values r = 25.4 and R = 31.1, plus the basic friction angle of the material: slate φ_b = 25 -

Figure 6 - Panoramic photography of El Atazar dam (Madrid, Spain) and the road curve where the studied slope is located.

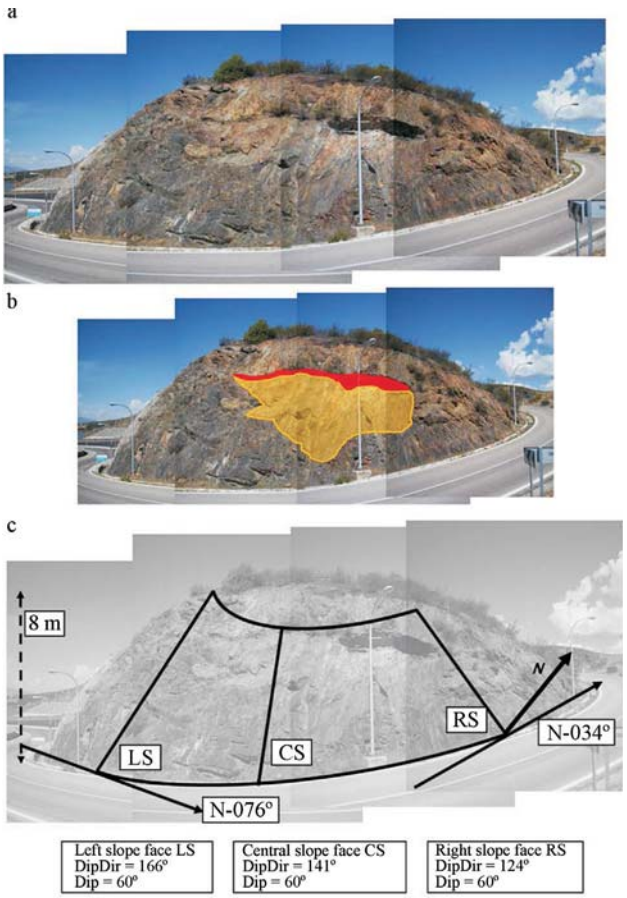

Figure 7 - Road curve where the curved sliding took place. The curved-convex multi-face slope studied herein presents two exterior tangent planes, denominated Left Slope Face and Right Slope Face (LS and RS). The central zone of the slope, where it is more probable to find the failure line, is denominated Central Slope Face.

30 (Barton, 1971). The average value within the interval is selected $\varphi_b = 27.5$. The values of residual friction and shear strength according to Equations 1 and 2 are:

$$\varphi_r = (27.5 - 20) + 20\left(\frac{25.4}{31.1}\right) = 23.8° \sim 24° \quad (11)$$

$$\tau = \sigma_n \times \tan\left[9 \times \log_{10}\frac{3.84}{\sigma_n} + 24\right]. \quad (12)$$

Obtainment of the equivalent Mohr Coulomb c and φ parameters involves linearization for a 6 m height and specific weight 0.026 MN/m^3 employing the Rocdata software (Rocscience). The result is instantaneous cohesion $c_i = 0.009$ MPa and instantaneous friction $\varphi_i = 33.85° \sim 34°$.

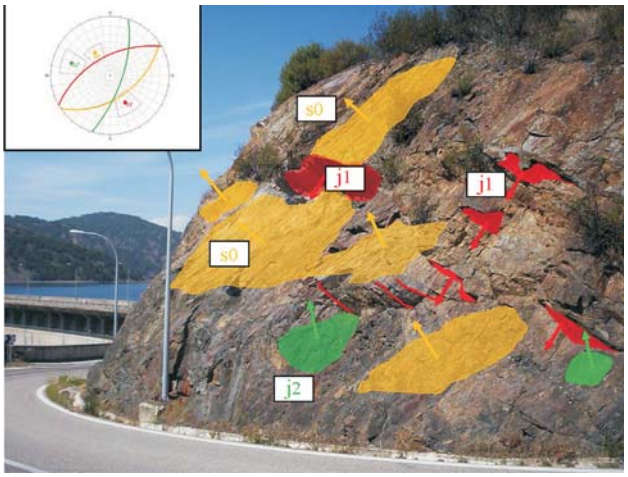

Figure 8 - Photography and simplified scheme of the main joint sets present in the El Atazar slope.

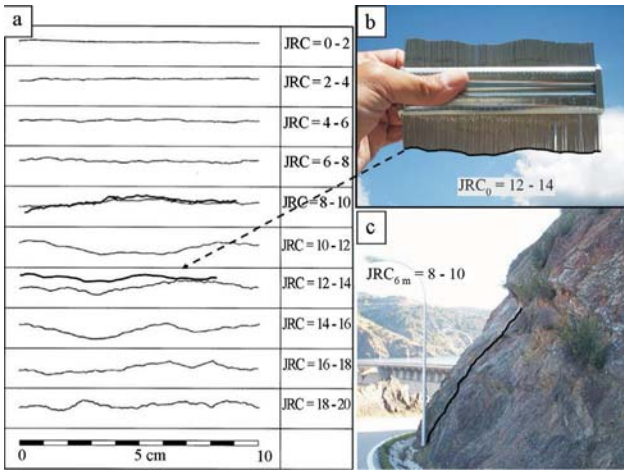

Figure 9 - Joint Roughness Coefficient in the foliation plane of the El Atazar slope: a) Barton & Choubey (1977) scheme, b) roughness JRC_0 according to a 10 cm profile, using "Barton's comb" and macro roughness JRC_n. Both roughness profiles JRC_0 and JRC_n ($JRC_{6\,m}$) are super-imposed in a) to obtain the value of JRC.

Table 1 - Main sets of discontinuities established at the El Atazar slope (Madrid).

Joint set	Dip direction (degrees)	Dip angle (degrees)	K Fisher distribution
J1	55°	330°	103
S0 (Slate -Foliation)	48°	146°	114
J2	67°	108°	74

For the friction cone, $\varphi = 34°$. Cohesion was not considered (Fig. 10).

The restricted daylight envelope (Figs. 10 and 11) was built for the curved slope of El Atazar, employing three auxiliary planes: central and two tangents (RS and LS). The stratification plane S_o presents only one pole, which falls within the colored zone, corresponding to an unstable slope pole. Therefore, as expected, a slope that has slided is clearly unstable, given that, in addition, the pole is far from the friction circle - this implies a $FoS < 1$.

Figure 11 explains the procedure for the construction of the stereogram and kinematic assessment of Fig. 10: Fig. 11a, daylight envelope for a single face LS (Left side); Fig. 11b, expanded daylight envelope for three faces; Fig. 11c, daylight envelope restricted by a 34º friction cone; Figure 11d, consideration of slip limits only for the outer tangential faces of the round-faced slope: LS-RS as internal slip limits are included into the single daylight envelopes. The pole of the bedding plane is located within the restricted daylight envelope, so it should be considered potentially unstable.

The methodology proposed is not opposed to the traditional solutions (*e.g.* Hoek &Bray, 1981; Lisle, 2004; Willie & Mah, 2004) but pretend to extend the traditional approach, which considers only single slopes, wherein for instance release surface are required. In the study site of El

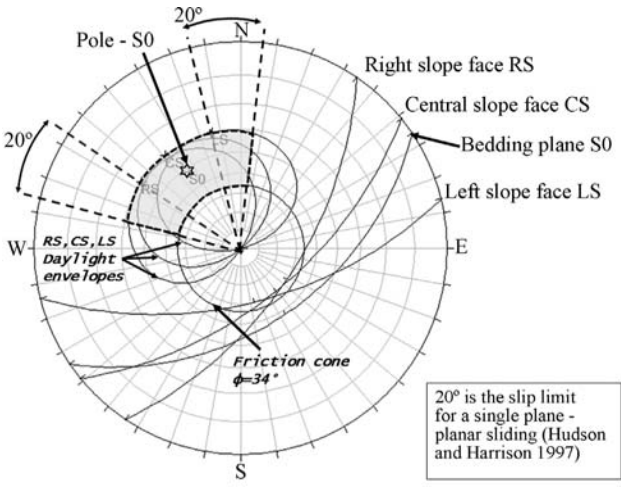

Figure 10 - Restricted daylight envelope and estereographic analysis of the planar failure of the curved slope of El Atazar.

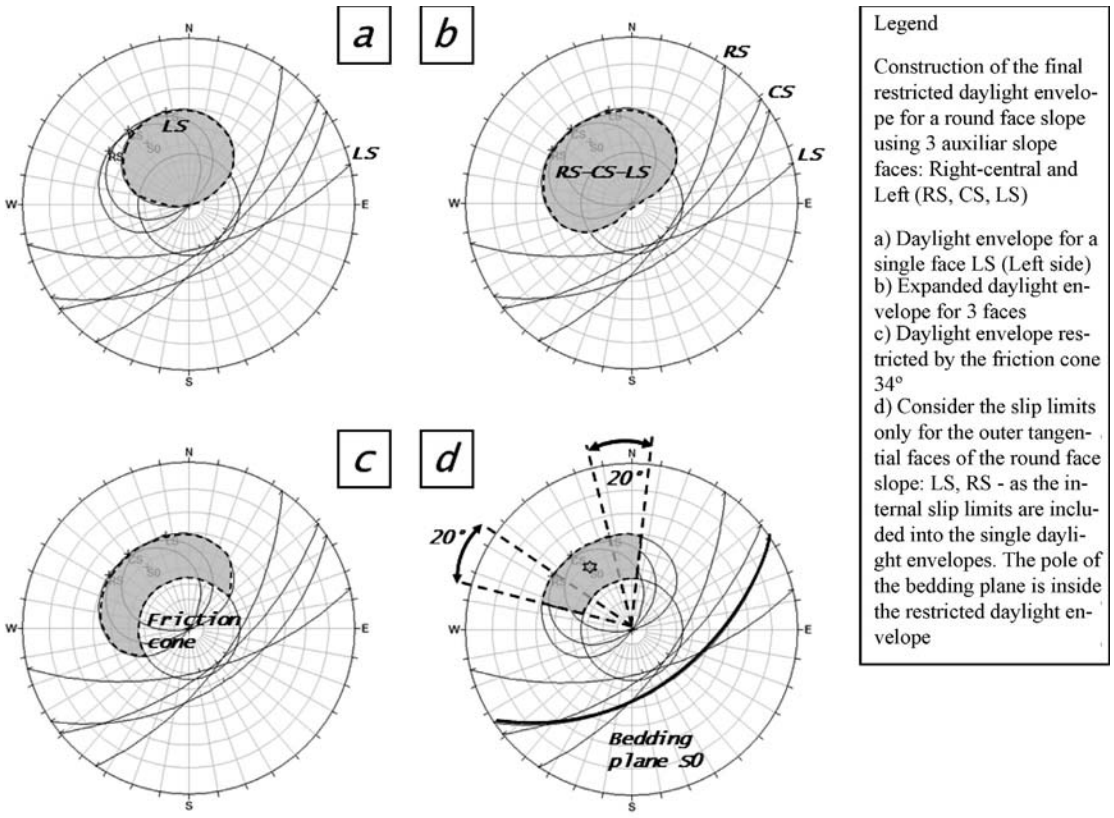

Figure 11 - Construction of the final restricted daylight envelope for a round-face slope using three auxiliary slope faces: Right, Central and Left (RS, CS, LS).

Atazar, the slope failed without any lateral - vertical - joint because the curved slope intersecting the planar failure surface generates a kinematic unstable block (together with the tension crack in the upper part of the slope).

5. Conclusions

Stereographic projection has been employed to represent and analyse the stability of multi-face rock slopes subjected to planar failure. The state-of-the-art has been reviewed and the existing methodology has been simplified through the combination of published methods for multi-face slope analysis (Yoon *et al.*, 2002) and more recent simplified slope analysis models that consider daylight envelopes and poles (Koca *et al.*, 2004; Richards, 2003). Back-analysis was carried out for a failed slope that presented a multi-face round convex slope. The applied methodology explained perfectly the situation produced.

As verified, it is habitual that real unstable slopes present complex geometries such as double-faces, multi-faces or even round-faces. These geometries can be analysed by Hemispherical Projection Methods (HPMs) and by the most usual and globally extended kinematic analysis that started with Markland (1972) and John (1968 and 1972).

The main contribution of the manuscript consists in reconsidering the methodology proposed by Yoon *et al.* (2002), which employs plane vector analysis for planar failure, and group it with pole vector analysis (widely utilized and well-known) through the utilization of daylight envelope for poles (Willie & Mah, 2004; Lisle, 2004).

In stereographic projections, all the conditions for planar failure are summarized in an envelope that is denominated "restricted daylight envelope", in such a way that all pole planes that fall within the area yield potential planar failures.

It is difficult to give guidelines of when the curved slope approach applies - perhaps more case studies of failed slopes are needed.

It is considered that with a sharp turn of 20º the difference in strike criteria proposed by several authors and compiled by Willie & Mah (2004) cannot be applied for the inner part of the slope and failure surface. In these cases only the external 20º strike difference is considered (Figs. 10 and 11d).

Acknowledgments

The work presented herein was funded by the Prometeo project of the Secretary of Super Education, Science, Technology and Innovation of the Republic of Ecuador.

References

Barton, N. (1971). Estimation of in situ shear strength from back analysis of failed slopes. Proc. Int. Symp. Rock Mech. Rock Fracture, Nancy paper II-27.

Barton, N.R. (1973). Review of a new shear strength criterion foor rock joints. Eng. Geol., 7:287-332.

Barton, N.R. (1976). The shear strength of rock and joints. Int. J. Mech. Min. Sci & Geomech. Abstr., 13(10):1-24.

Barton, N.R. & Choubey, V. (1977). The shear strength of rock joints in theory and practice. Rock Mech., 10(1-2):1-54.

Barton, N.R. & Bandis, S.C. (1982). Effects of block size on the shear behaviour of jointed rock. 23rd US Symp on rock mechanics, Berkeley, pp. 739-760.

Barton, N.R. & Bandis, S.C. (1990). Review of predictive capabilities of JRC-JCS model in engineering practice. In: Proc. Int. Symp. On Rock Joints. Balkema, Rotterdam, pp. 603-610.

Deere, D.U. & Miller, R.P. (1966). Engineering classification and index properties of rock. Technical Report Nº AFNL-TR-65-116. Albuquerque, NM. Air Force weapons laboratory.

Gonzalez de Vallejo, L.I.; Ferrer, M.; Ortuño, L. & Oteo, C. (2002). Ingeniería Geológica. Ed. Pearson Educación, Spain, 744 pp.

Hoek, E. (2007). Practical Rock Engineering. Set of course notes. Shear strength of discontinuities. www.rocscience.com/education/hoeks_corner (December 4, 2014).

Hoek, E.; Kaiser, P.K. & Bawden, W.F. (1995). Support of Underground Excavations in Hard Rock. 4th ed. Taylor & Francis, New York, 215 pp.

Hoek, E. & Bray, J. (1981). Rock Slope Engineering. 4th ed. Spon Press, New York, 431 pp.

Hudson, J.A. & Harrison, J.P. (1997). Engineering Rock Mechanics - An Introduction to the Principles. Pergamon, London, 546 pp.

John, K.W. (1968). Graphical stability analyses of slopes in jointed rock. Proc. Soil Mech. Fndn Div., ASCE , SM2, paper no. 5865.

John, K.W. (1972). Graphical methods for slope stability analysis. Muller, L. (ed), Rock Mechanics. Springer, Viena, pp. 222-239.

Koca, M.Y. & Kincal, C. (2004). Abandoned stone quarries in and around the Izmir city centre and their geo-environmental impacts - Turkey. Engineering Geology, 75:49-67.

Lisle, R.J. (2004). Calculation of the daylight envelope for plane failure of rock slopes. Geotechnique, 54:279-280.

Lisle R.J. & Leyshon, P.R. (2004). Stereographic Projection Techniques for Geologists and Civil Engineers. 2nd ed. Cambridge University Press, Cambridge, 112 pp.

Markland, J.T. (1972). A useful technique for estimating the stability of rock slopes when the rigid wedge sliding type of failure is expected. Imp. Coll. Rock Mech. Res. Rep., 10:10.

Richards, L. (2003). An alternative method for checking the kinematic admissibility of wedges. https://www.rocscience.com/library/rocnews/fall2003/WedgeKinematics.pdf.

Rocscience Inc. (2001). Dips version 5.0 Graphical and statistical analysis of orientation data. www.rocscience.com Toronto, Ontario, Canada.

Rocscience Inc. (2004). Rocdata version 3.0 Rock, soil and discontinuity strenght analysis www.rocscience.com Toronto, Ontario, Canada.

Wyllie, D. & Mah, C.W. (2004). Rock Slope Engineering. Civil and Mining. Spon Press, New York, 431 pp.

Yoon, K.S.; Jeong, U.J. & Kim, J.H. (2002). Kinematic analysis for sliding failure of multi-faced rock slopes. Engineering Geology, 67:51-61.

Data Extrapolation Method for The Dynamic Increasing Energy Test: SEM-CASE

E.C. Alves, M.M. Sales, P.M.F. Viana

Abstract. The dynamic increasing energy test has been widely used in pile load tests in Brazil in recent years. However, the ultimate strength of the single-foundation system is not mobilized in most of the tests because of various factors. In some cases, the equipment available cannot attain the necessary kinetic energy, or the structural element presents initial imperfections/ruptures. In this study, the authors present a method for extrapolating the mobilized static resistance *vs.* maximum displacement curve, which is obtained using the dynamic increasing energy test (DIET). Using the force and velocity signals collected by the PDA (Pile Driving Analyzer) system, it is possible to calculate the resistance and displacement by applying the Simplified CASE Method. An extrapolation method, the Simplified Extrapolation Method of the CASE Method (SEM-CASE), is presented based on the results of twenty-one precast concrete pile load tests that have been carried out in different soils. The estimated values of the ultimate complementary energy and ultimate strength were very close to the measured values in the presented load tests.

Keywords: extrapolation method; dynamic load test; driven pile; complementary energy; strain energy.

1. Introduction

The first methods used to estimate the bearing capacity of a driven pile were based on data obtained during the pile installation. Alternatively, the wave equation was initially applied to piles in the 1930s to estimate bearing capacity (Warrington, 1997; Hussein & Goble 2004). Smith (1960) presented a model that used a group of equations and calculation routines to describe the stress-wave displacement and its effects along the pile after a hammer blow. With the development of more powerful sensors and computers, Smith's model can now be applied and has become the fundamental basis for the methods employed in dynamic load test analysis.

In this context, considering the need to estimate the ultimate capacity of the pile based on the dynamic load test, this paper presents a method for extrapolating the mobilized static resistance (R) *vs.* maximum displacement (D) curve to obtain the behavior and ultimate strength capacity of the dynamic increasing energy test (dynamic load test).

The method is used for driven precast concrete piles, which mobilize the shaft and toe resistance during loading. The guiding principle of this method is the complementary energy criterion first presented by Aoki (1997), which uses the expression "mobilized static resistance" to indicate the resistance of the static portion that is mobilized after a hammer blow during the dynamic load test, as calculated by the simplified CASE method.

2. Dynamic Test and Numerical Analysis

2.1. Dynamic load test

The purpose of the dynamic load test is to estimate the ultimate static resistance of the pile-soil system and propose a load *vs.* virtual-settlement curve.

By applying a hammer blow to the head of the pile, generally through a pile driver, force and velocity signals are obtained at the pile head with deformation and acceleration sensors, respectively (Teferra *et al.*, 1996; Likins *et al.*, 2008). The signals obtained from the sensors are transferred to and stored in a portable computer, known as PDA (Pile Driving Analyzer).

After the data have been collected by the sensors, the PDA transcodes and processes the data to obtain the force and velocity signals, and the CASE numerical method provides the static resistance in each hammer blow at the moment of impact during the pile driving.

2.2. Dynamic increasing energy test - DIET

Two types of dynamic load tests can be used to obtain the pile-bearing capacity: constant or increasing energy. The dynamic constant energy test is the most traditional and widely used test worldwide. According to Aoki (1989a), the dynamic constant energy test is similar to a cyclic static load test in which the same load is always applied, and the same settlement is always obtained for the same strain energy.

Eder Chaveiro Alves, M.Sc., Civil Engineering, Agência Goiana de Transporte e Obras, AGETOP. Av. Gov. José Ludovico de Almeida, n° 20, 74775-013 Goiânia, GO, Brazil. e-mail: ederchaveiro@yahoo.com.br.
Maurício Martines Sales, Ph.D., Associate Professor, Escola de Engenharia Civil e Ambiental, Universidade Federal de Goiás, UFG. Praça Universitária, 1488, 74605-220 Goiânia, GO, Brazil. e-mail: sales.mauricio@gmail.com.
Paulo Márcio Fernandes Viana, Ph.D., Associate Professor, Departamento de Engenharia Civil, Universidade Estadual de Goiás, UEG. BR-153, Quadra área, km 99, 75132-903 Anápolis, GO, Brazil. e-mail: pmfviana@gmail.com.
Submitted on July 15, 2015; Final Acceptance on March 3, 2016; Discussion open until December 30, 2016.

The increasing energy test consists in the application of blows with variable and increasing fall heights, based on a level of energy that is lower than that of the driving end (free-fall impact system) (Aoki, 2000). Currently, the increasing energy method is the most frequently used method for performing the dynamic load test in Brazilian building foundations.

Aoki (1989a) presents the application of the dynamic increasing energy test to obtain a curve similar to the load *vs.* settlement curve obtained in the static load test, which is the mobilized static resistance *vs.* displacement curve.

2.3. Simplified CASE method

Developed by the Case Institute of Technology (currently Case Western Reserve University), the main objective of this method is to calculate the static resistance in real time and at the test site for each hammer blow. It was implicit that each blow was enough to mobilize the ultimate soil resistance.

This method is a closed-form solution of the wave equation, in which the signals of force and velocity are used and recorded in a particular pile section, just as the blow reaches its highest intensity in the section of the sensors (t_1) and just as the wave reflected at the end of the pile returns to the instrumented section (t_2).

Static resistance (R) is calculated by the difference between total resistance and dynamic resistance. Linkins & Rausche (1981) presented the start point of Case Method and in following paper, Rausche *et al.* (1985) expanded the formulation of static resistance as

$$R=\frac{(1-Jc)\times\left[Ft_1+\left(\frac{EA}{c}\right)vt_1\right]+(1+Jc)\times\left[Ft_2-\left(\frac{EA}{c}\right)vt_2\right]}{2} \quad (1)$$

where Ft_1, Ft_2, vt_1, and vt_2 are, respectively, the values of force and velocity calculated by means of the data obtained through the specific deformation and acceleration sensors at times t_1 and t_2. Jc is a dimensionless constant called the "dynamic damping coefficient" of the CASE method and is determined based on experiences of correlations with static load test results, E is the elastic modulus of pile material, A is the cross-sectional area of pile and c is the velocity of wave propagation. The relation (EA/c) is also known as the pile impedance.

3. Complementary Energy

Presented by Aoki (1989b), this criterion allows the pile-soil system to be in a state of dynamic equilibrium (elastic-perfectly plastic behavior) during the hammer impact, with the appearance of non-conservative inertial and damping forces, and the application of Hamilton's energy conservation principle is valid. It is also assumed that the system returns to its original state after each blow, *i.e.*, there is no significant change in the initial condition of the system. Clough & Penzien (1975) stated the principle as:

$$\int_{t_1}^{t_2}\delta(T-V)dt+\int_{t_1}^{t_2}\delta(W_{nc})dt=0 \quad (2)$$

where δ is the variation in the time interval (t_2 - t_1); T is the total kinetic energy in the system; V is the potential energy in the system; W_{nc} is the work done by non conservatives forces.

Soil rupture is characterized in the dynamic increasing energy test when a particular impact, corresponding to a point on the idealized mobilized static resistance-displacement curve, shows that a) the mobilized static bearing capacity (R) passes through a maximum R_u; b) the complementary kinetic energy (T_c) of the impact passes through a maximum T_{cu}; and c) the complementary potential energy (V_c) passes through a maximum V_{cu}.

Hamilton's principle, as applied to the maximum impact energy T_u, also can be expressed by

$$\{[T_u-(R_u\times K_u)/2]-[(R_u\times S_u)+W_{au}]\}=0 \quad (3)$$

where T_u is the maximum kinetic energy; S_u is the maximum permanent portion (penetration); and W_{au} is the work done by the non conservative forces.

The complementary energy V_c tends towards a constant value V_{cu} when the total strain energy V and the settlement S tend towards infinity, *i.e.*, the analysis of the variation of the complementary strain energy with loading shows how close rupture is because the rate of variation of this parameter is cancelled out when the reaction or resistance capacity of the system reaches an extreme, as shown in Fig. 1.

Aoki (2000) presented the new formulations for determining the values of potential energy V_s, complementary energy V_c, and work W done by the static portion of the forces. These made it possible to calculate area values that are more consistent with the mobilized static resistance (R) *vs.* displacement (D) curve. The expressions are given below for calculating the potential energy (Eq. 4), complementary energy (Eq. 5), and work (Eq. 6):

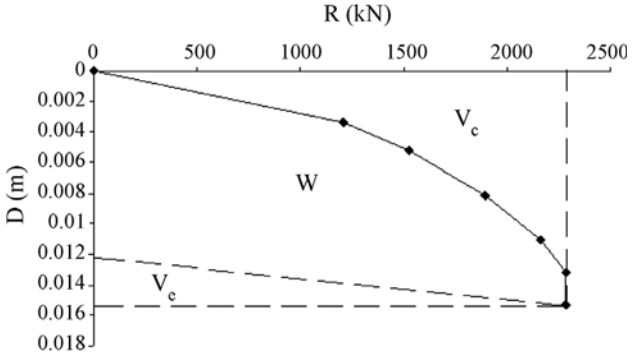

Figure 1 - The strain energies that form part of the mobilized static resistance (R) *vs.* maximum displacement (D) curve of DIET.

$$V_s = \sum_{i=1}^{n}\left(\frac{R_i + R_{i+1}}{2}\right)\times(D_i - D_{i-1}) \quad (4)$$

$$V_c \cong RD - \sum_{i=1}^{n}\left(\frac{R_i + R_{i+1}}{2}\right)\times(D_i - D_{i-1}) \quad (5)$$

$$W = (V_s - V_e) \quad (6)$$

where V_e is the portion of elastic strain energy (Fig. 1).

4. Fit Equations for *"R vs. D"* Curve

This section presents the use of the exponential, hyperbolic, and parabolic functions as possible models to represent the mobilized static resistance (R) *vs.* Displacement (D) curve, as shown in Fig. 2. Moreover, the equations for the calculation of complementary energy (V_c) were deduced by means of Eqs. 7 to 15 (see all detailing in the appendix), which present different approaches to represent the mobilized static resistance (R) *vs.* displacement curve, the complementary energy (V_c), and the ultimate complementary energy (V_{cu}), using the ultimate static resistance R_u and displacement (D_u) at the moment that the test mobilizes the ultimate static resistance. The other variables presented in this figure are: D_1 and D_2 are displacements before and after the ultimate static resistance, respectively; ΔD_1 and ΔD_2 are displacement variations; R_1 is the static resistance corresponding to a displacement "D_1"; ΔR is a static resistance variation; V is the potential energy; ΔV_1 and ΔV_2 are energy variations; ΔV_{c1} is the corresponding variation in the complementary energy.

- Exponential curve

$$R = R_u(1 - \exp^{-(\alpha D)}) \quad (7)$$

$$Vc = \left(\frac{R_u}{\alpha}\right)[1 - (1 + \alpha D)\exp^{-\alpha D}] \quad (8)$$

$$V_{cu} = \frac{R_u}{\alpha}. \quad (9)$$

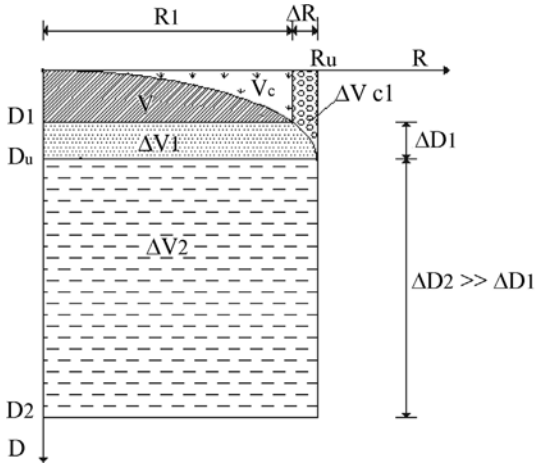

Figure 2 - Mobilized static resistance (R) *vs.* maximum displacement(D) curve of DIET (modified from Aoki, 2000).

- Hyperbolic curve

$$R = R_u\sqrt{1 - \left(1 - \frac{D}{D_u}\right)^2} \quad (10)$$

$$V_c = (R \times D_u) - \left(\frac{D_u}{R_u}\right)\left[\frac{R}{2}\sqrt{R_u^2 - R^2} + \frac{R_u^2}{2}\,arcsen\left(\frac{R}{R_u}\right)\right] \quad (11)$$

$$V_{cu} = 0{,}215 \times R_u \times D_u. \quad (12)$$

- Parabolic curve

$$R = \sqrt{R_u^2\left(\frac{D}{D_u}\right)} \quad (13)$$

$$V_c = D_u\left(\frac{R^3}{3R_u^2}\right) \quad (14)$$

$$V_{cu} = \frac{(D_u \times R_u)}{3}. \quad (15)$$

5. SEM-CASE Method

A new method is presented here for extrapolating the trajectory of the mobilized static resistance (R) *vs.* maximum displacement (D) curve, obtained by analyzing the CASE numerical method based on the complementary energy criterion. This methodology is hereafter called the Simplified Extrapolation Method of the Simplified CASE Method (SEM-CASE).

This method is applicable to precast concrete piles driven by a pile driver with a free-fall hammer and tested by the dynamic increasing energy test. In addition, the pile must have been designed to bear the working load using the portions of shaft and toe resistance, where the rupture is characterized by constant mobilized static resistance under the action of increasing kinetic energy with a well-defined vertical asymptote.

Some pile tests can present different forms of "resistance *vs.* displacement" curves. Sometimes the tests do not present an evident mobilization of static resistance. In others, the results are initially represented by an almost linear behavior in the graph R x D and then occurs an abrupt "failure". Both cases are consequences of particular pile-soil systems and can not be extrapolated or predicted by any method. Aoki (2000) discussed some examples of pile tests in such cases. The "SEM-CASE" method will not be able to extrapolate the maximum static resistance in such curves.

The data from a dynamic increasing energy test presented by Aoki (2000) were used to demonstrate the use of the method (Fig. 3). The concrete pile had a total length of 12 m, a driven length of 10.1 m, a diameter of 0.42 m, and a hollow cylindrical form with a section area of 0.09 m^2.

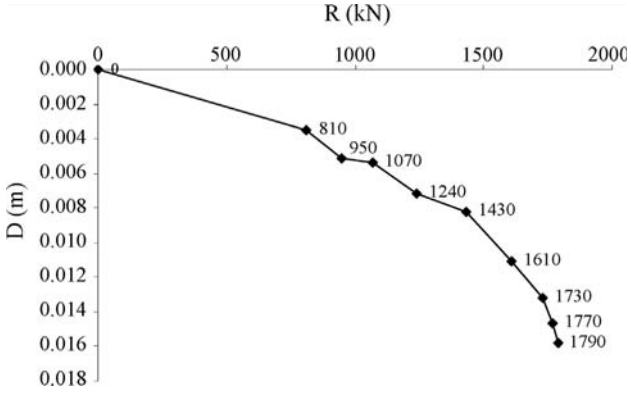

Figure 3 - R *vs. D* graph of a driven pile (modified from Aoki, 2000).

This pile reached the ultimate resistance during the test, according to the complementary energy criterion. However, to simulate a dynamic load test that did not mobilize the ultimate static resistance, Fig. 3 represents only part of the test as if it had been interrupted when the resistance reached 1790 kN (the other points beyond 1790 kN are not presented in Fig. 3).

The application of the method can be divided into three (3) steps:

- **Step 01**: The variation ratio of the mobilized static resistance (*Var. R*) to the variation of kinetic energy (*Var. T*) is calculated in each blow of the dynamic load test. The values obtained for the pile are shown in Table 1. The values for the ratio of *Var. R* to *Var. T* are plotted in Fig. 4, with the values of the mobilized static resistance *R* plotted on the abscissa using a logarithmic scale.

The graph in Fig. 4 has three (3) stages: Stage 1, Stage 2, and Stage 3.

Stage 1 has an almost 90° slope in relation to the *x*-axis. The first blows, with a lower fall height, *i.e.*, lower kinetic energy, generally form part of this stage.

Stage 2 has a slope tending from 90° to 0°, in relation to the x-axis, depending on the analyzed pile. Stage 3 tends to a 90° slope, regardless of the analyzed pile geometry.

The slope of the three stages of the *R vs. Var. R*/ *Var. T* graph varies according to the following characteristics of the pile foundation: a) Local surrounding soil; b) Pile geometry; c) Length of the structural element driven into the surrounding soil; and d) "Pile age" (time interval between the end of the driving and the start of the test).

From analyses of the 21 dynamic increasing energy tests studied by Alves (2010), it was observed that in stage 1, the test practically mobilizes only the lateral resistance. In stage 2, the test mobilizes the lateral and tip resistance of the pile, and in stage 3, the lateral resistance during the test is "exhausted" (remains constant), and only the tip resistance increases continuously and is mobilized until rupture (when the ratio of the variation of the mobilized static resistance - *Var. R* to the variation in applied kinetic energy - *Var. T* is equal to zero), indicating similarities with the results presented by Aoki (1989b).

Figure 5 uses the last five points, which are in stage 3 of Fig. 4, to present a simple linear regression. It shows good agreement between the points and the linear regression. This good agreement occurs when the portion of tip resistance of the pile is "significantly" mobilized.

The principle of extrapolation of the ultimate static resistance stems from the concept that when the ratio (*Var. R*/*Var. T*) is equal to zero, the pile reaches the ultimate resistance, *i.e.*, when the variation of the mobilized static resistance in two blows with increasing kinetic energy is equal to zero, the pile is subject to the mobilization of the ultimate static resistance. As stated by Aoki (2000), this kind of approach would be the upper boundary limit of the ultimate static resistance.

Figure 5 shows the linear regression of the points that is used to extrapolate the ultimate static resistance (R_u). This occurs when the straight line intercepts the *x*-axis.

Table 1 - Values of *D*, *R*, *T*, *Var. R*, *Var. T*, and *Var. R*/*Var. T*.

D (m)	*R* (kN)	*T* (kNm)	*Var. R* (kN)	*Var. T* (kNm)	*Var. R*/*Var. T* (1/m)
0	0	0	0	0	0
0.0035	810.0	1.9	810.0	1.9	426.32
0.0051	950.0	3.0	140.0	1.1	127.27
0.0054	1070.0	3.9	120.0	0.9	133.33
0.0072	1240.0	5.8	170.0	1.9	89.47
0.0082	1430.0	7.3	190.0	1.5	126.67
0.0111	1610.0	11.8	180.0	4.5	40.00
0.0132	1730.0	15.9	120.0	4.1	29.27
0.0147	1770.0	18.6	40.0	2.7	14.81
0.0158	1790.0	21.1	20.0	2.5	8.00

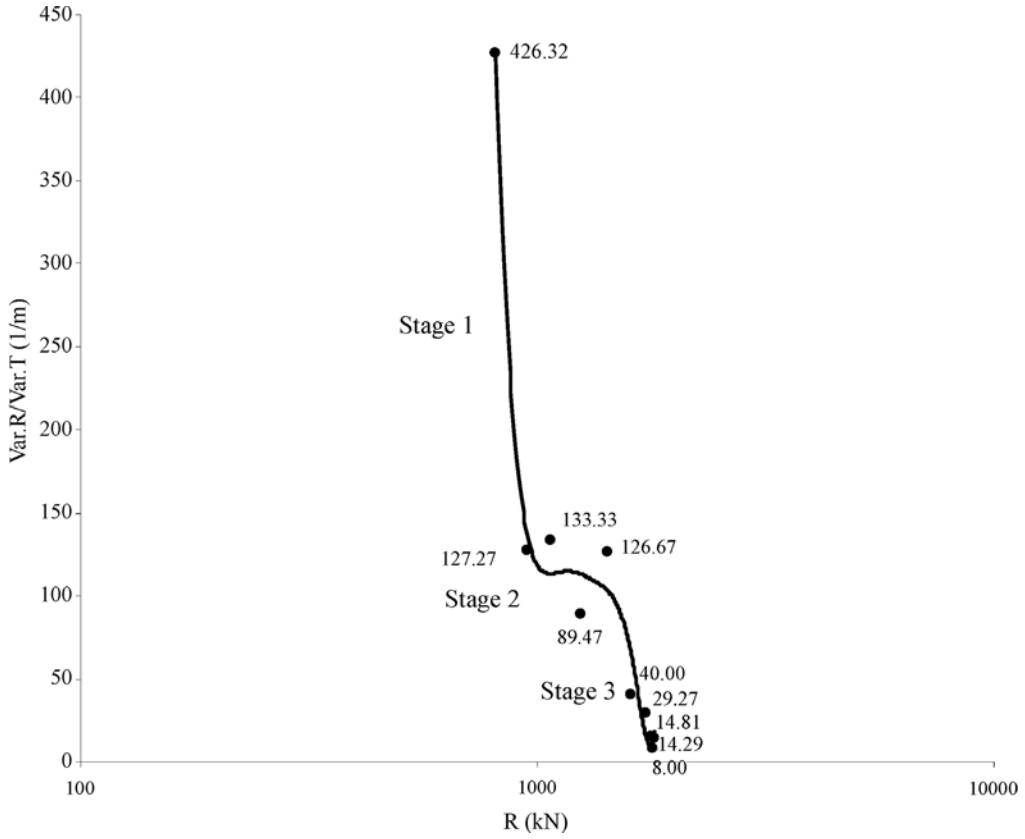

Figure 4 - R *vs. Var. R/ Var.T* graph of a driven pile.

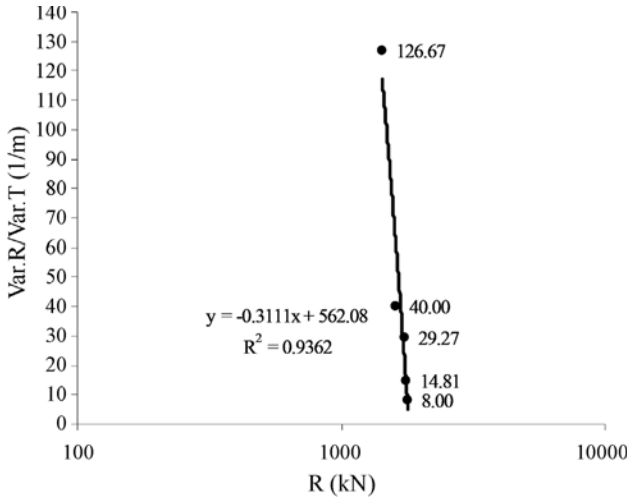

Figure 5 - Linear regression of the last five points of the *R vs. Var. R/Var. T* graph of a driven pile.

The linear regression expression is described below

$$y = ax + b \tag{16}$$

$$R_u = -\frac{b}{a}. \tag{17}$$

Note that the correlation coefficient (R^2) had a value of 0.9362. According to the studies of Alves (2010), values greater than 0.8 were found in all tests. Solving the linear regression expression in Fig. 5, an estimated ultimate static resistance value of 1806.8 kN can be obtained. Therefore, the extrapolated ultimate mobilized static resistance R_u is determined by Eq. 17.

- **Step 02:** The *R* x *D* curve in Fig. 3 is divided into equal maximum displacement segments (Fig. 6). The recommended division value is 1 mm, as used in this example. The values of mobilized static resistance – R_n are calculated by means of interpolation. This task produces a smoother curve in the segments where it has sudden variations in trajectory. The complementary energy values are calculated in each segment as

$$V_{cn} \cong \sum_{n=1}^{i}\left(\frac{D_n + D_{n-1}}{2}\right)\times(R_n - R_{n-1}). \tag{18}$$

Table 2 presents the values for maximum displacement adopted (D_n) for the interpolated mobilized static resistance (R_n) and the calculated values, with Eq. 18, and for the complementary energy in the analyzed segment (Vc_n) of the test.

The values of Vc_n *vs.* Vc_{n-1}, presented in Table 2, are plotted in Fig. 7. After the quadratic regression of the plotted points, this regression was extrapolated until it inter-

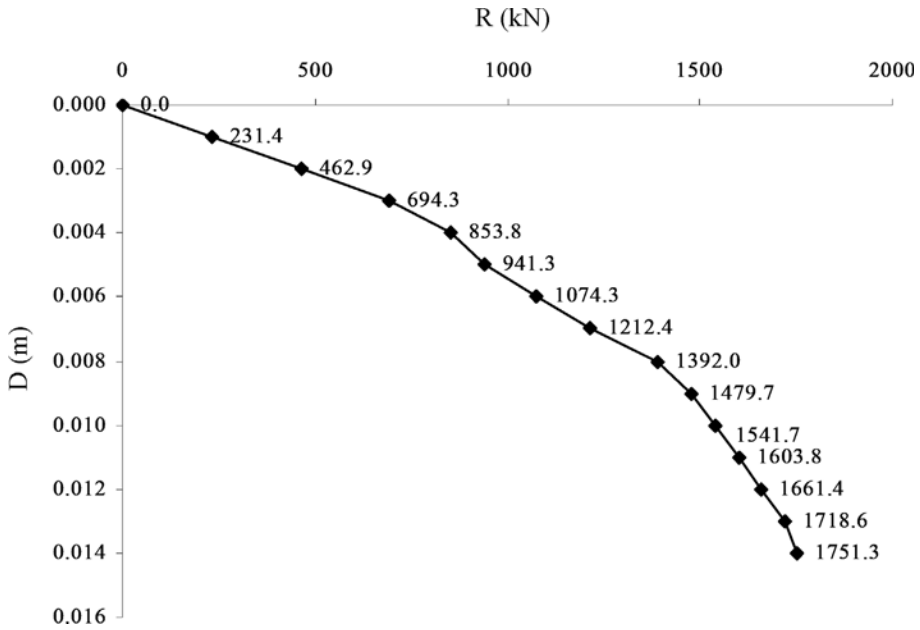

Figure 6 - *R vs. D* graph divided into equal maximum displacement segments.

Table 2 - Interpolated *D* and *R* values and the calculated *Vc*.

D (m)	R_n (kN)	R_{n-1} (kN)	Vc_n (kNm)	Vc_{n-1} (kNm)
0.0000	0.00	-	0.00	-
0.0010	231.43	0.00	0.12	0.00
0.0020	462.86	231.43	0.46	0.12
0.0030	694.29	462.86	1.04	0.46
0.0040	853.75	694.29	1.60	1.04
0.0050	941.25	853.75	1.99	1.60
0.0060	1074.29	941.25	2.72	1.99
0.0070	1212.38	1074.29	3.62	2.72
0.0080	1392.00	1212.38	4.97	3.62
0.0090	1479.66	1392.00	5.71	4.97
0.0100	1541.72	1479.66	6.30	5.71
0.0110	1603.79	1541.72	6.96	6.30
0.0120	1661.43	1603.79	7.62	6.96
0.0130	1718.57	1661.43	8.33	7.62
0.0140	1751.33	1718.57	8.78	8.33
0.0150	1776.92	1751.33	9.15	8.78

cepted the dotted line. The dotted line represents the points at which the values of Vc_n are equal to those of Vc_{n-1}, *i.e.*, a situation in which, under the complementary energy criterion, the test would mobilize the ultimate static resistance.

The quadratic equation, according to Eq. 19, is used to determine the ultimate complementary energy (V_{cu}) when the pile reaches its rupture point.

$$ax^2 + (b-1)x + c = 0. \quad (19)$$

The values of "*a*", "*b*", and "*c*", as found in the quadratic regression (Fig. 7), are substituted into Eq. 19. The unknown quantity "*b*" is reduced by 1 to arrive at the condition where both axis values are equal, *i.e.*, Vc_n is equal to Vc_{n-1}.

Solving the quadratic equation, Vc_{u1} and Vc_{u2} are found, discarding any Vc_u value that eventually is negative or has no physical significance.

In the example presented here, by solving the equation shown in Fig. 7, a Vc_u value of 10.06 kN is found.

- **Step 03:** Using the values obtained for the ultimate mobilized static resistance and for the ultimate complementary energy of the test, it is possible to extrapolate the remaining segment of the mobilized static resistance (*R*) *vs.* maximum displacement (*D*) curve. Eqs. 7 to 15 can be used for this purpose.

Finally, by substituting the values Vc_u = 10.06 kJ and R_u = 1806.8 kN into Eq. 9, Eq. 12 and Eq. 15, the parameters for the exponential, hyperbolic, and parabolic equations, respectively ($\alpha \approx 1179.6$, $D_u \approx 0.0259$ m, and $D_u \approx 0.0167$ m), can be obtained.

Figure 8 shows the comparison of the mobilized static resistance (*R*) x maximum displacement (*D*) curve measured in the dynamic increasing energy test with the curves calculated by the exponential, hyperbolic, and parabolic equations.

6. Results and Discussions

6.1. Analyzed tests

The dynamic load tests were carried out starting with the application of increasing dynamic axial loads, using a free fall hammer, in different Brazilian states.

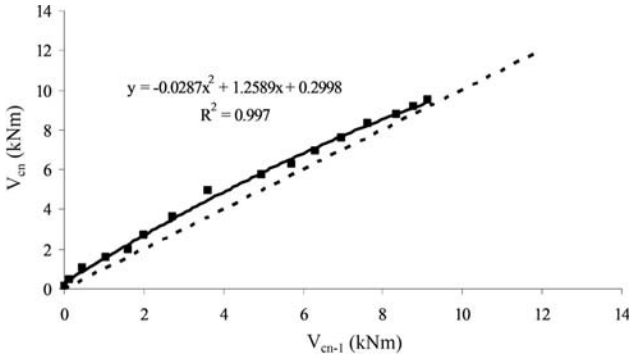

Figure 7 - Vc_{n-1} *vs.* Vc_n graph of a driven pile with quadratic regression.

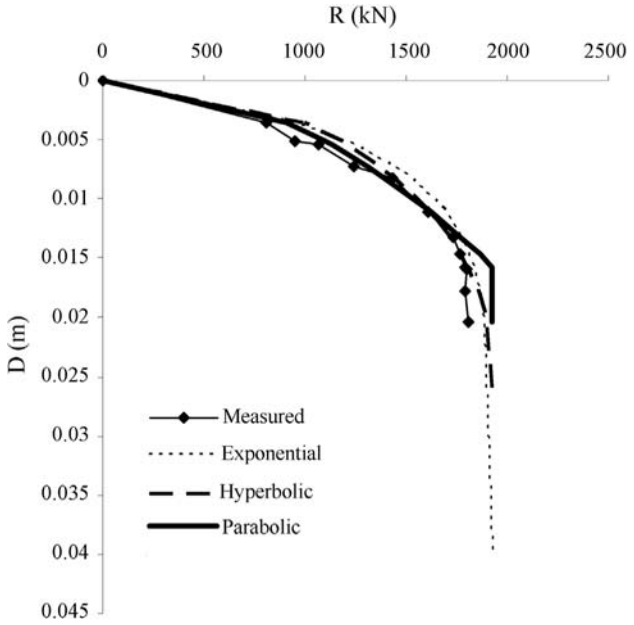

Figure 8 - Comparison of the measured and calculated *R vs. D* curves.

The data captured by the sensors fastened onto the piles were processed by the simplified CASE method and so obtaining *R*. The values of the soil damping coefficients of the CASE method (J_c) were obtained with the greater energy blow in each test, by a numerical analysis using the CAPWAP (Case Pile Wave Analysis Program) method. This J_c value was used to all blows of that test.

Complementary details, such as the values of the weights of the pile-driving hammers used in the test, the PDA (Pile Driving Analyzer) model used, the pile age (time elapsed from pile installation and test date), the J_c values adopted in the test analyses, the values for fall heights (H_{fall}) of the hammer during the test, the maximum displacement in each hammer blow (*D*) measured in the test, the values for mobilized static resistances (*R*) calculated by the CASE method, and the values of maximum kinetic energy (*T*) transferred to the pile, using the value of EMX given by the dynamic load test, can be found in Alves (2010).

All of the piles were made from precast reinforced concrete with metal splices at the ends. The concrete presented characteristic resistance (f_{ck}) of 35 MPa. When necessary, the splices of the elements were welded.

Table 3 shows the values for total length (L_{total}), driven length (*Lc*), diameter, section area, and dynamic modulus of elasticity of the structural elements of the studied piles.

The 21 tested piles were part of 12 different works in 7 Brazilian cities.

Free-fall pile drivers were used in all tests, with steel hammers weighting from 18.5 to 50 kN. The driving systems were equipped with a damping system that was composed of a metal helmet with a hardwood block and plywood cushion.

6.2. Comparison of different fit equations for extrapolation of the R *vs.* D curve

Table 4 shows the correlation coefficient values (R^2) of the three functions: exponential, hyperbolic, and para-

Table 3 - Geometric data of the piles.

Pile	L_{total} (m)	*Lc* (m)	Diam. (m)	Section area (m^2)	Dynamic Pile Elast. Modulus (GPa)
1	16.00	15.4	0.23*	0.04	26.0
2	15.80	14.1	0.50	0.13	26.1
3	7.00	4.5	0.40	0.08	25.6
4	8.00	5.8	0.27*	0.05	42.9
5	22.00	21.4	0.27*	0.05	26.1
6	11.00	9.6	0.42	0.09	31.7
7	12.00	8.7	0.42	0.09	31.7
8	13.00	11.5	0.33	0.06	26.1
9	14.00	12.5	0.33	0.06	26.1
10	12.90	11.2	0.33	0.06	26.1
11	12.00	10.1	0.42	0.09	26.1
12	9.00	6.0	0.38	0.06	26.1
13	18.00	17.2	0.42	0.09	26.1
14	14.15	7.3	0.40	0.08	25.6
15	7.00	5.5	0.40	0.08	25.6
16	7.00	5.7	0.27*	0.07	42.9
17	8.00	6.5	0.27*	0.07	42.9
18	20.00	18.7	0.27*	0.07	26.1
19	12.00	10.1	0.42	0.09	31.7
20	13.00	11.0	0.38	0.06	30.0
21	11.50	10.35	0.30	0.07	25.6

(*) = dimension of the side of the piles of square sections.

Table 4 - R^2 values of the exponential, hyperbolic, and parabolic functions.

Pile	Values of R^2		
	Exponential	Hyperbolic	Parabolic
1	0.935	**0.948**	0.776
2	**0.975**	0.913	0.880
3	**0.983**	0.943	0.919
4	0.925	**0.968**	0.556
5	**0.929**	0.827	0.888
6	**0.962**	0.944	0.913
7	**0.968**	0.884	0.856
8	**0.923**	0.901	0.769
9	**0.824**	0.679	0.719
10	**0.379**	0.175	0.151
11	**0.954**	0.908	0.925
12	0.818	0.784	**0.859**
13	**0.931**	0.929	0.918
14	**0.966**	0.880	0.867
15	0.899	0.877	**0.936**
16	0.541	**0.670**	0.378
17	0.374	0.520	**0.714**
18	**0.891**	0.820	0.856
19	0.818	0.784	**0.859**
20	**0.851**	0.657	0.675
21	0.756	0.721	**0.787**
Mean	**0.923**	0.877	0.856
Standard Deviation	**0.180**	0.190	0.200

bolic curves targeting the best fit for all of the pile load tests. The R^2 values in bold face are the ones that presented, among the three functions, the value closest to 1, *i.e.*, the function that presented the best fit in a particular pile.

It was observed that in 13 of the 21 studied piles, the best fit function for the *R vs. D* curve was the exponential function. Only five piles had the best fit for the parabolic function, and three piles had the best fit for the hyperbolic function.

Three tests call the attention in Table 4 by the lowest values of R^2. Test 10 presented a sudden rupture and tests 16 and 17 still presented a "very linear" behavior in the last stage of the test. As said before, in this situations any extrapolation method is not efficient in predicting the ultimate static resistance, and this the reason for lower R^2 values.

Among the three studied functions, the mean of the R^2 values that presented the value closest to one was also the exponential function. Moreover, this function was shown to have the lowest standard deviation of the studied functions.

6.3. Different ultimate load criteria applied in the *R vs. D* curves

The dynamic increasing energy tests were used in this analysis. The tests were conducted until the point of pile-soil rupture, however, to use the rupture criteria to estimate the R_u, only the results obtained after one hammer blow before pile rupture were considered. The piles (listed in Table 3) used in the present comparison were 02, 10, 11, 18, 20, and 21 because they mobilized the ultimate static resistance.

To compare the proposed method (SEM-CASE method), Table 5 presents the ratio of calculated R_u to measured R_u for the conventional methods that are usually applied for static load testing – SLT. All predictions were made using the same "*R vs. D*" curve measured in the dynamic increasing energy test.

Table 5 - Values of the ratio of calculated R_u to measured R_u for the extrapolation criteria of R_u for SLT and the SEM-CASE method of Piles 2, 10, 11, 18, 20,and 21.

Criterion/Pile	R_u Calculated/ R_u Measured					
	2	10	11	18	20	21
Van der Veen (1953)	1.154	1.001	1.078	1.082	1.204	1.008
80% Brinch Hansen (1963)	0.888	0.809	0.956	N/A	N/A	N/A
90% Brinch Hansen (1963)	0.999	0.91	1.076	N/A	N/A	N/A
Chin (1970)	1.462	1.107	1.389	N/A	2.564	1.344
Mazurkiewicz (1972)	1.07	1.024	1.097	1.111	N/A	1.083
Massad (1986)	1.066	1.452	1.139	1.544	1.573	1.074
Décourt (1996)	1.446	0.929	1.399	N/A	2.483	N/A
SEM-CASE	**1.042**	**1**	**1.004**	**1.042**	**1.043**	**1.025**

N/A = not available.

Figure 9 shows a 3D bar graph comparing all of the criteria shown in Table 5. It shows that the SEM-CASE method had the lower variation in the ratio of calculated R_u to measured R_u. The SEM-CASE presented a better prediction to all piles with relations "calculated/measured" very close to one. The predictions using the criteria of Van der Veen (1953), Brinch Hansen (1963) and Mazurkiewicz (1972) had a good behavior to this set of piles. The methods of Chin (1970), Massad (1986) and Décourt (1996) presented a higher variability, overpredicting in most of the cases.

7. Conclusions

This paper presents a new method, the Simplified Extrapolation Method of the Simplified CASE Method (SEM-CASE), to extrapolate the mobilized static resistance (R) *vs.* maximum displacement (D) behavior based on the complementary energy criterion. This method is mainly applicable to precast concrete piles and was calibrated with dynamic increasing energy tests.

With respect to the presented analyses, the following should be noted:

- The SEM-CASE method can be easily used and has an acceptable theoretical basis.
- The estimated values of the ultimate static resistance, obtained by the SEM-CASE method, were similar to the measured values, with an error below 10%.
- By evaluating three different functions (exponential, hyperbolic, and parabolic functions) to reach the best fit with the test, it was noted that the exponential function obtained better results in more than 60% of analyzed cases.

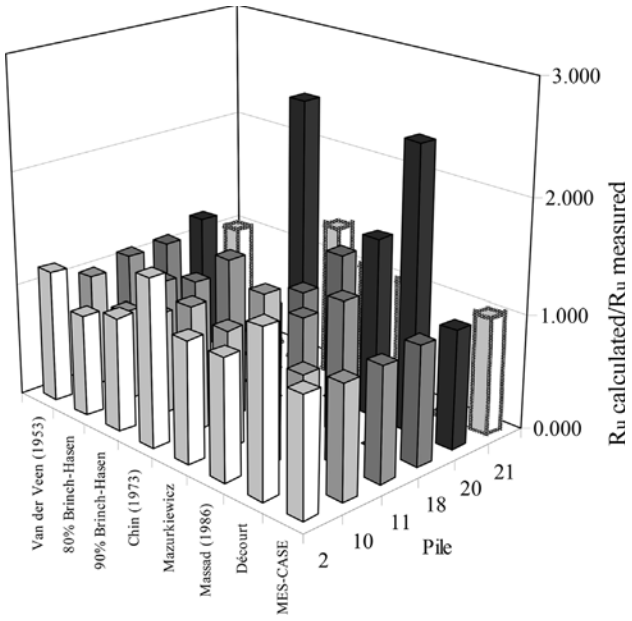

Figure 9 - Bargraph of the ratios of calculated R_u to measured R_u for all compared methods.

- The ability of classical methods to predict the ultimate load in static load tests was compared with the proposed SEM-CASE method. In the six presented dynamic load tests, the SEM-CASE resulted in better predictions that were closer to the ultimate measured resistance.
- The presented method was tested with a set of concrete driven piles. However, the same concept is surely valid for steel piles, since load tests on these piles normally present a well defined static resistance (R).
- As any other extrapolation method, the SEM-CASE method is applicable to tests that are gradually converging to the ultimate static resistance with a well-defined vertical asymptote.

Acknowledgments

The authors of this paper would like to thank the company SETE, Serviços Técnicos de Engenharia Ltd. for sharing the dynamic load tests used in this study, AGETOP, Agência Goiana de Transporte e Obras for its support, and CNPq, Conselho Nacional de Desenvolvimento Científico e Tecnológico for the financial support.

References

Alves, E.C. (2010). A New Extrapolation Method of Dynamic Load Tests: SEM-CASE. MSc Dissertation, School of Civil and Environmental Engineering. Federal University of Goias, Brazil, 250 p. (in Portuguese).

Aoki, N. (1989a). A new dynamic load test concept. Proc. 12th Int. Conf. on Soil Mechanics and Foundation Eng., ISSMFE, Rio de Janeiro, Session 14, Drivability of Piles. Japanese Society for Soil Mechanics and Foundation Engineering, Tokyo, v. 1, pp. 1-4.

Aoki, N. (1989b). Prediction of the behavior of vertical driven piles under static and dynamic conditions. Proc. 12th Int. Conf. on Soil Mechanics and Foundation Eng., ISSMFE, Rio de Janeiro, v. 2, pp. 56-61.

Aoki, N. (1997). Deformation of Ultimate Load Capacity of Driven Piles in Dynamic Increasing Energy Test. PhD Thesis, School of Civil Engineering, University of São Paulo, Brazil, (in portuguese).

Aoki, N. (2000). Improving the reliability of pile bearing capacity prediction by the dynamic increasing energy test (DIET). Proc. 6th Int. Conf. on the Application of Stress Wave Theory to Piles, São Paulo, pp. 635-651.

Brinch Hansen, J. (1963). Discussion: Hyperbolic stress-strain response: cohesive soils. American Society of Civil Engineers, J. of the Soil Mechanics and Foundation Div., 89(4):241-242.

Chin, F.K. (1970). Estimation of the ultimate load of piles not carried to failure. Proc. 2nd Southeast Asian Conference on Soil Engineering, pp. 81-90.

Clough, R.W. & Penzien, J. (1975). Dynamics of Structures. McGraw-Hill, New York.

Décourt, L. (1996). Evaluation of foundation rupture based on the concept of stiffness. Proc. III Seminário de Fundações Especiais, São Paulo-SP, Anais. ABMS, v. 2, pp. 215-224, (in Portuguese).

Hussein, M.H. & Goble, G.G. (2004). A brief history of the application of stress-wave. Theory to piles. Current Practices and Future Trends in Deep Foundations, Geotechnical Special Publication N. 125, ASCE, Reston, pp. 186-201.

Likins, G.E. & Rausche, F. (1981). Case method. The Second Seminar on the Dynamics of Pile Driving in Boulder, CO, Pile Dynamics, Inc., Cleveland, OH.

Likins, G.E.; Piscsalko, G.; Roppel, S. & Rausche, F. (2008). PDA testing: State of the art. Proc. 8th Int. Conf. on the Application of Stress Wave Theory to Piles, pp. 395-402.

Massad, F. (1986). Notes on the interpretation of failure load from routine pile loads tests. Soils and Rocks, 9(1):33-36.

Mazurkiewicz, B.K. (1972). Test Loading of Piles According to Polish Regulations. Royal Swedish Academy of Eng. Sciences, Committee on Pile Research, Report n. 35, Stockholm, 20 p.

Rausche, F., Goble, G.G. & Likins, G.E. (1985). Dynamic determination of pile capacity. ASCE Journal of Geotechnical Engineering, 111(3):367-383.

Smith, E.A.L. (1960). Pile driving analysis by the wave equation. J. Soil Mech. Found. Eng. Div., ASCE, 86(4):35-61.

Teferra, W.; Thendean, G. & Likins, G.E. (1996). Driving stress control during the installation of precast prestressed cylindrical concrete piles. Proc. 5th Int. Conf. on the Application of Stress-wave Theory to Piles, pp. 903-911.

Van der Veen, C. (1953). The bearing capacity of a pile. Proc. 3rd Int. Conf. on Soil Mechanics and Foundation Eng., Zurich, v. 2, pp. 84-90.

Warrington, D.C. (1997). Closed Form Solution of the Wave Equation for Piles. MSc Thesis, University of Tennessee at Chattanooga.

List of Symbols

a, b, c: parameters of regressions
A: cross-sectional area of pile
c: velocity of wave propagation
CAPWAP: Case Pile Wave Analysis Program
D, D_1, D_2: displacement
D_u: maximum displacement
DIET: dynamic increasing energy test
E: elastic modulus of pile material
Ft_1, Ft_2: values of forces
H_{fall}: fall heights of the hammer
J_c: dynamic damping coefficient
Lc: pile driven length
L_{total}: pile total length
PDA: Pile Driving Analyzer
R, R_1: mobilized static resistance
R_u: maximum resistance
R^2: values of correlation coefficient
S_u: maximum permanent penetration
t_1, t_2: time
T: total kinetic energy in the system
T_c: complementary kinetic energy
T_{cu}: maximum complementary kinetic energy
T_u: maximum kinetic energy
vt_1, vt_2: values of velocity
V: potential energy in the system
V_c: complementary potential energy
V_{cu}: maximum complementary potential energy
V_e: elastic strain energy
V_s: potential energy
W: work
W_{au}: work of the final damping forces
W_{nc}: work done by non conservatives forces
α: curve shape coefficient
δ: variation in the time interval (t_2-t_1)
ΔD, ΔD_1, ΔD_2: displacement increment or variation
ΔR : resistance variation
ΔV, ΔV_1, ΔV_2: energy variation

Appendix: Calculation of Complementary Energy When Using Different Fit Equations

As different fit equations could be used to represent the mobilized static resistance (R) *vs.* Displacement (D) curve, as shown in Fig. 2, this appendix explain how the complementary energy (V_c) is calculated in the three used functions in this paper: exponential, hyperbolic, and parabolic functions.

A) Exponential function

Based in Van der Veen (1953), Aoki (2000) proposed to express R x D relationship as:

$$R = R_u(1 - e^{-(\alpha D)}) \tag{20}$$

where R_u is the maximum resistance and α is a curve shape coefficient.

The potential energy (V_s) would be the integral of Eq. 20 from the origin to a generic value of "D":

$$V_s = \int_0^D R_u(1 - e^{-(\alpha D)})dD = \int_0^D R_u\,dD - \int_0^D R_u(e^{-(\alpha D)})dD \tag{21}$$

$$V_s = R_u\left[D - \frac{1}{\alpha}(1 - e^{-(\alpha D)})\right]. \tag{22}$$

The complementary energy can be calculated as:

$$V_c = RD - V_s. \tag{23}$$

Using the result of Eq. 22 in Eq. 23, results:

$$V_c = RD - R_u D + \frac{R_u}{a}(1 - e^{-(\alpha D)}) \quad (24)$$

and changing the value of "R" by Eq. 20, results:

$$V_c = \left(\frac{R_u}{\alpha}\right)\left[1 - (1 + \alpha D)e^{-\alpha D}\right]. \quad (25)$$

When D tends to large values of displacement, the limit complementary energy (V_{cu}) can be expressed as:

$$V_{cu} = \frac{R_u}{\alpha}. \quad (26)$$

B) Hyperbolic function

Using a hyperbolic relation between R x D:

$$R = R_u \sqrt{1 - \left(1 - \frac{D}{D_u}\right)^2} \quad (27)$$

where R_u is the maximum resistance and D_u is maximum displacement

This equation could be rewritten in different form:

$$D = D_u \left(1 - \sqrt{1 - \frac{R^2}{R_u^2}}\right). \quad (28)$$

In this form, the complementary energy (V_c) would be the integral of Eq. 27 from the origin up to a generic value of resistance (R):

$$\begin{aligned} V_c &= \int_0^R D_u \left(1 - \sqrt{1 - \frac{R^2}{R_u^2}}\right) dR \\ &= D_u \int_0^R dR - D_u \int_0^R \sqrt{1 - \frac{R^2}{R_u^2}} dR \end{aligned} \quad (29)$$

or

$$V_c = D_u R - \frac{D_u}{R_u}\left[\left(\frac{R}{2}\sqrt{R_u^2 - R^2}\right) + \left(\frac{R_u^2}{2}\arcsin\left(\frac{R}{R_u}\right)\right)\right]. \quad (30)$$

Replacing R by R_u, the limit complementary energy (V_{cu}) can be expressed as:

$$V_{cu} = D_u R_u \left[1 - \frac{1}{2}\arcsin(1)\right] \quad (31)$$

or approximately:

$$V_{cu} = 0.215 D_u R_u. \quad (32)$$

C) Parabolic function

Using a parabolic function where D would be proportional to the square of R, the relationship could be expressed as

$$D = \frac{R^2}{R_u^2} D_u. \quad (33)$$

The complementary energy (V_c) would be the integral of Eq. 33 from the origin up to a generic value of resistance (R):

$$V_c = \frac{D_u}{R_u^2}\int_0^R R^2 dR = \frac{D_u R^3}{3R_u^2}. \quad (34)$$

Replacing R by R_u, the limit complementary energy (V_{cu}) can be approximately expressed as:

$$V_{cu} = \frac{D_u R_u}{3}. \quad (35)$$

Geotechnical Parameters for the Variegated Soils of São Paulo Formation by Means of *In Situ* Tests

M. Caldo, F. Massad

Abstract. The purpose of this paper is to present geotechnical parameters of the variegated soils from the São Paulo Formation, aiming in particular to establish correlations between stress history parameters, earth pressure coefficients at rest, deformability modules and resistance obtained through piezocone and dilatometer tests. The performance of *in situ* tests has, as the major advantage over laboratory tests for obtaining soil parameters of the project site, minimization of sample disturbance effects. Using data from geotechnical investigation carried out during the basic design of the Green Line expansion for the Metrô - SP it was possible to obtain preconsolidation pressure (σ'_p), over consolidation ratio (*OCR*), earth pressure coefficients at rest (K_0), Young's module (E_i), initial shear module (G_0), constrained module (M) and undrained shear strength (s_u) for the variegated soils of the São Paulo Formation. These soils are characterized by interlayered levels of clays and sands, constituting a characteristic with different geotechnical parameters and perched water tables. These characteristics explain some of the knowledge gaps on these soils. Nevertheless, it was possible to validate the correlations between earth pressure coefficients at rest (K_0), over consolidation ratio (*OCR*), Young's module (E_i), undrained shear strength (s_u) and preconsolidation pressure (σ'_p) through field tests and the results of laboratory testing conducted by other authors.

Keywords: site investigation, dilatometer, piezocone, correlations, soil parameters.

1. Introduction

Nowadays, the biggest cities in the world need more investment in infrastructure, particularly in large capacity public transportation, such as trains and subways. For such projects, and their execution, there is increasingly demand for safety and efficiency. For this reason, *in situ* tests have proved hugely advantageous, allowing information to be gathered on site, thus increasing overall safety and efficiency, whilst simultaneously decreasing uncertainty and minimizing costs.

Tunnel construction carried out by Companhia do Metropolitano de São Paulo (Metrô - SP), the state subway company of São Paulo State (Brazil), provided the opportunity to perform a comprehensive program of *in situ* tests, such as the piezocone (CPTu) and the dilatometer (DMT), both of which are still not frequently used in Brazil, especially in the soils from São Paulo Sedimentary Basin.

Soils from São Paulo Sedimentary Basin comprise mostly the São Paulo and Resende Formations. Whilst many studies about the São Paulo Formation have been conducted, there is still a lack of information about some properties of the soils from São Paulo Sedimentary Basin. The most comprehensive and critical synthesis of knowledge on these soil properties to date can be found in Massad (2012).

This paper presents the results of important geological and geotechnical investigations of variegated soils from the São Paulo Formation carried out during the basic design of the Green Line expansion for the Metrô - SP. These results cover soil parameters, such as earth pressure coefficients at rest (K_0) over consolidation ratio (*OCR*), preconsolidation pressure (σ'_p),Young's module (E_i), initial shear module (G_0), constrained module (M) and undrained shear strength (s_u) obtained from the piezocones and the dilatometers carried out in twelve sites, numbered from 1 to 12. In order to validate the data obtained from this investigation, a comparison is made with the results of previous studies for the São Paulo Formation.

2. Studied Area

The geological and geotechnical investigations were carried out during the basic design of the Green Line expansion for the Metrô - SP, located in east of São Paulo, Brazil (Fig. 1).

Soils from São Paulo Sedimentary Basin, which was formed by the Brazilian Southeast Continental Rift during the Paleogene Period, are comprised mostly of the Resende and São Paulo Formations. The Resende Formation is characterized by distinct packs of sand (known as basal sands) and stiff overconsolidated clays (locally known as "taguá").

Mariana Caldo, Student, Geologist, Escola Politécnica, Universidade de São Paulo, R. Iperoig 858, apto. 92, Perdizes, 05016-000 São Paulo, SP, Brazil, e-mail: mariana@mapsolution.com.br.
Faiçal Massad, D.Sc, Civil Engineering, Escola Politécnica, Universidade de São Paulo, Av. Professor Almeida Prado 271, Trav. 2, Cidade Universitária, 05508-900 São Paulo, SP, Brazil, e-mail: faical.massad@poli.usp.br.
Submitted on August 20, 2015; Final Acceptance on May 3, 2016; Discussion open until December 30, 2016.

Figure 1 - Location of the studied site.

The São Paulo Formation is a depositional environment associated with fluvial meanders, comprising the variegated soils, and generally overlaid by a porous red clay. According to Massad (2012), the variegated soils are highly weathered sediments deposited in alternating layers of sand and clay, and are very heterogeneous. Their engineering properties vary widely due to the occurrence of very different types of soils, such as sands, clayey fine sands and sandy clays with silts. The clay content ranges from 20 to 80%. The activity index averages 0.65. In general, these soils are overconsolidated, but the preconsolidation pressure is not correlated with the weight of current or past overburden pressure. Massad *et al.* (1992) speculated that successive sedimentation cycles, associated with the drying of the soil, have affected the preconsolidation pressures through capillary tensions, which are greater for the finer the soil particles, or that there was a chemical cementation of the soil particles as a result of pedological evolution.

The Green Line extension (Line 2) crosses the Tiete River and streams of east São Paulo. Thus, there are many different hydrogeological conditions with regard to the São Paulo Basin. An example of this would be the perched water tables present in the upper soil layers. These are independent water levels that cause changes in the value of pore pressure along depth in each region and, due to the interleaving of sands and clays, suction may arise in the unsaturated parts of the subsoil. Their presence would cause the porous stone of the piezocone to lose its saturation, made with glycerin, adversely affecting the pore pressure measurements and any analysis of soil parameters that depend on it. This will be evidenced in analyzes presented along this paper.

As an example, Figs. 2-c and 3-c show the direct parameters of the CPTu and the intermediate parameters of the DMT, and the geological profiles of sites 1 and 3. The latter show perched water tables.

In both figures, the letters signify:

(a) q_c and q_t - measured and corrected cone tip resistances (from CPTu);

(b) f_s- sleeve friction (from CPTu);

(c) u_2- pore pressure measured at the base of the cone (from CPTu);

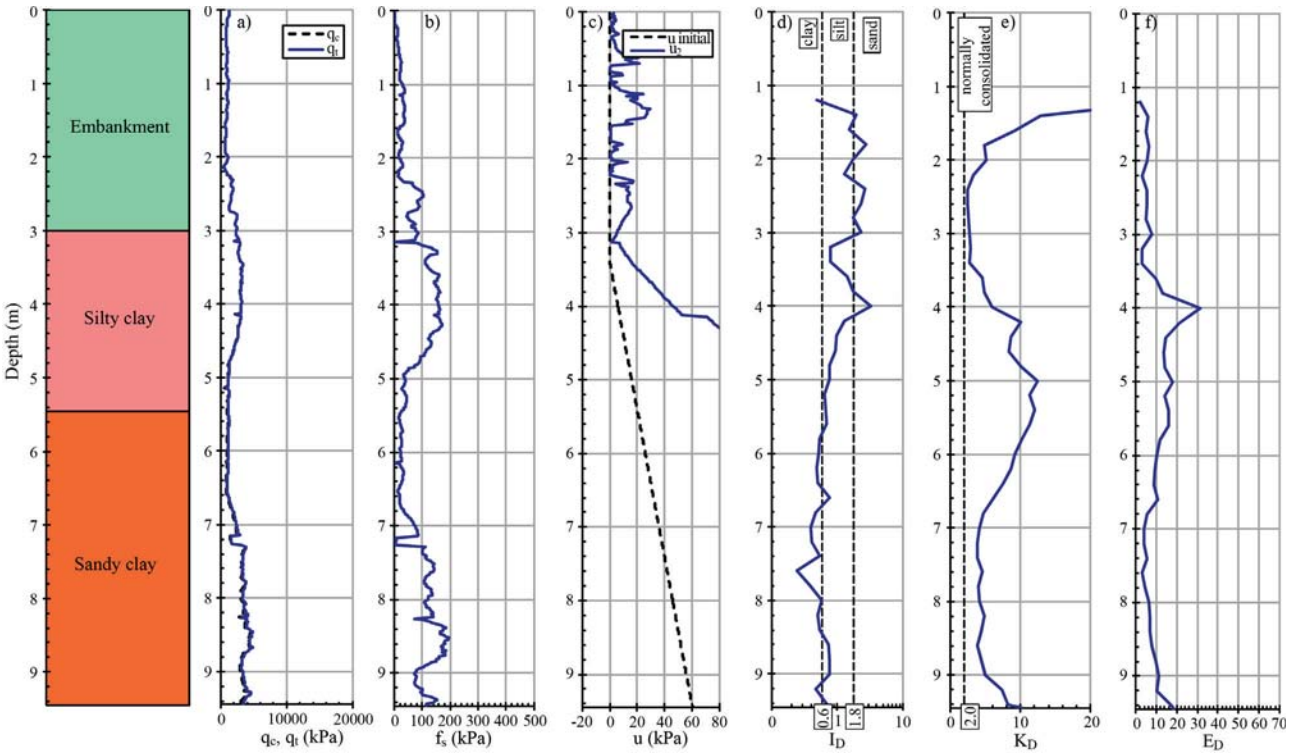

Figure 2 - Typical results from CPTu (a, b, c) and DMT (d, e, f) tests from Site 1.

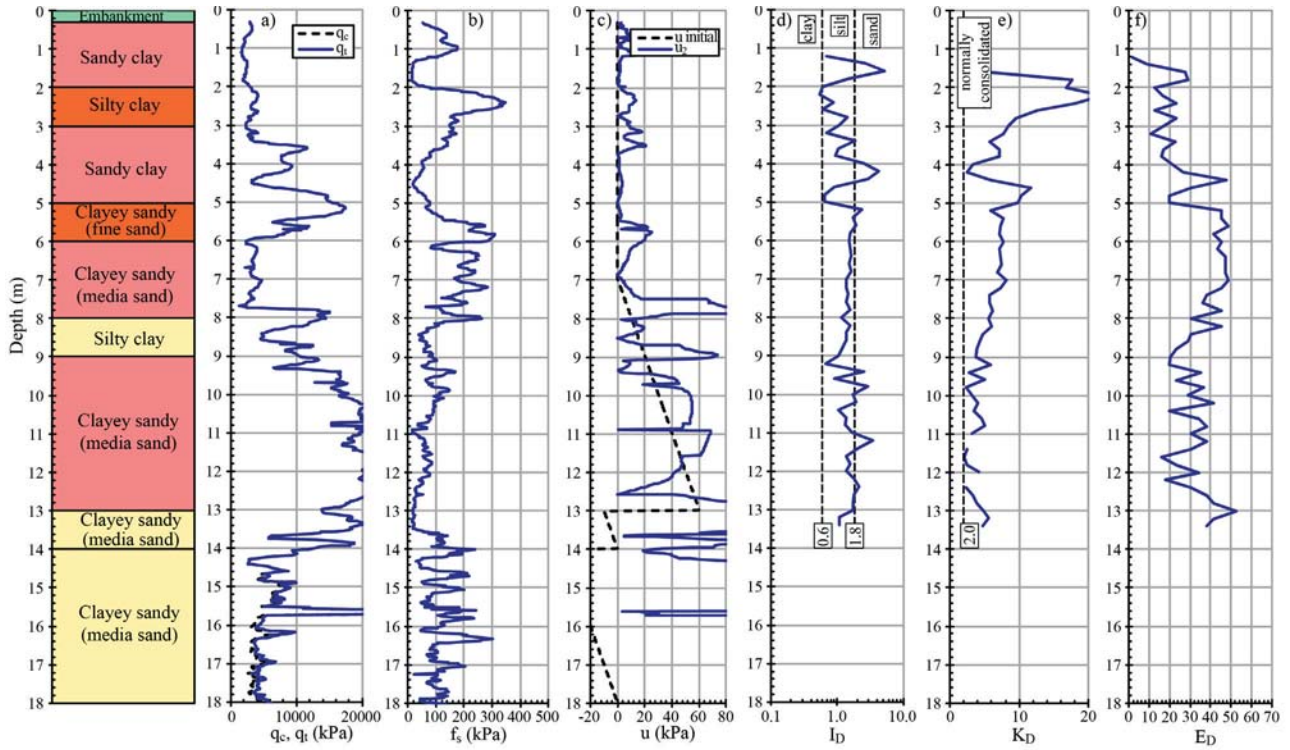

Figure 3 - Typical results from CPTu (a, b, c) and DMT (d, e, f) tests from Site 3.

(d) I_D - material index (from DMT);
(e) K_D- horizontal stress index (from DMT);
(f) E_D - dilatometer modulus (from DMT).

For other symbols, see the appended list of symbols.

3. Piezocone and Dilatometer Tests - Theoretical Background

The *in situ* tests have the advantage of being easy to conduct and involve the soil at the construction site. These characteristics give the tests more reliability.

The piezocone (CPTu) consists of an instrumented cone provided with a porous stone that is pushed into the ground at a controlled rate (speed of 20 mm/s ± 5 mm/s), allowing us making it possible to obtain relevant soil parameters through the measurement of the tip resistance (q_c), the lateral friction (f_s) and the pore pressure (u_2) generated during the process.

The flat dilatometer, or DMT, is a device used to determine the soil *in situ* lateral pressure and soil lateral stiffness. The test involves driving into the ground a flat blade with a steel membrane that is then expanded. Measurements of the corresponding pressure and deformation are taken, permitting the determination of relevant soil parameters.

3.1. Piezocone

Empirical equations were taken from the literature in order to obtain design parameters such as earth pressure coefficients at rest (K_0) , overconsolidation ratio (*OCR*), preconsolidation pressure (σ'_p), Young's module (E_i), constrained module (M), initial shear module (G_0) and undrained shear strength (s_u).

Two criteria were used in selecting the empirical equations: a) to avoid those that depend on the pore pressure, due to the aforementioned effect of the perched water table; and b) to validate the results through comparisons with laboratory test findings.

The preconsolidation pressure (σ'_p) was estimated through the Kulhawy & Mayne (1990) equation, given by:

$$\sigma'_p = 0.333(q_t - \sigma_{v0}) \quad (1)$$

For cohesive soils, it was possible to correlate E_i with the piezocone results, as in Eq. 2:

$$E_i = \alpha(q_t - \sigma_{v0}) \quad (2)$$

and, as far as the initial shear module is concerned, application was made of the equation:

$$G_0 = 50(q_t - \sigma_{v0}) \quad (3)$$

from Watabe *et al.* (2004).

The undrained shear strength varies, as demonstrated in the following:

$$s_u = \frac{(q_t - \sigma_{v0})}{N_{kt}} \quad (4)$$

The empirical parameters α and N_{kt} were set below.

The over consolidation ratio, defined through the relation between σ'_p and σ'_{vo}.

$$OCR = \frac{\sigma'_p}{\sigma'_{v0}} \quad (5)$$

is relatively easy to obtain when the soil is submerged. However, for the variegated soils its determination is very difficult due to the aforementioned perched water tables and their effect on pore pressure. It therefore becomes necessary to make use of cones to measure, either directly or indirectly, the suction. This issue is currently being investigated by Giacheti (2015) in his research on the use of tip TDR (Time Domain Reflectometry) to evaluate the suction effect in the CPTu results. A method adapting this tip for use in conjunction with piezocone - measuring the suction in unsaturated soil - was presented by Esquivel & Vaz (2009).

3.2. Dilatometer

With regard to the DMT, the preconsolidation pressure values were obtained from *OCR* and the *in situ* vertical effective stress, as follows:

$$\sigma'_p = OCR\sigma'_{v0} \quad (6)$$

Kamei & Iwasaki (1995) performed several tests in Japanese clay soils and proposed Eq. 7 to estimate the *OCR*.

$$OCR = 0.34K_D^{1.43} = (0.47K_D)^{1.43} \quad (7)$$

The *OCR* can also be calculated from Eqs. 8 and 9, of Marchetti (1980) and Lunne *et al.* (1989), respectively.

$$OCR = (0.5K_D)^{1.56} \quad (8)$$

$$OCR = (0.27K_D)^{1.17} \quad (9)$$

The choice of the equation that is best suited to variegated soils will be made later.

The earth pressure coefficient at rest (K_0) was estimated by the equations of Powell & Uglow (1988), Lacasse & Lunne (1988) and Lunne *et al.* (1990) for aged clays, given by:

$$K_0 = (0.4K_D)^{0.54} \quad \text{for} \quad \frac{s_u}{\sigma'_{v0}} > 0.8 \quad (10)$$

It also is possible to calculate K_0 from Marchetti (1980):

$$K_0 = \left(\frac{K_D}{1.5}\right)^{0.47} - 0.6 \quad (11)$$

For the initial Young's module (E_i) the following equation, from Robertson *et al.* (1989) and Campanella *et al.* (1985), was used:

$$E = F \cdot E_D \quad (12)$$

In this equation the conversion factor (F) was taken as equal to 5 for cohesive soils, and 2 for sandy soils.

For the initial shear modulus (G_0) Lunne *et al.* (1990) proposed the Eq. 13 for cohesive soils, that was adopted for the variegated soils:

$$G_0 = \alpha K_D \sigma'_{v0} \quad (13)$$

with α varying from 75 to 150. For the variegated soils a figure of 112.5 was adopted.

Finally, the determination of the undrained shear strength (s_u) was calculated by means of Eq. 14 from Marchetti (1980):

$$s_u = 0.22\sigma'_{v0}(0.5K_D)^{1.25} \quad (14)$$

4. Results and Analysis

Analyzing the twelve sites, it was possible to conclude that the subsoil is very heterogeneous, confirming the already mentioned extreme heterogeneity of the variegated soils, comprising alternating layers of sandy clays, and clayey sand with silt fractions. However, the horizontal stress index (K_D) revealed values higher than two, confirming the overconsolidation of the variegated soils, already mentioned in the literature.

Site 5 showed different results, potentially indicating a geological anomaly or problems in carrying out the tests. In order to avoid distortion of the data; it was disregarded.

For illustration purposes, the graphical representations with respect to depth of soil parameters obtained from the CPTu and the DMT are shown in Figs. 4 and 5, for sites 1 and 3 respectively.

The results obtained from the analysis of the sites are presented in Tables 1 and 2. The most reliable test was chosen to give each parameter, so as not to depending on the value of poropressure. In some cases, DMT and CPTu values were considered together.

From the analysis of the data presented in Table 1 it can be concluded that:

- The values of the preconsolidation pressure ranged between 100 and 5000 kPa;
- The *OCR* values ranged between 1 and about 40. The values below 1, associated with K_D lower than 2, were disregarded; and
- The values of the earth pressure coefficients at rest varied between 1 and 3.9.

In the same way, from the analysis of the data in Table 2 it can be concluded that:

- The range of undrained shear strength values (s_u) was 15-600 kPa;
- The Young's module (E_i) from CPTu data showed variation between 6 and 300 MPa and, from the DMT data, between 1 and 300 MPa;
- The initial shear module values (G_0) from CPTu tests varied between 15 and 600 MPa; and

The constrained module (M) values from CPTu tests ranged between 2.5 and 200 MPa. The values from DMT varied from 2 to 200 MPa.

The results obtained in these tests are summarized in Table 3 to determine the range of values of geotechnical parameters resulting from each site. The wide dispersion re-

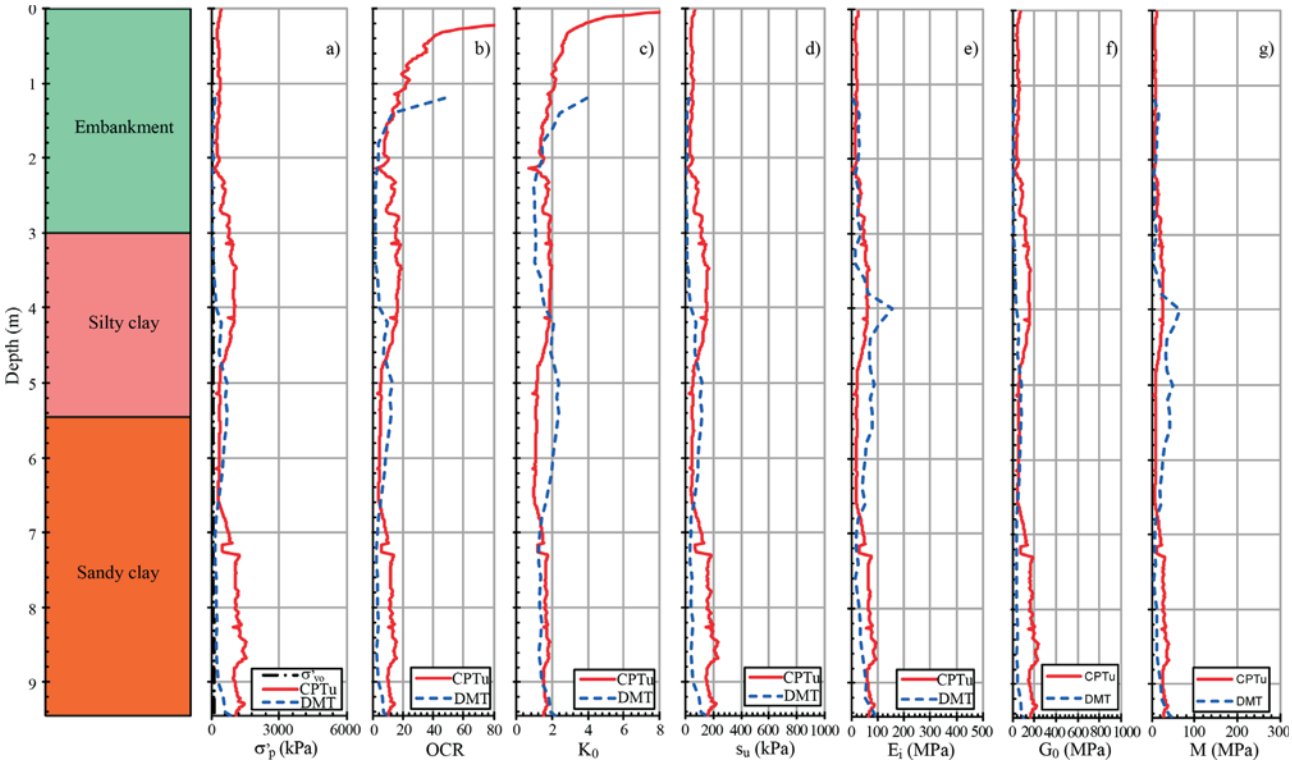

Figure 4 - Typical results of parameter from CPTu and DMT from Site 1.

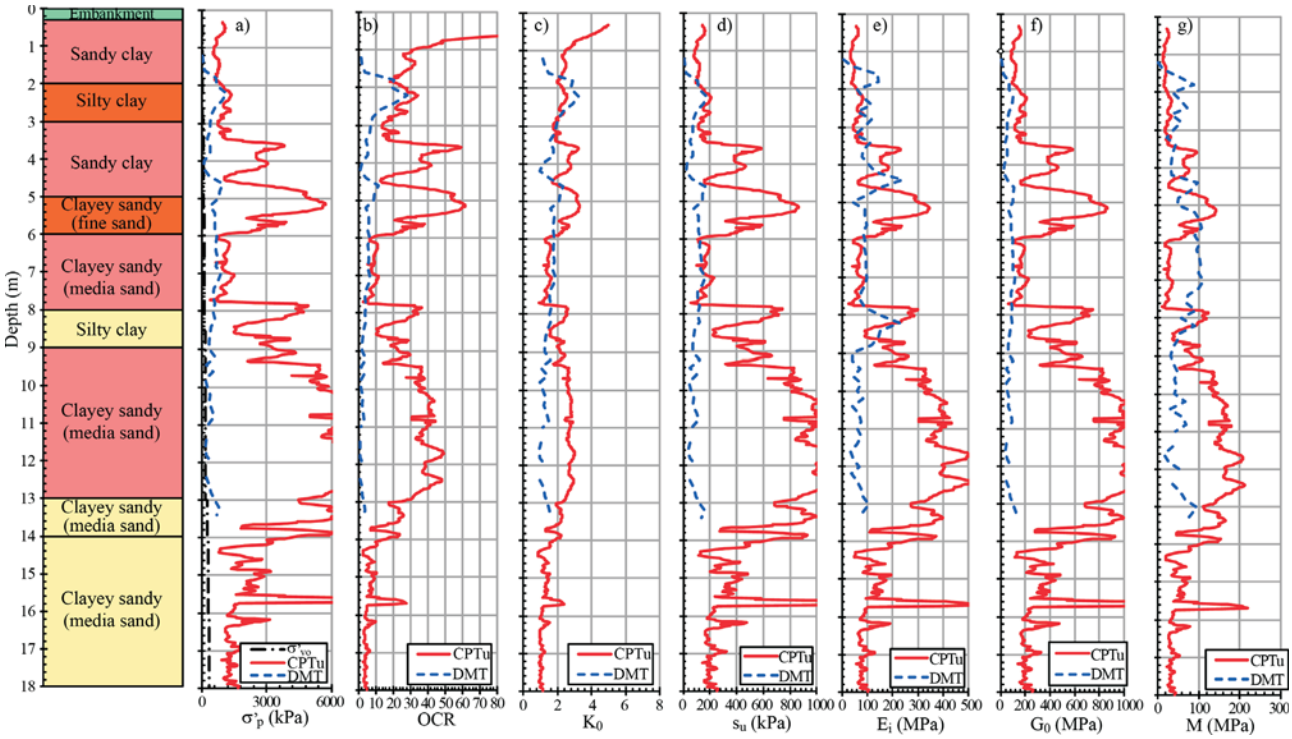

Figure 5 - Typical results of parameters from CPTu and DMT from Site 3.

Table 1 - Values from σ'_p, *OCR* and K_0 from the investigated sites.

Sites	σ'_p (kPa) - CPTu	*OCR* - DMT	K_0 - DMT
1	200-1500	1.3-13	1-2.4
2	120-2700	1-8	1-2.1
3	400-4200	1-12	1-3.3
4	100-5000	1-8	1-2.4
6	250-3000	1.3-18	1-3.7
7	400-3800	1.9-12	1.1-2.4
8	250-3000	2.6-16	1.3-2.6
9	250-2800	1.1-29	1-3.2
10	150-2800	2.2-30	1.2-3.9
11	270-2800	1-17	1-2.6
12	100-2800	1.1-40	1-4.3

vealed by the figures given in Table 3 is a result of the previously mentioned heterogeneity of variegated soils.

4.1. Earth pressure coefficients at rest (K_0) and over consolidation ratio (*OCR*)

To establish a relationship between earth pressure coefficients at rest (K_0) and over consolidation ratio (*OCR*) from DMT results, the corresponding pair of equations proposed by Marchetti (1980) (Eqs. 8 and 11), Lunne *et al.* (1998) (Eq. 9), Lunne *et al.* (1990) (Eq. 10) and Kamei & Iwasaki (1995) (Eq. 7) were combined through K_D. The results from the combinations are:

K_0 (Eq. 11 of Marchetti, 1980) and *OCR* (Eq. 8 of Marchetti, 1980):

$$K_0 = 1.14 OCR^{0.30} - 0.6 \quad (15)$$

K_0 (Eq. 10 of Lunne *et al.*, 1990) and *OCR* (Eq. 7 of Kamei & Iwasaki, 1995):

Table 3 - Values of relevant parameters from the investigated sites.

Parameter	Range of values	Other authors
σ'_p (kPa)	100-5000	100 e 1500 kPa (Massad, 2012)
OCR	1-40	
K_0	1-4.3	3.5 (Pinto & Abramento, 1998)
s_u (kPa)	15-600	
E_i (MPa)	1-300	
G_0 (MPa)	15-600	
M (MPa)	2-200	

$$K_0 = 0.92 OCR^{0.38} \quad (16)$$

K_0 (Eq. 10 of Lunne *et al.*, 1990) and *OCR* (Eq. 9 of Lunne *et al.*, 1989):

$$K_0 = 1.23 OCR^{0.46} \quad (17)$$

To assess which of the three Eqs. 15, 16 or 17 has the better outcome for the variegated soils. These equations are presented on Fig. 6 together with one K_0 value determined using the self-boring pressuremeter (Camkometer type) reported by Pinto & Abramento (1998) from the variegated clays of Ibirapuera, São Paulo.

As a result, it can be concluded that for the DMT, Eq. 16 fits fairly well the variegated soils: it is close to the point of Camkometer (Abramento & Pinto, 1998). It refers to the equations of Lunne *et al.* (1990) for K_0 and Kamei & Iwasaki (1995) for *OCR*. A similar result was obtained by Massad (2012) for the "taguá" of the Resende Formation.

Table 2 - Values from s_u, E_i, G_0 and *M* from the investigated sites.

Sites	s_u (kPa)	E_i (MPa)		G_0 (MPa)	*M* (MPa)	
	CPTu	CPTu	DMT	CPTu	CPTu	DMT
1	30-220	10-100	15-160	30-220	5-40	3.5-65
2	19-400	7-190	1-200	19-400	3-80	4-100
3	60-600	24-300	8-200	60-600	10-200	2-110
4	15-600	6-300	5-200	15-600	2.5-200	2-150
6	35-400	15-200	17-200	35-400	5.9-100	10-200
7	60-600	25-100	11-140	60-600	10-100	10-80
8	40-400	15-200	130-300	40-400	40-100	60-150
9	40-400	15-150	5.5-200	40-400	6.5-60	15-100
10	40-400	15-200	10-200	40-400	6-80	5-100
11	40-400	15-200	10-200	40-400	7-100	5-80
12	15-400	6-140	8-250	15-400	2.5-80	15-110

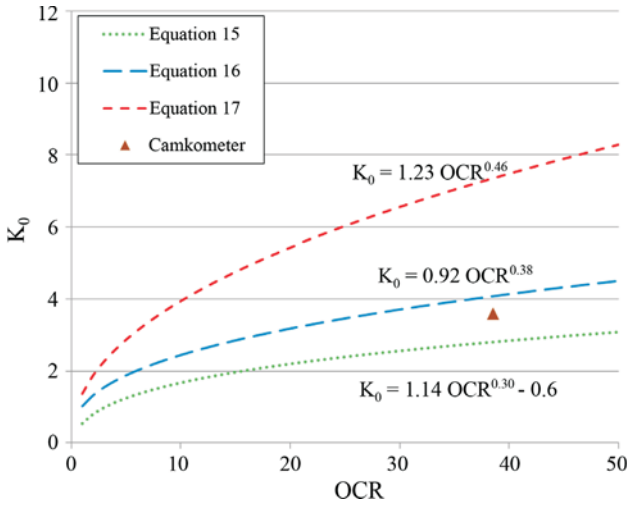

Figure 6 - Correlation between K_0 and *OCR*.

4.2. Young's modulus (E_i) and the undrained shear strength (s_u)

To define which equations best fit with the variegated soil in relation to initial Young's modulus (E_i) and the undrained shear strength (s_u), the equations from CPTu were compared with triaxial test data (consolidated undrained) carried out on samples of variegated soil of Clovis Bevilacqua Square, during construction of the Metro Blue Line-SP and presented by Massad (1980) and Massad *et al.* (1992). The comparison between the results is presented in Fig. 7.

As regards the results of laboratory tests (triaxial CU) conducted on variegated soil samples, these authors reported a range of values for the ratio E_i/s_u between 300 and 600, with an average equal to 400 or 0.40 if one takes into consideration E_i in MPa and s_u in kPa.

As far as the parameters E_i and s_u are concerned, the following procedure was adopted:

- s_u values were estimated using Eq. 4, with $N_{kt} = 20$, to be justified further on; and
- E_i values were estimated from Eq. 2, with α determined by comparison with results of laboratory tests (Clovis Bevilacqua Square). In fact, combining Eq. 2 with Eq. 4 results in:

$$\frac{E_i}{s_u} = 20\alpha \quad \text{or} \quad \alpha = \frac{E_i}{20 s_u} \tag{18}$$

As the laboratory average of E_i/s_u is equal to 400, it was possible to obtain:

$$\alpha = \frac{400}{20} = 20 \tag{19}$$

Figure 7 shows the ratio E_i/s_u from the CPTu of the twelve test sites together with the laboratory range of 300 to 600, for comparison.

For dilatometer tests the parameter s_u depends on σ'_{vo} (Eq. 14) which, in turn, is affected by the aforementioned uncertainty in the value of the pore pressure, due to the perched water tables. This uncertainty has caused a great

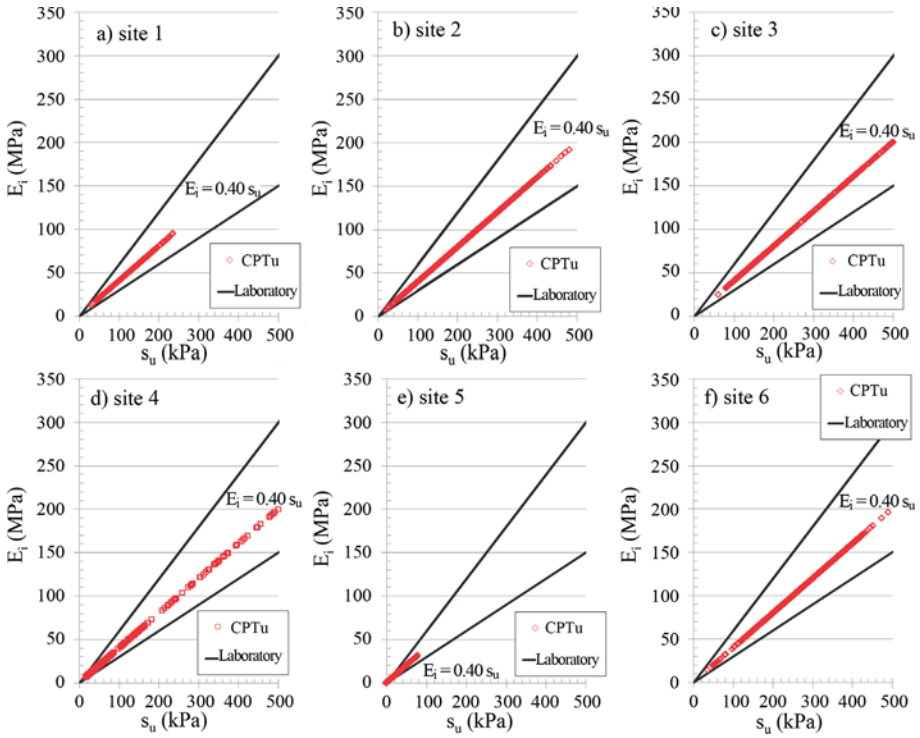

Figure 7 - Correlation between E_i e s_u from CPTu and DMT tests.

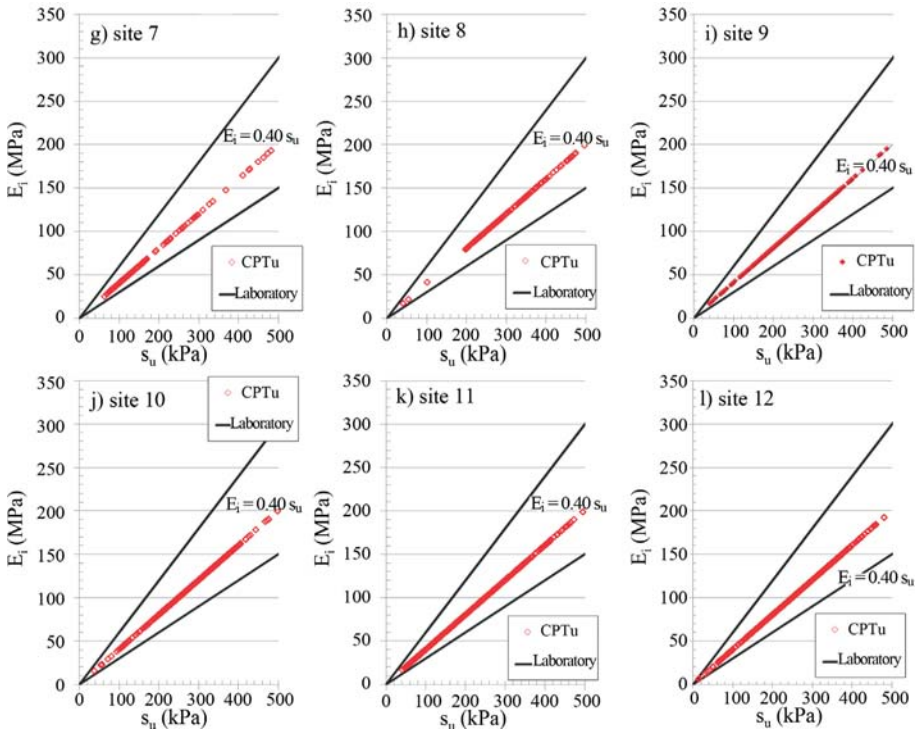

Figure 7 (cont.) - Correlation between E_i e s_u from CPTu and DMT tests.

dispersion in the s_u values and therefore they are not shown in Fig. 7.

4.3. Undrained shear strength (s_u) and preconsolidation pressure (σ'_p)

To define which equations best fit with the variegated soil in relation to the undrained shear strength (s_u) and preconsolidation pressure (σ'_p), the equations from CPTu and DMT were compared with laboratory tests (triaxial CU) presented by Massad (1980 and 2012).

For dilatometer tests the following equations were used:

a) Equation 14 from Marchetti (1980) to determine the undrained shear strength (s_u); and

b) Equation 6 from Kamei & Iwasaki (1995) to determine preconsolidation pressure (σ'_p).

Extracting the K_D from Eq. 6 and replace it in Eq. 14 one can get the following expression:

$$\frac{s_u}{\sigma'_p} = \frac{0.29}{OCR^{0.13}} \qquad (20)$$

The *OCR* depends obviously on σ'_{vo} and is therefore affected by perched water table problems. But fortunately the *OCR* exponent in Eq. 20 is small, which makes the relationship s_u/σ'_p relatively constant and independent of σ'_{vo}. This is demonstrated by the graphs shown in Fig. 8. It therefore follows that the ratio s_u/σ'_p ranges between 0.16 and 0.20 for DMT data.

For the piezocone tests the Eqs. 4 (N_{kt} = 20) and 1 (K_1 = 0.333) were used for determining s_u and σ'_p, respectively. Based on these equations it is easy to establish the following relationship:

$$\frac{s_u}{\sigma'_p} = \frac{1}{K_1 \cdot N_{kt}} = \frac{1}{0.33 \cdot 0.2} = 0.15 \qquad (21)$$

also included in the graphs of Fig. 8.

Massad (1980 and 2012) showed that for the variegated soil of the São Paulo Formation the ratio $c'/\sigma'_p \cong 0.10$ is valid, where c' is the effective cohesion intercept from CU triaxial tests in the overconsolidated range. As it is well known, in this range, the strength envelopes in terms of effective and total stresses practically coincide (see, for example, Pinto, 2000). Then, $s_u/\sigma'_p \cong 0.10$, which was included in Fig. 8 under the heading "Laboratory" and can be taken as a lower limit of this ratio, due to soil disturbance in laboratory tests.

As a result of this analysis, it is possible to conclude that the ratio s_u/σ'_p varies between 0.16 and 0.20 for the DMT data, averaging 0.18 with a standard deviation of 0.013.

Reporting referring again to Fig. 8, the ratio s_u/σ'_p from CPTu data ranges from 0.10 to 0.20, with the value of 0.15 in an intermediate position. This result can be considered a validation of the value of N_{kt} = 20 of Eq. 18, adopted in the analysis.

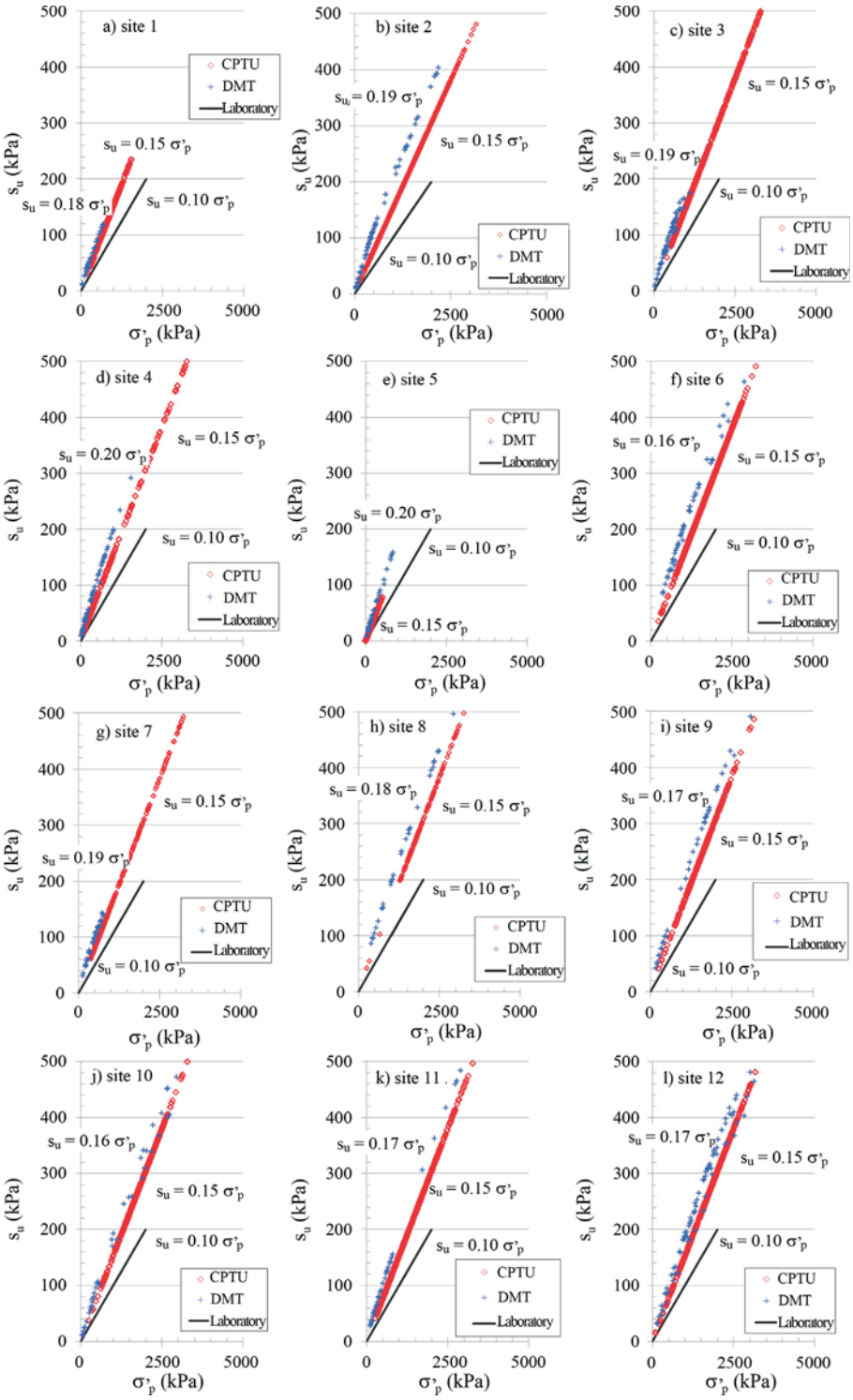

Figure 8 - Correlation between σ'_{vo} and s_u.

4.4. Initial shear module (G_0) and preconsolidation pressure (σ'_p)

To correlate the initial shear module (G_0) with preconsolidation pressure (σ'_p) Fig. 9 was prepared.

For CPTu data Eq. 3 from Watabe *et al.* (2004) was adopted to estimate the G_0 and Eq. 1 to estimate σ'_p with K_1 equal to 0.33. It is easy to see that the ratio $G_0/\sigma'_p = 50/0.333 = 150$ or 0.15 if the G_0 are in units of MPa and σ'_p in kPa.

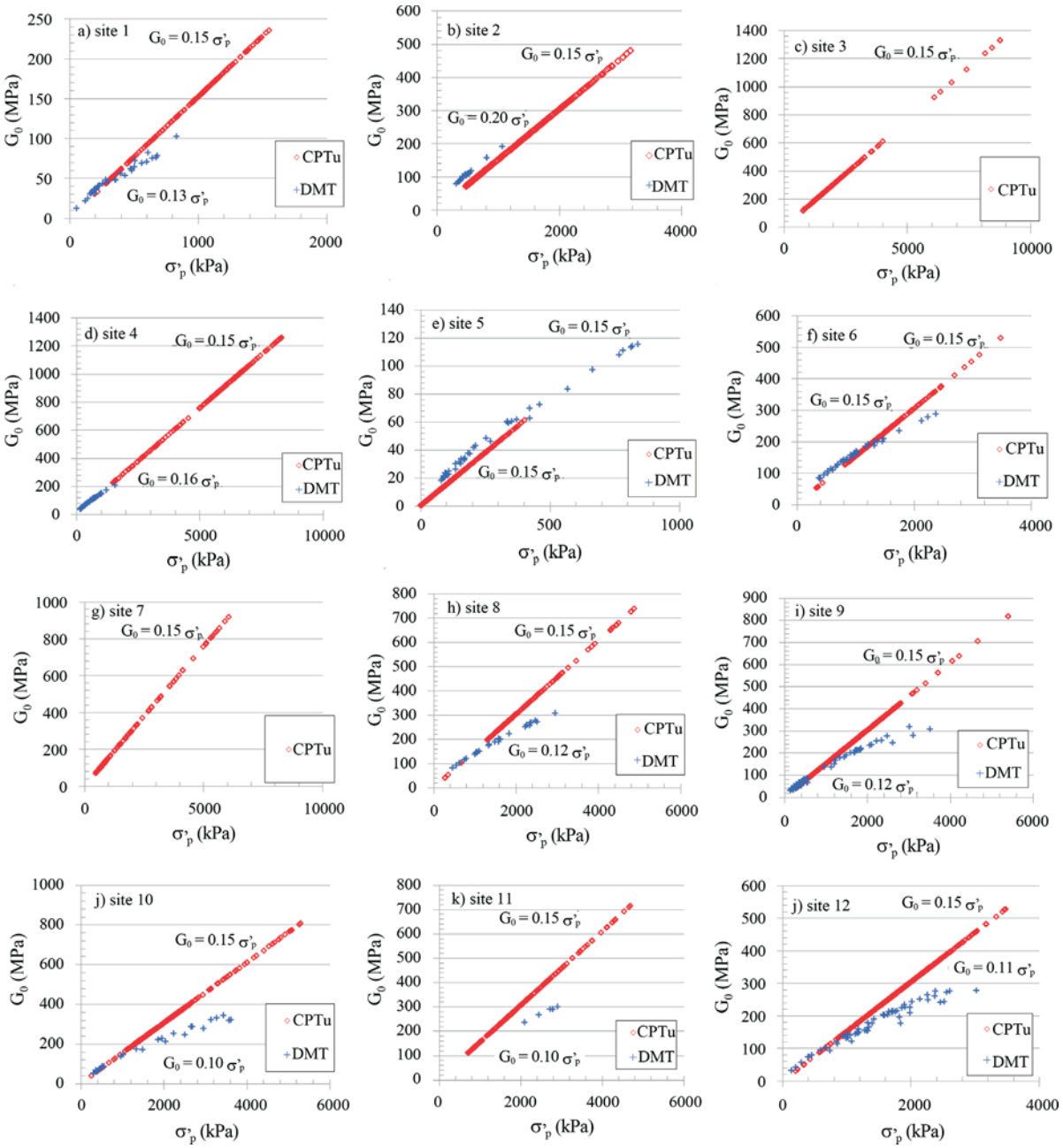

Figure 9 - Correlation between G_0 and σ'_p.

To determine G_0 and σ'_p from DMT data, Eqs. 6, 7 and 13 were used. As previously mentioned, the G_0 and σ'_p for dilatometer tests depend on σ'_{vo} with all aforementioned perched water table problems. Manipulating these three equations, it was possible to arrive at the following expression:

$$\frac{G_0}{\sigma'_p} = \frac{526.2}{(OCR)^{0.3}} \quad (22)$$

Similar to Eq. 20, there is a marked influence of σ'_{vo} but still relatively small in relation to G_0/σ'_p. The graphs in Fig. 9 show that this ratio varies from 0.10 to 0.20, with the figure of 0.15 from CPTu data in an intermediate position.

5. Conclusions

A comprehensive study of the variegated soils, with peculiar characteristics, has become necessary in view of its widespread occurrence in the central areas of the São Paulo City.

Based on in situ CPTU and DMT tests and on empirical equations taken from the literature, it was possible to arrive to some conclusions concerning stress history (σ'_p,

OCR and K_0), deformability modules (E_t, M and G_0) and undrained shear strength (s_u).

It became clear that the parameters K_0 and *OCR* from DMT data may be estimated using, respectively, the equations of Lunne *et al.* (1990) and Kamei & Iwasaki (1995). It was then possible to determine the correlation between these two parameters, resulting in $K_0 = 0.92OCR^{0.38}$. This correlation was validated with a K_0 value given by a test made with the pressuremeter (Camkometer) at the base of a stiff variegated clay layer in Ibirapuera, São Paulo.

The correlation between undrained shear strength (s_u) and preconsolidation pressure (σ'_p), obtained through the DMT data, was set using the Marchetti (1980) and Kamei & Iwasaki (1995) equations, respectively. This led to values between 0.16 and 0.20 for the ratio s_u/σ'_p, practically the same as that indicated by Massad (2012) for "taguá" from the Resende Formation. In addition, Massad (1980 and 2012) found that $s_u/\sigma'_p \cong 0.10$ for the variegated soils of São Paulo using triaxial laboratory tests. As far as the CPTu data are concerned, a ratio $s_u/\sigma'_p = 0.15$ was achieved adopting N_{kt} equal to 20 in the equation $s_u = (q_t-\sigma_{vo})/N_{kt}$, *i.e.*, the formula of the cylindrical cavity expansion. These findings were taken as a validation of the empirical factor N_{kt}.

The correlation of initial shear modulus (G_0) with preconsolidation pressure (σ'_p) from DMT data was obtained applying the Lunne *et al.* (1990) equation (for G_0) and the Kamei & Iwasaki equation (1995) (for *OCR* and then σ'_p). Although both parameters depend on σ'_{vo} with all the already mentioned perched water table problems, it was shown that the ratio G_0/σ'_p varied in a relatively narrow range, 0.10 to 0.20. On the other hand, for CPTu data, using the Watabe *et al.* equation (2004) for G_0, and the Kulhawy & Mayne equation (1990) for σ'_p, it was possible to obtain $G_0/\sigma'_p = 0.15$, an intermediate value between the former range of 0.10 to 0.20.

For the correlation between the Young's modulus (E_i) and undrained shear strength (s_u) the Kulhawy & Mayne equation (1990) (for E_i) and the formula of the cylindrical cavity expansion (for s_u), with $N_{kt} = 20$ were applied to the data of CPTu. Imposing $E/s_u = 400$, the average value obtained in laboratory by Massad (1980) and Massad *et al.* (1992), it was possible to conclude that $\alpha = 20$ in the Kulhawy & Mayne equation (1990) $E^i = \alpha(q_t - \sigma_{vo})$.

Finally, as a general conclusion, despite the extreme heterogeneity of the variegated soils, comprising alternating layers of sandy clays, and clayey sand with silt fractions, well defined correlations were obtained, consistent with results presented in the technical literature, confirming the potentiality of the piezocone and the dilatometer tests. However, future research should provide accurate measurements of the pore pressures, particularly the suction in layers of partially saturated soils, which can occur at different depths due to the occurrence of perched water tables, particularly in the upper parts of the São Paulo Formation.

Acknowledgments

The authors acknowledge the support given by the Companhia do Metropolitano de São Paulo (Metrô - SP) and by EPUSP - Escola Politécnica of University of São Paulo, where the study was carried out, within the Civil Engineering Postgraduate Program. The authors also thank James Dickson and Marlísio Cecílio Júnior.

References

Campanella, R.G.; Roberston, P.K.; Gillespie, D. & Grieg, J. (1985). Recent developments of *in situ* testings of soils. Proc. 11 th Int. Conf. Soil Mech. and Found. Engn., ISSMFE, San Francisco. v. 2, pp. 849-854.

Esquivel, E.R. & Vaz, C.M.P. (2009). Development of a new TDR probe for assessing the soil water content at different depths. Proc. 17th Int. Conf. on Soil Mech. and Geotech. Engn., Egito, v. 5, pp. 3443-3446.

Giachetti, H.L. (2015). Developing a coil TDR probe to use together with the CPT test. Universal Project CNPq Zone B, Nº 446424/2014-5.

Kamei, T. & Iwasaki, K. (1995). Evaluation of undrained shear strength of cohesive soils using a flat dilatometer. J. Soil Mech. Found. Engn., Japanese Society Soil Mechanics Foundation Engineering, 35(2):111-116.

Kulhawy, F.H. & Mayne, P.W. (1990). Manual on Estimating Soil Properties for Foundation Design. Geotechnical Engineering Group, Ithaca, 308 p.

Lacasse, S. & Lunne, T. (1988). Calibration of dilatometer correlations. Proc.1th Int. Symposium on Penetration Testing, Orlando, v. 1, pp. 539-548.

Lunne, T.; Lacasse, S. & Rad, N.S. (1989). SPT, CPT, pressuremeter testing and recent developments on *in situ* testing of soils. General Report Session. Proc. 12th Int. Conf. Soil Mech. and Found. Engn., Rio de Janeiro, pp. 2339-2404.

Lunne, T.; Powell, J.J.M.; Hauge, E.; Uglow, I.M. & Mokkelbost, K.H. (1990). Correlations of Dilatometer Readings with Lateral Stress in Clays. NGI Publ., Oslo, p. 183-193.

Marchetti, S. (1980). *In situ* tests by flat dilatometer. J. Geotech. Engineering Division, 106(GT3):299-321.

Massad, F. (1980). Characteristics and geotechnical properties of some Tertiary soils of São Paulo city. In: Geological and Geotechnical aspects of the Sedimentary Basin of São Paulo. Especial Publication from ABGE and SBG, S. Paulo, p. 53 (in portuguese).

Massad, F.; Pinto, C.S. & Nader, J.J. (1992). Strength and deformability. In: Soils of São Paulo City. ABMS/ABEF, São Paulo, p. 141-180 (in portuguese).

Massad, F. (2012) Shear strength and deformability of sedimentary soils of São Paulo. In: TwinCities - Soils of the Metropolitan Regions of São Paulo and Curitiba. ABMS/ABEF, São Paulo, 508 p. (in portuguese).

Pinto, C.S. (2000). Soil Mechanics - Basic Course. São Paulo, Oficina de Textos, 247 p. (in Portuguese).

Pinto, C.S. & Abramento, M. (1998). Characteristics of stiff and hard clay, gray-green of São Paulo determined by Camkometer. In: Proc. XI Brasilian Congresso f Soil Mechanics and Geotechnical Engineering, v. 2, p. 871-878 (in Portuguese).

Powell, J.J.M. & Uglow, I.M. (1988). Marchetti dilatometer tests in UK. Proc. 1th Int. Symp. on Penetration Testing, Orlando, v. 1, p. 555-562.

Robertson, P.K. & Campanella, R.G. (1989). Design Manual for Use of CPT and CPTu. University of British Columbia, Vancouver, 200 p.

Watabe, Y.; Tanaka, M. & Takemura, J. (2004). Evaluation of *in situ* K_0 for Ariake, Bangkok and Hai-Phong clays. Proc. 2th Int. Conf. on Site Characterization, Porto, Portugal, p. 167-175.

List of Symbols

E_i: Young's module

E_D: Dilatometer modulus (from DMT)

f_s: Sleeve friction (from CPTu)

F: Constant of Eq. 12

G_0: Initial shear module

I_D: Material index (from DMT)

K_1: Constant equal to 0.333 of Eq. 1

K_0: Earth pressure coefficients at rest

K_D: Horizontal stress index (from DMT)

M: Constrained module

N_{kt}: Empirical factor of Eq. 4

OCR: Over consolidation ratio

q_c : Measured cone tip resistances (from CPTu)

q_t: Corrected cone tip resistances (from CPTu)

u_2: Porepresure measured at the base of the cone (from CPTu)

s_u: Undrained shear strength

α: Constant of Eq. 2 or 13

σ'_p: Preconsolidation pressure

σ'_{vo}: *In situ* vertical effective stress

σ_{vo}: *In situ* total vertical stress

Technical Notes

Soils and Rocks
v. 39, n. 2

Mechanical Behavior of Basaltic Rocks from Serra Geral Formation Used as Road Material in Santa Catarina State, Brazil

A.C.R. Guimarães, L.M.G. Motta, M.L.A. Arêdes

Abstract. This work presents physical, petrographic and mechanical characteristics of basalt aggregates from Serra Geral Formation in the State of Santa Catarina, Brazil, used as layers of simple graded crushed stone in pavement. The simple graded crushed stone chosen for the study was obtained from a quarry in the municipality of São José do Cerrito/SC, located in the mountainous region of Santa Catarina. The aggregates of this quarry were used to pave a segment of highway BR-282/SC from 2002 to 2006. This study presents the results of thin section analysis, which identifies the mineralogical composition of the material and clarifies aspects associated with the rock texture. In addition, resilient modulus tests are conducted, followed by numerical evaluation of the pavement's structural behavior, field evaluation of elastic displacement with Benkelman beam testing, and comparison of the results. The entire highway segment was monitored throughout its implementation and was determined to be in good condition. The material used offers good performance as a pavement layer. Moreover, the methodology used for the design presents good correlation with the field tests.

Keywords: basaltic, Serra Geral formation, pavements, resilient modulus.

1. Introduction

The Serra Geral Formation, covering much of the southern region of Brazil and extending through parts of São Paulo, Mato Grosso do Sul and Minas Gerais states, includes the known world's largest occurrence of Earth fissure basaltic magmatism. This formation caps the Paraná sedimentary basin and is approximately 1,000 m thick in some sections. Owing to its immensity, this formation is an important element of study for Brazilian geotechnical engineers.

Accurate characterization of these basalts is important for the implementation of major geotechnical works because changes in this material can often pose engineering problems.

Characterization of the aggregate used in road paving is accomplished through physical and mechanical tests. Although not common for this purpose, thin section analysis can greatly contribute to understand the test results. The Serra Geral Formation is a source for asphalt aggregates used in layers of dry-bound macadam sub-base and simple graded crushed stone base in addition to asphalt mixtures for road paving in that region of Brazil.

Most of the Serra Geral Formation is characterized by a simple volcanic sequence represented by a wide predominance of basalt (97% in volume) and diabase dikes of approximately 133,000 years old. These rocks are dark gray to black, have very fine to medium granulation and are hypo crystalline, massive or vesicular. To a lesser extent, this formation presents a sequence of acidic rocks represented by rhyolites and rhyodacites with intermediate volcanic rocks including andesites and porphyritictrachyandesites (Schneider *et al.*, 1974). Figure 1 shows a geological map of Brazil, in which the hatched area to the south represents the basaltic lava flows of the Serra Geral Formation.

2. Petrologic Characteristics

The texture of a rock corresponds to the relationship among its components and is defined by the shape, arrangement and distribution of minerals in its composition (Bigarella *et al.*, 1985). Texture depends essentially on the relative size of mineral grains; thus, rocks formed by macrocrystals of distinct crystalline structure, such as granites, tend to disaggregate more easily under the action of the crushing process than fine-grained basalts. A good description of rock texture is linked to the degree of crystallization, the absolute size of the grains, the crystal shapes and the mutual relationship among these features. This fact highlights the importance of thin section analysis of rocks selected for crushing.

Basalt is an effusive rock of the gabbro family, the silica content of which varies from 45% to 55%. Its most common components are plagioclase, pyroxene, olivine and

Antônio Carlos Rodrigues Guimarães, DSc., Departamento de Engenharia Civil, Instituto Militar de Engenharia, Praça General Tibúrcio n° 80,Urca, Rio de Janeiro, RJ, Brazil. e-mail: cap-guimaraes@hotmail.com.
Laura Maria Goretti da Motta, DSc., Departamento de Engenharia Civil, Universidade Federal do Rio de Janeiro, Av. Horácio Macedo 2030, Block G, Sala 101, Cidade Universitária, Rio de Janeiro, RJ, Brazil. e-mail: laura@coc.ufrj.br.
Márcio Leandro Alves de Arêdes, MSc., Departamento de Engenharia Civil, Instituto Militar de Engenharia, Praça General Tibúrcio n° 80,Urca, Rio de Janeiro, RJ, Brazil. e-mail: engfcaredes@gmail.com.
Submitted on April 18, 2015; Final Acceptance on June , 2016; Discussion open until December 30, 2016.

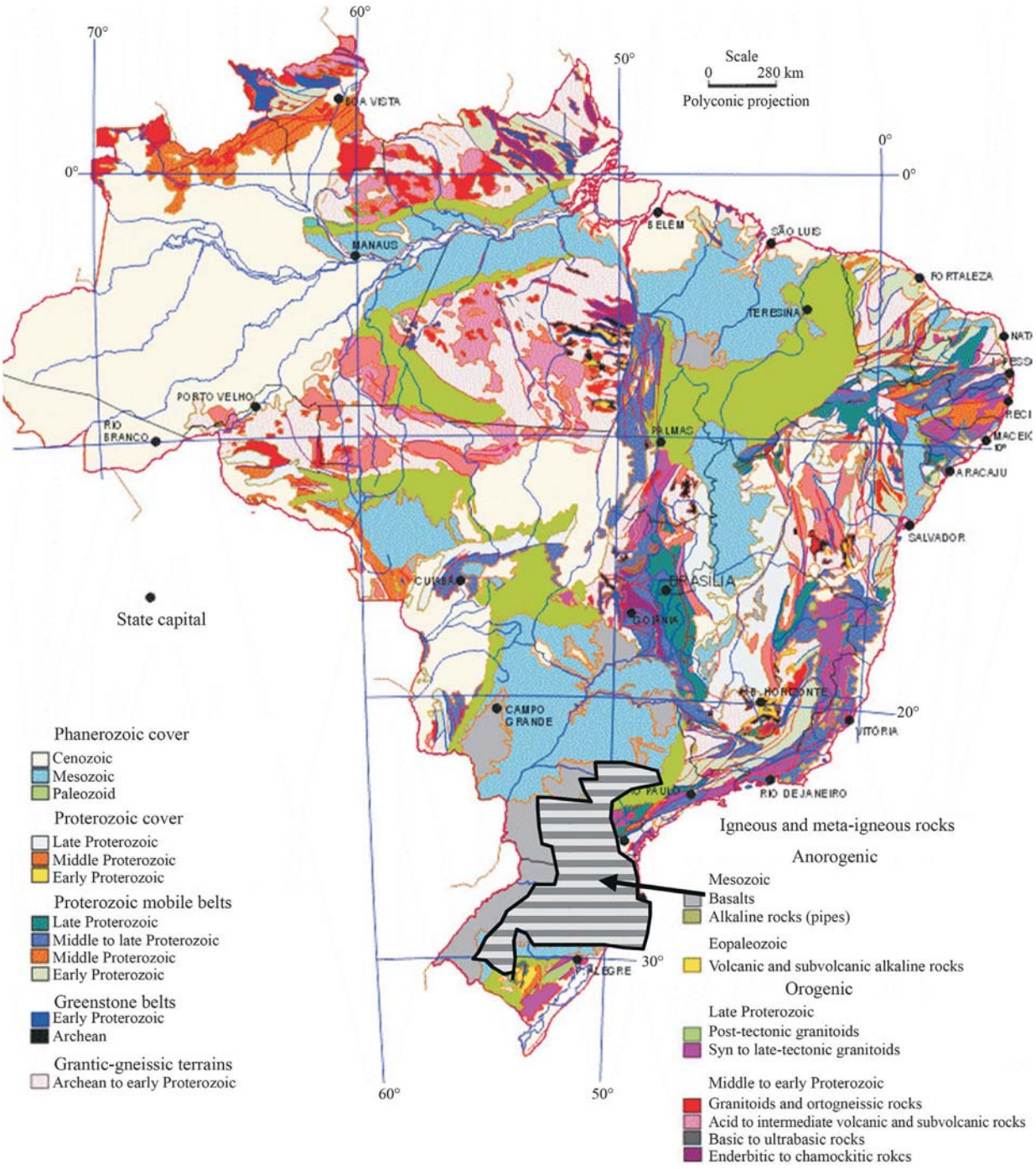

Figure 1 - Geological map of Brazil obtained by Mineral Resources Research Company (CPRM, 2015).

magnetite. It is a melanocratic rock that is dark, dense, finely granulated and holocrystalline or hypocrystalline.

A set of samples was collected from the Brazilian Army's quarry located at road mark km 254 of the BR-282/SC in the county of São José do Cerrito/SC. Thin section slides were created for the petrographic analyses presented herein. The rock is classified as basalt; complete petrographic analysis was reported by (Guimarães, 2007).

From a macroscopic perspective, this is a gray fine-grained rock of massive structure. From a microscopic perspective, this material has a subophitic holocrystalline texture with euhedralcrystals of pyroxene in an intergranular array composed of parallel and subparallel laths of labradorite and interstitial granules of pyroxene and opaque minerals.

Its essential mineral is labradorite plagioclase occurring in parallel and subparallel well-developed laths reach-

ing 0.7 mm. These crystals are sometimes zoned, and most are twinned according to the albite law. Figures 2, 3, 4, and 5 show photomicrographs of thin section analysis including images without polarized light (NL) and with polarized light (PL).

An additional set of samples was collected in a slope along the highway BR-282/SC section between Lages/SC and São José do Cerrito/SC, approximately 8 km from the aforementioned quarry. These samples have a more greenish color than the previously described samples and were subsequently classified as diabase, originating very likely from an intrusion in a basaltic rock pre-existing in place. The presence of diabase dikes is quite common in alkaline rocks of the Serra Geral Formation in the Paraná sedimentary basin.

From the macroscopic perspective, this rock is greenish gray colorless with massive structure and fine to medium granulation. From the microscopic perspective, it presents an intergranular holocrystalline texture in which heuhedral crystals of pyroxene occur in an intergranular array composed of parallel and subparallel laths and granules of labradorite and interstitial euhedral opaque crystals of pyroxene. In addition, many minerals of interstitial alteration are present as products of saussuritization of the interstitial plagioclase and uralitization of pyroxene with masses of interstitial micropegmatite.

Its essential minerals are labradorite plagioclase occurring in parallel and subparallel well-developed laths reaching 0.7 mm. These crystals are sometimes zoned, and most are twinned according to the albite law. Some, however, are completely changed through saussuritization into a yellowish green mass with chlorite and calcite occupying interstitial spaces. Pyroxene, augite and pigeonite occur in

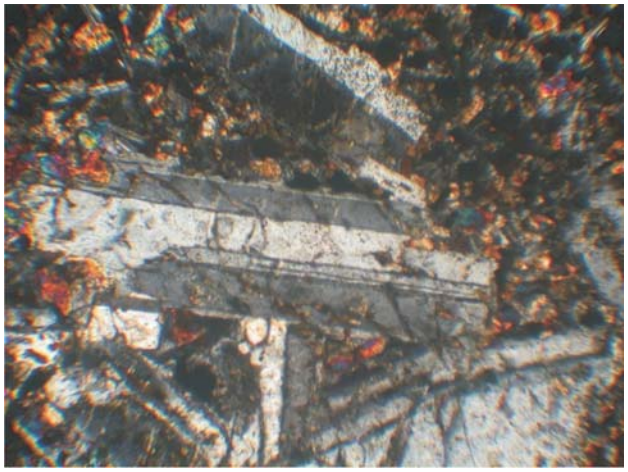

Figure 2 - Photomicrograph showing subophitic texture of basalt sample Pyroxene crystals occur in an array with labradorite plagioclase in form of parallel laths. The polarized light (PL) field width is 1.5 mm.

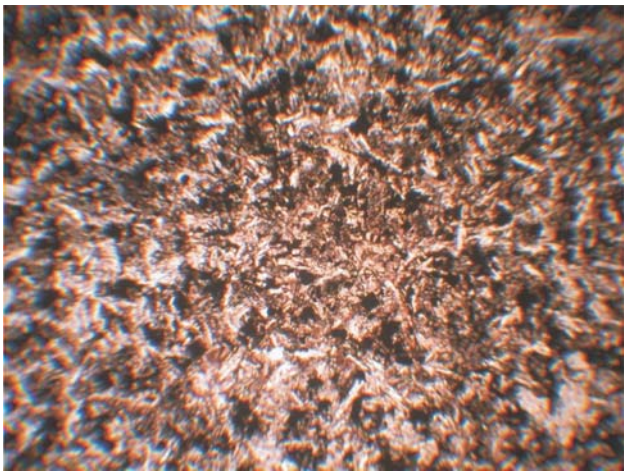

Figure 4 - Photomicrograph showing the subophitic texture of the basalt sample. Labradorite plagioclase crystals occur in laths; pyroxene occurs in grains between the plagioclase (with interference colors blue and yellow) and many euhedralopaques. The polarized light (PL) field width is 0.6 mm.

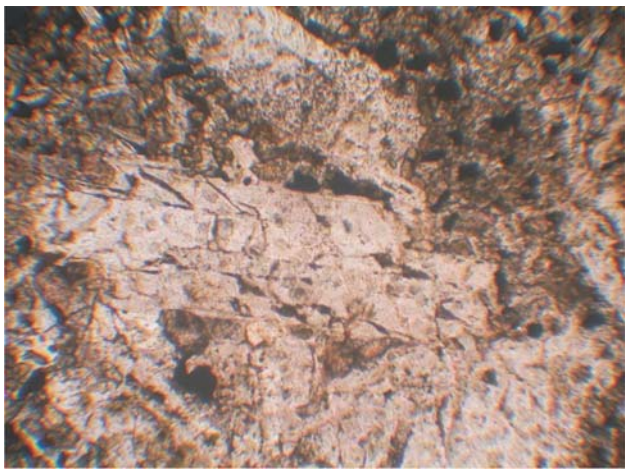

Figure 3 - Same rock section undernonpolarized light (NL) with afield width of 1.5 mm.

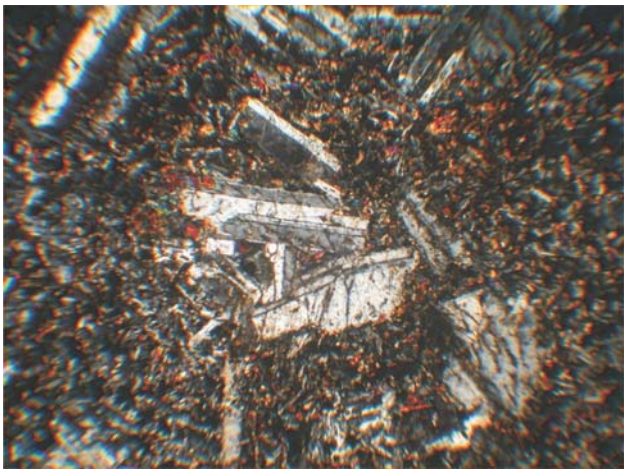

Figure 5 - Same rock section in which opaques appear in nonpolarized light (NL). The field width is 1.5 mm.

anhedral and euhedralgranular crystals occupying the gaps between plagioclase laths.

The opaque and sparse accessory minerals included in the mafics and between plagioclase laths are possibly ilmenite and magnetite. The secondary minerals form masses of micropegmatite with an intergrowth of vermicular quartz commonly found at the borders of plagioclase. Some deuteric calcite occurs as a secondary product of plagioclase. The products of uralitization and saussuritization include chlorophaite. The percentage of pyroxene is low. Figures 6 and 7 show photomicrographs of this material.

3. Materials

Graded crushed basalt samples selected for study of their mechanical behavior were collected from the quarry of the 10th Construction Engineering Battalion of the Brazilian Army, in São José do Cerrito/SC. This material was used to pave a segment of highway BR-282/SC.

3.1. Subgrade

The materials constituting the subgrade of the road, or the final layer of earthmoving, originated from slopes of excavation along the road and are composed of residual soils of basalts with high levels of change. The alteration is predominantly clay and is expansive in some cases. Table 1 presents some geotechnical characteristics of these materials; compaction energy equivalent to the standard proctor test was used for analysis.

Guimarães *et al.* (2004) showed that the subgrade soils of this highway present a low resilient modulus and have a significant negative influence on the fatigue life of the asphalt coating. This fact emphasizes the importance of using high-quality materials in the base and sub-base layers of pavement.

3.2. Dry-bound Macadam sub-base

Dry-bound macadam is a paving technique widely used in the southern region of Brazil and is usually associated with a subsequent layer of graded crushed stone. State road agencies such as the Highway Department of Rio Grande do Sul (DAER) and the Infrastructure Department of Santa Catarina (DER; currently DEINFRA) have established proper technical specifications for this service, such as DAER ESP 07/91 and DEINFRA-SC-ES-P-03/15. Coarse aggregate is limited from 2 inches to 4 inches, and the filling material particle size must be below 3/8 inch.

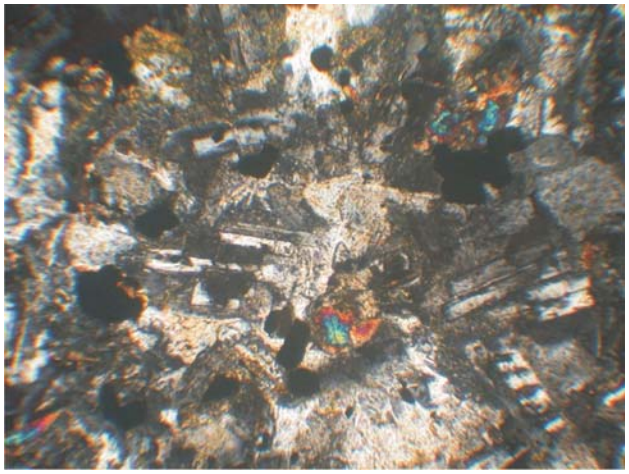

Figure 6 - Photomicrograph showing the intergranular holocrystalline texture of diabase. Labradorite plagioclase crystals occur in laths; pyroxene twinning (taking half of the field) occurs in a few granules among the plagioclase. The polarized light (PL) field width is 1.5 mm.

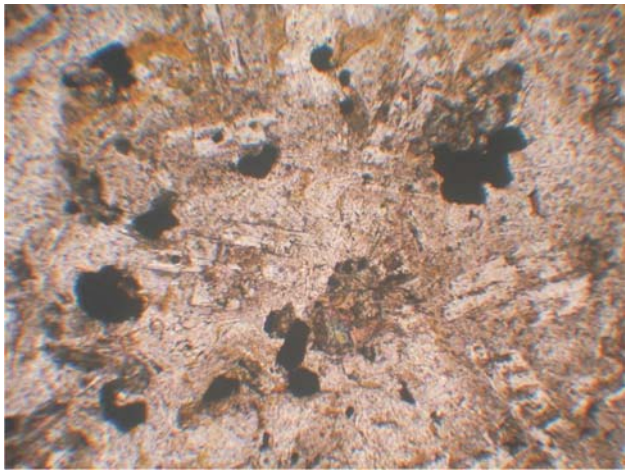

Figure 7 - Same rock section in which opaque appear in non-polarized light (NL). The field width is 1.5 mm.

Table 1 - Geotechnical characteristics of subgrade soil of Highway BR-282/SC.

Material	I_p (%)	w_{opt} (%)	CBR (%)	Exp%	TRB-ASSHTO soil classification
Deposit 1	23.0	41.2	6.2	0.1	A-7-5
Deposit 2	20.2	45.4	5.5	5.73	A-7-5
Deposit 3	14.1	36.3	9.7	0.6	A-7-5
Gravel pit 1	NP	26.6	18.9	0.14	A-4
Gravel pit 2	12.1	28.5	24.8	0.1	A-4
Gravel pit 3	NP	25.2	14.6	0.31	A-4

3.3. Simple graded crushed stone base

The crushed stone produced in the quarry of São José do Cerrito/SC is classified as grade A according to the National Department of Transport Infrastructure (DNIT) standard, as shown in Fig. 8.

4. Methodology

In addition to the microscopic characterization of the material through petrographic thin section slides, resilient modulus tests were conducted, followed by numerical evaluation of the pavement's structural behavior, field evaluation of its elastic displacement with Benkelman beam testing, and comparison of the results.

Preparation of aggregates and soils was carried out at the geothecnical laboratory of the Federal University of Rio de Janeiro (COPPE/UFRJ).

The study of highway BR-282/SC pavement included soils previously dried in an oven at 80 °C. In the case of fine soils, the clods were broken; in the case of soils with boulders, the clods were not broken. The hygroscopic moisture content was determined, and the samples were sealed in plastic bags.

The samples were then separated into samples of approximately 4 kg and were homogenized by adding water to achieve the optimum water content previously calculated. Each sample was then packaged in a plastic bag. The bags were then tightly closed and kept in a moist chamber for at least 12 h before the resilient modulus test was conducted.

On the day of the resilient modulus test, each sample was removed from the moist chamber and immediately subjected to mechanical compression in a tripartite cylinder 10 cm in diameter and 20 cm in height with compactation energy equivalent to the standard Proctor test for subgrade soil or modified Proctor test for crushed stone base.

The resilient modulus tests were conducted according to the COPPE/UFRJ method, as reported by Motta and Medina (2005). The instrumentation details of this method were reported by Guimarães *et al.* (2004).

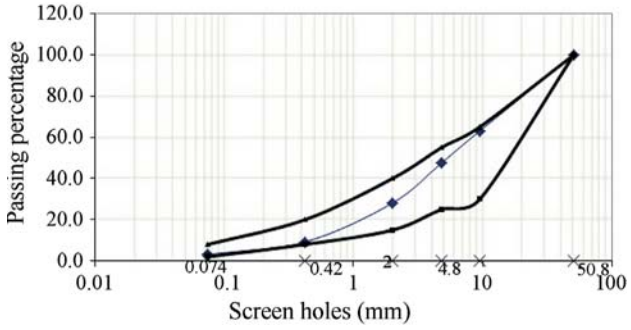

Figure 8 - National Department of Transport Infrastructure (DNIT) grain size distribution grade A for graded crushed stone produced in the quarry of the 10th Construction Engineering Battalion of the Brazilian Army. This material was used to pave Highway BR-282/SC.

5. Results - The Case for BR-282/SC

The pavement structure implemented along the segment of highway BR-282/SC analyzed in this study is presented in Fig. 9. Its resilient characteristics as presented below were employed for the achievement of structural responses of the pavement under loads.

5.1. Asphalt mix

The asphalt coating is composed of hot mix asphalt classified as grade C of the DNIT standard for implementation of well graded stabilized bases with a bitumen content of 6.3% (CAP 50/70). The value for the resilient modulus was 5,495 MPa and the tensile strength determined through split (Brazilian) test was 1.15 MPa. Figure 10 shows the fatigue behavior of such hot mix asphalt obtained through dynamic-repeated split tests over cylindrical samples.

It was determined that the values K1 and N for expression of the fatigue life of the coating are higher than

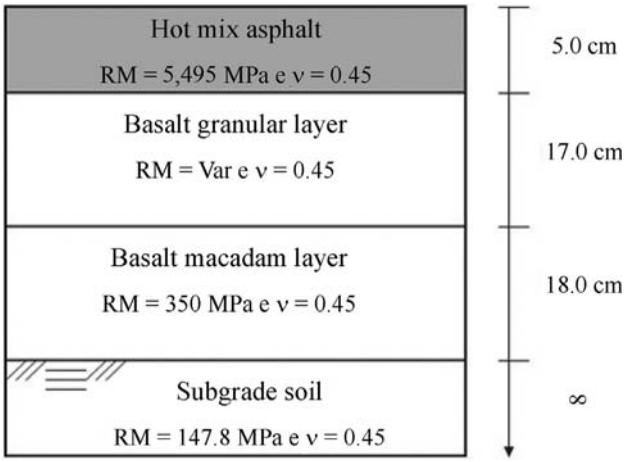

Figure 9 - Profile of the pavement segment of Highway BR-282/SC analyzed in this study.

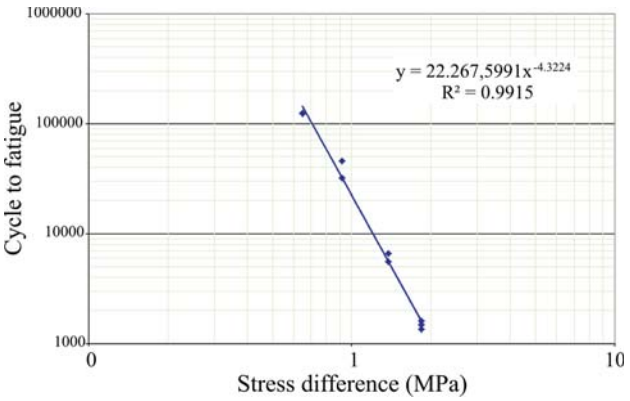

Figure 10 - Fatigue life of the asphalt mix used in the coating of Highway BR-282/SC.

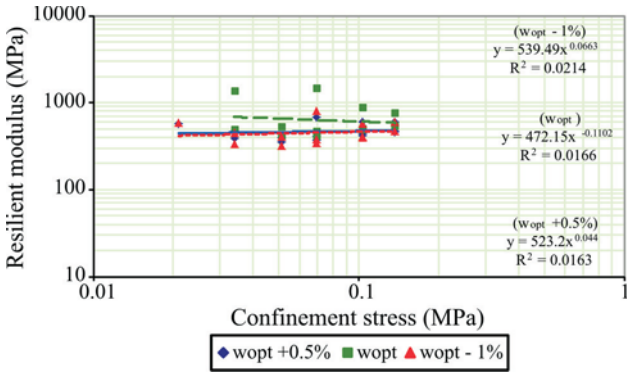

Figure 11 - Variation of the resilient modulus of graded crushed stone from BR-282/SC for moisture content. The tests were conducted with a cylinder 10 cm in diameter and 20 cm in height with energy equivalent to the modified Proctor test.

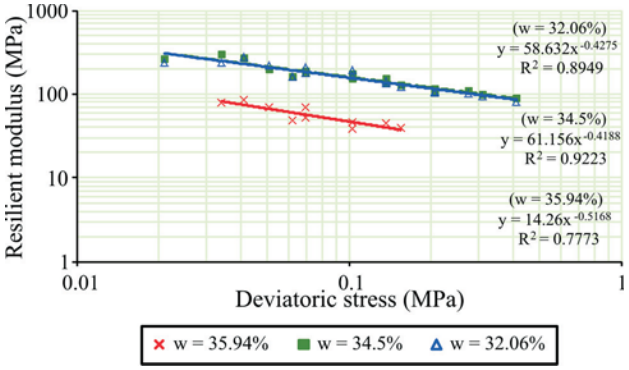

Figure 12 - Resilient modulus variation in moisture content for the subgrade of Highway BR-282/SC.

those presented by Motta and Pinto (1995) (K1 = 4,200 and N = 3.47) similar to asphalts mixtures, indicating that this material is of satisfactory quality.

5.2. Graded crushed basalt base

The resilient modulus tests with the graded crushed stone from BR-282/SC were performed with three different levels of compression moisture, as shown in Fig. 11. Good classification in the linear model was not obtained, as indicated by the R^2 value very close to zero in all cases. This fact indicates that the value of the resilient modulus can be considered approximately as constant in this case.

By adopting the model compound, as shown in Fig. 11, the equation in this case is obtained as follows:

$$MR = 155.8\sigma_3^{0.32} \cdot \sigma_d^{-1.13} \quad (1)$$

where MR: resilient modulus; σ_3 : confinement stress; and σ_d: deviatoric (axial) stress.

5.3. Dry-bound Macadam sub-base

In the case of the dry macadam sub-base, determination of the resilient modulus was not possible from conventional laboratory tests. Therefore, in this study, the modulus was obtained from backcalculation of deflection basins obtained on the dry bound macadam layer in the field. In this case, an approximate value of 200 MPa was adopted.

5.4. Subgrade soil

The material forming the subgrade of Highway BR-282/SC proved to be highly variable, as shown in Table 1. The values of the resilient modulus of soil from deposit 3 are shown in Fig. 12, considering three distinct cases of moisture content. In this deposit, the resilient modulus values for compaction moisture above the optimal levels were slightly lower than those in other soils. In addition, the proposed model shows good classification.

5.5. Field tests

During the implementation phase of each pavement layer, Benkelman beam deflection tests were conducted to evaluate the elastic deformability level of the layers. In addition, the homogeneity level of the surface was evaluated. Surveys were conducted for the coating layer in two phases. The first was performed immediately after the implementation of the coating, and the second was conducted after several months of road operation. For the survey immediately following implementation of the asphaltic mix, referred to as coating 1, the average values obtained were 45.7 x 10^{-2} mm at the surface central line and 58.6 x 10^{-2} mm at the right edge. The surface after four months of road operation, referred to as coating 2, had average deflection values of 37.3 x 10^{-2} mm at the surface central line and 40.8 x 10^{-2} mm at the right edge. Figure 13 shows the deflection values of the asphalt layer in the first phase. The results show significant dispersion, which was reduced in the second field measurement.

Figure 14 shows average deflection values for each layer of the pavement, considering the edges and the axle. It was noted that the deflection values significantly decreased with the implementation of subsequent layers.

Numerical simulation of the structural behavior was performed by using version 2 of Finite Element Analysis of Pavement Structures (FEPAVE2) software.

The total pavement deflection calculated by the software was 32 x 10^{-2} mm, whereas the average field values after four months of operation remained between 37.3 and 40.8 x 10^{-2} mm; there is therefore good correlation.

6. Conclusions

The soils of the subgrade of the road in which pavement has been studied were obtained from excavation slopes located along the road. These predominantly clay soils are residual soils of basalt showing a high degree of change and 5.7% expansion. Determined by compression of the testing materials, the resilient modulus of the subgrade proved to be significantly influenced by the moisture con-

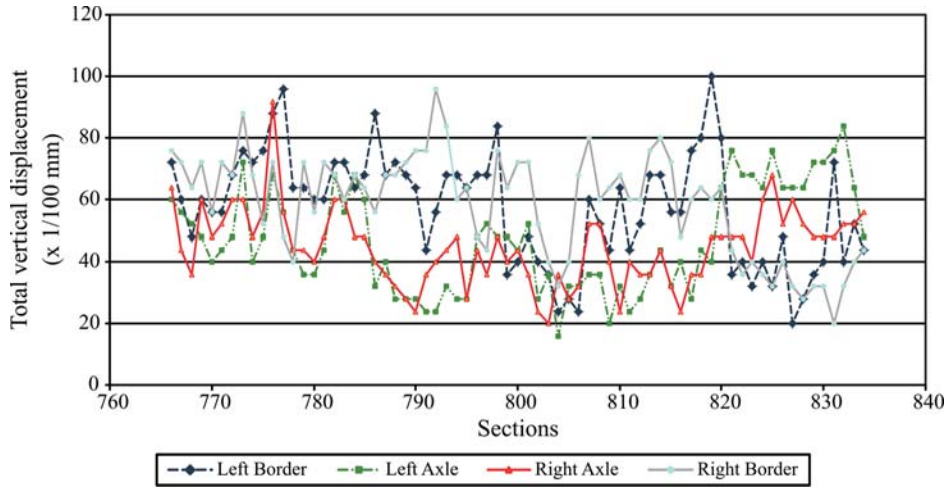

Figure 13 - Deflection survey of the asphalt layer immediately after its implementation: stakes 760 to 840.

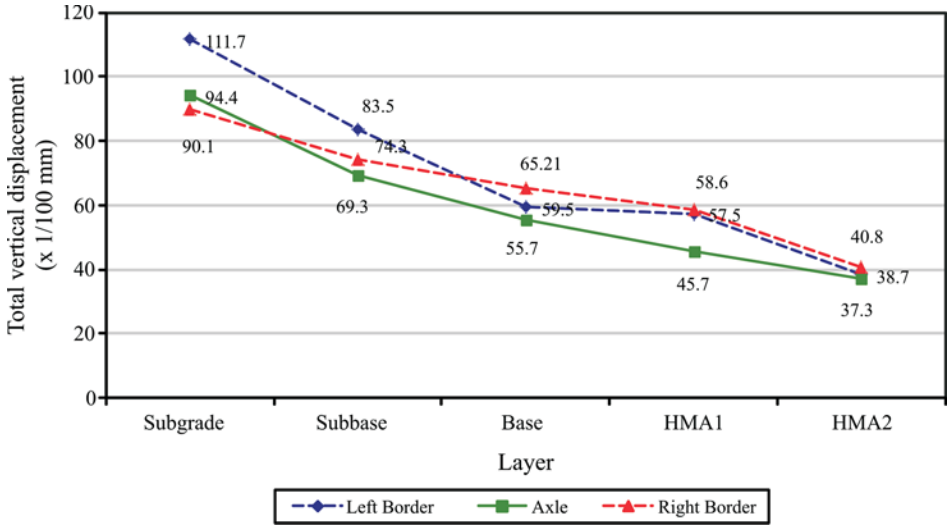

Figure 14 - Variation of average deflection per pavement layer.

tent. Very low values are related to higher humidity, although these values were within the limit of two percentage points acceptable by DNIT standards.

The simple graded crushed stone used as pavement base layer was classified as DNIT granulometric grade A, material granulometrically stabilized, and presented resilient modulus values almost constant and over 300 MPa. This result is considered very good for this type of paving material.

The sub-base resilient modulus result, obtained by backcalculation from deflection basins, using the Benkelman beam, was 200 MPa, indicating a dry-bound macadam layer with good bracing.

The deflection tests conducted with the Benkelman beam showed high levels of dispersion; however, the average values indicated a downward trend. In the case of road axle, the following levels were measured: subgrade, 94.4; sub-base, 69.3; base, 55.7; asphalt coating at first measure, 45.7; and asphalt coating at second measure, 37.3. This final value of final deflection measurement in the axle proved to be compatible with that obtained through numerical simulation of structural behavior, 32.0.

In general, it can be stated that the basalt aggregate from Serra Geral Formation, used in this analysis, presented satisfactory characteristics for use in paving and that the pavement presented very good structural behavior.

Acknowledgments

The first author, as a military engineer of the 10th Construction Engineering Battalion of the Brazilian Army, provided most of the data in this work through experience in road construction works in the State of Santa Catarina.

References

Bigarella, J.J.; Leprevost, A.E. & Bolsanello, A. (1985). Brazilian Rocks Rio de Janeiro. LTC - Livros Técnicos e Científicos, São Paulo, p. 77.

DAER - ESP 07/91 (1997). General Specifications. Dry Bound Macadam - ESP 07/91, Autonomous Department of Highways, Rio Grande do Sul, Brazil, p. 67-74.

DEINFRA-SC-ES-P-03/15 (2015) - General Specifications. Dry Macadam Layer, State Department of Infrastructure Santa Catarina, Santa Catarina, Brazil, 6 p.

Guimarães, A.C.R. (2007). A Comparative Study Between the Mineralogical Composition and the Deformability Parameters of Tropical Soils Forming Pavements. Monograph presented in the course of specialization in Quaternary and Environmental Geology. National Museum of UFRJ, Department of Geology and Paleontology. Rio de Janeiro, April, 2007.

Guimarães, A.C.R.; Motta L.M.G. & Vieira, A. (2004). Study of the Influence of the Subgrade on the Structural Behavior of Santa Catarina Mountain Range's Pavement. Records of the 35th Annual Paving Meeting of ABPv, Rio de Janeiro, October, 2004.

Motta, L.M.G. & Medina, J. (2005). Mecânica de Pavimentos. 2nd ed. Editora UFRJ, Rio de Janeiro, p. 193-212.

Pinto, S. & Motta, L.M.G. (1995). Catalog fatigue curves. Brazilian Association of paving. Technical Bulletin No. 16.

Schneider, R.L.; Mühlmann, H.; Tommasi, E.; Medeiros, R.A.; Daemon, R.F. & Nogueira, A.A. (1974). Stratigraphic review of the Paraná Basin. In: Proc. 28 International Congress of Geology, Porto Alegre, v. 1, p. 41-65.

Companhia de Pesquisa de Recursos Minerais - Serviço Geológico do Brasil (CPRM) available at http://geobank.cprm.gov.br/pls/publico/geobank.download.download layouts?p_webmap=N, downloaded on July 6, 2015.

SOILS and ROCKS
An International Journal of Geotechnical and Geoenvironmental Engineering

Publication of
ABMS - Brazilian Association for Soil Mechanics and Geotechnical Engineering
SPG - Portuguese Geotechnical Society
Volume 39, N. 2, May-August 2016

Author index

1. TECCO® SYSTEM³ teste em escala real, Suíça, outubro 2012
2. TECCO® SYSTEM³ instalação, B462, Alemanha
3. Ângulo máximo de inclinação de 85° durante o teste de campo

TECCO® SYSTEM³ – Seu talude estabilizado

... validado por teste em escala real com inclinação do talude de até 85°.

A malha de aço de alta resistência TECCO®, as placas de ancoragem e garras de conexão TECCO®, juntas, estabilizaram com sucesso 230 toneladas de cascalho com 85° de inclinação em um ensaio em escala real.

- moldura de teste com dimensões 10 x 12 x 1.2m
- espaçamento dos grapmos 2.5m x 2.5m, utilizando Gewi 28mm

Para um estudo preliminar de solução de estabilização ou de riscos de desastres naturais nas obras em que você atua, entre em contato conosco através do e-mail info@geobrugg.com

Assista ou escaneie nosso filme com instalação TECCO® em www.geobrugg.com/slopes

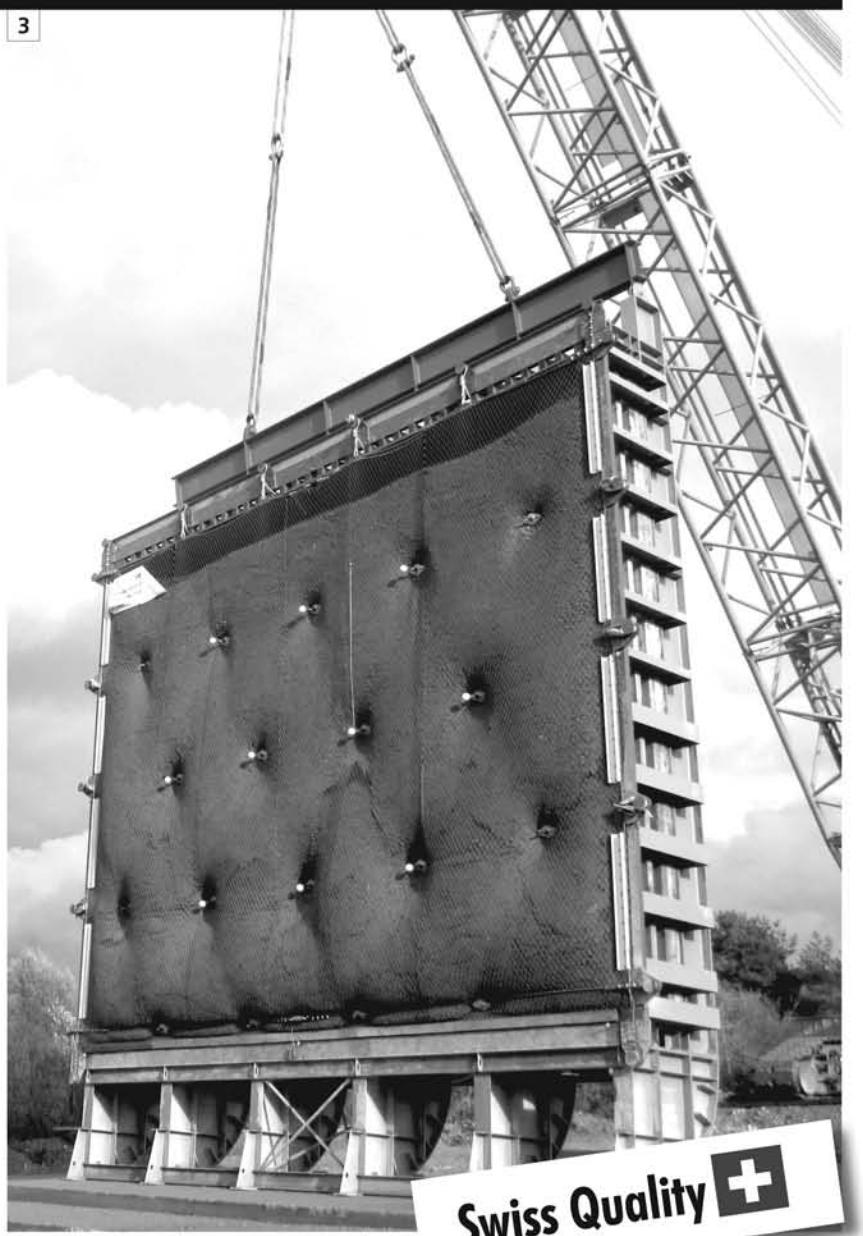

GEOBRUGG®
BRUGG

Geobrugg AG, Geohazard Solutions
Rua Visconde de Pirajá, 82 sl.606
Ipanema - Rio de Janeiro • 22410-003
Fone: +55 21 3624.1449
Cel: +55 21 99979.1288
www.geobrugg.com

SPECIALISTS IN GEOTECHNICAL IN-SITU TESTS AND INSTRUMENTATION

GEOTECHNICAL SERVICES (onshore and offshore)

- **IN-SITU TESTS**
  - Seismic CPT
  - Cone Penetration Testing Undrained-CPTu (cordless system)
  - Vane Shear Testing (electrical apparatus)
  - Pressuremeter Testing (Menard)
  - Flat Dilatometer Test-DMT (Machetti)
  - Standard Penetration Test-SPT-T
- **INSTRUMENTATION**
  - Instrumentation, installation and direct import
  - Routine Monitoring
  - Operation and Maintenance
  - Engineering analyses
  - Consultancy, design & geotechnical engineering services
- **SAMPLING**
  - Soil sampling and monitoring
  - Groundwater sampling and monitoring
  - Field and laboratory testing
- **ENVIRONMENTAL**
  - Environmental Services
  - Soil and groundwater sampling and monitoring
  - Field and laboratory testing

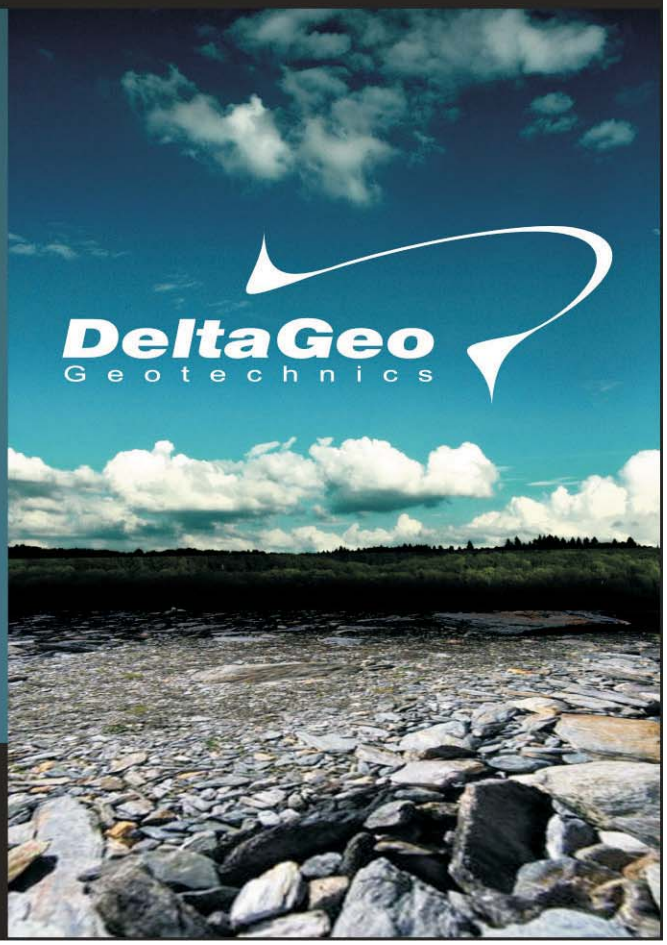

0800 979 3436
São Paulo: +55 11 8133 6030
Minas Gerais: +55 31 8563 2520 / 8619 6469
www.deltageo.com.br deltageo@deltageo.com.br

A strong, lasting connection.

With a history of over 150 years of pioneering in geosynthetics, we strive to create solutions for the most diverse engineering challenges.

Our business areas:

Earthworks and Foundations

Environmental Engineering

Roads and Pavements

Hydraulic Engineering

Talk to HUESKER Brasil:
www.HUESKER.com.br
HUESKER@HUESKER.com.br
+55 (12) 3903 9300

Follow HUESKER Brasil in social media:

HUESKER
Ideen. Ingenieure. Innovationen.

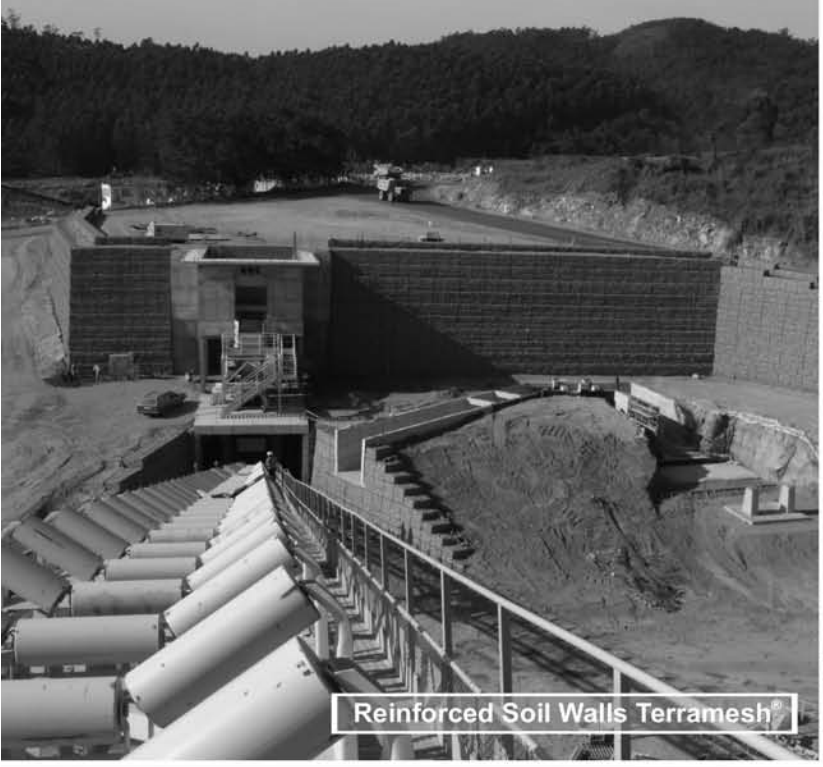

GREAT **GEOTECHNICAL WORKS** REQUIRES **GREAT SOLUTIONS**

BRASIL
Phone: 55 (11) 4525-5000
Fax: 55 (11) 4599-4275
info@br.maccaferri.com
www.maccaferri.com/br

PORTUGAL
Phone: (351) 218 968 282
Fax: (351) 218 968 078
info@es.maccaferri.com
www.maccaferri.com/es

MACCAFERRI

Engineering a better solution

TEIXEIRA DUARTE
ENGENHARIA E CONSTRUÇÕES, S.A.

- Head Office
  Lagoas Park – Edifício 2
  2740-265 Porto Salvo - Portugal
  Tel.:(+351) 217 912 300
  Fax: (+351) 217 941 120/21/26

- Algeria
  Parc Miremont – Rua A, Nº136 - Bouzareah
  16000 Alger
  Tel.:(+213) 219 362 83
  Fax: (+213) 219 365 66

- Spain
  Avenida Alberto Alcocer, nº24 – 7º C
  28036 Madrid
  Tel.:(+34) 915 550 903
  Fax: (+34) 915 972 834

- Angola
  Alameda Manuel Van Dunen 316/320 - A
  Caixa Postal 2857 - Luanda
  Tel.:(+34) 915 550 903
  Fax: (+34) 915 972 834

- Brazil
  Rua Iguatemi, nº488 – 14º - Conj. 1401
  CEP 01451 - 010 - Itaim Bibi - São Paulo
  Tel.: (+55) 112 144 5700
  Fax: (+55) 112 144 5704

- Mozambique
  Avenida Julyus Nyerere, 130 – R/C
  Maputo
  Tel.:(+258) 214 914 01
  Fax: (+258) 214 914 00

www.teixeiraduarte.pt

www.tpfplanege.pt www.cenor.pt

PLANEGE CENOR

GEOLOGY - GEOTECHNICS - SUPERVISION OF GEOTECHNICAL WORKS

EMBANKMENT DAMS - UNDERGROUND WORKS - RETAINING STRUCTURES

SPECIAL FOUNDATIONS - SOIL IMPROVEMENT - GEOMATERIALS

TPF PLANEGE CENOR

PORTUGAL | ANGOLA | ALGERIA | UNITED ARAB EMIRATES
MACAO | MOZAMBIQUE | ROMENIA | EAST TIMOR | TURKEY

Rua das Vigias, 2 . Piso 1 | Parque das Nações | 1990-506 LISBOA . PORTUGAL
T. +351.218 437 300 | F. +351.218 437 301 | E. cenor@cenor.pt

> Prospecção Geotécnica
Site Investigation
> Consultoria Geotécnica
Geotechnical Consultancy
> Obras Geotécnicas
Ground Treatment-Construction Services
> Controlo e Observação
Field Instrumentation Services and Monitoring Services
> Laboratório de Mecânica de Solos
Soil and Rock Mechanics Laboratory

Certificada ISO 9001 por

Geocontrole

Parque Oriente, Bloco 4, EN10
2699-501 Bobadela LRS
Tel. 21 995 80 00
Fax. 21 995 80 01
e.mail: mail@geocontrole.pt
www.geocontrole.pt

Geocontrole
Geotecnia e Estruturas de Fundação SA

ENGINEERING AND ENVIRONMENTAL CONSULTANTS


COBA


GEOLOGY AND GEOTECHNICS

Hydrogeology • Engineering Geology • Rock Mechanics • Soil Mechanics • Foundations and Retaining Structures • Underground Works • Embankments and Slope Stability Environmental Geotechnics • Geotechnical Mapping

Water Resources Planning and Management
Hydraulic Undertakings
Electrical Power Generation and Transmission
Water Supply Systems and Pluvial and Wastewater Systems
Agriculture and Rural Development
Road, Railway and Airway Infrastructures
Environment
Geotechnical Structures
Cartography and Cadastre
Safety Control and Work Rehabilitation
Project Management and Construction Supervision

PORTUGAL
CENTER AND SOUTH REGION
Av. 5 de Outubro, 323
1649-011 LISBOA
Tel.: (351) 210125000, (351) 217925000
Fax: (351) 217970348
E-mail: coba@coba.pt
www.coba.pt

Av. Marquês de Tomar, 9, 6º.
1050-152 LISBOA
Tel.:(351) 217925000
Fax:(351) 213537492

NORTH REGION
Rua Mouzinho de Albuquerque, 744, 1º.
4450-203 MATOSINHOS
Tel:(351) 229380421
Fax:(351) 229373648
E-mail: engico@engico.pt

ANGOLA
Praceta Farinha Leitão, edifício nº 27, 27-A - 2º Dto
Bairro do Maculusso, LUANDA
Tel./Fax: (244) 222338 513
Cell: (244) 923317541
E-mail: coba-angola@netcabo.co.ao

MOZAMBIQUE
Pestana Rovuma Hotel. Centro de Escritórios.
Rua da Sé nº114. Piso 3, MAPUTO
Tel./Fax: (258) 21 328 813
Cell:(258) 82 409 9605
E-mail: coba.mz@tdm.co.mz

ALGERIA
09, Rue des Frères Hocine
El Biar - 16606, ARGEL
Tel.: (213) 21 922802
Fax: (213) 21 922802
E-mail: coba.alger@gmail.com

BRAZIL
Rio de Janeiro
COBA Ltd. - Rua Bela 1128
São Cristóvão
20930-380 Rio de Janeiro RJ
Tel.: (55 21) 351 50 101
Fax: (55 21) 258 01 026

Fortaleza
Av. Senador Virgílio Távora 1701, Sala 403
Aldeota - Fortaleza CEP 60170 - 251
Tel.: (55 85) 3261 17 38
Fax: (55 85) 3261 50 83
E-mail: coba@esc-te.com.br

UNITED ARAB EMIRATES
Corniche Road – Corniche Tower - 5th Floor - 5B
P. O. Box 38360 ABU DHABI
Tel.: (971) 2 627 0088
Fax: (971) 2 627 0087

Instructions for Submission of Manuscripts

Category of the Papers

Soils and Rocks is the international scientific journal edited by the Brazilian Association for Soil Mechanics and Geotechnical Engineering (ABMS) and the Portuguese Geotechnical Society (SPG). The aim of the journal is to publish (in English) original research and technical works on all geotechnical branches.

According to its content the accepted paper is classified in one of the following categories: Article paper, Technical Note, Case Study or Discussion. An article paper is an extensive and conclusive dissertation about a geotechnical topic. A paper is considered as a technical note if it gives a short description of ongoing studies, comprising partial results and/or particular aspects of the investigation. A case study is a report of unusual problems found during the design, construction or the performance of geotechnical projects. A case study is also considered as the report of an unusual solution given to an ordinary problem. The discussions about published papers, case studies and technical notes are made in the Discussions Section.

When submitting a manuscript for review, the authors should indicate the category of the manuscript, and is also understood that they:

a) assume full responsibility for the contents and accuracy of the information in the paper;

b) assure that the paper has not been previously published, and is not being submitted to any other periodical for publication.

Manuscript Instructions

Manuscripts must be written in English. The text is to be typed in a word processor (preferably MS Word), **single column**, using ISO A4 page size, left, right, top, and bottom margins of 25 mm, Times New Roman 12 font, and line spacing of 1.5. All lines and pages should be numbered. The text should be written in the third person.

The first page of the manuscript must include the title of the paper followed by the names of the authors with the abbreviation of the most relevant academic title. The affiliation, address and e-mail must appear below each author´s name. An abstract of 200 words follows after the author´s names. A list with up to six keywords at the end of the abstract is required.

Although variations on the sequence and title of each section are possible, it is suggested that the text contains the following sections: Introduction, Material and Methods, Results, Discussions, Conclusions, Acknowledgements, References and List of Symbols. A brief description of each section is given next.

Introduction: This section should indicate the state of the art of the problem under evaluation, a description of the problem and the methods undertaken. The objective of the work should be clearly presented at the end of the section.

Materials and Methods: This section should include all information needed to the reproduction of the presented work by other researchers.

Results: In this section the data of the investigation should be presented in a clear and concise way. Figures and tables should not repeat the same information.

Discussion: The analyses of the results should be described in this section.

Conclusions: The content of this section should be based on the data and on the discussions presented.

Acknowledgenments: If necessary, concise acknowledgements should be presented in this section.

References: References to other published sources must be made in the text by the last name(s) of the author(s), followed by the year of publication, similarly to one of the two possibilities below:

…while Silva and Pereira (1987) observed that resistance depended on soil density… or *It was observed that resistance depended on soil density (Silva and Pereira, 1987).*

In the case of three or more authors, the reduced format must be used, *e.g.*: Silva *et al.* (1982) or (Silva *et al.*, 1982). Two or more citations belonging to the same author(s) and published in the same year are to be distinguished with small letters, *e.g.*: (Silva, 1975a, b, c.). Standards must be cited in the text by the initials of the entity and the year of publication, *e.g.*: ABNT (1996), ASTM (2003).

Full references shall be listed alphabetically at the end of the text by the first author´s last name. Several references belonging to the same author shall be cited chronologically. Some examples are listed next:

Papers: Bishop, A.W. & Blight, G.E. (1963). Some aspects of effective stress in saturated and unsaturated soils. Geotechnique, 13(2):177-197.

Books: Lambe, T.W & Whitman, R.V. (1979). Soil Mechanics, SI Version. John Wiley & Sons, New York, 553 p.

Book with editors: Sharma, H.D.; Dukes, M.T. & Olsen, D.M. (1990). Field measurements of dynamic moduli and Poisson's ratios of refuse and underlying soils at a landfill site. Landva, A. & Knowles, G.D. (eds), Geotechnics of Waste Fills - Theory and Practice, American Society for Testing and Materials - STP 1070, Philadelphia, pp. 57-70.

Proceedings (printed matter or CD-ROM): Jamiolkowski, M.; Ladd, C.C.; Germaine, J.T. & Lancellotta, R. (1985). New developments in field and laboratory testing of soils. Proc. 11th Int. Conf. on Soil Mech. and Found. Engn., ISSMFE, San Francisco, v. 1, pp. 57-153. (specify if CD ROM).

Thesis and dissertations: Lee, K.L. (1965). Triaxial Compressive Strength of Saturated Sands Under Seismic Loading Conditions. PhD Dissertation, Department of Civil Engineering, University of California, Berkeley, 521 p.

Standards: ASTM (2003). Standard Test Method for Particle Size Analysis of Soils - D 422-63. ASTM International, West Conshohocken, Pennsylvania, USA, 8 p.

Internet references: Soils and Rocks available at http://www.abms.com.br and downloaded on August 6th 2003.

On line first publications must also bring the digital object identifier (DOI) at the end.

Figures shall be either computer generated or drawn with India ink on tracing paper. Computer generated figures must be accompanied by the corresponding digital file (.tif, .jpg, .pcx, etc.). All figures (graphs, line drawings, photographs, etc.) shall be numbered consecutively and have a caption consisting of the figure number and a brief title or description of the figure. This number should be used when referring to the figure in text. Photographs should be black and white, sharp, high contrasted and printed on glossy paper.

Tables shall be numbered consecutively in Arabic and have a caption consisting of the table number and a brief title. This number should be used when referring to the table in the text. Units should be indicated in the first line of the table, below the title of each column. Acronyms should be avoided. When applicable, the units should come right below the corresponding column heading. Additional comments can be placed as footnotes.

Equations shall appear isolated in a single line of the text. Numbers identifying equations must be flushed with the right margin. International System (SI) units must be used. The definitions of the symbols used in the

equations must appear in the List of Symbols. It is recommended that the symbols used are in accordance with Lexicon in 8 Languages, ISSMFE (1981) and the ISRM List of Symbols.

The text of the submitted manuscript (including figures, tables and references) intended to be published as an article paper or a case history should not contain more than 30 pages, formatted according to the instructions mentioned above. Technical notes and discussions should have no more than 15 and 8 pages, respectively. Longer manuscripts may be exceptionally accepted if the authors provide proper explanation for the need of the required extra space in a cover letter.

Discussion

Discussions must be written in English. The first page of a discussion should contain:

The title of the paper under discussion;

Name of the author(s) of the discussion, followed by their position, affiliation, address and e-mail. The author(s) of the discussion should refer to himself (herself/themselves) as the reader(s) and to the author(s) of the paper as the author(s).

Figures, tables and equations should be numbered following the same sequence of the original paper. All instructions previously mentioned for the preparation of article papers, case studies and technical notes also apply to the preparation of discussions.

Editorial Review

Each paper will be evaluated by reviewers selected by the editors according to the subject of the paper. The authors will be informed about the results of the review process. If the paper is accepted, the authors will be required to submit a version of the revised manuscript with the suggested modifications. If the manuscript is rejected for publication, the authors will be informed about the reasons for rejection. In any situation comprising modification of the original text, classification of the manuscript in a category different from that proposed by the authors, or rejection, the authors can reply presenting their reasons for disagreeing with the reviewer comments.

Submission

The author(s) must upload a digital file of the manuscript to the Soils and Rocks website.

Follow Up

The online management system will provide a password to the corresponding author, which will enable him/her to follow the reviewing process of the submitted manuscript at the Soils and Rocks website.

Volume 39, N. 2, May-August 2016

Table of Contents